

**MARCHENKO-TYPE FOCUSING FUNCTIONS:
GENERALISATION, MODELLING AND IMAGING**

Leon Daniel DIEKMANN

Utrecht Studies in Earth Sciences
No. 285

ISBN: 978-90-6266-655-3

DOI: <https://doi.org/10.33540/1817>

Copyright © 2023, Leon Daniel Diekmann, Universiteit Utrecht

MARCHENKO-TYPE FOCUSING FUNCTIONS: GENERALISATION, MODELLING AND IMAGING

**MARCHENKO FOCUSFUNCTIES: GENERALISATIE,
MODELLEREN EN BEELDVORMING**
(met een samenvatting in het Nederlands)

Proefschrift

ter verkrijging van de graad van doctor aan de Universiteit Utrecht
op gezag van de rector magnificus, prof. dr. H.R.B.M. Kummeling,
ingevolge het besluit van het college voor promoties in het openbaar
te verdedigen op

woensdag 28 juni 2023 des middags te 4.15 uur

door

Leon Daniel DIEKMANN

geboren op 8 oktober 1993 te Erlangen, Duitsland

Promotor: prof. dr. J.A. Trampert

Copromotor: dr. I. Pires de Vasconcelos

Beoordelingscommissie: prof. dr. A. Curtis
prof. dr. A. Malcolm
prof. dr. E.C. Slob
prof. dr. R. Snieder
prof. dr. ir. C.P.A. Wapenaar

This thesis was accomplished with financial support from the Utrecht Consortium for Subsurface Imaging (UCSI).

Für meine Eltern

SUMMARY

Imaging is a field of mathematics and physics that aims to retrieve information about the internal structure of an object that can only be accessed on its boundary. Many imaging methods are based on the following principle: a source outside of the object emits a wave. The wave propagates through the object. Wherever the physical structure of the object changes, scattered waves are induced. These scattered waves are measured by receivers outside of the object, and these scattered data are used to invert for the interior composition, e.g. the scattering potential, of the medium under investigation.

The Marchenko integral was originally introduced for one-dimensional inverse scattering problems in the context of quantum mechanics. It can be related to Green's functions and so-called focusing functions – fields that produce a focus when injected into a medium from a single side. This quality of single-sided focusing is quite intriguing: by using the Marchenko equation one can record scattered data on only one side of an object and still retrieve a reliable image of its internal structure. About ten years ago, the Marchenko integral was extended to two and three dimensions. This paved the way for various new applications, particularly in geophysical imaging. Such applications involve the elimination of imaging artefacts due to multiple scattering and Green's function retrieval for virtual source locations, but a direct relation between the multidimensional Marchenko equation and the scattering potential is yet to be discovered. Furthermore, the extension to multiple dimensions is associated with limitations due to, e.g. wavefield decomposition, a technique that separates waves based on their direction of propagation. Hence, many questions about the full potential as well as the accuracy of the Marchenko equation in two and three dimensions remain unanswered.

In this thesis we present a new derivation for the multidimensional Marchenko integral. Our derivation is based on a generalised framework for wavefield focusing and circumvents the limiting assumptions of the previous extension. As we use partial differential equations rather than integral equations to define focusing functions, it allows for new physical insights. For instance, our approach indicates that it is possible to model Marchenko-type focusing functions with a conventional wave equation. Being able to model Marchenko-type focusing functions is crucial for understanding them. Ultimately, this enables us to study Marchenko-type focusing in different 2D and 3D media and learn about the accuracy of the concept. We develop different strategies for modelling Marchenko-type focusing functions in this thesis, all of which are consistent with our new focusing framework. We present a straightforward approach for 1D as well as a least-squares modelling approach for 2D and 3D. The latter suggests that the Marchenko integral might be inherently approximative in multiple dimensions. How good the approximation is, depends on the structure of the medium under investigation and the underlying acquisition surface. We also discuss Green's function retrieval with our newly derived Marchenko integral, i.e. without wavefield decomposition. This method allows for estimating Green's functions for virtual sources inside of

the medium. While it requires single-sided scattering data and an estimate of the first arrival of the desired Green's function there is no need to have an actual source or receiver inside of the medium. Our results demonstrate that we can retrieve good estimates of the full-spectrum Green's functions, involving evanescent and refracted waves, which were believed to not be retrievable with the previously derived Marchenko integral. The degree to which these wave types can be retrieved, however, heavily depends on the quality of the prior knowledge. Ultimately, we discuss imaging with these Marchenko-based Green's functions. Being able to include measurements for virtual sources inside of the medium allows for a natural linearisation of the imaging problem. Thus we use the Marchenko integral to linearise state-of-the-art imaging approaches, similar to full waveform inversion or least-squares reverse time migration, and estimate the scattering potential. Conventionally, this imaging problem is linearised by ignoring multiple scattering. Our Marchenko-based linearisation accounts for all orders of scattering and performs slightly better than a single-scattering approximation.

SAMENVATTING

Beeldvorming is een gebied van wis- en natuurkunde met als doel informatie te verkrijgen over de interne structuur van een object dat alleen op zijn randen kan worden onderzocht. Veel beeldvormende methoden zijn gebaseerd op het volgende principe: een bron buiten het object zendt een golf uit. De golf plant zich voort door het object. Overal waar de fysieke structuur van het object verandert, worden verstrooide golven geïnduceerd. Deze verstrooide golven worden gemeten door ontvangers buiten het object, en deze verstrooiing gegevens worden gebruikt om te inverteren voor de interne samenstelling, het verstrooiingspotentieel, van het onderzochte medium.

De Marchenko-integraal werd oorspronkelijk geïntroduceerd in de context van de kwantummechanica voor eendimensionale inverse verstrooiingsproblemen. Het relateert de Greense functies aan zogenoemde focusfuncties – golfvelden die een focus produceren wanneer ze vanaf één kant in een medium worden uitgezonden. De eigenschap van dit enkelzijdig focussen is behoorlijk intrigerend: door de Marchenko-vergelijking te gebruiken, kan men verstrooiingsgegevens vastleggen aan slechts één kant van een object en toch een betrouwbaar beeld krijgen van de interne structuur. Ongeveer tien jaar geleden werd de Marchenko-integraal uitgebreid naar twee en drie dimensies. Dit maakte de weg vrij voor verschillende nieuwe toepassingen, met name in geofysische beeldvorming. Dergelijke toepassingen omvatten het elimineren van beeldartefacten als gevolg van meervoudige verstrooiing en het verkrijgen van de Greense functie voor virtuele bronlocaties. Een directe relatie tussen de multidimensionale Marchenko-vergelijking en het verstrooiingspotentieel moet echter nog worden ontdekt. Verder gaat de uitbreiding naar meerdere dimensies gepaard met beperkingen als gevolg van bijvoorbeeld golfvelddecompositie, een techniek die golven scheidt op basis van hun voortplantingsrichting. Daarom zijn veel vragen over het volledige potentieel en de nauwkeurigheid van de Marchenko-vergelijking in twee en drie dimensies nog onbeantwoord.

In dit proefschrift presenteren we een nieuwe afleiding voor de multidimensionale Marchenko-integraal. Onze afleiding is gebaseerd op een algemeen raamwerk voor golfveldfocusering en omzeilt de beperkende aannames van de vorige uitbreiding. Door in plaats van integraalvergelijkingen partiële differentiaalvergelijkingen te gebruiken voor het definiëren van focusfuncties, ontstaan er nieuwe fysische inzichten. Onze benadering laat bijvoorbeeld zien dat het mogelijk is om Marchenko focusfuncties te modelleren met een conventionele golfvergelijking. Dit modelleren is cruciaal voor het begrijpen van de Marchenko focusfuncties. Uiteindelijk stelt dit ons in staat om Marchenko focusering te bestuderen in verschillende twee- en driedimensionale media en meer te weten te komen over de nauwkeurigheid van het concept. In dit proefschrift ontwikkelen we verschillende strategieën voor het modelleren van Marchenko focusfuncties die allemaal consistent zijn met ons nieuwe focusraamwerk. We presenteren een eenvoudige aanpak voor één dimensie, evenals een kleinste-kwadratenbenadering voor twee en drie dimensies. Dit laatste geeft aan dat de Marchenko-integraal inherent benaderend

kan zijn in hogere dimensies. Hoe goed de benadering is, hangt af van de structuur van het onderzochte medium en het onderliggende acquisitieoppervlak. We bespreken ook het verkrijgen van de Greense functie met onze nieuw afgeleide Marchenko-integraal, oftewel zonder golfvelddecompositie. Met deze methode kunnen de Greense functies worden geschat voor virtuele bronnen binnen het medium. Hoewel deze methode enkelzijdige verstrooiingsgegevens vereist en een schatting van de eerste aankomst van de gewenste Greense functie, is het niet nodig om een werkelijke bron of ontvanger in het medium te hebben. Onze resultaten tonen aan dat we goede schattingen kunnen maken van het volledige spectrum van Greense functies, inclusief uitdovende en gerefracteerde golven, waarvan werd aangenomen dat ze niet konden worden bepaald met de eerder afgeleide Marchenko-integraal. Als laatste bespreken we beeldvorming met deze op Marchenko gebaseerde Greense functies. De mogelijkheid om metingen voor virtuele bronnen in het medium op te nemen, zorgt voor een natuurlijke linearisering van het beeldvormingsprobleem. Daarom gebruiken we de Marchenko-integraal om state-of-the-art beeldvormingsbenaderingen te lineariseren, vergelijkbaar met volledige golfvorminversie of kleinste-kwadraten omgekeerde tijdmigratie, en schatten we het verstrooiingspotentieel. Conventioneel wordt dit beeldvormingsprobleem gelineariseerd door meervoudige verstrooiing te negeren. Onze op Marchenko gebaseerde linearisatie houdt rekening met alle ordes van verstrooiing en presteert iets beter dan een enkele verstrooiingsbenadering.

CONTENTS

Summary	vii
Samenvatting	ix
1 Introduction	1
1.1 The inverse scattering problem	1
1.2 The inverse scattering problem in controlled-source seismology	2
1.2.1 Data	3
1.2.2 Model building and imaging	4
1.3 The Marchenko integral.	4
1.4 Motivation	7
1.5 Outline	8
2 Preliminaries	11
2.1 Fourier transform	11
2.2 The wave equation	12
2.3 Rayleigh's reciprocity integral	13
3 Wavefield focusing using a generalised homogeneous Green's function	15
3.1 Introduction	15
3.2 Focusing terminology.	17
3.3 The homogeneous Green's function of the second kind	18
3.4 Examples of focusing functions	22
3.4.1 Trivial focusing functions	25
3.4.2 Focusing functions with a monopole source	25
3.4.3 Focusing functions with a dipole source	27
3.4.4 Time-compact focusing functions	28
3.5 Interferometry and Marchenko-like integrals	38
3.6 Discussion	41
3.7 Conclusion	43
4 Direct modelling of Marchenko-type focusing functions	47
4.1 Introduction	47
4.2 Focusing functions	48
4.3 Marchenko-type focusing functions	50
4.4 Direct, wave-equation-based modelling	51
4.5 Numerical examples	54
4.6 Discussion	55

5	Inverse source design for directional wavefield focusing	59
5.1	Introduction	59
5.2	Green's functions and focusing functions	61
5.3	Marchenko-type focusing functions	62
5.4	Concept of inverse source design	63
5.5	Inverse source design for modelling focusing functions.	64
5.6	Numerical example	68
5.7	A note on extending the method to heterogeneous media	76
5.8	Discussion	76
5.9	Conclusion	78
6	Green's function retrieval in three-dimensional inverse scattering	79
6.1	Introduction	80
6.2	Integral representations for focusing and Green's functions.	81
6.2.1	The homogeneous Green's function of the second kind	82
6.2.2	Integral representations	83
6.3	Solving the Marchenko integral for the Green's function	87
6.4	Numerical example: full wavefield retrieval in a heterogeneous medium	91
6.5	Discussion	97
6.6	Conclusion	100
7	A note on Marchenko-linearised full waveform inversion for imaging	103
7.1	Introduction	103
7.2	Lippmann-Schwinger integral	106
7.3	Marchenko-based Green's function retrieval	108
7.4	Solving the Marchenko-linearised integral for the scattering potential	111
7.5	Numerical examples	118
7.6	Discussion	122
7.7	Conclusion	125
8	Conclusion and outlook	129
	Bibliography	135
	Acknowledgements	149
	Curriculum Vitae	151

1.1. THE INVERSE SCATTERING PROBLEM

When a moving particle or a wave hits an obstacle it is scattered. Such an obstacle could be another particle or a variation of the physical parameters of the material through which the wave is travelling. Understanding the nature of scattering was essential for many fundamental discoveries in physics such as Lord Rayleigh's explanation of the colour of the sky (Rayleigh, 1871) or Ernest Rutherford's finding of the atomic nucleus (Rutherford, 1911). In fact scattering plays an important role in most fields of physics where, e.g., the acoustic, elastic, electro-magnetic or Schrödinger wave equations are studied.

The direct scattering problem refers to the question of how particles or waves are scattered – knowing the exact physical characteristics of the obstacles in the medium under investigation. These physical characteristics are often parametrised in terms of a scattering potential, i.e. a representation of the unknown part of the model relative to a given/known background, but can be described more generally as the physical medium properties.

In contrast to the direct problem, the inverse scattering problem aims to characterise the obstacles by measuring how they scatter particles or waves. The field that underpins all strategies and solutions for retrieving the physical medium properties from measured scattering data is called inverse scattering theory (Colton and Kress, 1998).

Apart from applications in quantum mechanics (Chadan and Sabatier, 2012), inverse scattering theory is particularly important for imaging, a branch of mathematics and physics that deals with resolving the interior properties of a medium that is only accessible from its boundary. A conventional imaging setup can be described as follows: a source outside of the medium of interest emits, e.g., an acoustic wave. This wave propagates through space, penetrates the medium and is scattered. The scattered waves are

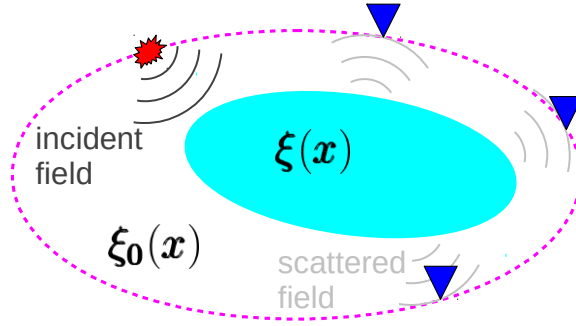


Figure 1.1: Sketch of an inverse scattering experiment. The source is red, the receivers are blue. The medium of interest is cyan and characterised by the variable $\xi(\mathbf{x})$. For an acoustic wave we would for instance have $\xi(\mathbf{x}) = [\rho(\mathbf{x}), c(\mathbf{x})]$, i.e. spatially varying density and wave speed, respectively. Between the acquisition surface (dashed magenta line) and the medium of interest, the volume is characterised by the variable $\xi_0(\mathbf{x})$ which might be a function of space but is assumed to be known.

recorded by receivers outside of the medium. Imaging aims to retrieve the internal physical structure of the medium, i.e. the scattering-inducing obstacles, from these measurements. This is illustrated in Figure 1.1. Note that multiple measurements with sources and receivers at different locations along the acquisition surface are necessary to obtain a reliable image.

Imaging can be based on different physical concepts, e.g., ultrasound or X-ray, and there are various fields of applications. Medical imaging (Szabo, 2004) allows to look into humans and diagnose diseases. Non-destructive testing (Müller et al., 2012) can be used to check the quality and evaluate the properties of materials without breaking them. Geophysical imaging allows for looking into planets, in particular the Earth, to localise resources (Ratcliffe et al., 2011) like hydrocarbons, minerals or groundwater, determine building sites (Soupios et al., 2007) for wind farms, tunnels or pipes, discover and monitor subsurface structures for CO₂ storage (Draganov et al., 2012), detect explosive ordnances (Sullivan et al., 2000) or discover buried archaeological structures (Hildebrand et al., 2002).

In this thesis we discuss the scattering of acoustic waves. Most of our numerical studies are related to geophysical imaging. Since nearly all chapters of this thesis are based on publications and therefore self-contained, we do not aim to deliver an exhaustive review of previous research and literature here – each relevant chapter will come with its own introduction. Instead, we want to introduce some of the key concepts and terms and provide further scientific context for this thesis.

1.2. THE INVERSE SCATTERING PROBLEM IN CONTROLLED-SOURCE SEISMOLOGY

Controlled-source seismology uses seismic sources and receivers for imaging the interior of the Earth. Conventionally, the extent of the target regions is in the order of several

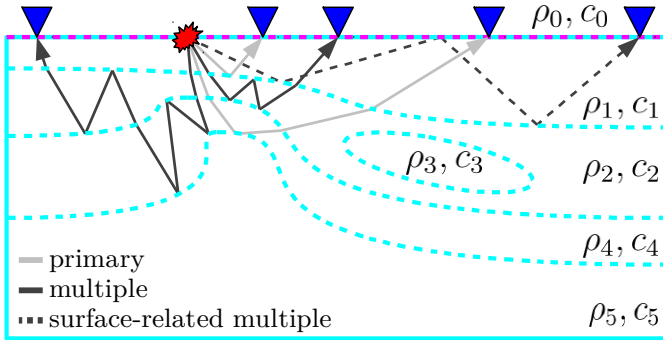


Figure 1.2: Illustration of the inverse scattering experiment for acoustic waves in controlled-source seismology. The source is red, the receivers are blue. The target medium is outlined by the solid cyan line and characterised by densities ρ and wave speeds c . Note that the sharp, distinct layering here is a simplification and serves illustrational purposes. The acquisition surface (dashed magenta line) is limited to the surface of the Earth. The grey arrows denote different reflection paths (we use rays rather than waves for a clear demonstration).

kilometres. The propagation of seismic waves is usually described by the elastic wave equation. Nonetheless, the simpler acoustic wave equation is a good approximation for many applications (Morgan et al., 2013).

1.2.1. DATA

Probably the most crucial and limiting factor that distinguishes geophysical imaging from, e.g., medical imaging is the inaccessibility of a large portion of the target medium's boundary. The regional subsurface of the Earth can only be probed by sources and receivers on its regional surface, such that targets in geophysical imaging can not usually be surrounded by sources and receivers. Hence, one is generally lacking information on how waves are scattered from the sides of the target medium as well as from below the target medium. This is also sketched in Figure 1.2. While boreholes generally allow for a slightly larger acquisition surface they are expensive. This limited accessibility is a challenge in geophysical imaging (Virieux and Operto, 2009).

Another common issue with seismic data is multiple scattering. This refers to waves that are not only scattered once (like primaries) but multiple times before reaching the receivers, see Figure 1.2. These multiply reflected arrivals are briefly referred to as multiples and their presence in seismic data often leads to imaging artefacts as they increase the non-linearity of the inverse scattering problem (Dragoet et al., 2010). Hence, one either aims at removing them from the data or at accurately addressing them via advanced inverse scattering techniques. The latter approach can actually improve the image quality rather than just suppressing artefacts (Malcolm et al., 2009). One often distinguishes between two types of multiples: surface-related multiples and internal multiples. The former are connected to waves that are scattered at the surface of the Earth. These reflections usually have high amplitudes due to the large reflection coefficient at the interface between subsurface and air (Verschuur et al., 1992). Internal multiples on the other hand are only scattered within the subsurface. Owing to the unknown subsurface

structure, predicting and eliminating internal multiples in seismic data tends to be a difficult task (Zhang and Slob, 2019). Hence, in this thesis we focus on the investigation of internal multiple scattering. In order to isolate the impact of internal multiples in our numerical studies we suppress surface-related multiples by using a transparent surface – implying that $\rho_0 = \rho_1$ and $c_0 = c_1$ in Figure 1.2.

Figure 1.3 shows an example of a numerical subsurface model (variable velocity, constant density) and the according seismic data. These seismic data contain many reflections and it is difficult to assign individual reflections to particular interfaces in the model. While the direct scattering problem can be solved by forward modelling with the acoustic wave equation for the given model, the inverse scattering problem requires elaborate inversion strategies.

1.2.2. MODEL BUILDING AND IMAGING

The inverse scattering problem in controlled-source seismology can be separated into two main tasks: (i) obtaining the smooth, long-wavelength model variations, i.e. a version of the model that accurately reproduces the travel times of the different events in the data. This step is usually referred to as model building. (ii) Obtaining the sharp, short-wavelength model variations that induce the scattered waves in the data. This process requires a smooth background model and aims to find the missing perturbations. These perturbations represent the structural image of the Earth – this second step is therefore called imaging.

There are many different strategies for solving the two tasks. Tomography is a common tool for model building (Rawlinson et al., 2010). It requires picked arrival times for particular wave modes, e.g. first arrivals. These picks are then matched by modelled travel times, e.g. using an Eikonal solver. The final tomographic model delivers the best match of modelled and picked travel times. Owing to modern computers, full waveform inversion (Virieux and Operto, 2009) has become a feasible alternative for model building. It does not require any picking but uses the wave equation to model data and directly minimises the misfit between measured and modelled data. However, full waveform inversion needs long-wavelength data including, e.g., diving waves to recover a reliable model.

The image is conventionally obtained by migration (Gray et al., 2001). Migration uses the smooth background model from model building to propagate the data, particularly the high-wavelength content, into the subsurface and locate the scatterers. Similar to model building, migration has evolved with increasing computational powers and shifted from Kirchhoff migration (based on travel times) to least-squares reverse time migration (based on the wave equation).

The line between model building and imaging, however, is blurry: full waveform inversion can retrieve highly resolved models and discover detailed subsurface structures and migration algorithms can be used to refine model information.

1.3. THE MARCHENKO INTEGRAL

The Marchenko integral is an essential equation in inverse scattering theory (Marchenko, 1955). For scattering problems in one dimension it can be used directly to infer the

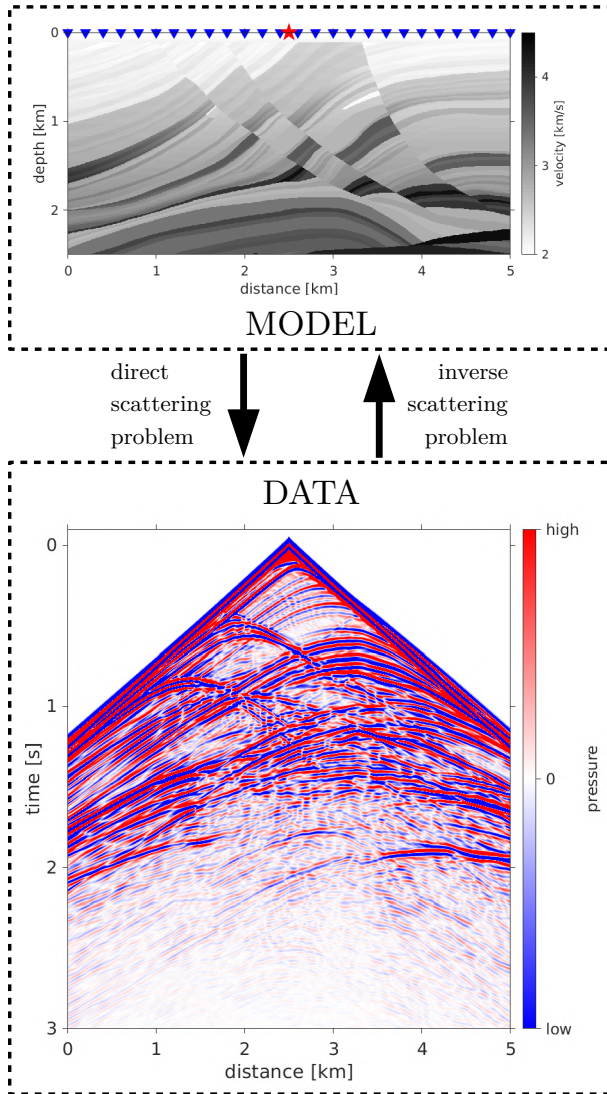


Figure 1.3: Numerical examples of a seismic model (top) and seismic data (bottom). The model is the Marmousi model. We use an acoustic wave equation with constant density and variable wave speed (often called velocity in geophysics) here. The source is red and receivers are blue in the model. Their locations are consistent with the displayed data. Getting the data from the model represents the direct scattering problem (or forward problem), getting the model from the data is the inverse scattering problem (or inverse problem). In order to reliably solve the inverse scattering problem one would require additional data for sources at other locations.

scattering potential from the single-sided measurement of the medium's scattering response. Single-sided implies that both the source and the receiver are at the same side of the unknown model perturbation. For a medium with varying physical parameters in the horizontal direction (1D) this means that the source and the receiver are, e.g., to the left of the model perturbation and measuring the scattered data for this setup is enough to image the interior structure of the unknown portion of the medium (Burridge, 1980). We stress that this relies on a given background model such that the unknown medium properties are spatially localised on one side of the source.

Rose (2001, 2002a,b) investigated the fields within the Marchenko integral and discovered that they focus when injected from a single side of the medium's boundary. This is a rather intriguing observation; conventionally, it was assumed that a wavefield had to be injected from the entire enclosing boundary (meaning both sides in 1D) to create a perfect focus.

Ten years later, Brogini et al. (2012) recognised the relation between the Marchenko integral and the homogeneous Green's function. The homogeneous Green's function (Oristaglio, 1989) is a fundamental wavefield in time reversal acoustics and can be interpreted as follows: the Green's function, that is the medium's response to an impulse source, can not only be obtained by this impulse source but also by injecting the time-reversed Green's function from an enclosing boundary into the medium under investigation – without having an actual source inside of the medium. Hence, the Marchenko integral was found to relate focusing functions (wavefields for single-sided focusing) and Green's functions. Brogini et al. (2012) also indicated the similarity of the Marchenko integral with seismic interferometry (Schuster, 2009). Interferometry also deploys integrals to relate different wavefields, however only including Green's functions, not focusing functions.

Shortly after these new insights, Wapenaar et al. (2013) extended the Marchenko integral to 2D and 3D. This new Marchenko-like integral was designed for a measurement setup similar to that in Figure 1.2 (a single-sided experiment in 2D and 3D). Hence, it was a significant step forward for multidimensional imaging problems in controlled-source seismology and triggered many applications.

The most prominent application in this thesis is Marchenko-based Green's function retrieval (Wapenaar et al., 2014b). It allows for estimating Green's function measurements at the receivers (on the surface of the Earth) for virtual source locations anywhere inside of the medium (in the subsurface). They are called virtual source locations for there are no actual sources inside the medium. Apart from the reflection data, this Marchenko-based Green's function retrieval only requires one additional ingredient: the first arrival of the desired Green's function. This first arrival is usually estimated by modelling in a smooth background medium (obtained via model building). The final Marchenko-based Green's functions, however, include all orders of scattering. This is what makes the approach so powerful: knowing a smooth background medium allows for modelling the first arrival, but due to the smoothness of the model one can not retrieve any scattering. The Marchenko integral on the other hand, retrieves the full Green's function with all primaries and multiples. This paves the way for, e.g., artefact-free imaging (Wapenaar et al., 2014b) by correctly addressing internal multiples in the data. Other applications include multiple elimination (Zhang and Slob, 2019), target-oriented imaging (Ravasi

et al., 2016; Cui et al., 2020) or monitoring (Brackenhoff et al., 2019a). This is also what sets the Marchenko integral apart from conventional interferometric integrals: by involving focusing functions rather than only Green's functions, one can use it to estimate Green's functions for virtual sources and receivers, while conventional interferometric integrals require actual, physical sources and receivers.

1.4. MOTIVATION

There are several open questions regarding the Marchenko integral and its role in imaging, in particular in multiple dimensions. The key ingredients to this integral are the **Marchenko-type focusing functions**, i.e. wavefields that focus when injected from a single side of the medium.

- **Generalisation:** Can we generalise the concept of Marchenko-type focusing?

The extension of the Marchenko integral to 2D and 3D comes with several limitations (Wapenaar et al., 2014b). Evanescent and refracted waves are excluded from the retrievable Green's functions due to a so-called up-/down-decomposition of wavefields and a truncated medium assumption in the derivation. The former technique is related to separating wavefields according to their direction of propagation, the latter to the concept of a medium that is reflection-free underneath the location of the virtual source of the Green's function. Furthermore, recent research points towards Marchenko-type integrals for other acquisition surfaces, not just a horizontal surface like that in Figure 1.2 (Meles et al., 2019b; Kiraz et al., 2020). And the relation between conventional seismic interferometry and the Marchenko integral still has to be fully understood.

Hence, we want to develop a new framework for focusing functions that circumvents previous limitations, generalises earlier focusing concepts, e.g., to account for arbitrary acquisition surfaces and relates the Marchenko integral with seismic interferometry.
- **Modelling:** Can we model Marchenko-type focusing functions?

While the Marchenko integral appears to deliver good approximations of Green's functions in various media, its limitations are not quite understood. Complicated, heterogeneous media are found to be a challenge (Vasconcelos and Sripanich, 2019), but precisely why the Marchenko integral would fail in 2D and 3D or to what extent it is a good approximation is unclear.

Consequently, we aim to investigate ways for modelling Marchenko-type focusing functions. Modelling Marchenko-type focusing functions and studying their behaviour in different heterogeneous media can help to understand the validity of the Marchenko integral in multiple dimensions.
- **Imaging:** Can we use the Marchenko integral for imaging?

We explained above that the Marchenko integral can be used directly for estimating the scattering potential in 1D. In multiple dimensions, however, this does not yet seem possible. Nonetheless, combining state-of-the-art algorithms like full waveform inversion or least-squares reverse time migration with the Marchenko

integral could be a powerful imaging tool. Correctly addressing multiple scattering might suppress artefacts and increase image resolution.

We propose to use Marchenko-based Green's functions for imaging. Including the estimated data for these virtual sources that are inside of the medium could help to linearise the inverse problem.

These main research items are also reflected in the title: We aim to generalise Marchenko-type focusing functions, model them and use them for imaging.

1.5. OUTLINE

In **Chapter 2** we present the basic equations that underlie all of the following chapters. These fundamental equations are consistently used throughout the thesis. In particular we introduce Rayleigh's reciprocity integral which plays an essential role in seismic interferometry.

We introduce a new derivation for the Marchenko integral in multiple dimensions in **Chapter 3**. Our new derivation is based on seismic interferometry and partial differential equations for focusing functions and Green's functions rather than directly relying on integral equations. This generalises the concept of focusing and allows for a new understanding of the Marchenko equation and an improved physical intuition. Furthermore, this new derivation circumvents up-/down-decomposition of the wavefields in the Marchenko integral, a limitation that previous derivations were built upon. Using partial differential equations also indicates that modelling Marchenko-type focusing functions should in principle be possible. We illustrate this with 1D examples in this chapter. The chapter was published as Diekmann et al. (2023c).

Chapter 4 presents a straightforward, one-step approach for modelling Marchenko-type focusing functions in 1D. The approach is based on our partial differential equations for focusing functions. This new modelling scheme is significantly simpler than previous methods as it does not require any recursive or sequential computations. The content of this chapter was published as Diekmann and Vasconcelos (2023).

Building on these findings, we discuss a method for modelling Marchenko-type focusing functions in 2D and 3D in **Chapter 5**. This technique is based on a least-squares approach for designing sources such that the related wavefields have particular, desired properties. We refer to this as inverse source design. While this technique is potentially interesting for other applications as well, we discuss using it for modelling Marchenko-type focusing functions. We focus on investigating modelling in homogeneous media but also discuss modelling in arbitrarily heterogeneous media. Owing to this new modelling strategy we are able to evaluate the accuracy of assumptions/approximations that form the basis for the Marchenko integral in multiple dimensions. The chapter is under review as Diekmann et al. (2023a).

Chapter 6 discusses the derivation of the Marchenko integral based on our new partial-differential-equation framework and a method for retrieving Green's functions from this Marchenko integral without up-/down-decomposition. This Green's function retrieval method requires some knowledge on the first arrival of the Green's function that can be obtained from, e.g., modelling in a smooth background medium. It allows for estimating Green's functions for virtual sources inside of an inaccessible half-space when

measuring the reflection response on the boundary of the half-space. We discuss and illustrate the effect of the quality of the background model on the retrieved Green's functions. Additionally, we show how these Green's functions contain all types of waves that were assumed to not be retrievable from the previously derived Marchenko integral, i.e. refracted and evanescent waves. The chapter was published as Diekmann and Vasconcelos (2021b).

Finally, in **Chapter 7** we propose a way for linearised imaging by full waveform inversion. The linearisation of this generally non-linear inverse problem is achieved by using Marchenko-derived Green's functions in the kernel of the Lippmann-Schwinger integral. In this context, we discuss the Lippmann-Schwinger and the Marchenko integral. We demonstrate how different a priori information on the desired models affects the inverted images. Furthermore, we compare our Marchenko-based linearisation with a conventional single-scattering approximation. The content of this chapter was published as Diekmann et al. (2023b).

Chapter 8 concludes this thesis by summarising its key insights and discussing possible directions for future research.

Most of the chapters in this thesis are published or under review for publication in peer-reviewed journals. Being stand-alone publications, these chapters contain partially redundant descriptions of previous research or explanations of theory. I, as the first author of all of these chapters, did the derivations, the coding, the analysis and the writing of the original chapters. Co-authors that contributed to this thesis are Ivan Vasconcelos, Kees Wapenaar, Roel Snieder, Evert Slob and Tristan van Leeuwen. These co-authors helped by initiating important discussions, providing feedback and input on writing and supervising me.

In this chapter we introduce fundamental theory that underlies all of the following chapters. In particular we aim to derive the wave equation and Rayleigh's reciprocity integral. As we will switch between time- and frequency-domain notations throughout this manuscript, we start by establishing a common Fourier convention.

2.1. FOURIER TRANSFORM

The Fourier transform of a time-domain function $u(\mathbf{x}, t)$ is given by

$$u(\mathbf{x}, \omega) = \mathcal{F}(u(\mathbf{x}, t)) = \int_{-\infty}^{\infty} u(\mathbf{x}, t) \exp(i\omega t) dt \quad , \quad (2.1)$$

where $\mathbf{x} = [x_1 \ x_2 \ x_3]^T$ is space and the exponent T denotes the transpose, t is time and ω is angular frequency. Furthermore, we have the imaginary unit $i = \sqrt{-1}$. Similarly, we have the inverse Fourier transform

$$u(\mathbf{x}, t) = \mathcal{F}^{-1}(u(\mathbf{x}, \omega)) = \frac{1}{2\pi} \int_{-\infty}^{\infty} u(\mathbf{x}, \omega) \exp(-i\omega t) d\omega \quad . \quad (2.2)$$

Regarding the Fourier transform of a time derivative of the function $u(\mathbf{x}, t)$, above Fourier convention leads to

$$\mathcal{F}\left(\frac{\partial}{\partial t} u(\mathbf{x}, t)\right) = \int_{-\infty}^{\infty} \left(\frac{\partial}{\partial t} u(\mathbf{x}, t)\right) \exp(i\omega t) dt \quad (2.3)$$

$$= [u(\mathbf{x}, t) \exp(i\omega t)]_{-\infty}^{\infty} - i\omega \int_{-\infty}^{\infty} u(\mathbf{x}, t) \exp(i\omega t) dt \quad (2.4)$$

$$= -i\omega u(\mathbf{x}, \omega) \quad , \quad (2.5)$$

where we use integration by parts and assume that $\lim_{t \rightarrow \pm\infty} u(\mathbf{x}, t) = 0$. Analogously, we obtain

$$\mathcal{F}\left(\frac{\partial^2}{\partial t^2} u(\mathbf{x}, t)\right) = -\omega^2 u(\mathbf{x}, \omega) \quad . \quad (2.6)$$

Equations 2.5 and 2.6 are important identities that will be used repeatedly in this manuscript to investigate partial differential equations in both the time and the frequency domain.

2.2. THE WAVE EQUATION

We start with the equation of motion

$$\nabla p(\mathbf{x}, t) + \rho(\mathbf{x}) \frac{\partial \mathbf{v}(\mathbf{x}, t)}{\partial t} = \mathbf{f}(\mathbf{x}, t) \quad (2.7)$$

and the deformation equation

$$\nabla \cdot \mathbf{v}(\mathbf{x}, t) + \kappa(\mathbf{x}) \frac{\partial p(\mathbf{x}, t)}{\partial t} = q(\mathbf{x}, t) \quad , \quad (2.8)$$

where we used the low-velocity approximations of the constitutive relations (Fokkema and van den Berg, 1993; Shearer, 2009). We have the Nabla operator

$$\nabla = \left[\frac{\partial}{\partial x_1} \quad \frac{\partial}{\partial x_2} \quad \frac{\partial}{\partial x_3} \right]^T \quad , \quad (2.9)$$

the pressure field $p(\mathbf{x}, t)$, density $\rho(\mathbf{x})$, particle velocity field

$$\mathbf{v}(\mathbf{x}, t) = [v_1(\mathbf{x}, t) \quad v_2(\mathbf{x}, t) \quad v_3(\mathbf{x}, t)]^T \quad (2.10)$$

and compressibility $\kappa(\mathbf{x}) = 1/(\rho(\mathbf{x})c^2(\mathbf{x}))$, where $c(\mathbf{x})$ is wave speed. The terms $\mathbf{f}(\mathbf{x}, t) = [f_1(\mathbf{x}, t) \quad f_2(\mathbf{x}, t) \quad f_3(\mathbf{x}, t)]^T$ and $q(\mathbf{x}, t)$ are sources of volume force density and volume injection rate density, respectively.

In the frequency domain, above equations for motion and deformation become

$$\nabla p(\mathbf{x}, \omega) - i\omega\rho(\mathbf{x})\mathbf{v}(\mathbf{x}, \omega) = \mathbf{f}(\mathbf{x}, \omega) \quad (2.11)$$

and

$$\nabla \cdot \mathbf{v}(\mathbf{x}, \omega) - i\omega\kappa(\mathbf{x})p(\mathbf{x}, \omega) = q(\mathbf{x}, \omega) \quad , \quad (2.12)$$

where we make use of Equation 2.5.

Dividing Equation 2.7 by density and applying an additional Nabla operator gives

$$\nabla \cdot \left(\frac{1}{\rho(\mathbf{x})} \nabla p(\mathbf{x}, t) \right) + \nabla \cdot \frac{\partial \mathbf{v}(\mathbf{x}, t)}{\partial t} = \nabla \cdot \left(\frac{1}{\rho(\mathbf{x})} \mathbf{f}(\mathbf{x}, t) \right) \quad . \quad (2.13)$$

Applying a time derivative to Equation 2.8 leads to

$$\nabla \cdot \frac{\partial \mathbf{v}(\mathbf{x}, t)}{\partial t} = \frac{\partial q(\mathbf{x}, t)}{\partial t} - \kappa(\mathbf{x}) \frac{\partial^2 p(\mathbf{x}, t)}{\partial t^2} \quad . \quad (2.14)$$

Plugging this into Equation 2.13 we get the following wave equation

$$\rho(\mathbf{x}) \nabla \cdot \left(\frac{1}{\rho(\mathbf{x})} \nabla p(\mathbf{x}, t) \right) - \frac{1}{c^2(\mathbf{x})} \frac{\partial^2 p(\mathbf{x}, t)}{\partial t^2} = \rho(\mathbf{x}) \nabla \cdot \left(\frac{1}{\rho(\mathbf{x})} \mathbf{f}(\mathbf{x}, t) \right) - \rho(\mathbf{x}) \frac{\partial q(\mathbf{x}, t)}{\partial t} \quad . \quad (2.15)$$

If there are no force sources the equation simplifies to

$$\rho(\mathbf{x}) \nabla \cdot \left(\frac{1}{\rho(\mathbf{x})} \nabla p(\mathbf{x}, t) \right) - \frac{1}{c^2(\mathbf{x})} \frac{\partial^2 p(\mathbf{x}, t)}{\partial t^2} = -\rho(\mathbf{x}) \frac{\partial q(\mathbf{x}, t)}{\partial t} \quad . \quad (2.16)$$

In the frequency domain this is

$$\rho(\mathbf{x}) \nabla \cdot \left(\frac{1}{\rho(\mathbf{x})} \nabla p(\mathbf{x}, \omega) \right) + \frac{\omega^2}{c^2(\mathbf{x})} p(\mathbf{x}, \omega) = \rho(\mathbf{x}) i\omega q(\mathbf{x}, \omega) \quad . \quad (2.17)$$

2.3. RAYLEIGH'S RECIPROCITY INTEGRAL

Let us consider two different wave states. These wave states can differ in terms of fields, sources and medium parameters. We will use frequency domain representations in the following for the derivation of Rayleigh's reciprocity theorem can be written more compactly in the frequency than in the time domain. The first wave state is denoted by

$$p^A(\mathbf{x}, \omega) \quad , \quad \mathbf{v}^A(\mathbf{x}, \omega) \quad , \quad q^A(\mathbf{x}, \omega) \quad , \quad \mathbf{f}^A(\mathbf{x}, \omega) \quad , \quad \rho^A(\mathbf{x}) \quad \text{and} \quad \kappa^A(\mathbf{x}) \quad . \quad (2.18)$$

For the second state we use

$$p^B(\mathbf{x}, \omega) \quad , \quad \mathbf{v}^B(\mathbf{x}, \omega) \quad , \quad q^B(\mathbf{x}, \omega) \quad , \quad \mathbf{f}^B(\mathbf{x}, \omega) \quad , \quad \rho^B(\mathbf{x}) \quad \text{and} \quad \kappa^B(\mathbf{x}) \quad . \quad (2.19)$$

Considering the frequency-domain equations for motion, Equation 2.11, and deformation, Equation 2.12, this leads a total of four equations for the two different wave states. Multiplication with $\mathbf{v}^B(\mathbf{x}, \omega)$, $p^B(\mathbf{x}, \omega)$, $\mathbf{v}^A(\mathbf{x}, \omega)$ and $p^A(\mathbf{x}, \omega)$, respectively, leads to

$$\mathbf{v}^B(\mathbf{x}, \omega) \cdot \nabla p^A(\mathbf{x}, \omega) - i\omega \rho^A(\mathbf{x}) \mathbf{v}^B(\mathbf{x}, \omega) \cdot \mathbf{v}^A(\mathbf{x}, \omega) = \mathbf{v}^B(\mathbf{x}, \omega) \cdot \mathbf{f}^A(\mathbf{x}, \omega) \quad (2.20)$$

$$p^B(\mathbf{x}, \omega) \nabla \cdot \mathbf{v}^A(\mathbf{x}, \omega) - i\omega \kappa^A(\mathbf{x}) p^B(\mathbf{x}, \omega) p^A(\mathbf{x}, \omega) = p^B(\mathbf{x}, \omega) q^A(\mathbf{x}, \omega) \quad (2.21)$$

$$\mathbf{v}^A(\mathbf{x}, \omega) \cdot \nabla p^B(\mathbf{x}, \omega) - i\omega \rho^B(\mathbf{x}) \mathbf{v}^A(\mathbf{x}, \omega) \cdot \mathbf{v}^B(\mathbf{x}, \omega) = \mathbf{v}^A(\mathbf{x}, \omega) \cdot \mathbf{f}^B(\mathbf{x}, \omega) \quad (2.22)$$

$$p^A(\mathbf{x}, \omega) \nabla \cdot \mathbf{v}^B(\mathbf{x}, \omega) - i\omega \kappa^B(\mathbf{x}) p^A(\mathbf{x}, \omega) p^B(\mathbf{x}, \omega) = p^A(\mathbf{x}, \omega) q^B(\mathbf{x}, \omega) \quad . \quad (2.23)$$

Next, we add Equations 2.20 and 2.23 and subtract Equations 2.21 and 2.22. Making use of

$$\begin{aligned} \mathbf{v}^B(\mathbf{x}, \omega) \cdot \nabla p^A(\mathbf{x}, \omega) + p^A(\mathbf{x}, \omega) \nabla \cdot \mathbf{v}^B(\mathbf{x}, \omega) - \mathbf{v}^A(\mathbf{x}, \omega) \cdot \nabla p^B(\mathbf{x}, \omega) - p^B(\mathbf{x}, \omega) \nabla \cdot \mathbf{v}^A(\mathbf{x}, \omega) = \\ \nabla \cdot \left(p^A(\mathbf{x}, \omega) \mathbf{v}^B(\mathbf{x}, \omega) - p^B(\mathbf{x}, \omega) \mathbf{v}^A(\mathbf{x}, \omega) \right) \quad , \quad (2.24) \end{aligned}$$

this leads

$$\begin{aligned} \nabla \cdot \left(p^A(\mathbf{x}, \omega) \mathbf{v}^B(\mathbf{x}, \omega) - p^B(\mathbf{x}, \omega) \mathbf{v}^A(\mathbf{x}, \omega) \right) = \\ \mathbf{v}^B(\mathbf{x}, \omega) \cdot \mathbf{f}^A(\mathbf{x}, \omega) + p^A(\mathbf{x}, \omega) q^B(\mathbf{x}, \omega) - p^B(\mathbf{x}, \omega) q^A(\mathbf{x}, \omega) - \mathbf{v}^A(\mathbf{x}, \omega) \cdot \mathbf{f}^B(\mathbf{x}, \omega) \\ + i\omega p^A(\mathbf{x}, \omega) p^B(\mathbf{x}, \omega) (\kappa^B(\mathbf{x}) - \kappa^A(\mathbf{x})) - i\omega \mathbf{v}^A(\mathbf{x}, \omega) \cdot \mathbf{v}^B(\mathbf{x}, \omega) (\rho^B(\mathbf{x}) - \rho^A(\mathbf{x})) \quad . \quad (2.25) \end{aligned}$$

Finally, we integrate over a volume V bounded by ∂V and use Gauss's theorem to obtain

$$\begin{aligned} \int_{\tilde{\mathbf{x}} \in \partial V} \left(p^A(\tilde{\mathbf{x}}, \omega) \mathbf{v}^B(\tilde{\mathbf{x}}, \omega) - p^B(\tilde{\mathbf{x}}, \omega) \mathbf{v}^A(\tilde{\mathbf{x}}, \omega) \right) \cdot d\mathbf{S} = \\ \int_{\mathbf{x} \in V} \left(\mathbf{v}^B(\mathbf{x}, \omega) \cdot \mathbf{f}^A(\mathbf{x}, \omega) + p^A(\mathbf{x}, \omega) q^B(\mathbf{x}, \omega) - p^B(\mathbf{x}, \omega) q^A(\mathbf{x}, \omega) - \mathbf{v}^A(\mathbf{x}, \omega) \cdot \mathbf{f}^B(\mathbf{x}, \omega) \right) dV \\ + \int_{\mathbf{x} \in V} \left(i\omega p^A(\mathbf{x}, \omega) p^B(\mathbf{x}, \omega) (\kappa^B(\mathbf{x}) - \kappa^A(\mathbf{x})) - i\omega \mathbf{v}^A(\mathbf{x}, \omega) \cdot \mathbf{v}^B(\mathbf{x}, \omega) (\rho^B(\mathbf{x}) - \rho^A(\mathbf{x})) \right) dV, \quad (2.26) \end{aligned}$$

where $\tilde{\mathbf{x}}$ is on the boundary ∂V . This is Rayleigh's reciprocity theorem for acoustic waves (Rayleigh, 1894; Fokkema and van den Berg, 1993). It forms the basis for many applications in seismic interferometry (Wapenaar et al., 2010a,b). When transforming it to the time domain, multiplications of frequency-domain functions become convolutions.

WAVEFIELD FOCUSING USING A GENERALISED, POTENTIALLY ASYMMETRIC HOMOGENEOUS GREEN'S FUNCTION

Marchenko-type integrals typically relate so-called focusing functions and Green's functions via the reflection response measured on the open surface of a volume of interest. Originating from one dimensional inverse scattering theory, the extension to two and three dimensions set in motion various new developments regarding imaging in complex materials. This extension, however, is based on wavefield decomposition inside the volume and a truncated medium state, i.e. a version of the medium that is reflection-free underneath the focusing location, suggesting that evanescent, refracted and diving waves can not be included in the representation. We elaborate on a new derivation for Marchenko-like integrals that (i) extends the concept of wavefield focusing by using a generalised homogeneous Green's function, (ii) is based on partial differential equations and thereby allows for additional insights and a new physical intuition for Marchenko equations, (iii) unifies wavefield focusing for open and closed boundary systems, (iv) does not require wavefield decomposition or a truncated medium state, thus including the full wavefield Green's function, (v) enables using forward modelling to obtain, e.g., Marchenko-type, time-compact focusing functions. We place a particular focus on the latter point, illustrating and investigating how to solve the underlying partial differential equations for various types of focusing functions. This paves the way for a deeper understanding of focusing functions as well as advanced full wavefield Marchenko schemes. While the derivations are generally presented for the 3D case, we show numerical examples in 1D.

3.1. INTRODUCTION

Inverse scattering theory (Chadan and Sabatier, 2012; Colton and Kress, 1998) is a field of mathematical physics that aims to retrieve the physical properties of a medium based on its remotely observed scattering response to, e.g., acoustic, seismic or electro-magnetic

The content of this chapter was published as Diekmann et al. (2023c).

waves. It is relevant to, for instance, quantum mechanics (Deift and Trubowitz, 1979), optics (Jost, 2012), geophysics (Weglein et al., 1997; Zuberi and Alkhalifah, 2014; Alkhalifah and Guo, 2019), medical imaging (Shea et al., 2010) and non-destructive testing (Rose, 1989). The Marchenko integral is an essential equation in inverse scattering theory (Marchenko, 1955; Burridge, 1980; Newton, 1980). It is well defined in one dimension, where it can be used to directly infer the medium's scattering potential.

Following investigations of the focusing properties (Rose, 2001, 2002a) of the Marchenko integral and its relation to the homogeneous Green's function (Broggini et al., 2012; Broggini and Snieder, 2012), Wapenaar et al. (Wapenaar et al., 2014a,b) extended the concept to two and three dimensions. While the Marchenko scheme bears similarities with Green's function retrieval via conventional seismic interferometry (Schuster, 2009; Bakulin and Calvert, 2006; Curtis et al., 2006), there are several, significant differences: (i) conventional interferometry allows to retrieve the response to a virtual source at the location of a physical receiver inside of a medium. The Marchenko scheme can be used to obtain the response to a virtual source anywhere in the medium without the need to have an actual, physical receiver at the target location (Broggini et al., 2012). (ii) Conventional interferometric relations involve solely Green's functions, whereas the Marchenko-type representations involve Green's and focusing functions. (iii) Conventional interferometry usually produces artefacts for open boundary (single-sided) representations because the underlying integral equation becomes approximate (Löer et al., 2014; Wapenaar and Thorbecke, 2017). The Marchenko method on the other hand remains accurate even for open boundary integrals (Wapenaar et al., 2017). Hence, the extension of the Marchenko method to two and three dimensions paved the way for various new methodologies and applications, like Marchenko imaging (Wapenaar et al., 2014b), target-oriented imaging (Ravasi et al., 2016), multiple elimination (Zhang and Slob, 2019; Staring and Wapenaar, 2020) and monitoring (Brackenhoff et al., 2019a; van IJsseldijk and Wapenaar, 2021). While most of these applications are for acoustic waves, the Marchenko scheme was recently also extended to elastodynamic waves (da Costa Filho et al., 2014; Reinicke and Wapenaar, 2019; Reinicke et al., 2020; van der Neut et al., 2022).

The extension of the Marchenko method to two and three dimensions also has some drawbacks. For complex, laterally varying media, i.e. inducing complicated wave scattering, the method tends to become unstable and may require further knowledge of the medium properties (Vasconcelos and Sripanich, 2019; Vargas et al., 2021). Furthermore, when using the method for Green's function retrieval one requires an estimate of the first arrival of the Green's function, e.g. from a smooth estimate of the actual medium (Wapenaar et al., 2014a). In addition to these intrinsic limitations, it was until recently assumed that the representation would not include evanescent, refracted and diving waves in the Green's function. This was a consequence of the derivation relying on up-/down-decomposition of the wavefields inside the medium as well as a truncated medium state (Wapenaar et al., 2014b). A first step towards including evanescent waves was made by Wapenaar (Wapenaar, 2020a). Additionally, evanescent and refracted waves were studied in more detail (Reinicke and Wapenaar, 2019; Kiraz et al., 2021a). Recently, a new derivation for a Marchenko-type equation was presented that circumvents these wavefield decomposition assumptions altogether, thus arguing that the Marchenko integral

includes the full wavefield Green's function (Chapter 6). This derivation is different from previous approaches as it is based on a partial differential equation definition for focusing functions. Similar conclusions were presented by Wapenaar et al. (Wapenaar et al., 2021), using a different derivation that is overall closer to previous strategies. Studies for closed boundary Marchenko-like schemes (Meles et al., 2019b) also made the observation that up-/down-decomposition inside the medium is not a necessity (Kiraz et al., 2021b).

In this paper we further extend, discuss and illustrate the novel approach to focusing functions, see Chapter 6 and Diekmann and Vasconcelos (2021b). We follow the original derivation in defining focusing functions by means of a partial differential equation and study the respective source terms in more detail. These source terms were only poorly understood before but play an essential role as they connect the focusing wavefields with the physical medium parameters. Being able to make this connection paves the way for, e.g., modelling reference focusing functions or setting up inversion methods to retrieve medium properties from given focusing functions. Above all, their investigation leads to a deeper understanding of focusing functions within this new framework, going beyond classical, Marchenko-type focusing functions. Based on this definition of focusing functions, we generalise the homogeneous Green's function (Oristaglio, 1989), which represents a fundamental relation between anti-causal and causal field solutions, by presenting the so-called homogeneous Green's function of the second kind (Chapter 6). We illustrate and discuss these homogeneous Green's functions of the second kind, in particular their focusing properties and their relation to the conventional homogeneous Green's function. In this context we compare different classes of focusing functions, illustrated by numerical 1D examples. In particular, we investigate time-compact focusing functions for both double- and single-sided configurations. We use reciprocity theorems to derive Marchenko-like representations for both closed and open boundary integrals based on the underlying homogeneous Green's function of the second kind. These representations do not require any wavefield decomposition inside the medium, i.e. they deliver the full wavefield Green's function. While the numerical examples are in 1D, most of the theory is given for the general three dimensional case.

3.2. FOCUSING TERMINOLOGY

In this section we briefly discuss common terminology in the field of wave focusing. We consider this clarification important as we aim to connect different fields of research (that do not typically use the same terminology) in this paper. Conventionally, the term focus is used to describe a wavefield, e.g. pressure or particle velocity, that is concentrated around a certain point in space at a certain point in time (Rose, 2002b). In other words, if you take a snapshot of such a wavefield at the specific focusing time it will show a field that is collapsed to the area around the specific focusing point in space. The size of this focal area depends on the bandwidth of the wavefield – in the ideal case of infinite bandwidth it reduces to a point. We will refer to this as a focus in space. In time reversal acoustics, the process of injecting a wavefield into a medium in order to obtain such a focus in space is often referred to as time reversal focusing (Fink, 2008). The incident wavefield that yields the focus is sometimes referred to as a focusing field, i.e. a

field that focuses. When the Marchenko scheme was extended to 2D and 3D, the higher dimensional equivalents to solutions in classical 1D derivations (Lamb Jr, 1980) were named focusing functions (Wapenaar et al., 2014a). By definition, these focusing functions are wavefields that collapse to a certain point in time at a certain point in space when injected into a truncated version of the actual medium from an open boundary (Wapenaar et al., 2017). Hence, if you pick the particular focusing point in space and look at the entire wavefield at this location over time it will exhibit what we will call a focus in time. We will illustrate the differences between focusing in space and time in Section 3.4. Furthermore, we want to stress that our definition of focusing functions in this paper as well as our reasoning for calling them such differs from previous work in the context of 2D and 3D Marchenko (Wapenaar et al., 2014a) but is consistent with time reversal acoustics. We will come back to these differences and explain their implications in Sections 3.3 and 3.4.

3.3. THE HOMOGENEOUS GREEN'S FUNCTION OF THE SECOND KIND

In this paper, we investigate acoustic waves in a lossless medium. Most of the concepts, however, in principle generalise to other partial differential equations, e.g. to the case of non-dissipative elastic media (Snieder et al., 2007; Wapenaar and Douma, 2012). The acoustic wave equation is given by

$$\mathcal{L}(\mathbf{x})u(\mathbf{x}, t) = -\rho(\mathbf{x})\frac{\partial}{\partial t}s(\mathbf{x}, t) \quad , \quad (3.1)$$

with the acoustic wave operator

$$\mathcal{L}(\mathbf{x}) = \rho(\mathbf{x})\nabla \cdot \left(\frac{1}{\rho(\mathbf{x})}\nabla \right) - \frac{1}{c^2(\mathbf{x})}\frac{\partial^2}{\partial t^2} \quad , \quad (3.2)$$

where $u(\mathbf{x}, t)$ is the pressure wavefield (in N/m²) at location $\mathbf{x} = (x, y, z)$ and time t , $\rho(\mathbf{x})$ denotes mass density (in kg/m³), $s(\mathbf{x}, t)$ is a source term of volume injection rate density (in 1/s) and $c(\mathbf{x})$ is wave speed (in m/s). We define the Green's function $g(\mathbf{x}, t; \mathbf{x}_f)$ as the causal medium response in terms of acoustic pressure to an impulsive point source at location \mathbf{x}_f and time zero (de Hoop, 1995), i.e.

$$\mathcal{L}(\mathbf{x})g(\mathbf{x}, t; \mathbf{x}_f) = -\rho(\mathbf{x})\delta(\mathbf{x} - \mathbf{x}_f)\frac{\partial}{\partial t}\delta(t) \quad . \quad (3.3)$$

Thus, the time-reversed Green's function $g(\mathbf{x}, -t; \mathbf{x}_f)$ obeys

$$\mathcal{L}(\mathbf{x})g(\mathbf{x}, -t; \mathbf{x}_f) = \rho(\mathbf{x})\delta(\mathbf{x} - \mathbf{x}_f)\frac{\partial}{\partial t}\delta(t) \quad . \quad (3.4)$$

Since we defined $g(\mathbf{x}, t; \mathbf{x}_f)$ as a causal field response, $g(\mathbf{x}, -t; \mathbf{x}_f)$ has to be anti-causal, i.e. it propagates prior to the associated source pulse at $t = 0$. The homogeneous Green's function (Oristaglio, 1989) is the superposition of the Green's function and the time-reversed Green's function, thus obeying

$$\mathcal{L}(\mathbf{x})(g(\mathbf{x}, t; \mathbf{x}_f) + g(\mathbf{x}, -t; \mathbf{x}_f)) = 0 \quad . \quad (3.5)$$

The homogeneous Green's function is thus a source-free wavefield. Let us consider a bounded volume that contains \mathbf{x}_f in a medium that is scattering-free outside the volume. The time-reversed, anti-causal Green's function is then purely in-coming with respect to that volume. It injects energy into the volume. The wavefield focuses at \mathbf{x}_f and $t = 0$ before propagating onwards as the out-going, causal Green's function.

We now establish the auxiliary focal solution $f(\mathbf{x}, t; \mathbf{x}_f, q(\mathbf{x}, t))$ as the causal wavefield that obeys

$$\mathcal{L}(\mathbf{x})f(\mathbf{x}, t; \mathbf{x}_f, q(\mathbf{x}, t)) = \frac{\rho(\mathbf{x})\delta(\mathbf{x} - \mathbf{x}_f)}{2} \frac{\partial}{\partial t} \delta(t) + q(\mathbf{x}, t) \quad , \quad (3.6)$$

where the source function $q(\mathbf{x}, t)$ is in principle arbitrary but is constrained to be symmetric in time, such that $q(\mathbf{x}, t) = q(\mathbf{x}, -t)$, see Chapter 6 and Diekmann and Vasconcelos (2021b). In that sense, we can write any choice of a discrete source distribution $q(\mathbf{x}, t)$ as a superposition of individual sources $q_i(\mathbf{x}, t)$ according to

$$q(\mathbf{x}, t) = \sum_{i=1}^n q_i(\mathbf{x}, t) = \sum_{i=1}^n w_i \rho(\mathbf{x}) (\delta(t - t_i) \star s_i(t) + \delta(t + t_i) \star s_i(-t)) \delta(\mathbf{x} - \mathbf{x}_i) \quad , \quad (3.7)$$

where n is the total number of terms that make up $q(\mathbf{x}, t)$, w_i is a weighting factor, \mathbf{x}_i and t_i are particular locations and times, respectively, $s_i(t)$ is an arbitrary wavelet and the \star denotes convolution. The auxiliary focal solutions being causal means that for each source the energy emittance precedes the energy propagation through the volume – analogously to the definition of the Green's function. Hence, there might be propagating energy before $t = 0$ due to sources in $q(\mathbf{x}, t)$ at negative times. Note that the auxiliary focal solution can be expressed as

$$f(\mathbf{x}, t; \mathbf{x}_f, q(\mathbf{x}, t)) = -\frac{1}{2}g(\mathbf{x}, t; \mathbf{x}_f) + f_q(\mathbf{x}, t; q(\mathbf{x}, t)) \quad , \quad (3.8)$$

where $f_q(\mathbf{x}, t; q(\mathbf{x}, t))$ is the causal medium response to the source distribution $q(\mathbf{x}, t)$. The time-reversed auxiliary focal solution satisfies

$$\mathcal{L}(\mathbf{x})f(\mathbf{x}, -t; \mathbf{x}_f, q(\mathbf{x}, t)) = -\frac{\rho(\mathbf{x})\delta(\mathbf{x} - \mathbf{x}_f)}{2} \frac{\partial}{\partial t} \delta(t) + q(\mathbf{x}, t) \quad . \quad (3.9)$$

As $f(\mathbf{x}, t; \mathbf{x}_f, q(\mathbf{x}, t))$ is purely causal, $f(\mathbf{x}, -t; \mathbf{x}_f, q(\mathbf{x}, t))$ is an anti-causal field. By subtracting Equation 3.9 from Equation 3.6 we get

$$\mathcal{L}(\mathbf{x})\left(f(\mathbf{x}, t; \mathbf{x}_f, q(\mathbf{x}, t)) - f(\mathbf{x}, -t; \mathbf{x}_f, q(\mathbf{x}, t))\right) = \rho(\mathbf{x})\delta(\mathbf{x} - \mathbf{x}_f) \frac{\partial}{\partial t} \delta(t) \quad . \quad (3.10)$$

Using Equation 3.8 this can be written as

$$\begin{aligned} \mathcal{L}(\mathbf{x})\left(-\frac{1}{2}g(\mathbf{x}, t; \mathbf{x}_f) + \frac{1}{2}g(\mathbf{x}, -t; \mathbf{x}_f) + f_q(\mathbf{x}, t; q(\mathbf{x}, t)) - f_q(\mathbf{x}, -t; q(\mathbf{x}, t))\right) = \\ \rho(\mathbf{x})\delta(\mathbf{x} - \mathbf{x}_f) \frac{\partial}{\partial t} \delta(t) \quad . \end{aligned} \quad (3.11)$$

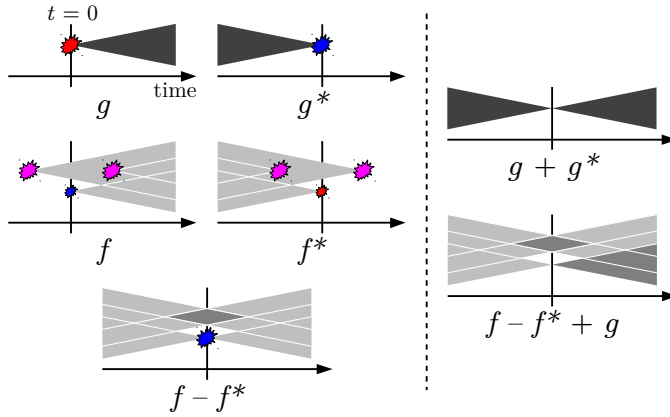


Figure 3.1: Illustration of different wavefield causalities. Cones that open to the right are causal, cones that open to the left are anti-causal. The * denotes time-reversed wavefields. Axis are labelled only in the top left sketch for the sake of a cleaner figure. Wavefields with sources are shown to the left of the dotted vertical line, source-free wavefields are shown to the right of the line. The red and blue explosions denote the source terms related to the Green's function and the time-reversed – opposite sign – Green's function, respectively, where the size of the symbol correlates with the source magnitude. The pink explosions mark the source distribution $q(\mathbf{x}, t)$. Dark grey cones are related to Green's functions, light grey cones to auxiliary focal solutions. The medium grey color indicates interference of either forward and time-reversed auxiliary focal solutions or auxiliary focal solutions and Green's functions. Note that the vertical shift of the pink sources compared to the sources of the Green's functions is arbitrary, solely indicating a potentially different location in space.

Note that Equations 3.10 and 3.11 involve the same wavefield – only the representation of the wavefield is different. The solution of this wave equation obeys the same source term as the time-reversed Green's function, Equation 3.4. However, it is a fundamentally different wavefield. Firstly, it has both causal and anti-causal contributions. Secondly, it is non-unique, i.e. different choices of $q(\mathbf{x}, t)$ lead to different wavefields. Take for instance the trivial case $q(\mathbf{x}, t) = 0$, such that only the Green's functions remain. Equation 3.11 can then be interpreted as describing a source that emits its energy in both time directions, backwards and forwards in time, governing both an anti-causal and a causal Green's function. As the wavefield propagates both forwards and backwards in time, each Green's function comes with a factor of 1/2. Alternatively, we can interpret the wavefields in the sense of purely increasing time as follows: consider a bounded volume that contains \mathbf{x}_f in a medium that is scattering-free outside the volume. The time-reversed, half-amplitude Green's function is then purely in-coming with respect to that volume. The source acts as a sink and absorbs all of the in-coming energy. Furthermore, it emits additional energy into the medium, which then propagates forwards as the outgoing, negative, half-amplitude Green's function. In the general case of $q(\mathbf{x}, t) \neq 0$ we additionally get the field contribution $f_q(\mathbf{x}, t; q(\mathbf{x}, t)) - f_q(\mathbf{x}, -t; q(\mathbf{x}, t))$, which is source-free since the source distributions $q(\mathbf{x}, t)$ cancel each other – analogously to the homogeneous Green's function.

Because Equation 3.10 has the same source term as the time-reversed Green's function, we can obtain a source-free field by adding the Green's function, i.e. we add Equation 3.3

to get

$$\mathcal{L}(\mathbf{x})\left(f(\mathbf{x}, t; \mathbf{x}_f, q(\mathbf{x}, t)) - f(\mathbf{x}, -t; \mathbf{x}_f, q(\mathbf{x}, t)) + g(\mathbf{x}, t; \mathbf{x}_f)\right) = 0 \quad . \quad (3.12)$$

We call the wavefield obeying Equation 3.12 the homogeneous Green's function of the second kind. Just like the homogeneous Green's function in Equation 3.5, the homogeneous Green's function of the second kind is a source-free wavefield that contains the causal Green's function. Note that adding the time-reversed of Equation 3.12 to Equation 3.12 gives the equation for the conventional homogeneous Green's function, Equation 3.5. Consider a bounded volume that contains \mathbf{x}_f in a medium that is scattering-free outside the volume. Furthermore, let $q(\mathbf{x}, t) = 0$ for all \mathbf{x} outside the volume. The negative, time-reversed auxiliary focal solution $-f(\mathbf{x}, -t; \mathbf{x}_f, q(\mathbf{x}, t))$ in Equation 3.12 is then purely in-coming and injects energy into the volume. The resulting wavefield, after focusing or scattering, keeps on propagating as the out-going, causal auxiliary focal solution $f(\mathbf{x}, t; \mathbf{x}_f, q(\mathbf{x}, t))$ and the out-going, causal Green's function. The homogeneous Green's function of the second kind always has a focus in space at \mathbf{x}_f and $t = 0$ – because the only non-zero contribution to the wavefield at zero time stems from the Green's function. In that sense the negative, time-reversed auxiliary focal solution $-f(\mathbf{x}, -t; \mathbf{x}_f, q(\mathbf{x}, t))$ is a focusing field. Just like the time-reversed Green's function in time reversal acoustics it can be injected into a source-free volume to create a focus in space, compare Section 3.2. The name *auxiliary focal solution* refers to the relation of these wavefields to focusing in space. From now on we will call $\phi(\mathbf{x}, t; \mathbf{x}_f, q(\mathbf{x}, t)) = -f(\mathbf{x}, -t; \mathbf{x}_f, q(\mathbf{x}, t))$ a focusing function and $f(\mathbf{x}, t; \mathbf{x}_f, q(\mathbf{x}, t))$ a negative, time-reversed focusing function. Note that the focusing function is an anti-causal field that focuses, whereas the negative, time-reversed focusing function is a causal field that expands.

As we already stated, our nomenclature – referring to the general fact that focusing functions are related to focusing in space – differs from the conventional reasoning, where the name was used for a specific type of function that is related to focusing in time (Wapenaar et al., 2014a). We will later on find these previously introduced functions that focus in time to form a specific subset of our focusing functions.

We can use Equation 3.8 to rewrite the homogeneous Green's function of the second kind as

$$\mathcal{L}(\mathbf{x})\left(\frac{1}{2}g(\mathbf{x}, t; \mathbf{x}_f) + \frac{1}{2}g(\mathbf{x}, -t; \mathbf{x}_f) + f_q(\mathbf{x}, t; q(\mathbf{x}, t)) - f_q(\mathbf{x}, -t; q(\mathbf{x}, t))\right) = 0 \quad , \quad (3.13)$$

highlighting the similarity with the conventional homogeneous Green's function. This representation shows that the homogeneous Green's function of the second kind can in fact be written as a superposition of symmetric and anti-symmetric wavefields in time. The representation in Equation 3.12 on the other hand underlines the potentially asymmetric appearance in time of the homogeneous Green's function of the second kind. Of course one can also construct other homogeneous wavefields in a similar fashion, e.g.

$$\mathcal{L}(\mathbf{x})\left(f(\mathbf{x}, t; \mathbf{x}_f, q(\mathbf{x}, t)) - f(\mathbf{x}, -t; \mathbf{x}_f, q(\mathbf{x}, t)) - g(\mathbf{x}, -t; \mathbf{x}_f)\right) = 0 \quad , \quad (3.14)$$

i.e. by combining focusing and Green's functions. We will, however, focus our discussion in this paper on the homogeneous Green's function of the second kind in Equation 3.12.

In this section we introduced focusing functions. Such focusing functions allow for the construction of the homogeneous Green's function of the second kind, Equation 3.12. All important wavefields are also sketched in Figure 3.1. In the next section we discuss and illustrate different focusing functions.

3.4. EXAMPLES OF FOCUSING FUNCTIONS

In this section we discuss different focusing functions – with the objective of illustrating how our partial differential equation scheme represents physical focusing wave-states including (but not limited to) those obtainable by previous approaches. In that sense, some of the upcoming examples represent entirely new focusing wave states that can only now be investigated by studying source terms $q(\mathbf{x}, t)$ in our new framework. All focusing functions have a fundamental, unifying property: when superimposing the corresponding homogeneous Green's functions of the second kind and their time-reversed counterparts one always obtains the conventional homogeneous Green's functions. This implies that the homogeneous Green's functions of the second kind always have a single delta pulse at the focusing location \mathbf{x}_f and are zero elsewhere at zero time, i.e. the wavefields focus in space. This will also become evident in the examples below.

Despite this property, focusing functions vary significantly in appearance. We discuss four groups in the following: focusing functions for the trivial choice $q(\mathbf{x}, t) = 0$, functions with a simple monopole source, with a simple dipole source, and time-compact focusing functions. The initial, simple examples are used to illustrate fundamental properties of focusing functions and explain how we can enforce interesting interference patterns within the fields. Based on these concepts we can then construct more complex, time-compact focusing functions. The numerical examples are in 1D to allow for optimum illustrations. The concepts that we discuss, however, are not necessarily limited to 1D, although more elaborate schemes might be necessary for higher dimensional investigations, incorporating, e.g., angle-dependent reflectivity and geometrical spreading. In 1D the spatial coordinate \mathbf{x} becomes the scalar x , e.g. the focusing location reads x_f . The numerical examples are based on the velocity and density model in Figure 3.2(a) and consider the point $x_f = 1.15$ km. As a reference for later results, Figure 3.2(b) shows the Green's function for $x_f = 1.15$ km, obtained via finite difference modelling according to Equation 3.3. Note that all wavefields that we show in this paper are convolved with a 20 Hz Ricker wavelet (Ricker, 1953) for improved visualisation. Furthermore, all wavefields are clipped at the same amplitudes as Figure 3.2(b) to allow for a good comparison. Owing to the orientation of the spatial axis in this plot we will refer to leftwards and rightwards travelling events in space. Note, however, that in multiple dimensions it is also common to differentiate between up- and down-going waves in space, corresponding to left- and right-going waves, respectively, in our 1D figures. Figure 3.2(c) gives the respective homogeneous Green's function, obtained by superimposing the field in Figure 3.2(b) and its time-reversed version. Alternatively, the homogeneous Green's function could be obtained by injecting the time-reversed Green's function from the boundary ∂V , i.e. from $x = 0$ km and $x = 2$ km, into the source-free medium. This process is referred to as time reversal acoustics (Fink, 1992, 2008). Using reciprocity and a radiation condition (Schuster, 2009) to get the respective equivalent sources, the homogeneous

Green's function then follows for \mathbf{x} in V by modelling according to

$$\mathcal{L}(\mathbf{x})(g(\mathbf{x}, t; \mathbf{x}_f) + g(\mathbf{x}, -t; \mathbf{x}_f)) = - \int_{\mathbf{x}_r \in \partial V} \frac{2}{c(\mathbf{x}_r)} \delta(\mathbf{x} - \mathbf{x}_r) \frac{\partial}{\partial t} g(\mathbf{x}_r, -t; \mathbf{x}_f) d\mathbf{S} \quad , \quad (3.15)$$

where we assume that V contains \mathbf{x}_f and that the medium is reflection-free outside V (Fokkema and van den Berg, 1993; Snieder and Van Wijk, 2015). However, this modelled homogeneous Green's function might be numerically less accurate than the one we obtain from superimposing the Green's function and its time-reversed version. This is due to the fact that the Green's function generally is a time-infinite field response, i.e. even at very large recording times one might still record multiple scattered events. Consequently, we would have to record the Green's function until the amplitudes of these late arrivals become negligible – otherwise the Green's function is missing energy and injecting its time-reversed version into the medium will not accurately reproduce the homogeneous Green's function. In our numerical example we still have considerable events at 1.5 s, i.e. at the end of the recorded data. Therefore, we choose not to use modelling with Equation 3.15 in order to obtain the best quality reference homogeneous Green's function. Figure 3.2(c) shows the focus in space of the homogeneous Green's function at $t = 0$. Note that owing to the symmetry of the wavefield, the time derivative of the displayed pressure field is zero.

For the homogeneous Green's functions of the second kind on the other hand, we do use time reversal modelling with the goal of actually illustrating the wave propagation through the source-free medium. Similar to Equation 3.15 we then obtain for \mathbf{x} in V

$$\mathcal{L}(\mathbf{x}) \left(f(\mathbf{x}, t; \mathbf{x}_f, q(\mathbf{x}, t)) - f(\mathbf{x}, -t; \mathbf{x}_f, q(\mathbf{x}, t)) + g(\mathbf{x}, t; \mathbf{x}_f) \right) = \int_{\mathbf{x}_r \in \partial V} \frac{2}{c(\mathbf{x}_r)} \delta(\mathbf{x} - \mathbf{x}_r) \frac{\partial}{\partial t} f(\mathbf{x}_r, -t; \mathbf{x}_f, q(\mathbf{x}, t)) d\mathbf{S} \quad , \quad (3.16)$$

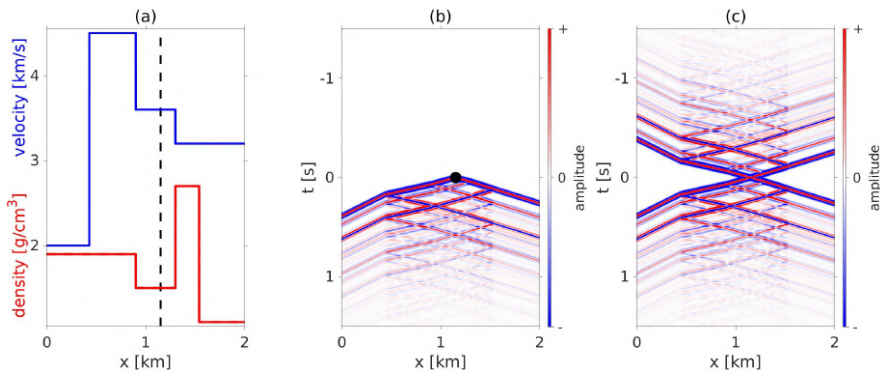


Figure 3.2: (a) Velocity and density model in blue and red, respectively. The black dotted line marks the focusing location $x_f = 1.15$ km. (b) Green's function. The black dot denotes the focusing location, i.e. source location, at $x_f = 1.15$ km and $t = 0$ s. (c) Homogeneous Green's function. The colour bars in (b) and (c) are clipped at about 14 % of the maximum absolute value of the Green's function.

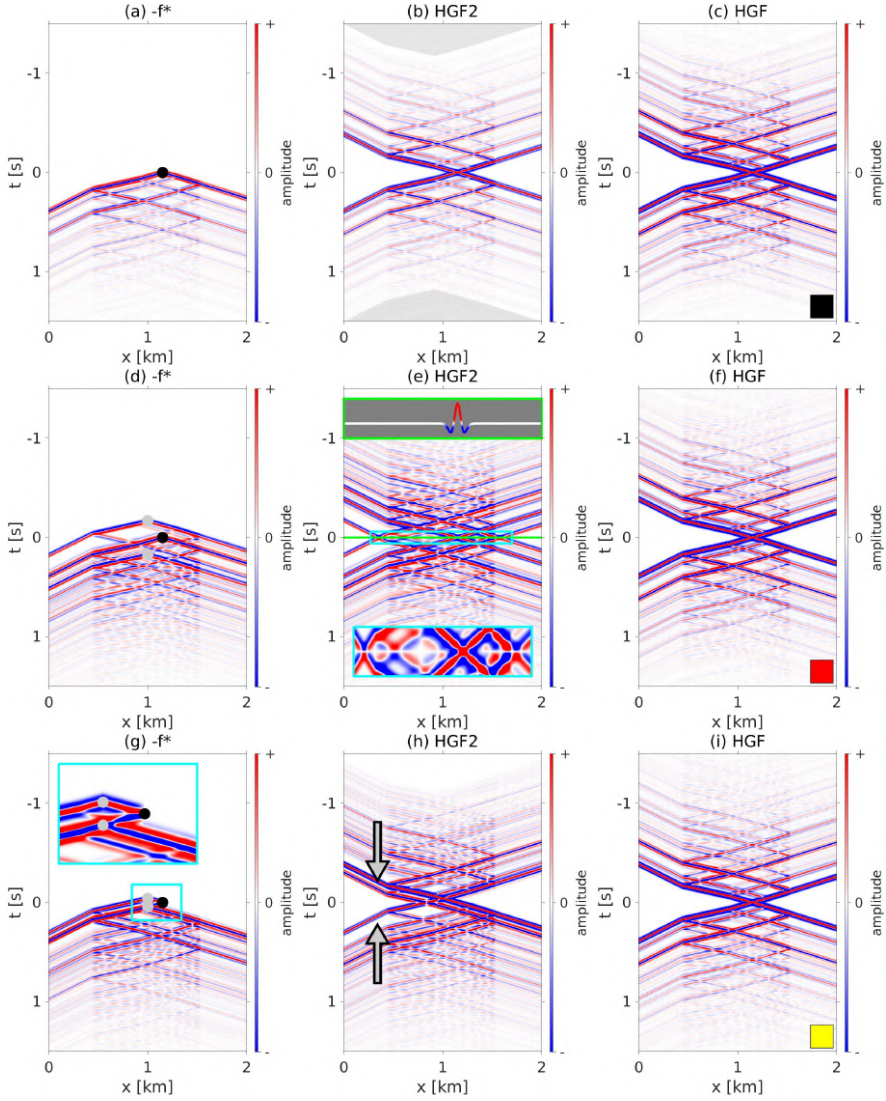


Figure 3.3: Left column: negative, time-reversed focusing functions (abbreviated with $-f^*$ in the title) obtained from finite difference modelling with Equation 3.6. Black dots mark the locations of the Green's function source at x_f , grey dots the locations of the source distributions $q(x, t)$ and $q(x, t; x_f)$, respectively. Central column: homogeneous Green's functions of the second kind (*HGF2* in the title), obtained via modelling according to Equation 3.16. Right column: homogeneous Green's functions (*HGF* in the title) obtained by superimposing the homogeneous Green's functions of the second kind and their time-reversed versions. The coloured squares in the bottom right corners refer to Figure 3.7. (a), (b) and (c) are for $q(x, t) = 0$. (d), (e) and (f) are for a monopole $q(x, t)$ without time derivative. (g), (h) and (i) are for a monopole $q(x, t; x_f)$ with a time derivative. Zoomed regions are denoted by cyan windows. The trace in the green window shows the wavefield in (e) at time zero.

where we assume that the medium is reflection-free outside the bounded volume as well as that V contains \mathbf{x}_f . While the source distribution is arbitrary within V , we assume $q(\mathbf{x}, t) = 0$ for all \mathbf{x} outside V , such that $-f(\mathbf{x}_r, -t; \mathbf{x}_f, q(\mathbf{x}, t))$ is the only in-coming wavefield.

3.4.1. TRIVIAL FOCUSING FUNCTIONS

First, we consider the trivial, negative, time-reversed focusing function $f(\mathbf{x}, t; \mathbf{x}_f) = -1/2 g(\mathbf{x}, t; \mathbf{x}_f)$ for $q(\mathbf{x}, t) = 0$, as shown in Figure 3.3(a). Compared to the Green's function in Figure 3.2(b) the polarity is reversed and the amplitudes are divided by two. According to Equation 3.13 the homogeneous Green's function of the second kind equals the conventional homogeneous Green's function divided by two in this case. In a way, the conventional homogeneous Green's function can therefore be considered a special case of the homogeneous Green's function of the second kind. For $q(\mathbf{x}, t) = 0$ Equation 3.16 gives Equation 3.15. Modelling the homogeneous Green's function of the second kind accordingly, i.e. emitting the focusing function from the boundaries $x = 0$ km and $x = 2$ km into the medium, delivers the wavefield in Figure 3.3(b). It is similar to the homogeneous Green's function in Figure 3.2(c), but the amplitudes differ by a factor of two. The grey polygon in Figure 3.3(b) on the top, i.e. above -1 s, denotes the area of the data that is unaffected by the injected wavefield – this is a consequence of causality, as it takes time for the injected wavefield to travel from the injection boundaries to the interior of the volume. The lower grey polygon is its time-reversed version. As we know that the wavefield in Figure 3.3(b) should be symmetric in time (being the half amplitude homogeneous Green's function), we should have the same solution in both polygons, suggesting that the wavefield should be zero within the lower grey polygon – which is not quite the case in this example. This is why, as mentioned before, time reversal modelling tends to be inaccurate for short recording times. Finally, Figure 3.3(c) shows the homogeneous Green's function, obtained by superimposing the wavefield in Figure 3.3(b) and its time-reversed version. This wavefield is indeed a reasonable estimate of the homogeneous Green's function in Figure 3.2(c).

3.4.2. FOCUSING FUNCTIONS WITH A MONOPOLE SOURCE

Let us consider $q(\mathbf{x}, t)$ with a single term, i.e. $n = 1$ in Equation 3.7. We discuss two different choices for $s_1(t)$ in the following.

First, we consider the simple case $s_1(t) = -\delta(t)$. Furthermore, we use $x_1 = 1$ km and $t_1 = 0.17$ s for this example. The weighting term w_1 is chosen such that the amplitude of the resulting signal is a quarter of that of the Green's function. Figure 3.3(d) shows the negative, time-reversed focusing function, obtained by forward modelling via Equation 3.6. Since the additional source term $q(\mathbf{x}, t)$ does not contain a time derivative, the resulting signal appears to be convolved with a 20 Hz Ricker wavelet that was integrated over time, i.e. its wavelet does not match the wavelet of the Green's function. When injecting the focusing function into the medium via Equation 3.16 we get the homogeneous Green's function of the second kind in Figure 3.3(e). This wavefield differs from the conventional homogeneous Green's function. At $t = 0$, the wavefield is only non-zero at the focusing location x_f – there are, however, various other events in space right

before and after $t = 0$. These events are related to the portion of the wavefield that is anti-symmetric in time. In the zoomed area (cyan box), one can see that these events change polarity when comparing negative and positive times and are zero at zero time. The only actual event at zero time is the focus at $x_f = 1.15$ km, i.e. the field exhibits a focus in space. This focus can also be seen in the green box, showing the wavefield at time zero. Note, however, that the derivative of the wavefield in Figure 3.3(e) is different from zero, leading to a significantly different appearance of the focusing compared to Figure 3.2(c). When adding the homogeneous Green's function of the second kind and its time-reversed version we obtain the conventional homogeneous Green's function, see Figure 3.3(f). The Green's function that was previously polluted by the signal of the source distribution $q(x, t)$, see Figure 3.3(d), is now isolated. This is a result of the fact that the Green's functions in Equation 3.13 are symmetric in time, while the fields $f_q(x, t; q(x, t))$ are anti-symmetric in time.

The second option we present is $\varepsilon_1 = -\partial\delta(t)/\partial t$, leading to

$$q(x, t; x_f) = w_1 \rho(x) \left(-\frac{\partial}{\partial t} \delta(t - t_1) + \frac{\partial}{\partial t} \delta(t + t_1) \right) \delta(x - x_1) \quad . \quad (3.17)$$

This produces a wavelet similar to that of the Green's function, enabling a potentially interesting interference of the two terms $-1/2 g(x, t; x_f)$ and $f_q(x, t; q(x, t))$ within the negative, time-reversed focusing function, see Equation 3.8. Note that this interference is only possible for $t_1 \neq 0$, because for $t_1 = 0$ we get $q(x, t) = 0$, leading to the trivial focusing function. Since this source distribution is supposed to interfere with the source at x_f , we write $q(x, t; x_f)$ here rather than $q(x, t)$. Note that the source distribution then generally also depends on the physical properties of the medium. We choose $x_1 = 1$ km, such that x_1 is in the same layer as x_f . Then we use $t_1 = (x_f - x_1)/c_3$, where c_3 is the velocity in this, i.e. the third, layer. On choosing $w_1 = -1/2$ we get a source at $t = -t_1$ that leads to destructive interference with the rightwards travelling portion of the negative, half-amplitude Green's function, see Figure 3.3(g). As a consequence, it seems as if the source at x_f was only radiating energy to the left. The respective homogeneous Green's function of the second kind is shown in Figure 3.3(h). While the previous homogeneous Green's functions of the second kind clearly revealed a superposition of perfectly symmetric and anti-symmetric fields in time, Figure 3.3(h) is asymmetric in time. The grey arrows point to an event in the left part of the model that is present at negative but missing at positive times. This asymmetry is a consequence of the interference of $-1/2 g(x, t; x_f)$ and $f_q(x, t; q(x, t; x_f))$ within the negative, time-reversed focusing function. Such an interference would also be possible if x_1 was not in the same layer as the source of the Green's function, however, it would require an adjusted scaling value w_1 . The respective conventional homogeneous Green's function, obtained by summing the wavefield in Figure 3.3(h) and its time-reversed, can be seen in Figure 3.3(i).

While the first example illustrated the effect of a simple, random source term, the second example nicely showed that we can produce interesting, destructive interference by applying particularly designed sources.

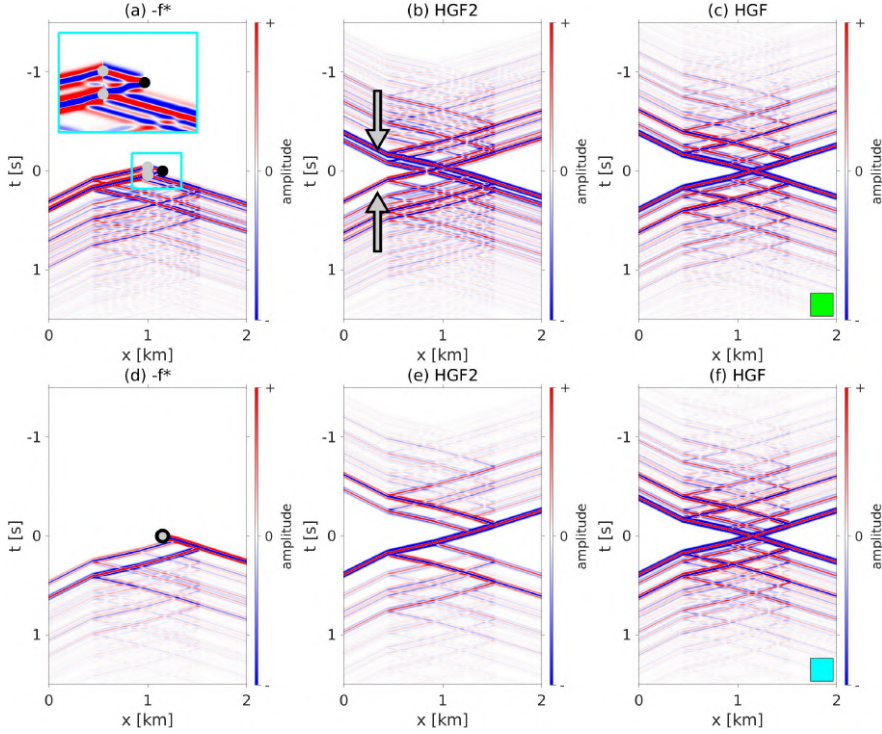


Figure 3.4: Left column: negative, time-reversed focusing functions. Black dots mark the locations of the Green's function source at x_f , grey dots the locations of the $q(x, t; x_f)$ sources. Central column: homogeneous Green's functions of the second kind. Right column: homogeneous Green's functions obtained from the homogeneous Green's functions of the second kind. (a), (b) and (c) are for the dipole $q(x, t; x_f)$ related to $t_1 \neq 0$. (d), (e) and (f) are for the dipole $q(x, t; x_f)$ related to $t_1 = 0$. Zoomed regions are denoted by cyan windows.

3.4.3. FOCUSING FUNCTIONS WITH A DIPOLE SOURCE

In the previous subsection, we argued that a monopole source $q(x, t; x_f)$ with a time derivative at x_1 and $t_1 = 0$ can not interfere with the signal of the negative half-amplitude Green's function, but only delivers the trivial focusing function. Dipole sources on the other hand do not have such a limitation. Regarding the 1D version of Equation 3.7 we use $n = 1$ and $s_1(t) = -c(x_1)\delta(t)\partial/\partial x$ – note that $s_1(t)$ is a function of only the variable t but includes a spatial derivative. The source term therefore becomes

$$q(x, t; x_f) = -w_1\rho(x)c(x_1)(\delta(t - t_1) + \delta(t + t_1))\frac{\partial}{\partial x}\delta(x - x_1) \quad . \quad (3.18)$$

We stress that the velocity $c(x_1)$ represents scaling with a particular velocity, i.e. at x_1 , whereas the density $\rho(x)$ is a function under the action of the spatial Dirac delta. This becomes important later on when considering dipole sources at interfaces. This source produces a wavelet similar to that of the Green's function, but without delivering a trivial homogeneous Green's function of the second kind for $t_1 = 0$. In our finite difference code, we mimic the dipole source by two monopole sources with opposite polarity. We

illustrate two different choices for the source time t_1 in the following, i.e. $t_1 \neq 0$ and $t_1 = 0$.

For the first numerical example we use the values from the preceding experiment, that is $x_1 = 1$ km, $t_1 = (x_f - x_1)/c_3$ and $w_1 = -1/2$, see Figure 3.4(a). The resulting negative, time-reversed focusing function is similar to that in Figure 3.3(g), only the polarities of some events appear reversed. Note that the two monopole sources in Figure 3.3(g) that are associated with $q(x, t; x_f)$ have different polarities, while the two dipole sources in Figure 3.4(a) exhibit the same polarity. The character of the homogeneous Green's function of the second kind follows our previous observations, i.e. Figure 3.4(b) is slightly asymmetric, see grey arrows. Summing this wavefield and its time-reversed version gives the conventional homogeneous Green's function in Figure 3.4(c).

Next, let us consider the case $t_1 = 0$. In order for $-1/2 g(x, t; x_f)$ and $f_q(x, t; q(x, t; x_f))$ to interfere destructively, we choose $x_1 = x_f$ and $w_1 = 1/4$ (note that the source is fired twice in Equation 3.18). The negative, time-reversed focusing function is shown in Figure 3.4(d). It appears the source at x_f now only emits energy to the right. There are no additional, polluting signals from the $q(x, t; x_f)$ source – instead, its wavefield masks the left-going Green's function. Thus, the remaining wavefield represents the negative, right-going part of the Green's function, i.e. all its contributions that travel into greater depth first. The homogeneous Green's function of the second kind, Figure 3.4(e), thus shows the time-reversed, positive, right-going part of the Green's function first, i.e. at negative times, followed by the positive, left-going part. Note that the scaling matches that of the actual Green's function. By adding left- and right-going parts, i.e. adding the homogeneous Green's function of the second kind and its time-reversed version, we obtain the conventional homogeneous Green's function, Figure 3.4(f).

The first dipole experiment demonstrated how to achieve destructive interference similar to that in the previous subsection, however, the source signatures are now obviously different. The second example illustrated destructive interference generated by a source at zero time, an effect that can only be produced with dipole sources.

3.4.4. TIME-COMPACT FOCUSING FUNCTIONS

In the preceding subsections we introduced source distributions $q(x, t; x_f)$ that excite wavefields that interfere with the Green's function. Since dipole sources appear to be slightly more flexible than monopole sources, i.e. choosing $t_i = 0$ does not deliver a trivial focusing function, we use solely $s_i(t) = -c(x_i)\delta(t)\partial/\partial x$ in this subsection. Building on the findings described above, we illustrate and discuss particularly interesting wavefields in the following, i.e. so-called time-compact focusing functions. As the name suggests, these focusing functions occupy only a limited window in time, meaning that the wavefields are zero outside a certain time range. In contrast, Green's functions are generally time-infinite wavefields that keep on propagating for arbitrarily long time and it is only owing to their decreasing amplitude with each scattering interaction that we can usually neglect late arrivals. The time-compact focusing functions in this section relate to auxiliary focal solutions in classical 1D inverse scattering theory (Burridge, 1980) and to the previously introduced subset of focusing functions in 2D and 3D Marchenko (Wapenaar et al., 2014b).

We propose a simple scheme for designing these time-compact focusing functions, con-

sisting of two main steps: (i) get all space and time coordinates x_i and t_i , (ii) set up a linear system of equations to describe the scattering and obtain the weights w_i . Then, we can model the negative, time-reversed focusing functions via Equations 3.6 and 3.7. We present three different time-compact focusing functions below.

DOUBLE-SIDED SOURCES AT ZERO TIME

In order to design a time-compact focusing function, we first have to specify either the time or the space coordinates of the sources. The easiest approach is to assume that all sources in the distribution $q(x, t; x_f)$ are at $t_i = 0$ (implying a necessity for dipole sources). Furthermore, we assume that the sources may be anywhere in space, i.e. above and below x_f , thus we refer to this example as double-sided. For the negative, time-reversed focusing function (and consequently the focusing function) to be time-compact, each reflection of $-1/2 g(x, t; x_f)$ in Equation 3.8 has to be cancelled by a source in $q(x, t; x_f)$, compare Figure 3.5. Thus, when choosing $t_i = 0$ for all $n = 6$ sources in $q(x, t; x_f)$, we can compute the coordinates x_i that allow for a possible interference via ray tracing or, in the example on hand, simple travel time considerations. The source $q_1(x, t; x_f)$ for instance has to cancel the first reflection of the negative, half-amplitude Green's function at the first interface. Hence, the wave emitted from $q_1(x, t; x_f)$ should reach the first interface at the same time as the first arrival of the Green's function. The source $q_3(x, t; x_f)$ is supposed to cancel the first reflection of the negative, half-amplitude Green's function at the second interface. The wave emitted from $q_3(x, t; x_f)$ should therefore reach the second interface at the same time as the first arrival of the Green's function. The source $q_2(x, t; x_f)$ on the other hand has to eliminate the reflection at the first interface that is induced by the wavefield from $q_3(x, t; x_f)$. The wave emitted from $q_2(x, t; x_f)$ should consequently reach the first interface at the same time as the first arrival of the wave coming from $q_3(x, t; x_f)$. Similar considerations hold for the remaining sources. Overall, this gives the following space coordinates:

$$x_1 = \xi_1 - \left(\frac{x_f - \xi_2}{c_3} + \frac{\xi_2 - \xi_1}{c_2} \right) c_1 \quad (3.19)$$

$$x_2 = \xi_1 - \frac{x_3 - \xi_1}{c_2} c_1 \quad (3.20)$$

$$x_3 = \xi_2 - \frac{x_f - \xi_2}{c_3} c_2 \quad (3.21)$$

$$x_4 = \xi_3 + \frac{\xi_3 - x_f}{c_3} c_4 \quad (3.22)$$

$$x_5 = \xi_4 + \frac{\xi_4 - x_4}{c_4} c_5 \quad (3.23)$$

$$x_6 = \xi_4 + \left(\frac{\xi_3 - x_f}{c_3} + \frac{\xi_4 - \xi_3}{c_4} \right) c_5 \quad , \quad (3.24)$$

where ξ_j with $j = 1, 2, 3, 4$ is the location of the j -th interface of our five layer model and c_k with $k = 1, 2, 3, 4, 5$ is the velocity in the k -th layer. Note that we assume that $x_3 > \xi_1$ and $x_4 < \xi_4$ in our considerations. In other words we assume that $q_3(x, t; x_f)$ is located

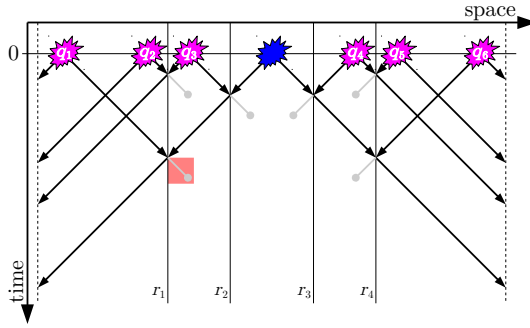


Figure 3.5: Sketch of the time-compact, time-reversed focusing function using double-sided sources at zero time in a five layer medium. The reflection coefficient r_1 marks the first, r_2 the second, r_3 the third and r_4 the fourth interface. The blue explosion refers to the source of the negative, half-amplitude Green's function at x_f . The pink explosions denote the source distribution $q(x, t; x_f)$. Note that each $q_i(x, t; x_f)$ in this sketch actually represents two overlapping sources, compare Equation 3.7. The black arrows represent propagating events, the grey lines imply reflections which are suppressed in the time-compact focusing function. The red square marks a region of interest which is studied in detail in the text. Note that the arrows in this sketch are straight for the sake of simplicity, but the wave speed in the different layers might actually vary.

in the second layer and $q_4(x, t; x_f)$ in the fourth layer. Depending on the medium velocities, $q_3(x, t; x_f)$ could also fall within the first layer and $q_4(x, t; x_f)$ within the last, meaning that the sources $q_2(x, t; x_f)$ and $q_5(x, t; x_f)$ would become unnecessary and the coordinate calculations for x_3 and x_4 would change. The overall concept, however, remains the same. In addition, we assume that the sources lie within the layers, not at interfaces.

Now we know the space and time coordinates of the sources, but we still need to find out the six weights w_i . Note that we also have six equations, i.e. one for each grey line in Figure 3.5 where a reflected wave is supposed to be cancelled. Let us consider the point marked by the red square in Figure 3.5. There are three different events that reach this point: the negative, half-amplitude Green's function is transmitted at the second and reflected at the first interface, its amplitude is proportional to $\rho(x_f)c(x_f)r_1(1-r_2)/2$, where $r_j = (\rho_{j+1}c_{j+1} - \rho_j c_j) / (\rho_{j+1}c_{j+1} + \rho_j c_j)$ is the reflection coefficient of the j -th interface. Note that its actual amplitude corresponds to $\rho(x_f)c(x_f)r_1(1-r_2)/4$ – the additional factor of $1/2$, however, turns up for all sources and is thus contained in the proportionality factor here. The wave from $q_3(x, t; x_f)$ is reflected at both the second and the first interface, its amplitude is therefore proportional to $r_1 r_2 2\rho(x_3)c(x_3)w_3$. Note that we use dipole sources $q_i(x, t; x_f)$ that emit leftwards with positive and rightwards with negative amplitude for positive weights w_i . Furthermore, it is important to remember that there are two sources in each $q_i(x, t; x_f)$ in Equation 3.7, one at positive and one at negative time – hence, we get the factor of two. The wave from $q_1(x, t; x_f)$ is transmitted at the first interface and has an amplitude proportional to $-(1+r_1)2\rho(x_1)c(x_1)w_1$. Thus we get the equation

$$-(1+r_1)\rho(x_1)c(x_1)w_1 + r_1 r_2 \rho(x_3)c(x_3)w_3 = -\frac{\rho(x_f)c(x_f)}{2} \frac{r_1(1-r_2)}{2}, \quad (3.25)$$

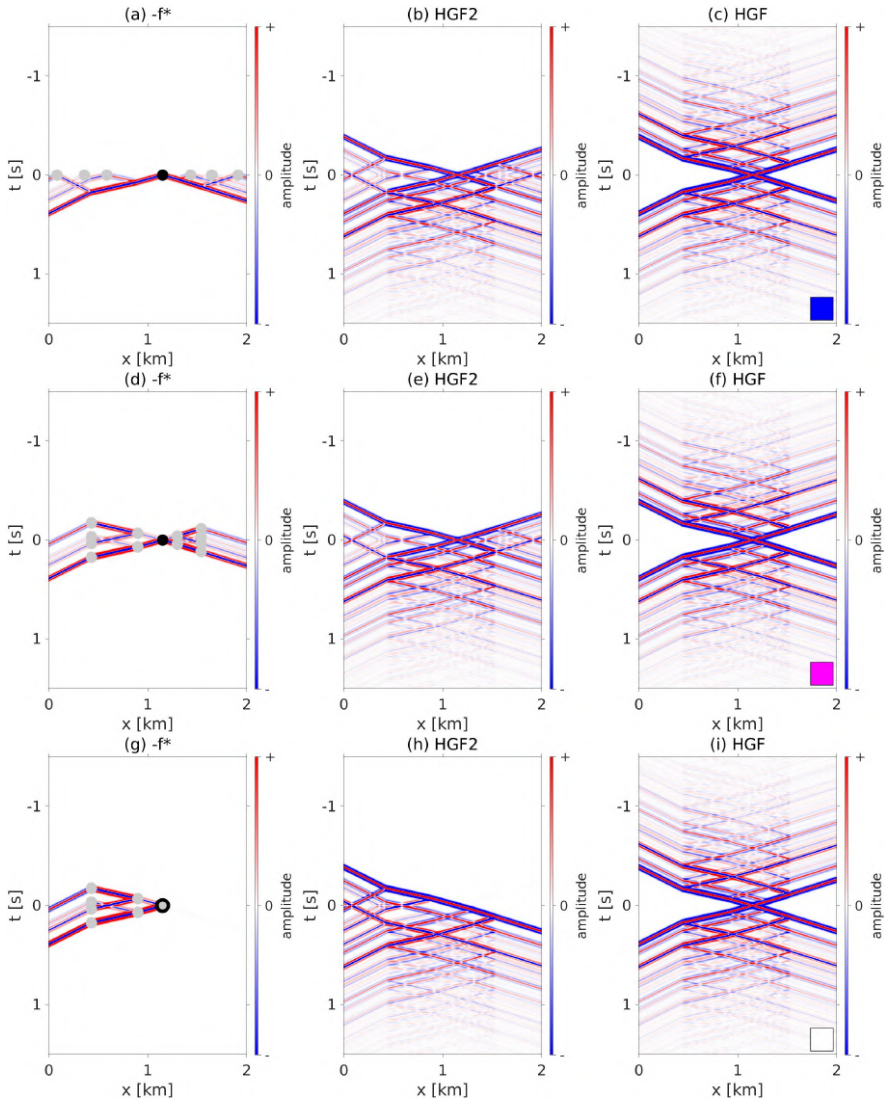


Figure 3.6: Left column: negative, time-reversed time-compact focusing functions. Black dots mark the locations of the Green's function source at x_f , grey dots the locations of the source distributions $q(x, t; x_f)$. Central column: homogeneous Green's functions of the second kind. Right column: homogeneous Green's functions obtained from the homogeneous Green's functions of the second kind. (a), (b) and (c) are for double-sided $q(x, t; x_f)$ sources at zero time. (d), (e) and (f) are for double-sided $q(x, t; x_f)$ sources at the interfaces. (g), (h) and (i) are for single-sided $q(x, t; x_f)$ sources at the interfaces.

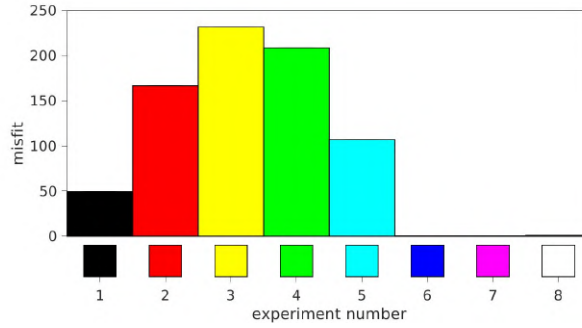


Figure 3.7: Misfit between the actual homogeneous Green's function in Figure 3.2(c) and the estimated homogeneous Green's functions obtained via the focusing functions. The colour encoding matches the rectangles in the bottom right corners of each of the estimated homogeneous Green's functions, i.e. experiment number 1 is for Figure 3.3(c), 2 for Figure 3.3(f), 3 for Figure 3.3(i), 4 for Figure 3.4(c), 5 for Figure 3.4(f), 6 for Figure 3.6(c), 7 for Figure 3.6(f) and 8 for Figure 3.6(i).

which states that the events should cancel each other out. Repeating this procedure for the areas denoted by the five other grey lines in Figure 3.5 we get the following linear system

$$\begin{bmatrix} -(1+r_1) & 0 & r_1 r_2 & 0 & 0 & 0 \\ 0 & -(1+r_1) & -r_1 & 0 & 0 & 0 \\ 0 & 0 & -(1+r_2) & 0 & 0 & 0 \\ 0 & 0 & 0 & 1-r_3 & 0 & 0 \\ 0 & 0 & 0 & -r_4 & 1-r_4 & 0 \\ 0 & 0 & 0 & -r_3 r_4 & 0 & 1-r_4 \end{bmatrix} \begin{bmatrix} \rho(x_1)c(x_1) \\ \rho(x_2)c(x_2) \\ \rho(x_3)c(x_3) \\ \rho(x_4)c(x_4) \\ \rho(x_5)c(x_5) \\ \rho(x_6)c(x_6) \end{bmatrix} \circ \begin{bmatrix} w_1 \\ w_2 \\ w_3 \\ w_4 \\ w_5 \\ w_6 \end{bmatrix} = \frac{\rho(x_f)c(x_f)}{2} \begin{bmatrix} -r_1(1-r_2)/2 \\ 0 \\ -r_2/2 \\ r_3/2 \\ 0 \\ (1+r_3)r_4/2 \end{bmatrix}, \quad (3.26)$$

where \circ is the Hadamard product. The determinant of the matrix is $(r_1 + 1)^2(r_2 + 1)(r_3 - 1)(r_4 - 1)^2$ which is different from zero for all reflection coefficients $|r_j| < 1$ with $j = 1, 2, 3, 4$, thus its inverse exists for all physically reasonable scenarios. We can solve the above system of equations to obtain the weights w_i and then model the negative, time-reversed focusing function via Equation 3.6, where each of the $n = 6$ sources in Equation 3.7 is given by

$$q_i(x, t; x_f) = -2w_i \rho(x)c(x_i) \delta(t) \frac{\partial}{\partial x} \delta(x - x_i) \quad . \quad (3.27)$$

The accordingly modelled negative, time-reversed focusing function is shown in Figure 3.6(a). This wavefield is indeed only propagating between $t = 0$ s and about $t = 0.4$ s.

Afterwards, there is no more energy travelling within the bounded volume between $x = 0$ km and $x = 2$ km. Note that this negative, time-reversed focusing function (and consequently the focusing function) is focused in time, i.e. at $x = x_f$ the field is only non-zero at $t = 0$. This is the eponymous focusing property of focusing functions in previous Marchenko literature (Wapenaar et al., 2014a). In the context of our theory, however, only particular focusing functions, i.e. those which are compact in time, have such a focus in time – all focusing functions, however, can be related to a focus in space via the homogeneous Green's function of the second kind. Thus, these previously introduced functions form a subgroup of focusing functions in our framework.

The homogeneous Green's function of the second kind is given in Figure 3.6(b). The asymmetry of the field is much more pronounced than before, as the wavefield is in fact zero before about -0.4 s but it keeps on propagating for infinitely long at positive times. This suggests that time reversal modelling is more accurate when using such a time-compact focusing function instead of, e.g., a time-reversed Green's function, because we do not need long recording times of the injected wavefield to achieve high accuracy. In contrast, we only need about 0.4 s of data. Let us define the data misfit as $\iint (d(x, t; x_f) - d_{est}(x, t; x_f))^2 dt dx$, where $d(x, t; x_f) = g(x, t; x_f) + g(x, -t; x_f)$ is the ground truth in Figure 3.2(c) and $d_{est}(x, t; x_f)$ its estimate from the respective focusing function. Indeed, we find this data misfit to be significantly smaller for the new homogeneous Green's function, Figure 3.6(c), than that for Figure 3.3(c). This can also be seen in Figure 3.7. While there is a significant misfit for all of the five preceding experiments, it is nearly zero for the time-compact focusing function. Note that if we had used larger recording times (greater than 1.5 s) for the previous experiments, the misfits would have appeared smaller in Figure 3.7 – however, it would have been a subjective task to decide where to stop the recording in these scenarios whereas it is immediately clear with the time-compact focusing function that only requires a finite recording time of about 0.4 s in this example.

While this source setup works fairly well and is relatively straightforward, there is only one issue: in order for $q(x \notin V, t; x_f) = 0$ to hold, the respective volume V has to be relatively large. This can be seen in Figure 3.5, where $q_1(x, t; x_f)$, $q_2(x, t; x_f)$, $q_5(x, t; x_f)$ and $q_6(x, t; x_f)$ are beyond the actual scattering region, i.e. the area bounded by the first interface r_1 on the left and the last interface r_4 on the right. For many experimental setups, however, it is desirable to consider only a smaller volume, limited to the actual scattering region, such that the volume does not have to be homogeneously extended beyond the first and last interface. Thus, it might make sense to think about other configurations.

DOUBLE-SIDED SOURCES AT THE INTERFACES

Rather than picking times t_i for the source coordinates first, we can also pick locations x_i instead. In this context it might make sense to refer to the model features, i.e. we can put the sources at the interfaces between the five layers. We still keep the setup such that sources can be both above and below x_f . Hence, we now discuss double-sided sources at the interfaces. As before, each reflection of $-1/2 g(x, t; x_f)$ in Equation 3.8 has to be cancelled by a source in $q(x, t; x_f)$, see Figure 3.8(a). Thus, we have $x_1 = \xi_1$, $x_2 = \xi_1$, $x_3 = \xi_2$, $x_4 = \xi_3$, $x_5 = \xi_4$ and $x_6 = \xi_4$. The time coordinates t_i that enable the desired interference can be computed by similar travel time considerations as before, compare

Equations 3.19 to 3.24. The source $q_1(x, t; x_f)$ for instance has to emit energy when the negative, half-amplitude Green's function first arrives at the first interface. Since this is happening at a time different from zero, the two sources of $q_1(x, t; x_f)$ in Equation 3.7 now appear distinctly separated in the sketch, one at $-t_1$ and one at t_1 . Overall, we get the following time coordinates:

$$t_1 = t_3 + \frac{\xi_2 - \xi_1}{c_2} \quad (3.28)$$

$$t_2 = t_3 - \frac{\xi_2 - \xi_1}{c_2} \quad (3.29)$$

$$t_3 = \frac{x_f - \xi_2}{c_3} \quad (3.30)$$

$$t_4 = \frac{\xi_3 - x_f}{c_3} \quad (3.31)$$

$$t_5 = t_4 - \frac{\xi_4 - \xi_3}{c_4} \quad (3.32)$$

$$t_6 = t_4 + \frac{\xi_4 - \xi_3}{c_4} \quad , \quad (3.33)$$

where in contrast to the preceding source setup, all six sources always exist.

Similar to before, we can set up a linear system of equations for the weights. However, the amplitude considerations are more complex in this case because the dipole sources are located at interfaces, implying slightly modified radiation characteristics. In the preceding example, the dipoles were within the layers such that each source would emit a wave with same amplitude but reversed polarity into the two directions (leftwards and rightwards). For a dipole source at an interface, the leftwards propagating wave has an initial, unweighted amplitude (before any further transmission/reflection losses occur and without applying the individual weight w_i) proportional to

$$\mu_j = \frac{(\rho_j + \rho_{j+1})c(\xi_j)}{1 - \gamma_j} \quad , \quad (3.34)$$

where $c(\xi_j)$ is the velocity at the j -th interface. While this velocity might be ill-defined, it is purely a constant scaling factor, making the assigned value irrelevant – we use $c(\xi_j) = (c_j + c_{j+1})/2$ for instance. Note that we only define four different amplitudes μ_j for the six sources since the initial, unweighted source amplitude only depends on the interface at which the source is located. Furthermore, we use $\gamma_j = -(1 + r_j)/(1 - r_j)$. The rightwards propagating wave has an initial, unweighted amplitude proportional to $\gamma_j \mu_j$. See Appendix I for details on the derivation of these amplitudes. Including the adjusted amplitudes we can follow the same recipe as before, i.e. for each area marked by a grey line in Figure 3.8(a) we can sum up all the contributions from the different sources and set

the result to zero. The linear system for the weights then reads

$$\begin{bmatrix}
 \gamma_1 & -r_1 r_2 \gamma_1 & -r_1 & -r_1(1-r_2) & 0 & -r_1(1-r_2)(1-r_3) \\
 -r_1 r_2 \gamma_1 & \gamma_1 & -r_1 & 0 & 0 & 0 \\
 0 & (1+r_2)\gamma_1 & \gamma_2 & -r_2 & 0 & -r_2(1-r_3) \\
 (1+r_2)r_3\gamma_1 & 0 & r_3\gamma_2 & 1 & 1-r_3 & 0 \\
 0 & 0 & 0 & r_4\gamma_3 & 1 & -r_3 r_4 \\
 (1+r_2)(1+r_3)r_4\gamma_1 & 0 & (1+r_3)r_4\gamma_2 & r_4\gamma_3 & -r_3 r_4 & 1
 \end{bmatrix}
 \begin{bmatrix}
 \mu_1 \\
 \mu_1 \\
 \mu_2 \\
 \mu_3 \\
 \mu_4 \\
 \mu_4
 \end{bmatrix}
 \circ
 \begin{bmatrix}
 w_1 \\
 w_2 \\
 w_3 \\
 w_4 \\
 w_5 \\
 w_6
 \end{bmatrix}
 =
 \rho(x_f)c(x_f)
 \begin{bmatrix}
 -r_1(1-r_2)/2 \\
 0 \\
 -r_2/2 \\
 r_3/2 \\
 0 \\
 (1+r_3)r_4/2
 \end{bmatrix},
 \quad (3.35)$$

where we have nearly the same right hand side as before, but the matrix on the left hand side appears to be more complex due to the fact that the two sources in each $q_i(x, t; x_f)$ do not overlap in time any more. The inverse of this matrix exists for all physically reasonable cases, see Appendix II. After solving the above system for w_i we can model the negative, time-reversed focusing function using Equation 3.6 where for the sources in Equation 3.7 we have

$$q_i(x, t; x_f) = -w_i \rho(x) c(x_i) (\delta(t - t_i) + \delta(t + t_i)) \frac{\partial}{\partial x} \delta(x - x_i) \quad . \quad (3.36)$$

Again, note that the velocity $c(x_i)$ is only a constant scaling factor and not a function of x , whereas the density $\rho(x)$, which is different in the limits from above and below the interface, is under the action of the Dirac delta. The resulting negative, time-reversed focusing function for double-sided sources at the interfaces is shown in Figure 3.6(d). Since there are sources at positive and negative times now, i.e. at $-t_i$ and t_i , this focusing function lives in a larger time window than the previous one. Note that the focusing functions on the boundaries of the volume, that is at $x = 0$ km and at $x = 2$ km, are exactly the same in both Figures 3.6(a) and 3.6(d). In that sense the combined focusing functions $f(x, t; x_f, q(x, t; x_f)) - f(x, -t; x_f, q(x, t; x_f))$, i.e. the wavefields in Equation 3.10, are exactly the same. This illustrates the ambiguity of the source distribution $q(x, t; x_f)$. The source distribution of the new focusing function, see Figure 3.6(d) for its negative, time-reversed version, however, is spatially more compact, i.e. there are no sources outside the scattering region of the volume. In other words, all sources are within the region between the first and the last interface, such that $q(x \notin V, t; x_f) = 0$ holds true for any volume that contains the scattering interfaces. When injecting the focusing function from the boundary, we get – as expected – the same homogeneous Green's function of the second kind as before, see Figure 3.6(e). Figure 3.6(f) gives the resulting homogeneous Green's function. As observed before, the accuracy of this homogeneous Green's function is higher than that of those retrieved via non-time-compact focusing functions, see Figure 3.7.

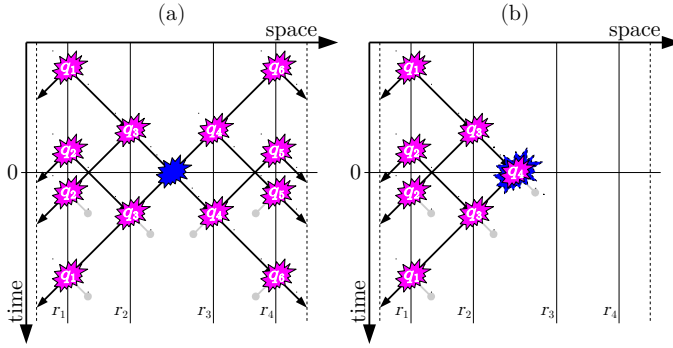


Figure 3.8: Sketch of the time-reversed, time-compact focusing functions using (a) double-sided and (b) single-sided sources at the interfaces. The reflection coefficients r_1 mark the first interface, r_2 the second and so on. The blue explosions refer to the sources of the negative, half-amplitude Green's functions at x_f . The pink explosions denote the source distribution $q(x, t; x_f)$. Note that each q_i appears twice in this sketch, once at positive and once at negative time, and both together make up the actual source $q_i(x, t; x_f)$. The only exception is q_4 in (b), which is at zero time and thus denotes two overlapping sources. Furthermore, it overlaps with the source of the negative, half-amplitude Green's function – its blue explosion symbol is therefore increased in size to allow for a proper visualisation. The black arrows represent propagating events, the grey lines imply reflections which are suppressed in the time-compact focusing functions.

Thus far, we illustrated how different sources $q(x, t; x_f)$ may deliver the same homogeneous Green's function of the second kind. For a focusing point in the third layer of a five layer medium, we have proven that one can always obtain a time-compact focusing function from double-side sources at the interfaces, such that $q(x, t; x_f) = 0$ everywhere beyond the scattering portion of the volume.

SINGLE-SIDED SOURCES AT THE INTERFACES

This final example is similar to the preceding one, but for the case of having sources only at locations $x_i \leq x_f$ – thus, we refer to this setup as single-sided (analogously, one could of course use sources only at locations $x_i \geq x_f$). Since we want to obtain the most time-compact focusing function, it follows that the focusing function should not penetrate any deeper than x_f . If there was energy propagating beyond this point it would induce scattering at the third and fourth interface and suppressing this scattering with sources at $x_i \leq x_f$ (if at all possible) would require a significantly larger time window for the focusing function. Hence, the most time-compact focusing functions for single-sided sources only propagate in a half-space, bounded by x_f . The source configuration is sketched in Figure 3.8(b). While the time and space coordinates of $q_1(x, t; x_f)$, $q_2(x, t; x_f)$ and $q_3(x, t; x_f)$ remain unchanged compared to the preceding example sketched in Figure 3.8(a), $q_4(x, t; x_f)$ is now at $x_4 = x_f$ and $t_4 = 0$. Note that this is the only source which is not at an interface. Sources $q_5(x, t; x_f)$ and $q_6(x, t; x_f)$ become unnecessary in this setup, i.e. $n = 4$ in Equation 3.7.

As depicted by the grey lines in Figure 3.8(b) we have four equations that describe the

annihilating wavefields of the four sources related to $q(x, t; x_f)$. The linear system reads

$$\begin{bmatrix} \gamma_1 & -r_1 r_2 \gamma_1 & -r_1 & -r_1(1-r_2) \\ -r_1 r_2 \gamma_1 & \gamma_1 & -r_1 & 0 \\ 0 & (1+r_2)\gamma_1 & \gamma_2 & -r_2 \\ (1+r_2)\gamma_1 & 0 & \gamma_2 & -1 \end{bmatrix} \begin{bmatrix} \mu_1 \\ \mu_1 \\ \mu_2 \\ 2\rho(x_f)c(x_f) \end{bmatrix} \circ \begin{bmatrix} w_1 \\ w_2 \\ w_3 \\ w_4 \end{bmatrix} = \rho(x_f)c(x_f) \begin{bmatrix} -r_1(1-r_2)/2 \\ 0 \\ -r_2/2 \\ 1/2 \end{bmatrix}. \quad (3.37)$$

The determinant of this matrix is $(r_1+1)^2(r_2+1)$ which is different from zero for all $|r_1| < 1$ and $|r_2| < 1$, i.e. the inverse matrix exists for all physically reasonable scenarios. Using the time and space coordinates t_i and x_i as well as the weights we obtain from solving above system of equations for w_i , we can model the negative, time-reversed focusing function via Equation 3.6, where for each of the $n = 4$ sources in Equation 3.7 we use the relation given in Equation 3.36.

The retrieved negative, time-reversed focusing function is shown in Figure 3.6(g). It is similar to the previous result in Figure 3.6(d), however, the wavefield now only propagates between $x = 0$ and $x = x_f$. Furthermore, the amplitudes are slightly different. The energy that is necessary to cancel the negative, half-amplitude Green's function in Equation 3.8 comes solely from the left in this single-sided example – implying generally higher amplitudes for this focusing function. Note that this wavefield has quite an unusual appearance, being not only time-compact but also spatially bounded to the region to the left of x_f . This shows that we can inject energy into a medium such that it only propagates to one side. Measuring the wavefield at the other side will not show any arriving energy. But this is not due to attenuation, it is merely a consequence of choosing the correct sources for the medium under investigation, such that all rightwards travelling wavefields interfere destructively. As a consequence of the vanishing focusing function at the right boundary, we may choose to inject the focusing function from only the left boundary in Equation 3.16. The homogeneous Green's function of the second kind is shown in Figure 3.6(h). As before this wavefield is asymmetric in time. Furthermore, the spatial asymmetry is significantly more pronounced due to the single-sided source configuration, i.e. the entire top right corner (to the right of $x = x_f$ and above $t = 0$) is zero. The conventional homogeneous Green's function obtained from this result is given in Figure 3.6(i). Note that this homogeneous Green's function is obtained from drastically reduced boundary data, i.e. we use a focusing function that is only different from zero on the left boundary and within a limited time window. Again, this homogeneous Green's function is a significantly better estimate than those obtained from non-time-compact focusing functions. However, due to an increased impact of numerical inaccuracies, the misfit is marginally higher than that of the previous two, double-sided experiments, see Figure 3.7.

In summary, we presented and discussed different focusing functions in this section – going beyond those achievable by previous descriptions. In particular, we showed how to obtain time-compact focusing functions. While we did neither strictly prove that these

time-compact focusing functions always exist for arbitrary 1D media nor describe how to obtain them in 2D and 3D, these examples clearly illustrate the concept of the source distribution $q(x, t; \mathbf{x}_f)$ and how it can lead to perfect destructive interference and thereby time-compact wavefields. In that sense, our chosen benchmark examples demonstrate the applicability of the general equations in Section 3.3. Our main intention was to show how our new framework can be used to forward model focusing functions, i.e. how to obtain different types of focusing functions when given the physical properties of the medium. This is an important step in understanding focusing functions and might potentially lead to further progress, e.g., in inversion schemes based on focusing functions (Diekmann et al., 2021). Furthermore this might be helpful in understanding the extent to which, e.g., single-sided focusing works in complex 2D and 3D media. The next section will discuss an approach to obtaining focusing functions without knowledge of the medium parameters.

3.5. INTERFEROMETRY AND MARCHENKO-LIKE INTEGRALS

In the preceding sections we introduced and illustrated focusing functions and homogeneous Green's functions of the second kind. In this section we want to establish the connection of our work with the Marchenko integral by means of seismic interferometry (Curtis et al., 2006; Schuster, 2009; Wapenaar et al., 2010a,b). In addition, we discuss the role of time-compact focusing functions.

Similar to time reversal modelling we can use reciprocity to obtain the interferometric relation

$$\frac{\partial}{\partial t} u(\mathbf{x}_s, t) = - \int_{\mathbf{x}_r \in \partial V} \int_{-\infty}^{\infty} \frac{2}{\rho(\mathbf{x}_r)} \nabla g(\mathbf{x}_r, t - \tau; \mathbf{x}_s) u^{in}(\mathbf{x}_r, \tau) d\tau \cdot d\mathbf{S} \quad , \quad (3.38)$$

where ∂V is the closed boundary of a volume V that contains \mathbf{x}_s and the wavefield $u(\mathbf{x}, t)$ has no sources in V (Wapenaar, 2007; Fokkema and van den Berg, 1993). Furthermore, the medium is supposed to be scattering-free outside the volume V such that the Green's function is a purely out-going wavefield. The wavefield $u^{in}(\mathbf{x}, t)$ is the part of the total field $u(\mathbf{x}, t)$ that is in-coming with respect to the bounded volume V . The gradient operator ∇ acts on the coordinate \mathbf{x}_r . Note that the equation involves a convolution of the Green's function and the in-coming wavefield $u^{in}(\mathbf{x}, t)$. This general relation allows for retrieving the full wavefield $u(\mathbf{x}_s, t)$ at \mathbf{x}_s within the volume when knowing the in-coming field $u^{in}(\mathbf{x}_r, t)$ at \mathbf{x}_r along the boundary as well as the Green's function $g(\mathbf{x}_r, t; \mathbf{x}_s)$. Thus, it is necessary to have a source for the Green's function at \mathbf{x}_s within the volume. For some applications this might be unrealistic because the interior of the volume V is inaccessible. In this case, we might have \mathbf{x}_s to be just within the volume but very close to the boundary (in practice meaning that sources \mathbf{x}_s and receivers \mathbf{x}_r of the Green's function are distributed along the surface of the volume of interest). This is the setup we will assume for the remaining part of this paper. Then, we can write Equation 3.38 as

$$\frac{\partial}{\partial t} u^{out}(\mathbf{x}_s, t) = - \int_{\mathbf{x}_r \in \partial V} \int_{-\infty}^{\infty} \frac{2}{\rho(\mathbf{x}_r)} \nabla g(\mathbf{x}_r, t - \tau; \mathbf{x}_s) u^{in}(\mathbf{x}_r, \tau) d\tau \cdot d\mathbf{S} \quad , \quad (3.39)$$

where using the spatial derivative of the Green's function only reconstructs the out-going part of the wavefield $u(\mathbf{x}_s, t)$.

Let us take the homogeneous Green's function, Equation 3.5, as a first example for a wavefield $u(\mathbf{x}, t)$. This is indeed a source-free wavefield. Assuming that V contains \mathbf{x}_f , the in-coming part at ∂V is given by $g(\mathbf{x}, -t; \mathbf{x}_f)$ and the out-going part by $g(\mathbf{x}, t; \mathbf{x}_f)$. Thus, we obtain

$$\frac{\partial}{\partial t} g(\mathbf{x}_s, t; \mathbf{x}_f) = - \int_{\mathbf{x}_r \in \partial V} \int_{-\infty}^{\infty} \frac{2}{\rho(\mathbf{x}_r)} \nabla g(\mathbf{x}_r, t + \tau; \mathbf{x}_s) g(\mathbf{x}_r, \tau; \mathbf{x}_f) d\tau \cdot d\mathbf{S} \quad , \quad (3.40)$$

where we now have a correlation between the two Green's functions. Note that this representation excludes evanescent waves on the boundary, but contains the full wavefield inside the volume. This equation, however, is – for the same reasoning as before – not very useful since we are not necessarily able to have a source at \mathbf{x}_f inside the volume.

For the homogeneous Green's function of the second kind on the other hand, we obtain the following equation:

$$\begin{aligned} \frac{\partial}{\partial t} \left(g(\mathbf{x}_s, t; \mathbf{x}_f) + f(\mathbf{x}_s, t; \mathbf{x}_f, q(\mathbf{x}, t)) \right) = \\ \int_{\mathbf{x}_r \in \partial V} \int_{-\infty}^{\infty} \frac{2}{\rho(\mathbf{x}_r)} \nabla g(\mathbf{x}_r, t + \tau; \mathbf{x}_s) f(\mathbf{x}_r, \tau; \mathbf{x}_f, q(\mathbf{x}, t)) d\tau \cdot d\mathbf{S} \quad , \quad (3.41) \end{aligned}$$

where we assume that V contains \mathbf{x}_f and $q(\mathbf{x} \notin V, t; \mathbf{x}_f) = 0$ such that the wavefield $-f(\mathbf{x}_r, -t; \mathbf{x}_f, q(\mathbf{x}, t))$ is the only in-coming field. This is the closed boundary representation that relates Green's and focusing functions for \mathbf{x}_s near the boundary. As in the previous case, evanescent waves are only neglected on the boundary but accounted for inside the volume. Kiraz et al. (Kiraz et al., 2021b) present another approach to obtain a similar closed boundary representation. Let us consider a special configuration where the volume is bounded by a horizontal plane ∂V_0 at $z = 0$ and the surface of a half-sphere ∂V_1 below. Since we know that there are many different focusing functions, we are free to consider only the subset of focusing functions $-f(\mathbf{x}_s, -t; \mathbf{x}_f, \bar{q}(\mathbf{x}, t; \mathbf{x}_f))$ that vanish at ∂V_1 – note that we use the source distribution $\bar{q}(\mathbf{x}, t; \mathbf{x}_f)$ to emphasise that this is a subset of focusing functions only. Furthermore, this source distribution generally depends on the focal location \mathbf{x}_f . We have already introduced an example of such a focusing function in Figure 3.6(g). We do not actually prove the general existence of these focusing functions here – for complex media in two and three dimensions they might in fact not exist and investigating this remains a topic of ongoing research. Assuming that there are such focusing functions, Equation 3.41 becomes

$$\begin{aligned} g(\mathbf{x}_s, t; \mathbf{x}_f) + f(\mathbf{x}_s, t; \mathbf{x}_f, \bar{q}(\mathbf{x}, t; \mathbf{x}_f)) = \\ - \int_{\mathbf{x}_r \in \partial V_0} \int_{-\infty}^{\infty} r(\mathbf{x}_r, t + \tau; \mathbf{x}_s) f(\mathbf{x}_r, \tau; \mathbf{x}_f, \bar{q}(\mathbf{x}, t; \mathbf{x}_f)) d\tau d\mathbf{S} \quad , \quad (3.42) \end{aligned}$$

with

$$\frac{\partial}{\partial t} r(\mathbf{x}_r, t; \mathbf{x}_s) = \frac{2}{\rho(\mathbf{x}_r)} \frac{\partial}{\partial z_r} g(\mathbf{x}_r, t; \mathbf{x}_s) \quad . \quad (3.43)$$

This is the single-sided or open boundary representation. Note that this equation only holds for focusing functions that vanish on ∂V_1 . It would not be sufficient to consider

a focusing function that was purely out-going on ∂V_1 : this would imply that the time-reversed focusing function was in-coming on ∂V_1 such that the integral over ∂V_1 would not vanish. The very same equation was derived in previous publications (Wapenaar et al., 2013, 2014b), however, involving several limitations regarding the Green's function. In particular, these derivations required up-/down-decomposition of the wavefields inside the volume as well as a truncated medium state, leading to a neglect of evanescent, refracted and diving waves. Our derivation does not involve any such assumptions, i.e. Equation 3.42 contains the full wavefield Green's function inside the volume. Similar conclusions were recently presented by Wapenaar et al. (Wapenaar et al., 2021), however, using a derivation built on a different definition of the focusing function. In particular, their focusing functions are source-free and focus on the surface ∂V_0 rather than inside the volume. Our scheme follows the concept introduced in (Diekmann and Vasconcelos, 2021b), where focusing functions are related to a source term $q(\mathbf{x}, t)$ and focus in space at \mathbf{x}_f when injected into a source-free volume. This approach explains both closed and open boundary integral representations. Note that our Equation 3.42 is slightly different from the conventional representation (Wapenaar et al., 2014b) because we define the negative, time-reversed auxiliary focal solution as the in-coming focusing function. Substituting $\phi(\mathbf{x}_s, t; \mathbf{x}_f, \bar{q}(\mathbf{x}, t; \mathbf{x}_f)) = -f(\mathbf{x}_s, -t; \mathbf{x}_f, \bar{q}(\mathbf{x}, t; \mathbf{x}_f))$ yields the traditional form. This single-sided representation is interesting for several reasons, mainly: (i) it allows us to retrieve a Green's function by injecting a wavefield from only one side. This is rather unusual since interferometry (just like time reversal acoustics) for open boundaries is conventionally prone to artefacts, compare Equation 3.40 where the time-reversed Green's function needs to be injected from the entire, closed boundary for accurate Green's function retrieval. (ii) Equation 3.42 can (under circumstances) be solved for the focusing and Green's function when an estimate of the first arrival of the Green's function is available. The underlying assumption is that there is a focusing function $-f(\mathbf{x}_s, -t; \mathbf{x}_f, \hat{q}(\mathbf{x}, t; \mathbf{x}_f))$ that is separated in time from the Green's function. We denote this additional constraint by the source $\hat{q}(\mathbf{x}, t; \mathbf{x}_f)$. This is where the previously introduced time-compact focusing functions come into play again, see Figures 3.6(a), 3.6(d) and 3.6(g). Such a time-compact focusing function only overlaps with the Green's function in the vicinity of the first arrival of the Green's function. Hence, we can define a window function $\theta(\mathbf{x}_s, t; \mathbf{x}_f)$ that removes all arrivals before $-t_{first}(\mathbf{x}_s; \mathbf{x}_f)$ and after $t_{first}(\mathbf{x}_s; \mathbf{x}_f)$, where $t_{first}(\mathbf{x}_s; \mathbf{x}_f)$ is the time of the first arrival of the wavefield for a source at \mathbf{x}_f and a receiver at \mathbf{x}_s (Wapenaar et al., 2012, 2014b; van der Neut et al., 2015b; Zhang et al., 2018). In other words, we have $\theta(\mathbf{x}_s, t; \mathbf{x}_f) = 0$ for all $|t| > t_{first}(\mathbf{x}_s; \mathbf{x}_f)$ and $\theta(\mathbf{x}_s, t; \mathbf{x}_f) = 1$ otherwise. Applying the window operator to Equation 3.42 we get:

$$\begin{aligned}
 & g_{first}(\mathbf{x}_s, t; \mathbf{x}_f) + f(\mathbf{x}_s, t; \mathbf{x}_f, \hat{q}(\mathbf{x}, t; \mathbf{x}_f)) = \\
 & -\theta(\mathbf{x}_s, t; \mathbf{x}_f) \int_{\mathbf{x}_r \in \partial V_0} \int_{-\infty}^{\infty} r(\mathbf{x}_r, t + \tau; \mathbf{x}_s) f(\mathbf{x}_r, \tau; \mathbf{x}_f, \hat{q}(\mathbf{x}, t; \mathbf{x}_f)) d\tau d\mathbf{S} \quad . \quad (3.44)
 \end{aligned}$$

This expression is a Marchenko-like integral (Burrige, 1980; Newton, 1980; Rose, 2001, 2002a; Brogini et al., 2012; Wu and You, 2021). Assuming that the first arrival of the Green's function $g_{first}(\mathbf{x}_s, t; \mathbf{x}_f)$ is known (e.g. from modelling in a smooth estimate of the medium), the equation contains only one unknown quantity, i.e. the focusing function. Thus, we can solve for the focusing function and, subsequently, via Equation 3.42

for the Green's function. Since the focus of this paper is on the derivation of the representations and not on their solutions, we refer the interested reader to other papers for the traditional approach (Wapenaar et al., 2014b; van der Neut et al., 2015b) or for a solution without up-/down-decomposed fields (Chapter 6). This equation forms the basis for many applications in geophysics, e.g. Green's function retrieval, multiple elimination and Marchenko imaging.

In this section we connected the insights from the previous sections with the concept of single-sided Green's function retrieval, i.e. we derived a Marchenko-like equation without up-/down-decomposition of the wavefields based on a partial differential equation framework for focusing functions. Note that we did not imply that solutions $f(\mathbf{x}_s, t; \mathbf{x}_f, \hat{q}(\mathbf{x}, t; \mathbf{x}_f))$ always exist for arbitrary media and conditions. However, we may say that if we find a focusing function using such an approach it obviously exists and obeys our constraints, i.e. it vanishes at ∂V_1 and is separated from the Green's function in time. So far, our experience with numerical examples confirms solutions do often exist and can be retrieved from boundary data, but to what extent that is the case in general is the subject of ongoing research. Our derivation does not include any approximations regarding the Green's function, i.e. if the focusing function exists under our constraints the reconstructed Green's function will contain the full-spectrum.

3.6. DISCUSSION

In this paper, we discuss and illustrate a new, generalised framework for wavefield focusing. Building on the concept introduced in Chapter 6 we add explanations to the definition of the focusing function as well as its relation to the Green's function. The underlying partial differential equation allows us to obtain the homogeneous Green's function of the second kind, a source-free, potentially asymmetric wavefield that contains the causal Green's function. This potential asymmetry stems from the fact that the homogeneous Green's function of the second kind comprises one in-coming field, i.e. the focusing function, and two out-going fields, i.e. the negative, time-reversed focusing function and the Green's function. When adding the homogeneous Green's function of the second kind and its time-reversed version, one always obtains the conventional homogeneous Green's function. This unifying property of focusing functions, or more precisely of their respective homogeneous Green's functions of the second kind, also implies a focus in space of the homogeneous Green's functions of the second kind at \mathbf{x}_f and zero time. It is due to this focus that we call the underlying fields focusing functions. Focusing functions have already been studied in the context of Marchenko-based schemes in geophysics (Wapenaar et al., 2014b; van der Neut et al., 2015b), however, our new definition generalises the concept of focusing and establishes a source term that enables modelling of focusing functions.

The numerical examples illustrate the concept of focusing and show how focusing functions can be built to destructively interfere with the local Green's function. Ultimately, we can construct focusing functions which are compact in time and, if desired, vanish on particular parts of the boundary. Using such time-compact focusing functions rather than Green's functions for time reversal modelling actually enables a superior accuracy of the retrieved homogeneous Green's functions. We find that the source distribution

$q(\mathbf{x}, t)$ that governs the focusing function might be ambiguous, i.e. different sources deliver the same combined focusing functions $f(\mathbf{x}_s, t; \mathbf{x}_f, q(\mathbf{x}, t)) - f(\mathbf{x}_s, -t; \mathbf{x}_f, q(\mathbf{x}, t))$. Although the numerical examples are in 1D, we think that similar approaches exist for 2D and 3D. These approaches will have to be more elaborate though, including, e.g. geometrical spreading and angle-dependent reflection coefficients. The results presented in this paper illustrate how we can use the full (two-way) wave equation to model time-compact focusing wavefields. Using a different approach, Elison et al. (Elison et al., 2021) recently presented modelled focusing functions in 2D. The way that we constructed the time-compact focusing fields is very example-specific and a generalisation to arbitrary media (as well as to 2D and 3D) is a topic for future research. The main goal of the numerical examples in this paper is simply the illustration of focusing functions in the light of our new definition.

The implications of our approach go beyond the ability to model focusing functions and increase the accuracy of time reversal acoustics. We also derived representations for Green's and focusing functions without up-/down-decomposed wavefields or a truncated medium assumption, suggesting that our derivation includes the full wavefield Green's function, involving diving, refracted and evanescent waves. Since we present a unified approach to wavefield focusing, we can derive such integrals for both closed and open boundary systems as both follow in a straightforward fashion from our underlying theory. The closed boundary representation is entirely general, i.e. valid for any focusing function. The open boundary representation on the other hand requires that the associated focusing function vanishes on the remaining boundary, i.e. this integral is only valid for a subset of focusing functions. In fact, it might even be that the open boundary representation is only valid for one unique focusing function (or none at all in complex media) since Equation 3.42 can often be directly inverted for $-f(\mathbf{x}_s, -t; \mathbf{x}_f, \bar{q}(\mathbf{x}, t; \mathbf{x}_f))$ when the Green's function is given (Vargas et al., 2021). If we want to solve the integral for the focusing and Green's functions based on an estimate of the first arrival Green's function we additionally need to assume that focusing and Green's functions can be separated in time. Using this separability assumption we obtain a Marchenko-like equation. It remains to be investigated, when exactly Equations 3.42 and 3.44 break, i.e. when and to what extent single-sided focusing in 2D and 3D becomes implausible. The separability assumption used in Equation 3.44 to solve the representation for focusing and Green's functions is known to fail for complex velocity and density models in 2D and 3D due to the related scattering patterns, including, e.g., diffractions (Schwarz, 2019; Vargas et al., 2021; van der Neut et al., 2021). Hence, even if there is a unique, single-sided focusing function $-f(\mathbf{x}_s, -t; \mathbf{x}_f, \bar{q}(\mathbf{x}, t; \mathbf{x}_f))$ for Equation 3.42 it might not necessarily obey the time-separability constraint (Vargas et al., 2021).

We suspect that our new partial differential equation approach might help to investigate these questions further. The underlying partial differential equations might also prove useful when it comes to combining Marchenko-like approaches with full waveform inversion (Virieux and Operto, 2009; Cui et al., 2020; Diekmann and Vasconcelos, 2020; Shoja et al., 2020; Diekmann et al., 2021). In 1D it is known how to extract the scattering potential from the focusing functions directly (Agranovich and Marchenko, 1963; Ware and Aki, 1969; Lamb Jr, 1980; Slob et al., 2020). For higher dimensions we might gain further understanding of the relation between the focusing function and the scat-

tering potential by studying our scheme more explicitly in 2D and 3D. Last but not least, our derivation shows that the representations, e.g., Equation 3.42 include the full wave Green's function. This might allow for more advanced data applications and experiments in the future, including evanescent, refracted and diving waves.

3.7. CONCLUSION

We present a partial differential equation framework for generalised wavefield focusing. In particular we define focusing functions that govern the homogeneous Green's function of the second kind. These homogeneous Green's functions of the second kind can be quite asymmetric both in time and space, but they always have a focus in space at \mathbf{x}_f and zero time. Furthermore, they deliver the conventional homogeneous Green's function when adding their time-reversed version. While our definition generalises the idea of focusing functions that were previously introduced in the context of Marchenko-like schemes, it also represents an entirely new way to describe these functions, paving the way for new insights and improved understanding. We discuss and illustrate different families of focusing functions with numerical examples, where our partial differential equation framework allows us to go beyond focusing functions described in previous approaches. In particular, we demonstrate how our equations allow for constructing time-compact focusing functions for closed and open boundary systems. Last but not least, we use reciprocity to obtain Marchenko-like integrals that relate focusing and Green's functions based on the homogeneous Green's function of the second kind. Owing to the unifying character of our wavefield focusing approach, we obtain these Marchenko-like integral representations for both closed and open boundaries. This derivation does not require up-/down-decomposed wavefields inside the medium and thus circumvents the limitations of most previous approaches.

ACKNOWLEDGEMENTS

The authors are thankful to Dirk-Jan van Manen, David Vargas, Andreas Tataris, Haorui Peng and Tristan van Leeuwen for discussions. Leon Diekmann is financially supported by the Utrecht Consortium for Subsurface Imaging (UCSI). Kees Wapenaar acknowledges funding from the European Research Council (ERC) under the European Union's Horizon 2020 research and innovation programme (grant agreement 742703). The authors are grateful to Giovanni Angelo Meles and an anonymous reviewer for their constructive feedback that helped to improve the paper.

APPENDIX I: DIPOLE SOURCE AMPLITUDES AT INTERFACES

In order to compute the amplitudes for a dipole source at an interface we have to exploit two relations: (i) the direct wavefield at the interface itself should have zero amplitude and (ii) the total emitted energy should be proportional to the physical properties of the medium around the interface. As stated in the text, we mimic the dipole by two monopoles with opposite polarity. Thus, one monopole is above the interface and the other below, see also Figure 3.9. Considering the point denoted by the triangle in this sketch, which is supposed to be infinitesimally far away from the interface, the first re-

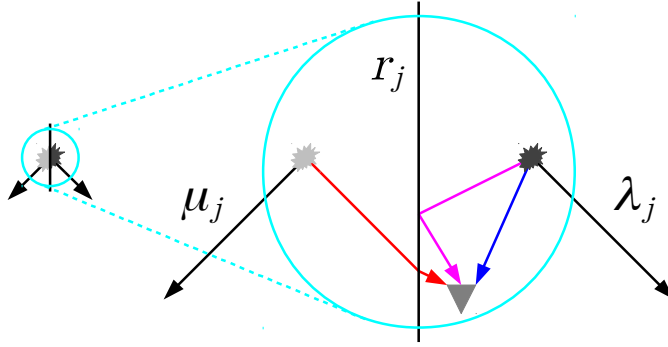


Figure 3.9: Sketch of a dipole source at an interface. Left: apparent source. Right: actual source used for modelling, consisting of two monopole sources. The reflectivity is denoted by r_j , μ_j and λ_j are proportional to the amplitudes of the apparent dipole source.

lation (i) means that the three direct field contributions indicated by the blue, magenta and red arrows cancel each other. This gives

$$\mu_j(1 + r_j) + \lambda_j(1 - r_j) = 0 \quad , \quad (3.45)$$

where μ_j and λ_j are proportional to the amplitudes of the dipole source as sketched in Figure 3.9, μ_j is positive and λ_j is negative. The second relation (ii) can be described by

$$|\mu_j| + |\lambda_j| = \mu_j - \lambda_j = (\rho_j + \rho_{j+1})c(\xi_j) \quad , \quad (3.46)$$

i.e. the amplitudes are proportional to the densities of the layers above and below the interface, scaled by an arbitrary velocity. From Equation 3.45 we obtain $\lambda_j/\mu_j = -(1 + r_j)/(1 - r_j)$ which equals the previously defined γ_j . Thus, the rightwards propagating wave has an initial, unweighted amplitude proportional to $\lambda_j = \gamma_j\mu_j$. Dividing Equation 3.46 by μ_j and using $\lambda_j/\mu_j = \gamma_j$ we obtain Equation 3.34.

APPENDIX II: EXISTENCE OF INVERSE MATRIX IN EQUATION 3.35

The determinant of the matrix in Equation 3.35 is

$$\frac{-(r_1 + 1)^2(r_4 + 1)(r_2 + 1)(r_1 r_2 + r_1 r_3 + r_1 r_4 + r_2 r_3 + r_2 r_4 + r_3 r_4 + r_1 r_2 r_3 r_4 + 1)}{(r_1 - 1)^{-1}(r_2 - 1)^{-1}} \quad , \quad (3.47)$$

where for all terms except for the fourth one it is straightforward to see that they are always different from zero for $|r_j| < 1$ with $j = 1, 2, 3, 4$. The fourth term is zero for

$$r_1 = -\frac{r_2 r_3 + r_2 r_4 + r_3 r_4 + 1}{r_2 + r_3 + r_4 + r_2 r_3 r_4} \quad , \quad (3.48)$$

or regarding the absolute value

$$|r_1| = \left| \frac{r_2 r_3 + r_2 r_4 + r_3 r_4 + 1}{r_2 + r_3 + r_4 + r_2 r_3 r_4} \right| = \left| \frac{p + r_4}{1 + p r_4} \right| \geq 1 \quad , \quad (3.49)$$

with $p = (1 + r_2 r_3)/(r_2 + r_3)$. By showing that the right-most inequality above holds true, we prove that the determinant can never be zero for the ranges of physically reasonable reflection coefficients that we consider. The inequality can be rewritten according to

$$(p + r_4)^2 \geq (1 + p r_4)^2 \Leftrightarrow p^2 - 1 \geq r_4^2 (p^2 - 1) \Leftrightarrow 1 \geq |r_4| \quad , \quad (3.50)$$

where the last inequality follows if $|p| > 1$ and then is true because we have $|r_4| < 1$. Thus, we have to show that

$$|p| > 1 \Leftrightarrow (1 + r_2 r_3)^2 > (r_2 + r_3)^2 \Leftrightarrow r_2^2 (r_3^2 - 1) > r_3^2 - 1 \Leftrightarrow |r_2| < 1 \quad , \quad (3.51)$$

where we use $r_3^2 - 1 < 0$ for $|r_3| < 1$ to obtain the last inequality. This last inequality is true such that the determinant is always different from zero for $|r_j| < 1$ with $j = 1, 2, 3, 4$.

DIRECT, WAVE-EQUATION-BASED MODELLING OF MARCHENKO-TYPE FOCUSING FUNCTIONS

Focusing functions are wavefields that focus at a single point when injected into a source-free volume from its boundary. Focusing functions that are related to the Marchenko equation can be injected from an open part of the boundary only, while vanishing on the remaining boundary. Building on this property, a method for direct, wave-equation-based modelling of Marchenko-type focusing functions in arbitrarily complex media is presented. The method naturally extends on conventional frequency-domain modelling. While the numerical examples are for 1D, a similar concept should in principle be applicable to the general 3D case.

4.1. INTRODUCTION

Time reversal acoustics (Fink, 1992, 1997) largely builds on the concept of homogeneous Green's functions (Oristaglio, 1989): when injecting a time-reversed Green's function into a source-free volume from its boundary, it contracts and focuses; then, it expands again and propagates out of the volume, delivering the (non-time-reversed) Green's function. This concept was recently generalised to the homogeneous Green's function of the second kind (Chapter 6), going beyond the time-symmetry of conventional time reversal acoustics. In this framework a so-called focusing function is injected into a source-free medium from its boundary. It produces a focus but also two expanding wavefields that propagate out of the volume: a negative, time-reversed focusing function and a Green's function. This homogeneous Green's function of the second kind is intimately linked to the Marchenko equation (Burrige, 1980; Broggini and Snieder, 2012; Tataris and van Leeuwen, 2022), a fundamental equation in inverse scattering theory (Colton and Kress, 1998). Marchenko-type focusing functions, the key ingredient of the Marchenko equation, can be injected into a volume from only an open part of its boundary to produce a focus (Chapter 3). Initially derived for 1D, the extension of the Marchenko integral

The content of this chapter was published as Diekmann and Vasconcelos (2023).

to 2D and 3D (Wapenaar et al., 2014a,b) paved the way for various applications like target-oriented imaging (Ravasi et al., 2016), multiple elimination (Zhang and Slob, 2019) and seismic monitoring (Brackenhoff et al., 2019a). While the original extension came with some limitations due to wavefield decomposition assumptions, recent approaches present less restrictive derivations, see Chapter 6 and Wapenaar et al. (2021).

Owing to these applications, modelling Marchenko-type focusing functions is a topic of great interest (Kiraz et al., 2021b). It enables a comparison of Marchenko-type focusing functions obtained from boundary data via data-driven schemes (Wapenaar et al., 2014b) with modelled reference results and generally allows to investigate and understand the physical properties of these wavefields better. There are different approaches to modelling focusing functions for a given medium: (i) They can be obtained by modelling a transmission response and inverting it (Wapenaar et al., 2017). (ii) They can be obtained using a recursive wavefield extrapolation scheme (Wapenaar, 1993; Elison et al., 2020; Wapenaar and de Ridder, 2022; Wapenaar, 2022). (iii) They can be obtained by computing a source term and then modelling a wave equation with this source (Chapter 3). All of these approaches, however, rely on a series of steps, i.e. there is no one-step strategy for modelling focusing functions – particularly not involving direct use of well-known wave-equation operators.

We present a novel method in this paper that allows for a direct, i.e. one-step, computation of Marchenko-type focusing functions. We rely on numerical representations of the wave-equation operator commonly used in modelling, e.g., via Helmholtz solvers. Our method is similar to (iii) in that it is based on the recent partial-differential-equation framework for focusing functions (Chapter 3). However, we seek to jointly model the Marchenko-type focusing function and its negative, time-reversed version. This is based on previous findings, suggesting a non-uniqueness of Marchenko-type focusing functions within a wave-equation framework, i.e. different source terms can give the same wavefield on the boundary of the volume (Chapter 3). Similar to (ii) it is crucial for our approach to model in the frequency domain. Our method, however, is based on solving a simple wave equation with an extra term. Ultimately, our scheme allows for modelling Marchenko-type focusing functions by solving a single linear inverse problem – similar to modelling Green's functions in the frequency domain. We show numerical examples in 1D.

4.2. FOCUSING FUNCTIONS

We define the Green's function $g(\mathbf{x}, \omega; \mathbf{x}_f)$ in the frequency domain as the solution to the following wave equation:

$$\mathfrak{L}(\mathbf{x}, \omega)g(\mathbf{x}, \omega; \mathbf{x}_f) = \rho i \omega \delta(\mathbf{x} - \mathbf{x}_f) \quad , \quad (4.1)$$

where the constant-density acoustic wave operator is

$$\mathfrak{L}(\mathbf{x}, \omega) = \nabla^2 + \frac{\omega^2}{c^2(\mathbf{x})} \quad (4.2)$$

and $g(\mathbf{x}, \omega; \mathbf{x}_f)$ is causal, i.e. it obeys radiation conditions for out-going waves at infinity (e.g., Oristaglio, 1989). The vector \mathbf{x} denotes space, ω represents frequency, \mathbf{x}_f is the

source location (which will be referred to as focusing location below), ρ mass density and $c(\mathbf{x})$ wave speed. Furthermore, we use the imaginary unit i and the Dirac delta $\delta(\mathbf{x} - \mathbf{x}_f)$. While we illustrate our approach with the constant-density acoustic wave equation, it should generally be applicable to other, lossless partial differential equations as well, e.g., the elastic wave equation. The complex-conjugate (or, in the time domain, time-reversed) Green's function $g^*(\mathbf{x}, \omega; \mathbf{x}_f)$ consequently obeys

$$\mathfrak{L}(\mathbf{x}, \omega) g^*(\mathbf{x}, \omega; \mathbf{x}_f) = -\rho i \omega \delta(\mathbf{x} - \mathbf{x}_f) \quad (4.3)$$

with an in-coming radiation condition, i.e. it is an anti-causal wavefield. We note that Equation 4.3 implies a lossless medium so that $\mathfrak{L}(\mathbf{x}, \omega)$ is indeed real-valued. Similarly, we define the focusing function $-f^*(\mathbf{x}, \omega; \mathbf{x}_f, q(\mathbf{x}, \omega))$ by

$$\mathfrak{L}(\mathbf{x}, \omega) \left(-f^*(\mathbf{x}, \omega; \mathbf{x}_f, q(\mathbf{x}, \omega)) \right) = -\frac{\rho i \omega \delta(\mathbf{x} - \mathbf{x}_f)}{2} - q(\mathbf{x}, \omega) \quad , \quad (4.4)$$

where $q(\mathbf{x}, \omega) \in \mathbb{R}$ and the focusing function is an anti-causal wavefield (Chapter 6). Anti-causal implies that for all sources the wave propagation precedes the energy emission at the respective source. Consequently, there can be propagating waves at both positive and negative times due to sources at positive and negative times in $q(\mathbf{x}, \omega)$. Note that while the source term $q(\mathbf{x}, \omega)$ has to be real-valued, it is otherwise arbitrary. Thus, Equation 4.4 defines a class of solutions. We will explain the focusing function terminology in the last paragraph of this section. The negative, conjugate focusing function $f(\mathbf{x}, \omega; \mathbf{x}_f, q(\mathbf{x}, \omega))$ follows according to

$$\mathfrak{L}(\mathbf{x}, \omega) f(\mathbf{x}, \omega; \mathbf{x}_f, q(\mathbf{x}, \omega)) = -\frac{\rho i \omega \delta(\mathbf{x} - \mathbf{x}_f)}{2} + q(\mathbf{x}, \omega) \quad (4.5)$$

and is a causal wavefield – this might appear confusing at first sight, given the name negative, conjugate focusing function. Here, we stress that the attribute *conjugate* in the name refers to the focusing function which is per definition a complex-conjugate field itself. By adding Equations 4.4 and 4.5 we get the time-isotropic focal response $f(\mathbf{x}, \omega; \mathbf{x}_f, q(\mathbf{x}, \omega)) - f^*(\mathbf{x}, \omega; \mathbf{x}_f, q(\mathbf{x}, \omega))$ as the wavefield that obeys

$$\mathfrak{L}(\mathbf{x}, \omega) \left(f(\mathbf{x}, \omega; \mathbf{x}_f, q(\mathbf{x}, \omega)) - f^*(\mathbf{x}, \omega; \mathbf{x}_f, q(\mathbf{x}, \omega)) \right) = -\rho i \omega \delta(\mathbf{x} - \mathbf{x}_f) \quad . \quad (4.6)$$

The name time-isotropic focal response refers to the fact that the source term is related to a single impulse at the focal point \mathbf{x}_f , equivalent to the source of the Green's function, that emits energy isotropically in both time directions (Chapter 3). Note that Equation 4.6 is non-unique with respect to the wavefield solution. Different sources $q(\mathbf{x}, \omega)$ in Equation 4.4 lead to different time-isotropic focal responses even though $q(\mathbf{x}, \omega)$ does not appear explicitly in Equation 4.6. Adding Equations 4.1 and 4.3 gives the equation for the homogeneous Green's function, adding Equations 4.1 and 4.6 delivers the equation for the homogeneous Green's function of the second kind (Chapter 6):

$$\mathfrak{L}(\mathbf{x}, \omega) \left(g(\mathbf{x}, \omega; \mathbf{x}_f) + f(\mathbf{x}, \omega; \mathbf{x}_f, q(\mathbf{x}, \omega)) - f^*(\mathbf{x}, \omega; \mathbf{x}_f, q(\mathbf{x}, \omega)) \right) = 0 \quad . \quad (4.7)$$

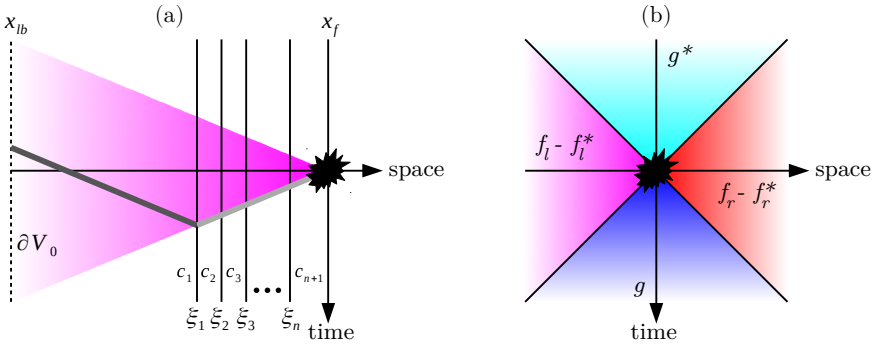


Figure 4.1: (a) Sketch illustrating the condition for separating the focusing function and its negative, conjugate version on the boundary ∂V_0 . The dashed line represents the boundary, vertical solid lines are interfaces where physical properties, e.g. wave speed, change. The black explosion marks the source location. The dark and light grey lines represent the space-time paths of a wave travelling from x_{fb} to ξ_1 and from x_f to ξ_1 , respectively. Note that we use straight lines for simplicity even though the wave speed might vary for the light grey path. The pink cone is analogous to that in (b). (b) Cones (or triangles) illustrating the propagation through space-time for the four discussed wavefield solutions, i.e. the Green's function (g , blue), the left-directed focal response ($f_l - f_l^*$, magenta), the conjugate Green's function (g^* , cyan) and the right-directed focal response ($f_r - f_r^*$, red). The black explosion marks the source location.

This wavefield is source-free and can be described in the following way: the focusing function $-f^*(\mathbf{x}, \omega; \mathbf{x}_f, q(\mathbf{x}, \omega))$ is an in-coming wavefield (with respect to a sphere around \mathbf{x}_f of infinite radius) that propagates towards the focal spot \mathbf{x}_f . After scattering and focusing, two out-going wavefields emerge: the negative, conjugate focusing function $f(\mathbf{x}, \omega; \mathbf{x}_f, q(\mathbf{x}, \omega))$ and the Green's function. As the homogeneous Green's function of the second kind has a focus at zero time at \mathbf{x}_f , the in-coming wavefield $-f^*(\mathbf{x}, \omega; \mathbf{x}_f, q(\mathbf{x}, \omega))$ is referred to as a focusing function, i.e. a wavefield that generates a focus when injected into a source-free medium. This homogeneous Green's function of the second kind is a useful concept for inverse scattering problems, as it is closely related to the Marchenko integral, see Burridge (1980), Wapenaar et al. (2014b) and Chapter 3. For further information on the use of focusing functions we refer the interested reader to the afore-mentioned literature, for in this paper we focus on a novel approach for direct, wave-equation-based modelling of Marchenko-type focusing functions.

4.3. MARCHENKO-TYPE FOCUSING FUNCTIONS

Marchenko-type focusing functions form a particularly interesting subset of focusing functions. Consider a volume V bounded by ∂V such that $\mathbf{x}_f \in V$ and $q(\mathbf{x} \notin V, \omega) = 0$. Furthermore, we assume that the medium is reflection-free outside of V . We can then use

$$\begin{aligned} \mathcal{L}(\mathbf{x}, \omega) \left(f(\mathbf{x}, \omega; \mathbf{x}_f, q(\mathbf{x}, \omega)) - f^*(\mathbf{x}, \omega; \mathbf{x}_f, q(\mathbf{x}, \omega)) \right) &= -\rho i \omega \delta(\mathbf{x} - \mathbf{x}_f) \\ &\quad - \int_{\mathbf{x}_r \in \partial V} \frac{2i\omega}{c(\mathbf{x}_r)} \delta(\mathbf{x} - \mathbf{x}_r) f^*(\mathbf{x}_r, \omega; \mathbf{x}_f, q(\mathbf{x}, \omega)) dS \end{aligned} \quad (4.8)$$

to model the wavefield within the volume, i.e. for $\mathbf{x} \in V$ (Schuster, 2009; Fokkema and van den Berg, 1993) – see also Appendix for details on derivation. We stress that Equation 4.8 is only valid within V , while Equation 4.6 is valid for all \mathbf{x} . Next, we split the boundary in two parts, namely ∂V_0 and ∂V_1 . Owing to the arbitrary source term $q(\mathbf{x}, \omega)$ in Equation 4.5 there are infinitely many focusing functions and we can constrain solutions by adding extra conditions. For instance we can choose focusing functions that vanish on ∂V_1 . This requires a particular source configuration $\bar{q}(\mathbf{x}, \omega)$ that depends on the location \mathbf{x}_f as well as the medium properties and the appearance of the boundary ∂V_0 . For complex 2D and 3D media it is not clear yet whether these sort of focusing functions always exist – we hope that the method presented in this paper might help to further investigate this in future research. In 1D, however, focusing functions that vanish on the left or right part of the boundary exist, see Burridge (1980) and Chapter 3 – note that the boundary of a 1D domain consists of only two points and we assume a horizontal space direction here. Assuming that a focusing function exists such that $-f^*(\mathbf{x}_r, \omega; \mathbf{x}_f, \bar{q}(\mathbf{x}, \omega)) = 0 \quad \forall \mathbf{x}_r \in \partial V_1$, Equation 4.8 simplifies to:

$$\begin{aligned} \mathfrak{L}(\mathbf{x}, \omega) \left(f(\mathbf{x}, \omega; \mathbf{x}_f, \bar{q}(\mathbf{x}, \omega)) - f^*(\mathbf{x}, \omega; \mathbf{x}_f, \bar{q}(\mathbf{x}, \omega)) \right) &= -\rho i \omega \delta(\mathbf{x} - \mathbf{x}_f) \\ &\quad - \int_{\mathbf{x}_r \in \partial V_0} \frac{2i\omega}{c(\mathbf{x}_r)} \delta(\mathbf{x} - \mathbf{x}_r) f^*(\mathbf{x}_r, \omega; \mathbf{x}_f, \bar{q}(\mathbf{x}, \omega)) dS \quad , \end{aligned} \quad (4.9)$$

where $-f^*(\mathbf{x}, \omega; \mathbf{x}_f, \bar{q}(\mathbf{x}, \omega))$ is a Marchenko-type focusing function, i.e. a focusing function that vanishes on an open part of the boundary.

4.4. DIRECT, WAVE-EQUATION-BASED MODELLING

A discrete version of Equation 4.1 can be written as

$$\mathbf{L}\mathbf{g} = \mathbf{d} \quad , \quad (4.10)$$

where \mathbf{L} is a square matrix replacing the operator in Equation 4.2, \mathbf{d} is the vectorial form of the right-hand side of Equation 4.1 and \mathbf{g} is the Green's function vector in the frequency domain. For Equation 4.9 we get

$$\mathbf{L}(\mathbf{f} - \mathbf{f}^*) = -\mathbf{d} - \mathbf{R}^T \Lambda \mathbf{R} \mathbf{f}^* \quad , \quad (4.11)$$

where $-\mathbf{f}^*$ is the focusing function vector in the frequency domain, \mathbf{R} is a restriction matrix that only keeps the elements on the boundary ∂V_0 of the vector on which it is acting and Λ is a scaling matrix that accounts for $\lambda 2i\omega/c(\mathbf{x}_r)$ with the factor λ being related to the integration. The product $\mathbf{R}^T \mathbf{R}$ gives a matrix of the same size as \mathbf{L} which mutes all elements of the volume that are not on the boundary. Note that the same assumptions as before, see Equations 4.8 and 4.9, apply: Equation 4.11 gives the wavefield within a bounded volume V for a medium that is reflection-free outside V . In practice this requires to include, e.g., absorbing boundaries within the matrix \mathbf{L} (Engquist and Majda, 1977).

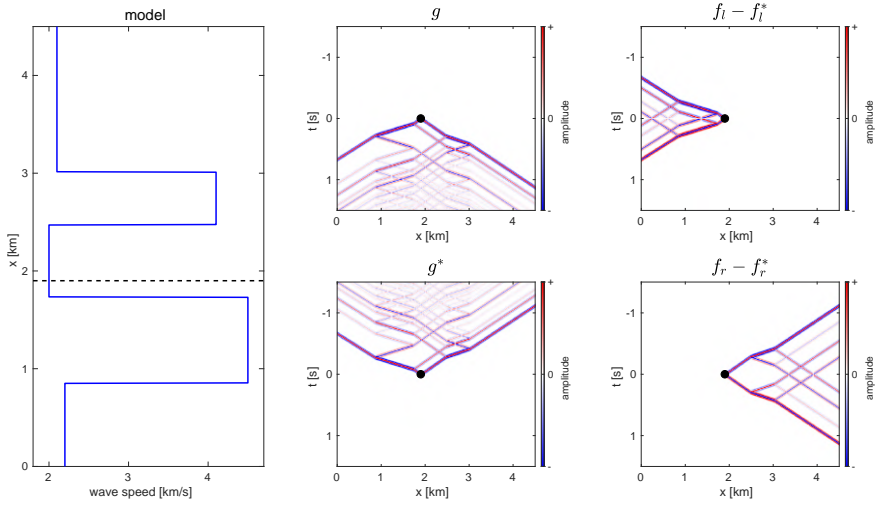


Figure 4.2: Wave speed model, where the black dotted line marks the focal location (model, left), Green's function (g , top center), conjugate Green's function (g^* , bottom center), left-directed focal response ($f_l - f_l^*$, top right), right-directed focal response ($f_r - f_r^*$, bottom right). The black dots denote the source location. All wavefields are plotted with the same amplitude scaling for direct comparison.

Our aim is to rewrite Equation 4.11 such that it only contains a single unknown wavefield, i.e. the time-isotropic focal response $\mathbf{f} - \mathbf{f}^*$. In this regard, we note that the incoming focusing function and the out-going negative, conjugate focusing function appear separated from each other in time on the boundary ∂V_0 under the following condition in 1D: the time it takes for a wave to travel from the, e.g., left boundary ∂V_0 at x_{lb} to the first reflecting interface at ξ_1 has to be greater than the time it takes from the source at x_f to ξ_1 . This is also illustrated in Figure 4.1(a). More precisely, this can be formulated as

$$\frac{\xi_1 - x_{lb}}{c_1} > \sum_{i=2}^n \frac{\xi_i - \xi_{i-1}}{c_i} + \frac{x_f - \xi_n}{c_{n+1}}, \quad (4.12)$$

where c_i with $i = 1, 2, \dots, n+1$ is the wave speed in the i -th layer and ξ_i with $i = 1, 2, \dots, n$ is the location of the i -th interface. This condition is related to the fact that multiple scattering at the first interface has to be suppressed by the last event in the focusing function. Note that this separability condition is fundamentally different from time-separating Green's and focusing functions in Marchenko schemes (Wapenaar et al., 2014b). The latter process relies on potentially restrictive assumptions about medium properties (particularly in 2D and 3D). We stress here that time-separating the focusing function and its negative, conjugate version (within a given bandwidth) on ∂V_0 should always be possible when extending the homogeneous space between ∂V_0 and ξ_1 sufficiently far. A similar condition likely applies to 2D and 3D, though this is a subject of ongoing research. Assuming that Equation 4.12 holds, we can replace the in-coming focusing function on the

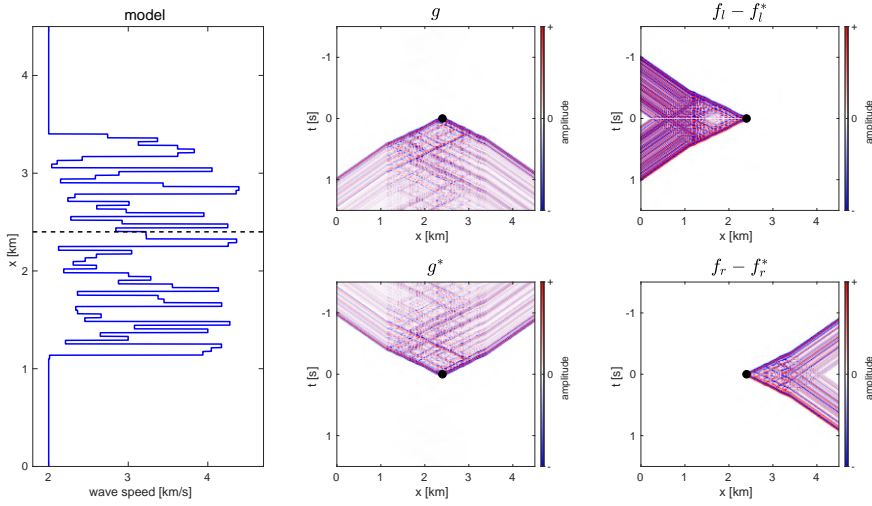


Figure 4.3: Wave speed model, where the black dotted line marks the focal location (model, left), Green's function (g , top center), conjugate Green's function (g^* , bottom center), left-directed focal response ($f_l - f_l^*$, top right), right-directed focal response ($f_r - f_r^*$, bottom right). The black dots denote the source location. All wavefields are plotted with the same amplitude scaling for direct comparison.

boundary ∂V_0 in Equation 4.11, i.e. $-\mathbf{R}\mathbf{f}^*$, by an expression in terms of $\mathbf{f} - \mathbf{f}^*$ according to

$$-\mathbf{R}\mathbf{f}^* = -\mathbf{F}\mathbf{T}\mathbf{M}\mathbf{F}^{\mathbf{T}}\mathbf{R}(\mathbf{f} - \mathbf{f}^*) \quad , \quad (4.13)$$

where \mathbf{F} and $\mathbf{F}^{\mathbf{T}}$ are the forward and inverse Fourier transform matrices, respectively, \mathbf{M} is a matrix that mutes everything at negative times and \mathbf{T} is a time reversal matrix. Hence, we separate \mathbf{f} from $\mathbf{f} - \mathbf{f}^*$ on the boundary by muting (as justified by Equation 4.12) and time-reverse the result to get \mathbf{f}^* . Using a different muting matrix, that mutes all data at positive times, and no time reversal matrix would not work because this would allow for the Green's function to be a solution. Instead, it is important to link the out-going field to the in-coming field and thus enforce the anti-symmetry in time of the time-isotropic focal response by means of the time reversal operator. Note that Equation 4.13 requires the vector $\mathbf{f} - \mathbf{f}^*$ to contain the entire wavefield at all frequencies of interest. In practice, the discrete frequency support, in other words the amount and rate of frequency samples, depends on the desired time-domain wavelet used to describe the impulse source \mathbf{d} .

Combining Equations 4.11 and 4.13 gives

$$(\mathbf{L} + \mathbf{R}^{\mathbf{T}} \mathbf{\Lambda} \mathbf{F} \mathbf{T} \mathbf{M} \mathbf{F}^{\mathbf{T}} \mathbf{R})(\mathbf{f} - \mathbf{f}^*) = \mathbf{K}(\mathbf{f} - \mathbf{f}^*) = -\mathbf{d} \quad , \quad (4.14)$$

i.e. a linear system for the time-isotropic focal response $\mathbf{f} - \mathbf{f}^*$. While \mathbf{L} can be chosen to be an $n_x \times n_x$ matrix for a single frequency in Equations 4.10 and 4.11, it must be an $n_x n_\omega \times n_x n_\omega$ matrix here, where n_x is the number of volume samples and n_ω is the number of frequency samples. This system can be solved by various methods. In particular, any, e.g. Helmholtz, solver can be used for building the matrix \mathbf{L} and inverting the

equation for the wavefield. In 2D and 3D the matrix \mathbf{K} becomes very large, albeit sparse, and linear operator toolboxes might be helpful (Ravasi and Vasconcelos, 2020). Note the similarity between Equations 4.10 and 4.14; however, Equation 4.10 can be solved for the Green's function per frequency, while Equation 4.14 has to be solved for all frequencies simultaneously. We know that Marchenko-type focusing functions exist in some cases (Chapters 3 and 6) but investigating the full space of solutions is ongoing research. Note that this has implications for the physical meaning of numerical solutions for the inverse of \mathbf{K} . In 1D, however, it is well established that Marchenko-type focusing functions generally exist (Burridge, 1980). Note that the source term $q(\mathbf{x}, \omega)$ in Equation 4.4 is not needed to compute $\mathbf{f} - \mathbf{f}^*$. The individual fields \mathbf{f} and $-\mathbf{f}^*$, however, obey wave equations with non-zero $q(\mathbf{x}, \omega)$ sources (Chapter 3).

4.5. NUMERICAL EXAMPLES

In this section we show numerical examples in 1D to demonstrate the applicability of the modelling scheme. We consider constant density acoustics, but the approach could generally be used for variable density and even non-dissipative elastic media as well.

The first example we consider is a five layer medium as depicted in Figure 4.2. The Green's function and the conjugate Green's function are computed by solving Equation 4.10 and $\mathbf{L}^* \mathbf{g}^* = -\mathbf{d}$ for a bounded volume. Note that the matrix \mathbf{L} is not usually real-valued for a bounded volume (due to absorbing boundaries) and $\mathbf{d}^* = -\mathbf{d}$. The wavefields are convolved with a 20 Hz Ricker wavelet and plotted in the time domain for a better interpretation. As explained before, the Green's function in Figure 4.2 propagates forward in time, i.e. it is an out-going (with respect to the volume bounded by 0 km and 4.5 km in this example), causal field. Causality means that the wave propagation follows after the source emits energy.

The conjugate Green's function is the time-reversed Green's function in the time domain (see Figure 4.2). It is an in-coming, anti-causal wavefield, i.e. it induces energy into the medium and contracts until it focuses at the source, where the energy is absorbed.

Next, we model the time-isotropic focal response via Equation 4.14. Note that there are two options in 1D: we can either have a focusing function that vanishes on the right boundary, meaning that the injection boundary ∂V_0 is on the left, or a focusing function that vanishes on the left, such that ∂V_0 is on the right. We will refer to these options as a left-directed focal response $\mathbf{f}_l - \mathbf{f}_l^*$ and a right-directed focal response $\mathbf{f}_r - \mathbf{f}_r^*$. Left- and right-directed refer to the fact that these wavefields are per definition only propagating towards one side. Note that left- and right-directed focal responses will have different matrices \mathbf{K}_l and \mathbf{K}_r in Equation 4.14 (due to different restriction operators \mathbf{R}_l and \mathbf{R}_r for the left and right boundary, respectively), but the same source. We omit the attribute time-isotropic in the name here because such a left-/right-directed field is generally only possible for time-isotropic functions. The left-directed focal response is shown in Figure 4.2 (top-right). It contains an in-coming, anti-causal field, i.e. the focusing function, as well as an out-going, causal field, i.e. the negative, conjugate focusing function. The only source within the bounded volume, however, is the impulse source at \mathbf{x}_f which is the same source as that of the conjugate Green's function. In accordance with our separability condition, see Equation 4.12, all events at ∂V_0 , i.e. the left boundary in this case,

recorded at negative times belong to the focusing function, while the events at positive times belong to the negative, conjugate focusing function. The left-directed focal response is an intriguing wavefield: it is purely propagating between the left boundary and the source location at \mathbf{x}_f and it is compact in time, meaning that for every point in space the wavefield has a distinct, finite duration. Within our bounded volume for instance, there are no waves before -0.7 s and after 0.7 s. In fact, the left-directed focal response propagates in a region of space-time that the Green's functions (both forward and time-reversed) can not reach – except for a small overlap of the first arrival of the Green's function and the last arrival of the negative, conjugate focusing function (and equivalently at negative times). This is also illustrated in Figure 4.1(b). Note that this separability of the left-directed focal response and the Green's function was not used as a constraint for modelling but is instead an inherent feature of one-dimensional Marchenko-type focusing functions (Burridge, 1980; Wapenaar et al., 2014b).

The right-directed focal response is also shown in Figure 4.2. It behaves similarly to the left-directed focal response but covers a different portion of space-time, see also Figure 4.1(b). Ultimately, the four solutions, i.e. the Green's function, the conjugate Green's function, the left-directed focal response and the right-directed focal response, are all separated from each other in space-time, but together they span the entire space-time. In this context, one can think of the Green's function as a future-directed focal response (a response to a single impulse source that is expanding away from $t = 0$ s towards increasing time) and the conjugate Green's function as a past-directed focal response (contracting towards increasing time until $t = 0$ s).

Finally, in Figure 4.3 we show an example of a randomly-layered medium. Our modelling scheme does not require computing specific scattering interactions between the different layers, instead we just solve Equation 4.14 like in the previous example. Owing to the multitude of reflectors in the model, the Green's functions (forward and time-reversed) now show numerous scattering events and, therefore, substantially more complex interference patterns within their respective propagation cones. Similarly, the left- and right-directed focal responses are much more complicated than in the preceding example. Nonetheless, the focusing functions and their negative, conjugate versions can still be separated on ∂V_0 . In fact, one can observe how the complex interference patterns of the left-directed focal response in Figure 4.3 fade out while the waves propagate through the first layer (between x_{lb} and ξ_1 , compare Figure 4.1(a)) towards the left boundary – and equivalently for the right-directed focal response. Just as before, the left- and right-directed focal responses propagate purely between ∂V_0 and \mathbf{x}_f and are compact in time for a fixed point in space.

4.6. DISCUSSION

We present a method for direct, wave-equation-based modelling of time-isotropic focal responses. The method is based on a simple linear system, Equation 4.14, similar to frequency-domain Green's function modelling. Hence, any solver for frequency-domain wave equations can be deployed. The key difference to modelling Green's functions is that Equation 4.14 has to be solved for all frequencies simultaneously.

In our approach we separate the in-coming focusing function and the out-going neg-

ative, conjugate focusing function on the boundary ∂V_0 in time. This requires a sufficiently thick, homogeneous boundary layer (compare Equation 4.12). Nonetheless, this is a straightforward assumption for modelling, where such a thick, homogeneous boundary layer can easily be added for any numerical experiment. Such numerical studies help to gain further and deeper understanding of focusing functions. Alternatively, one might investigate other methods for separating \mathbf{f} and $-\mathbf{f}^*$ on ∂V_0 , e.g., based on wavefield decomposition (Slob et al., 2014).

We stress that our approach allows for modelling $\mathbf{f} - \mathbf{f}^*$ but not, e.g., only the focusing function $-\mathbf{f}^*$. This is due to the ambiguity of the source term, i.e. the same left/right-directed focal response can be retrieved from different source configurations $\bar{q}(\mathbf{x}, t)$ (Chapter 3). Note, however, that the focusing function on the boundary can be extracted from $\mathbf{f} - \mathbf{f}^*$ by taking the wavefield at negative times. Similarly, it is not immediately possible to model a closed-boundary time-isotropic focal response, i.e. a response that can propagate to both boundaries in 1D, by using Equation 4.8 rather than Equation 4.9. The reason for this is that any focusing function obeys this closed-boundary integral. For instance, $(-\mathbf{g} + \mathbf{g}^*)/2$ would be such a time-isotropic focal response – but there are also time-compact solutions like $(\mathbf{f}_l - \mathbf{f}_l^* + \mathbf{f}_r - \mathbf{f}_r^*)/2$. Even when adding a constraint for time-compactness, however, it is unclear how to split the energy left and right, e.g. $(\mathbf{f}_l - \mathbf{f}_l^*)/4 + (\mathbf{f}_r - \mathbf{f}_r^*)(3/4)$ or $\mathbf{f}_l - \mathbf{f}_l^*$ are both valid solutions.

As we showed in the examples, Marchenko-type focusing functions vanish on one side of the boundary in 1D. Furthermore, the related left/right-directed focal responses are compact in time. This compactness is an important feature in Marchenko schemes (Wapenaar et al., 2014b), however, it is violated in complex 2D and 3D media (Vargas et al., 2021). Therefore, the existence and uniqueness of solutions to Equation 4.14 in 2D and 3D media and for finite, open acquisition surfaces remain to be investigated. If there are in fact no perfect solutions, a least squares approach might be useful.

An extension of our scheme to 2D and 3D is crucial, since Marchenko-type focusing in these higher dimensions remains a challenging and intriguing topic. Although such an extension can be based on the same theoretical framework, the solution strategy might have to involve regularised least squares and potentially more advanced solvers (Engquist and Ying, 2011). Furthermore, the problem, i.e. the matrix \mathbf{K} in Equation 4.14, becomes significantly larger requiring an elaborate implementation. In general, having such a straightforward, direct modelling scheme for Marchenko-type focusing functions is an extremely helpful tool for investigating and understanding focusing.

ACKNOWLEDGEMENTS

The authors are grateful to Kees Wapenaar and Andreas Tataris for discussions. This research was financially supported by the Utrecht Consortium for Subsurface Imaging (UCSI).

APPENDIX

In this section we discuss the derivation of Equation 8 in the paper. We start from Rayleigh's reciprocity theorem for acoustic waves (Fokkema and van den Berg, 1993):

$$\begin{aligned} & \int_{\mathbf{x}_r \in \partial V} \left(p^A(\mathbf{x}_r, \omega) \mathbf{v}^B(\mathbf{x}_r, \omega) - p^B(\mathbf{x}_r, \omega) \mathbf{v}^A(\mathbf{x}_r, \omega) \right) \cdot d\mathbf{S} = \\ & \int_{\mathbf{x} \in V} \mathbf{v}^B(\mathbf{x}, \omega) \cdot \mathbf{f}^A(\mathbf{x}, \omega) + p^A(\mathbf{x}, \omega) s^B(\mathbf{x}, \omega) - p^B(\mathbf{x}, \omega) s^A(\mathbf{x}, \omega) - \mathbf{v}^A(\mathbf{x}, \omega) \cdot \mathbf{f}^B(\mathbf{x}, \omega) dV \\ & + \int_{\mathbf{x} \in V} i\omega p^A(\mathbf{x}, \omega) p^B(\mathbf{x}, \omega) (\kappa^B(\mathbf{x}) - \kappa^A(\mathbf{x})) - i\omega \mathbf{v}^A(\mathbf{x}, \omega) \cdot \mathbf{v}^B(\mathbf{x}, \omega) (\rho^B(\mathbf{x}) - \rho^A(\mathbf{x})) dV \quad , \end{aligned} \quad (\text{I})$$

where we have two wave states denoted by the superscripts A and B in a volume V bounded by ∂V . The variables $p(\mathbf{x}, \omega)$ and $\mathbf{v}(\mathbf{x}, \omega) = [v_1(\mathbf{x}, \omega) \ v_2(\mathbf{x}, \omega) \ v_3(\mathbf{x}, \omega)]^T$ represent the pressure field and the particle velocity field. The sources $\mathbf{f}(\mathbf{x}, \omega) = [f_1(\mathbf{x}, \omega) \ f_2(\mathbf{x}, \omega) \ f_3(\mathbf{x}, \omega)]^T$ and $s(\mathbf{x}, \omega)$ are sources of volume force density and volume injection rate density. The medium is characterised by compressibility $\kappa(\mathbf{x}) = 1/(\rho(\mathbf{x})c^2(\mathbf{x}))$ and mass density $\rho(\mathbf{x})$. In our paper we study a setup with zero force sources such that $\mathbf{f}^A(\mathbf{x}, \omega) = \mathbf{f}^B(\mathbf{x}, \omega) = \mathbf{0}$. This leads to $\mathbf{v}(\mathbf{x}, \omega) = (\rho(\mathbf{x})i\omega)^{-1} \nabla p(\mathbf{x}, \omega)$. Furthermore, we consider two wave states with identical medium parameters and constant density such that $\kappa^A(\mathbf{x}) = \kappa^B(\mathbf{x})$. Consequently, the last integral in above equation is zero. This delivers

$$\begin{aligned} & \int_{\mathbf{x}_r \in \partial V} \frac{1}{\rho i\omega} \left(p^A(\mathbf{x}_r, \omega) \nabla p^B(\mathbf{x}_r, \omega) - p^B(\mathbf{x}_r, \omega) \nabla p^A(\mathbf{x}_r, \omega) \right) \cdot d\mathbf{S} = \\ & \int_{\mathbf{x} \in V} p^A(\mathbf{x}, \omega) s^B(\mathbf{x}, \omega) - p^B(\mathbf{x}, \omega) s^A(\mathbf{x}, \omega) dV \quad . \end{aligned} \quad (\text{II})$$

In order to get Equation 8 in the paper we consider the following two wave states:

$$\mathfrak{L}(\mathbf{x}, \omega) \overbrace{\left(f(\mathbf{x}, \omega; \mathbf{x}_f, q(\mathbf{x}, \omega)) - f^*(\mathbf{x}, \omega; \mathbf{x}_f, q(\mathbf{x}, \omega)) \right)}^{p^A(\mathbf{x}, \omega)} = \rho i\omega \overbrace{\left(-\delta(\mathbf{x} - \mathbf{x}_f) \right)}^{s^A(\mathbf{x})} \quad \text{for state A,} \quad (\text{III})$$

$$\mathfrak{L}(\mathbf{x}, \omega) \underbrace{g(\mathbf{x}, \omega; \mathbf{x}_s)}_{p^B(\mathbf{x}, \omega)} = \rho i\omega \underbrace{\delta(\mathbf{x} - \mathbf{x}_s)}_{s^B(\mathbf{x})} \quad \text{for state B.} \quad (\text{IV})$$

Hence for a volume V that contains \mathbf{x}_s and \mathbf{x}_f and $q(\mathbf{x} \notin V, \omega) = 0$, $p^A(\mathbf{x}, \omega)$ contains both in-coming waves $p_{\text{in}}^A(\mathbf{x}, \omega) = -f^*(\mathbf{x}, \omega; \mathbf{x}_f, q(\mathbf{x}, \omega))$ and out-going waves $p_{\text{out}}^A(\mathbf{x}, \omega) = f(\mathbf{x}, \omega; \mathbf{x}_f, q(\mathbf{x}, \omega))$, whereas $p^B(\mathbf{x}, \omega)$ is entirely out-going. Using, e.g., far-field (Sommer-

feld) radiation conditions (Schuster, 2009) we find that Equation II becomes

$$\int_{\mathbf{x}_r \in \partial V} \frac{1}{\rho i \omega} \left(p^A(\mathbf{x}_r, \omega) \frac{i \omega}{c(\mathbf{x}_r)} p^B(\mathbf{x}_r, \omega) - p^B(\mathbf{x}_r, \omega) \frac{i \omega}{c(\mathbf{x}_r)} p^A(\mathbf{x}_r, \omega) + p^B(\mathbf{x}_r, \omega) \frac{i \omega}{c(\mathbf{x}_r)} p_{\text{in}}^A(\mathbf{x}_r, \omega) \right) d\mathbf{S} = \int_{\mathbf{x} \in V} p^A(\mathbf{x}, \omega) s^B(\mathbf{x}, \omega) - p^B(\mathbf{x}, \omega) s^A(\mathbf{x}, \omega) dV \quad , \quad (\text{V})$$

which can be simplified to obtain

$$\int_{\mathbf{x}_r \in \partial V} \frac{2}{\rho c(\mathbf{x}_r)} p_{\text{in}}^A(\mathbf{x}_r, \omega) p^B(\mathbf{x}_r, \omega) d\mathbf{S} = \int_{\mathbf{x} \in V} p^A(\mathbf{x}, \omega) s^B(\mathbf{x}, \omega) - p^B(\mathbf{x}, \omega) s^A(\mathbf{x}, \omega) dV \quad . \quad (\text{VI})$$

Plugging Equations III and IV into this delivers

$$- \int_{\mathbf{x}_r \in \partial V} \frac{2}{\rho c(\mathbf{x}_r)} f^*(\mathbf{x}_r, \omega; \mathbf{x}_f, q(\mathbf{x}, \omega)) g(\mathbf{x}_r, \omega; \mathbf{x}_s) d\mathbf{S} = f(\mathbf{x}_s, \omega; \mathbf{x}_f, q(\mathbf{x}, \omega)) - f^*(\mathbf{x}_s, \omega; \mathbf{x}_f, q(\mathbf{x}, \omega)) + g(\mathbf{x}_f, \omega; \mathbf{x}_s) \quad . \quad (\text{VII})$$

Next, we substitute \mathbf{x}_s with \mathbf{x} and multiply both sides with the wave operator $\mathfrak{L}(\mathbf{x}, \omega)$:

$$- \int_{\mathbf{x}_r \in \partial V} \frac{2i\omega}{c(\mathbf{x}_r)} f^*(\mathbf{x}_r, \omega; \mathbf{x}_f, q(\mathbf{x}, \omega)) \delta(\mathbf{x} - \mathbf{x}_r) d\mathbf{S} = \mathfrak{L}(\mathbf{x}, \omega) \left(f(\mathbf{x}, \omega; \mathbf{x}_f, q(\mathbf{x}, \omega)) - f^*(\mathbf{x}, \omega; \mathbf{x}_f, q(\mathbf{x}, \omega)) \right) + \rho i \omega \delta(\mathbf{x} - \mathbf{x}_f) \quad , \quad (\text{VIII})$$

where we use Equation 1 from the paper and invoke source-receiver reciprocity. Equation VIII is identical to Equation 8 in the paper. We stress that Equation VIII is only valid for \mathbf{x} in V . However, if one aims to solve the equation for the wavefield by modelling, it is necessary to solve for a domain D that expands beyond V to include the sources on the boundary ∂V . The resulting wavefield modelling is unphysical for $\mathbf{x} \notin V$ but accurate for $\mathbf{x} \in V$. Furthermore, we note that an absorbing boundary condition should be applied outside of the volume V and its boundary ∂V to ensure that all sources of Equation VIII are modelled correctly.

INVERSE DESIGN FOR DIRECTIONAL SOURCE MULTIPOLES AND WAVEFIELD FOCUSING

We present a method for designing sources such that their related acoustic wavefields have specific, desired radiation properties. In particular, we use this source design strategy to study directional wavefield focusing: we seek to find a wavefield that is incident from only one half of a volume and focuses at a single point. Such focusing wavefields are relatively well understood in one dimension and play an important role in inverse scattering and imaging problems. The extent to which these fields are approximative in two and three dimensions, however, is yet to be understood. We approach this question by investigating the related problem of finding directional source multipoles that emit energy in a preferred direction only. Hence these sources produce wavefields that vanish in one half of the volume. While we focus on investigating directional sources and wavefield focusing in homogeneous media, we also discuss the underlying procedure in the context of arbitrarily heterogeneous media. For our numerical examples, we find that directional focusing wavefields are inherently approximative in 2D, meaning that the wavefields from the directional sources do not actually vanish completely in one half-space. They are, however, so close to zero within the desired region that the approximation seems justifiable.

5.1. INTRODUCTION

The ability to control wavefield radiation is of great interest in physics, geoscience, engineering and material science. For example, photonic crystals are materials that have a particular effect on electromagnetic waves by having a specifically arranged sub-wavelength structure (Joannopoulos et al., 1997). As a result, these structures might absorb (Park et al., 2009) or focus waves (Kurt et al., 2008). Similarly, phononic crystals affect elastic waves (Håkansson et al., 2007). In this context, inverse design – i.e. optimising crystal structures to yield a desired wavefield outcome – has proven to be a very power-

The content of this chapter is under review as Diekmann et al. (2023a).

ful technique (Sanchis et al., 2004).

Inspired by such inverse design strategies, we present a method that we refer to as inverse source design. Hence, we want to obtain a wavefield with certain qualities for a given material/model and design the source accordingly. Such a wavefield quality could be a preferred directionality for instance. The resulting source is a multipole. Our inverse source design approach allows to go beyond classical, analytically tractable multipoles like dipole or quadrupole sources (Bilbao and Hamilton, 2018).

The main question we seek to investigate with inverse source design in this paper is the following: Can we create a wavefield that is incident from only one half of a two-dimensional homogeneous volume and focuses at a single point? In that context we also discuss the related question: Can we create a source multipole in two dimensions that emits a wavefield in one direction only? In one dimension, these sources and wavefields are known to exist for arbitrarily heterogeneous media (Burrige, 1980). Such a wavefield, for instance, can be injected into a volume from one side and delivers a perfect focus, meaning that the wavefield collapses to a single point in the volume at a particular time (Chapter 3). In multiple dimensions, however, these wavefields, so-called Marchenko-type focusing functions, are not yet fully understood.

Hence, we propose inverse source design as a method for constructing Marchenko-type focusing functions in 2D and 3D (Chapters 3 and 6). These wavefields are related to the Marchenko integral (Burrige, 1980; Newton, 1980), a fundamental equation in one dimensional inverse scattering theory (Colton and Kress, 1998). While conventional focusing functions are wavefields that focus when injected into a source-free medium from its closed boundary, Marchenko-type focusing functions can be injected from a limited portion of the boundary only and still deliver a precise focus (Chapter 3). This is possible because Marchenko-type focusing functions are zero on the remaining boundary. The original Marchenko integral (Burrige, 1980; Brogгинi and Snieder, 2012) was extended to 2D and 3D about ten years ago (Wapenaar et al., 2014b, 2013). Recent research has overcome initial limitations about wavefield decomposition, see Chapter 6 and Kiraz et al. (2021b), Wapenaar et al. (2021), and generalised the concept by using a framework based on partial differential equations rather than integral equations (Chapter 3). As indicated before, Marchenko-type focusing functions are relatively well understood in 1D, see Burrige (1980) and Chapters 3 and 4, their limitations in multiple dimensions, however, are subject to ongoing research (Wapenaar, 2020a). Marchenko-type focusing functions are used for predicting and suppressing the effects of multiple scattering (Zhang and Slob, 2019), target-oriented imaging (Cui et al., 2020; Shoja et al., 2023) and limited-aperture artefact-free imaging (Wapenaar et al., 2014b; Diekmann et al., 2021).

In this paper we present a method for modelling Marchenko-type focusing functions in 2D. While we primarily investigate homogeneous media, the method appears to be extendable to modelling in heterogeneous media. Being able to model these wavefields is a crucial step in understanding them. It allows for investigating the fields in different media and evaluating the accuracy of underlying theoretical assumptions. Different strategies for modelling Marchenko-type focusing functions have been proposed: one can model Green's functions and invert the Marchenko integral (Wapenaar et al., 2017) or use recursive wavefield extrapolation schemes (Elison et al., 2020; Wapenaar and de Ridder, 2022). Alternatively, one can formulate the task as a wavefield reconstruc-

tion problem (Hajjaj et al., 2022). All of these approaches, however, rely on the fact that the Marchenko-type focusing function is only non-zero on a horizontal boundary above (or, equivalently, below) the model – an assumption that does not necessarily hold for arbitrarily heterogeneous media in 2D and 3D. Direct wave-equation-based modelling is successful in 1D, where the Marchenko-type focusing function does in fact vanish on a portion of the boundary (Chapter 4). Alternatively, one can compute a source term for the Marchenko-type focusing function first and then insert it into the wave equation (Chapter 3). Constructing such source terms is relatively straightforward in 1D, but in more dimensions it is a difficult task. Hence, we propose inverse source design. This allows us to model Marchenko-type focusing functions that obey the wave equation and approximately (in a least-squares sense) vanish on a portion of the boundary. In that sense this approach is consistent with the physics of focusing functions, i.e. our resulting Marchenko-type focusing functions will produce perfect foci but the radiation condition, meaning that the functions vanish in a particular direction, is only fulfilled to the extent that is possible.

We present a numerical example of a Marchenko-type focusing function in a 2D homogeneous medium and discuss its implications. In particular, we illustrate how a Marchenko-type focusing function can vanish on a portion of the boundary. We also discuss how to apply our inverse design approach to other, arbitrarily heterogeneous media.

While our research is strongly connected to the Marchenko integral it has implications beyond this context. Directional sources might be useful for various experiments in acoustics and Marchenko-type focusing functions can generally be employed for producing a focus inside of a medium that is only accessible from an open portion of its boundary.

5.2. GREEN'S FUNCTIONS AND FOCUSING FUNCTIONS

In this paper we investigate acoustic waves $u(\mathbf{x}, t)$ in a two dimensional medium with constant density ρ and velocity c , obeying the following wave equation:

$$\left(\nabla^2 - \frac{1}{c^2} \frac{\partial^2}{\partial t^2} \right) u(\mathbf{x}, t) = -\rho \frac{\partial s(\mathbf{x}, t)}{\partial t} \quad , \quad (5.1)$$

where t is time, $\mathbf{x} = [x \ z]^T$ denotes space and $s(\mathbf{x}, t)$ is a source of volume injection rate density. Using the Fourier transform

$$u(\mathbf{x}, \omega) = \int_{-\infty}^{\infty} u(\mathbf{x}, t) \exp(i\omega t) dt \quad , \quad (5.2)$$

Equation 5.1 becomes the Helmholtz equation

$$\left(\nabla^2 + \frac{\omega^2}{c^2} \right) u(\mathbf{x}, \omega) = \rho i \omega s(\mathbf{x}, \omega) \quad , \quad (5.3)$$

where we use the frequency ω , the imaginary unit $i = \sqrt{-1}$ and $s(\mathbf{x}, \omega)$ is the frequency domain source term.

A Green's function $g(\mathbf{x}, \omega; \mathbf{x}_f)$ obeys Equation 5.3 for $s(\mathbf{x}, \omega) = \delta(\mathbf{x} - \mathbf{x}_f)$, i.e. it is the

medium's impulse response for a source at \mathbf{x}_f . It is a causal, out-going (with respect to a volume V bounded by ∂V that contains the source location \mathbf{x}_f) wavefield (Oristaglio, 1989). While the Green's function of a homogeneous medium in 2D can be accurately described by a weighted Hankel function of the first kind of zeroth order, it can be approximated more compactly for $k(\omega)r(\mathbf{x}; \mathbf{x}_f) \gg 1$ (in the far field) by (Groenenboom and Snieder, 1995)

$$g(\mathbf{x}, \omega; \mathbf{x}_f) = \frac{\rho i \omega}{4\sqrt{\pi/2}} \frac{\exp(i(k(\omega)r(\mathbf{x}; \mathbf{x}_f) - 3\pi/4))}{\sqrt{k(\omega)r(\mathbf{x}; \mathbf{x}_f)}} , \quad (5.4)$$

where we use the wavenumber $k(\omega) = \omega/c$ and the distance of propagation $r(\mathbf{x}; \mathbf{x}_f) = \sqrt{(\mathbf{x} - \mathbf{x}_f)^T (\mathbf{x} - \mathbf{x}_f)}$.

A focusing function $-f^*(\mathbf{x}, \omega; \mathbf{x}_f, q(\mathbf{x}, \omega))$ represents a field solution of

$$\left(\nabla^2 + \frac{\omega^2}{c^2} \right) \left(-f^*(\mathbf{x}, \omega; \mathbf{x}_f, q(\mathbf{x}, \omega)) \right) = -\frac{\rho i \omega \delta(\mathbf{x} - \mathbf{x}_f)}{2} - q(\mathbf{x}, \omega) , \quad (5.5)$$

where $q(\mathbf{x}, \omega)$ is real-valued but otherwise an arbitrary source term (Chapter 3). The symbol $*$ marks complex conjugation, which corresponds to time reversal in the time domain. The focusing function is an anti-causal, in-coming wavefield for a volume V with $\mathbf{x}_f \in V$ and $q(\mathbf{x} \notin V, \omega) = 0$. Anti-causal means that for each source the energy propagates prior to being absorbed at the respective source. The condition that $q(\mathbf{x}, \omega)$ is real-valued implies a time-symmetric source $q(\mathbf{x}, t)$ in the time domain.

Combining Green's functions and focusing functions we can build the homogeneous Green's function of the second kind (Chapter 3) as the solution of

$$\left(\nabla^2 + \frac{\omega^2}{c^2} \right) \left(g(\mathbf{x}, \omega; \mathbf{x}_f) + f(\mathbf{x}, \omega; \mathbf{x}_f, q(\mathbf{x}, \omega)) - f^*(\mathbf{x}, \omega; \mathbf{x}_f, q(\mathbf{x}, \omega)) \right) = 0 . \quad (5.6)$$

Here, the focusing function is the only in-coming wavefield while both the Green's function and the negative, time-reversed focusing function are out-going. The homogeneous Green's function of the second kind is a source-free field. In the most trivial case of $q(\mathbf{x}, \omega) = 0$ the homogeneous Green's function of the second kind is identical to the conventional homogeneous Green's function, i.e. $g(\mathbf{x}, \omega; \mathbf{x}_f) + g^*(\mathbf{x}, \omega; \mathbf{x}_f)$ (Oristaglio, 1989).

5.3. MARCHENKO-TYPE FOCUSING FUNCTIONS

We define a Marchenko-type focusing function as a focusing function with an additional property: it vanishes on a particular part of the closed boundary ∂V of the volume V for which $\mathbf{x}_f \in V$ and $q(\mathbf{x} \notin V, \omega) = 0$ (Chapter 3). This property allows for formulating an open-boundary reciprocity integral, similar to the Marchenko integral, see Burrige (1980), Rose (2001), Broggini and Snieder (2012) and Chapter 3, that relates Marchenko-type focusing functions with Green's functions. While the Marchenko integral is well

understood in 1D, its limitations in 2D and 3D scattering problems (Wapenaar et al., 2014b) are unclear. We use the variable $q(\mathbf{x}, \omega)$ to indicate that it is only a particular type of focusing function sources that governs these Marchenko-type focusing functions. In this paper we discuss a way of modelling these Marchenko-type focusing functions in 2D. Furthermore, we illustrate and investigate the degree to which the fundamental assumption that the Marchenko-type focusing function vanishes on a portion of ∂V is feasible. On that note we make use of the following time reversal modelling formulation of Equation 5.6 (Chapter 4):

$$\begin{aligned} \left(\nabla^2 + \frac{\omega^2}{c^2} \right) \left(g(\mathbf{x}, \omega; \mathbf{x}_f) + f(\mathbf{x}, \omega; \mathbf{x}_f, q(\mathbf{x}, \omega)) - \right. \\ \left. f^*(\mathbf{x}, \omega; \mathbf{x}_f, q(\mathbf{x}, \omega)) \right) = \\ - \int_{\mathbf{x}_r \in \partial V} \frac{2i\omega}{c} \delta(\mathbf{x} - \mathbf{x}_r) f^*(\mathbf{x}_r, \omega; \mathbf{x}_f, q(\mathbf{x}, \omega)) d\mathbf{S} \quad . \end{aligned} \quad (5.7)$$

This equation is correct for \mathbf{x} in V (but unphysical for $\mathbf{x} \notin V$) and simulates injecting the in-coming wavefield, i.e. the focusing function, into the volume V . This holds true for all focusing functions.

If we split the boundary ∂V in two parts and consider a Marchenko-type focusing function that is different from zero on ∂V_0 and vanishes on ∂V_1 we get

$$\begin{aligned} \left(\nabla^2 + \frac{\omega^2}{c^2} \right) \left(g(\mathbf{x}, \omega; \mathbf{x}_f) + f(\mathbf{x}, \omega; \mathbf{x}_f, \underline{q}(\mathbf{x}, \omega)) - \right. \\ \left. f^*(\mathbf{x}, \omega; \mathbf{x}_f, \underline{q}(\mathbf{x}, \omega)) \right) = \\ - \int_{\mathbf{x}_r \in \partial V_0} \frac{2i\omega}{c} \delta(\mathbf{x} - \mathbf{x}_r) f^*(\mathbf{x}_r, \omega; \mathbf{x}_f, \underline{q}(\mathbf{x}, \omega)) d\mathbf{S} \quad . \end{aligned} \quad (5.8)$$

This equation forms the basis for the Marchenko integral, but it is not clear if such focusing functions, i.e. focusing functions that are zero on the boundary ∂V_1 , actually exist in 2D and 3D. We will illustrate this time reversal modelling of Marchenko-type focusing functions in 2D below.

5.4. CONCEPT OF INVERSE SOURCE DESIGN

We refer to the following procedure as inverse source design because we start by formulating constraints for a wavefield that we would like to obtain and then invert for the sources that govern this wavefield – or the closest, wave-equation-consistent version of it in a least-squares sense. We invert for sources within a bounded area (active region) and match the desired wavefield in a particular portion of the far field (matching region). The part of the field that belongs to neither the active nor the matching region is referred to as passive region. We will give an explicit example for how exactly to define these regions in the next section.

We make use of the following relation between the sources $s(\mathbf{x}, \omega)$ and the wavefield

$u(\mathbf{x}, \omega)$:

$$u(\mathbf{x}, \omega) = \int_{\mathbf{x}_s \in V_{act}} s(\mathbf{x}_s, \omega) g(\mathbf{x}, \omega; \mathbf{x}_s) d\mathbf{x}_s \quad , \quad (5.9)$$

exploiting that any field $u(\mathbf{x}, \omega)$ can be written as a weighted superposition of Green's functions, where $s(\mathbf{x}, \omega)$, analogous to Equation 5.3, acts as a weighting function. The location \mathbf{x}_s is supposed to be within the volume V_{act} , i.e. within the active region.

Let \mathbf{u} and \mathbf{s} be the discretely sampled vectorial forms of $u(\mathbf{x}, \omega)$ and $s(\mathbf{x}_s, \omega)$ for a single frequency. While \mathbf{u} is a vector for all locations \mathbf{x} within the volume under investigation, \mathbf{s} is a vector for all locations \mathbf{x}_s within the active region. We minimise the following objective function $v(\mathbf{s}, \alpha)$ for a given regularisation value $\alpha \in \mathbb{R}^+$ to estimate the source term \mathbf{s} :

$$v(\mathbf{s}, \alpha) = \left\| \underbrace{\mathbf{R}\mathbf{W}\mathbf{M}}_{\mathbf{Q}} \mathbf{s} - \underbrace{\mathbf{R}\mathbf{W}\mathbf{u}}_d \right\|_2^2 + \alpha \|\mathbf{s}\|_2^2 \quad , \quad (5.10)$$

where we have the real-valued restriction operator \mathbf{R} that only keeps the wavefield in the matching region, the real-valued weighting operator \mathbf{W} that compensates for amplitude decay due to geometrical spreading, i.e. by multiplication with a factor of $\sqrt{r(\mathbf{x}; \mathbf{x}_f)}$, and the complex modelling operator \mathbf{M} that uses the analytical Green's functions (Equation 5.4) to compute the superimposed wavefield that is generated by the individual monopole sources in \mathbf{s} analogous to Equation 5.9. We assume a homogeneous medium here, allowing for cheap computations of these Green's functions and a trivial weighting operator. Both matrices \mathbf{R} and \mathbf{W} are diagonal, \mathbf{R} is additionally zero for several values on the diagonal. This represents a linear inverse problem. We find the minimum of Equation 5.10 for

$$\mathbf{s} = \left(\mathbf{Q}^\dagger \mathbf{Q} + \alpha \mathbf{I} \right)^{-1} \left(\mathbf{Q}^\dagger d \right) \quad , \quad (5.11)$$

where \mathbf{I} is the identity matrix.

Note that we investigate a homogeneous medium in this study, which allows for a cheap computation of the weighting operator \mathbf{W} and the Green's functions to get \mathbf{M} . However, the method is not in any way limited to homogeneous media. Heterogeneous media can be examined by using, e.g., a Helmholtz solver to compute $g(\mathbf{x}, \omega; \mathbf{x}_s)$ in Equation 5.9. While the weighting operator theoretically becomes more complex for heterogeneous media, a homogeneous, e.g. effective medium, approximation might often be sufficient to estimate \mathbf{W} . Furthermore, we focus on 2D in this paper but the method can easily be extended to 3D.

5.5. INVERSE SOURCE DESIGN FOR MODELLING BAND-LIMITED, MARCHENKO-TYPE FOCUSING FUNCTIONS

The aim of this paper is to investigate band-limited Marchenko-type focusing functions in 2D. Hence, we aim to find sources $s(\mathbf{x}, \omega) = s_f(\mathbf{x}, \omega)$ via Equation 5.11 that govern a negative, time-reversed focusing function $u(\mathbf{x}, \omega) = f(\mathbf{x}, \omega; \mathbf{x}_f, q(\mathbf{x}, \omega))$ (we choose the

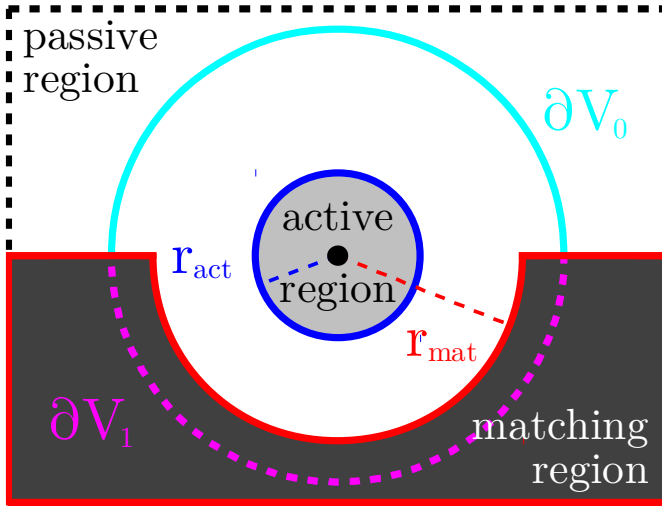


Figure 5.1: Sketch of the active (blue outline), passive and matching region (red outline) used to model Marchenko-type focusing functions. The active region is defined by the radius r_{act} while the matching region follows from the radius r_{mat} and the depth of the focusing location \mathbf{x}_f (black dot). The latter indicates the horizontal upper boundary of the matching region. The variables ∂V_0 (cyan) and ∂V_1 (magenta) are related to Equation 5.8. Note that the precise shapes of the regions are consistent with our numerical experiments, but not a methodological restriction of any sorts.

negative, time-reversed version for it is a causal field and, thus, can be modelled in the time domain later). From Equation 5.5 we know that we get

$$s_f(\mathbf{x}, \omega) = -\frac{\delta(\mathbf{x} - \mathbf{x}_f)}{2} - i \frac{q(\mathbf{x}, \omega)}{\rho\omega} \quad (5.12)$$

in the case of a focusing function source. Since $q(\mathbf{x}, \omega)$ is a real-valued function (Chapter 3), $s_f(\mathbf{x}, \omega)$ is imaginary everywhere except at \mathbf{x}_f where it is complex with real part $-\delta(\mathbf{x} - \mathbf{x}_f)/2$.

We are trying to model Marchenko-type focusing functions, i.e. focusing functions that vanish on the portion ∂V_1 of the boundary ∂V that encloses the volume V (compare Equation 5.8 and Figure 5.1). Hence, we do not require any particular prior knowledge of the field $f(\mathbf{x}, \omega; \mathbf{x}_f, \underline{q}(\mathbf{x}, \omega))$ if we restrict the matching region V_{mat} to the area where

$$f(\mathbf{x} \in V_{\text{mat}}, \omega; \mathbf{x}_f, \underline{q}(\mathbf{x}, \omega)) = 0 \quad , \quad (5.13)$$

see Figure 5.1. Thus, our matching region covers the far field in the lower half of the volume, where we want the focusing function to vanish. This is extremely useful because it means that we can find sources for the Marchenko-type focusing function when the only prior information we have on the wavefield is that it is zero in a particular region. We can then simplify the source term, Equation 5.12, by changing the desired wavefield

to

$$u(\mathbf{x}, \omega) = \frac{g(\mathbf{x}, \omega, \mathbf{x}_f)}{2} \quad \forall \quad \mathbf{x} \in V_{\text{mat}} \quad , \quad (5.14)$$

leading to the purely imaginary auxiliary source term $s(\mathbf{x}, \omega) = s_a(\mathbf{x}, \omega)$ with

$$s_a(\mathbf{x}, \omega) = -i \frac{q(\mathbf{x}, \omega)}{\rho \omega} \quad . \quad (5.15)$$

Note that there is no trivial solution to this problem: we are looking for an imaginary source term that governs a Green's function on ∂V_1 while the actual source of the Green's function is $\delta(\mathbf{x} - \mathbf{x}_f)$, which is real-valued. If we solve the simplified problem with Equations 5.14 and 5.15 we get our desired source term for the Marchenko-type focusing function via

$$s_f(\mathbf{x}, \omega) = s_a(\mathbf{x}, \omega) - \frac{\delta(\mathbf{x} - \mathbf{x}_f)}{2} \quad . \quad (5.16)$$

Finally, we want to obtain a band-limited version of a Marchenko-type focusing function. Hence, we are matching a band-limited wavefield $u(\mathbf{x}, \omega)$, i.e. including a multiplication with the band-limited frequency-domain wavelet $\mathfrak{w}(\omega)$. We use a Ricker wavelet for this purpose. Furthermore, we have to multiply the impulse source in Equation 5.16 by $\mathfrak{w}(\omega)$. These two steps ensure that we relate our Marchenko-type focusing function to a band-limited Green's function with the wavelet $\mathfrak{w}(\omega)$.

Employing all of the above constraints, we can estimate a source \mathbf{s} by minimising the following objective function

$$\nu(\mathbf{s}, \alpha) = \left\| \begin{bmatrix} -\mathbf{R}\mathbf{W}\Im(\mathbf{M}) \\ \mathbf{R}\mathbf{W}\Re(\mathbf{M}) \end{bmatrix} \mathbf{s} - \begin{bmatrix} \mathbf{R}\mathbf{W}\Re(\mathbf{u}) \\ \mathbf{R}\mathbf{W}\Im(\mathbf{u}) \end{bmatrix} \right\|_2^2 + \alpha \|\mathbf{s}\|_2^2 \quad (5.17)$$

with \mathbf{u} and \mathbf{s} being the vectorial forms of

$$u(\mathbf{x}, \omega) = \frac{g(\mathbf{x}, \omega; \mathbf{x}_f) \mathfrak{w}(\omega)}{2} \quad (5.18)$$

and

$$s(\mathbf{x}, \omega) = \frac{1}{i} s_a(\mathbf{x}, \omega) \quad . \quad (5.19)$$

Similar to before, Equation 5.17 can be solved for \mathbf{s} by using Equation 5.11 with an accordingly adjusted \mathbf{Q} and \mathbf{d} . The final source follows from

$$s_f(\mathbf{x}, \omega) = s_a(\mathbf{x}, \omega) - \frac{\delta(\mathbf{x} - \mathbf{x}_f) \mathfrak{w}(\omega)}{2} \quad . \quad (5.20)$$

By using a band-limited wavelet $\mathfrak{w}(\omega)$ we are able to compute $s_f(\mathbf{x}, \omega)$ for all frequencies within a frequency range of interest and can convert the solution to the time domain via

$$s_f(\mathbf{x}, t) = \frac{1}{2\pi} \int_{-\infty}^{\infty} s_f(\mathbf{x}, \omega) \exp(-i\omega t) d\omega \quad . \quad (5.21)$$

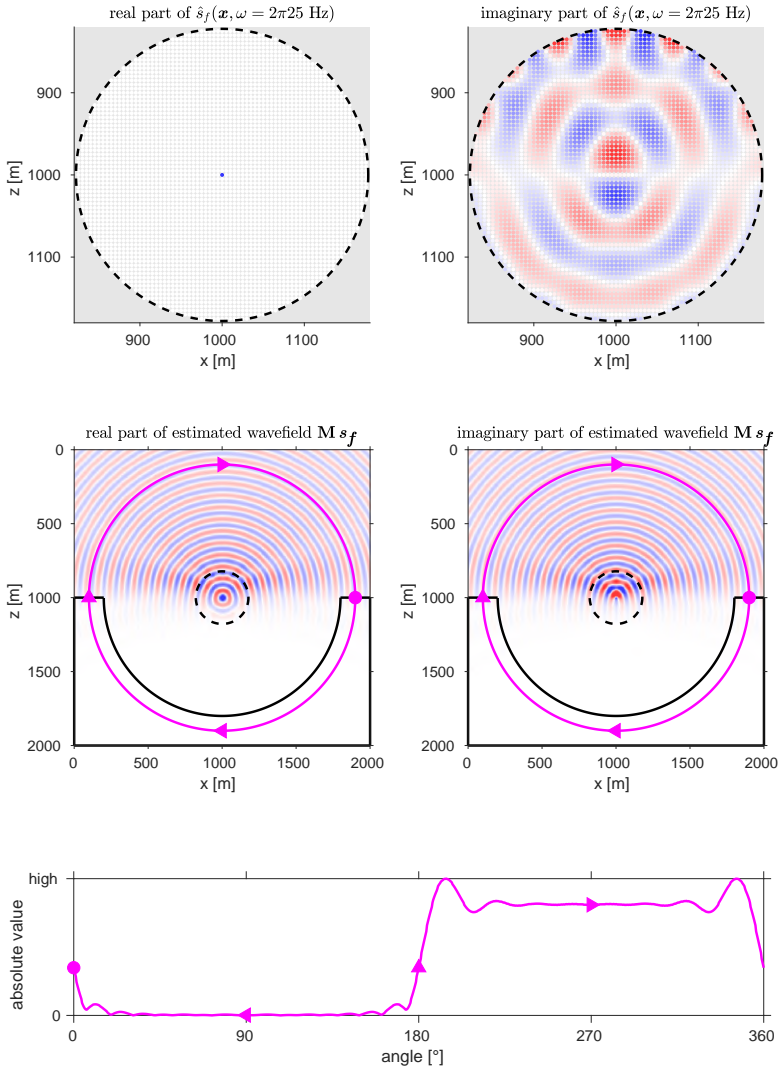


Figure 5.2: Top: inverted source term $s_f(\mathbf{x}, \omega)$ at 25 Hz. Real part (top-left) and imaginary part (top-right) at the same scaling. Centre: estimated wavefield, obtained by applying the modelling operator \mathbf{M} to the inverted focusing function source vector \mathbf{s}_f . Real part (centre-left) and imaginary part (centre-right) at the same scaling. The dashed black circles denote the active region, the solid black lines show the outline of the matching region. Note that the inverted source term (top plots) is only shown for the active region, while the wavefield (centre plots) is shown for the full volume. The magenta circles mark a distance of 900 m to \mathbf{x}_f , where the circular marker denotes an angle of 0° and the different triangles mark 90° , 180° and 270° . The orientation of these triangles is the same in the wavefield plots (centre) and the bottom plot such that, e.g., the left-facing triangle is at 90° . Blue colors indicate negative and red colors positive values. Bottom: absolute value (power) of estimated wavefield in a distance of 900 m as a function of angle, see magenta circles in wavefield plots.

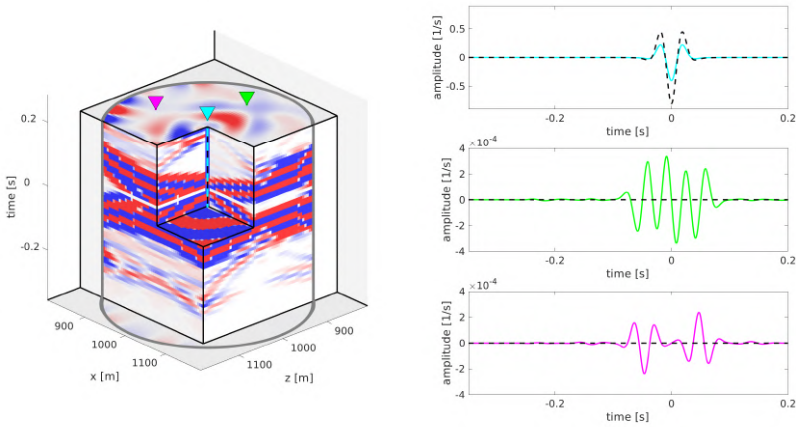


Figure 5.3: Time-domain source term $s_f(\mathbf{x}, t)$. Left: cube to illustrate the source as a function of space and time. Blue colour is related to negative, red to positive amplitudes. For the locations marked by the three triangles we show the source as a function of only time on the right. The grey cylinder outlines the active region. Right: source as a function of time for three exemplary locations. The cyan line is at \mathbf{x}_f . The black curves show the signal $s_f(\mathbf{x}, t) + s_f(\mathbf{x}, -t)$ for the respective \mathbf{x} locations.

This time-domain source function can then be used in Equation 5.1 to model the related wavefield:

$$\left(\nabla^2 - \frac{1}{c^2} \frac{\partial^2}{\partial t^2} \right) f(\mathbf{x}, t; \mathbf{x}_f, \underline{q}(\mathbf{x}, t)) = -\rho \frac{\partial s_f(\mathbf{x}, t)}{\partial t} \quad , \quad (5.22)$$

where $f(\mathbf{x}, t; \mathbf{x}_f, \underline{q}(\mathbf{x}, t))$ is the negative, time-reversed version of a band-limited, Marchenko-type focusing function. We note that this wavefield obeys our definition of a focusing function in Equation 5.5. Hence, this is a perfect, full-spectrum focusing function. The condition in Equation 5.13, however, is only fulfilled approximately (in a least-squares sense). By using finite difference modelling in the time domain to obtain the negative, time-reversed focusing function, we can confirm the quality of the inverted source term.

5.6. NUMERICAL EXAMPLE

In this section we illustrate the process of inverse source design for modelling band-limited, Marchenko-type focusing functions. Our main emphasis is on studying the accuracy of the assumption in Equation 5.13: can a focusing function actually vanish on the boundary ∂V_1 ? This is of interest for inverse scattering theory as this assumption underlies the Marchenko integral and it remains unclear to what extent it is valid in 2D and 3D.

We study a medium with $c = 2000$ m/s and $\rho = 1800$ kg/m³. The focusing location is at $x_f = 1000$ m and $z_f = 1000$ m. The volume under investigation extends 2000 m in x - and

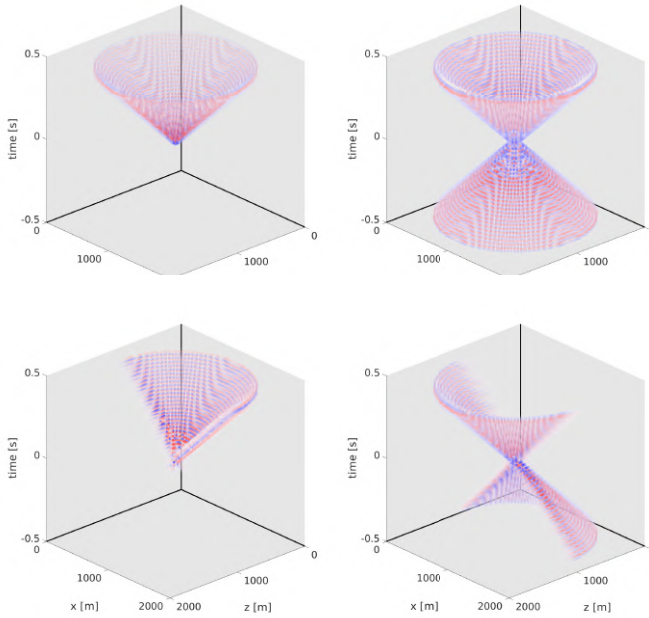


Figure 5.4: Modelling results for the Green's function (top-left) and the Marchenko-type focusing function (bottom-left). Modelling results for the homogeneous Green's function (top-right) and the homogeneous Green's function of the second kind (bottom-right). Note that we only show the wavefields within the injection boundary here (compare Figure 5.5 where we show the wavefields everywhere).

2000 m in z -direction, sampled in a 5 m interval. The wavelet is a filtered Ricker wavelet (Ricker, 1953) with a peak frequency of 20 Hz and a compact frequency support on the range between 0 Hz and 62.5 Hz. The frequencies are sampled with 0.5 Hz.

We use an active region with a radius of about 177 m (containing 3985 individual source monopoles) and a matching region with a radius of 800 m, see Figure 5.1. Consequently, the focusing function should vanish in the far field of the lower half of the model (at ∂V_1).

Inverting for $s_f(\mathbf{x}; \omega)$ at 25 Hz using Equation 5.20 gives the source in Figure 5.2 (top). We choose the optimal regularisation parameter α by means of an L-curve, which gives $\alpha = 10^{15}$. As expected, this source follows Equation 5.12 in that it is imaginary everywhere except at \mathbf{x}_f , see the blue dot in the centre of the real part of the inverted source multipole. The imaginary part has an interesting structure: while it is symmetric with respect to the z -axis (through \mathbf{x}_f), it is non-symmetric with respect to the x -axis (through \mathbf{x}_f).

Before proceeding with other frequencies, we can evaluate the estimated wavefield at 25 Hz by applying the modelling operator \mathbf{M} to the inverted focusing function source s_f

(note that this refers to the vectorial form of $s_f(\mathbf{x}, \omega)$ here and not the source in Equation 5.19). This estimated wavefield is the best possible realisation of a Marchenko-type focusing function. Hence it should, at least approximately, obey Equation 5.13. In fact, the wavefield in Figure 5.2 (centre) is close to zero (white color) in the lower half of the model. This is also shown in Figure 5.2 (bottom), where the absolute value of the focusing function is close to zero between about 0° and 180° . We stress that we get this wavefield without any prior knowledge on its appearance other than its approximate vanishing at ∂V_1 . While this radiation condition, i.e. that the focusing function vanishes at ∂V_1 , is only met approximately, the wave Equations 5.5 and 5.6 are obeyed perfectly.

We can repeat the process of estimating \mathbf{s}_f for all frequencies and ultimately use Equation 5.21 to get $s_f(\mathbf{x}, t)$. This time-domain source function is displayed in Figure 5.3. As before, this source is related to a focusing function: the source is anti-symmetric in time everywhere except at \mathbf{x}_f . This is also visualised by the black dotted lines in Figure 5.3. For the cyan scenario, i.e. at \mathbf{x}_f , the superposition of $s_f(\mathbf{x}_f, t) + s_f(\mathbf{x}_f, -t)$ delivers the symmetric wavelet $-\mathfrak{w}(t)$. For all other points \mathbf{x} this superposition leads to zero. This is again consistent with the band-limited time-domain interpretation of Equation 5.12.

Once we have the time-domain source term $s_f(\mathbf{x}, t)$, we can use it in Equation 5.22 to model the Marchenko-type focusing function. For comparison we show the Green's function in Figure 5.4 (top-left) along with the Marchenko-type focusing function (bottom-left). While the Green's function resembles a cone where the wave is propagating isotropically in space and forwards in time, our focusing function vanishes for about $z > 1000$ m. Thus, its propagation is anisotropic in space with a distinctly preferred directionality towards small z values. This is consistent with our frequency domain observation in Figure 5.2: this focusing function should, in accordance with Equation 5.13, vanish on ∂V_1 .

As a next step, we can inject our modelled focusing function into the volume V from its boundary ∂V to obtain the homogeneous Green's function of the second kind via time reversal modelling, see Equation 5.7. For comparison we also model the homogeneous Green's function as the field solution to

$$\left(\nabla^2 + \frac{\omega^2}{c^2}\right) \left(g(\mathbf{x}, \omega; \mathbf{x}_f) + g^*(\mathbf{x}, \omega; \mathbf{x}_f)\right) = \int_{\mathbf{x}_r \in \partial V} \frac{2i\omega}{c} \delta(\mathbf{x} - \mathbf{x}_r) g^*(\mathbf{x}_r, \omega; \mathbf{x}_f) dS \quad . \quad (5.23)$$

The homogeneous Green's function is displayed in Figure 5.4 (top-right) along with the homogeneous Green's function of the second kind (bottom-right). The homogeneous Green's function has the shape of an hour glass. The in-coming wavefield (the time-reversed Green's function) contracts at negative times until it focuses at zero time. As there is no source to absorb the energy, the wavefield keeps on propagating and expands at positive times. This out-going wavefield is the Green's function. The homogeneous Green's function of the second kind looks fairly similar but it appears to lack one half of the hour glass – different halves at negative and positive times. Remember that the homogeneous Green's function of the second kind can be described by three field contributions: the focusing function (in-coming), the negative, time-reversed focusing function (out-going) and the Green's function (out-going), see Equation 5.6. We

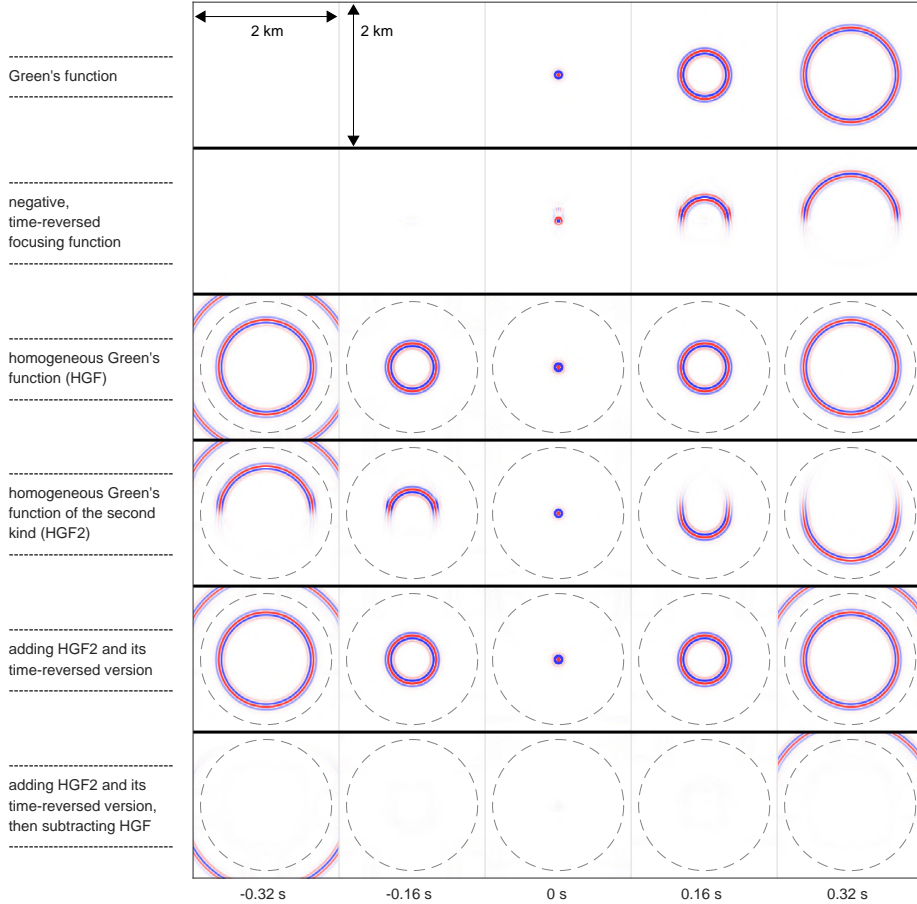


Figure 5.5: Snapshots for different wavefields and times. Left to right is increasing time, see bottom labels. Top to bottom is for different wavefields, see labels on the left. The four bottom rows involve time reversal modelling with a field injection from the closed boundary ∂V . This injection boundary is indicated by the grey, dotted lines. Note that we show the full wavefields, including the fields outside of the injection boundaries that were muted in Figure 5.4. This leads to, e.g., the wavefront for the homogeneous Green's function at -0.32 s outside of the injection boundary. This is an out-going wave and an artefact of the time reversal modelling. The fields within the injection boundaries, however, are accurate. All plots are at the same scaling. Red indicates positive, blue negative amplitudes.

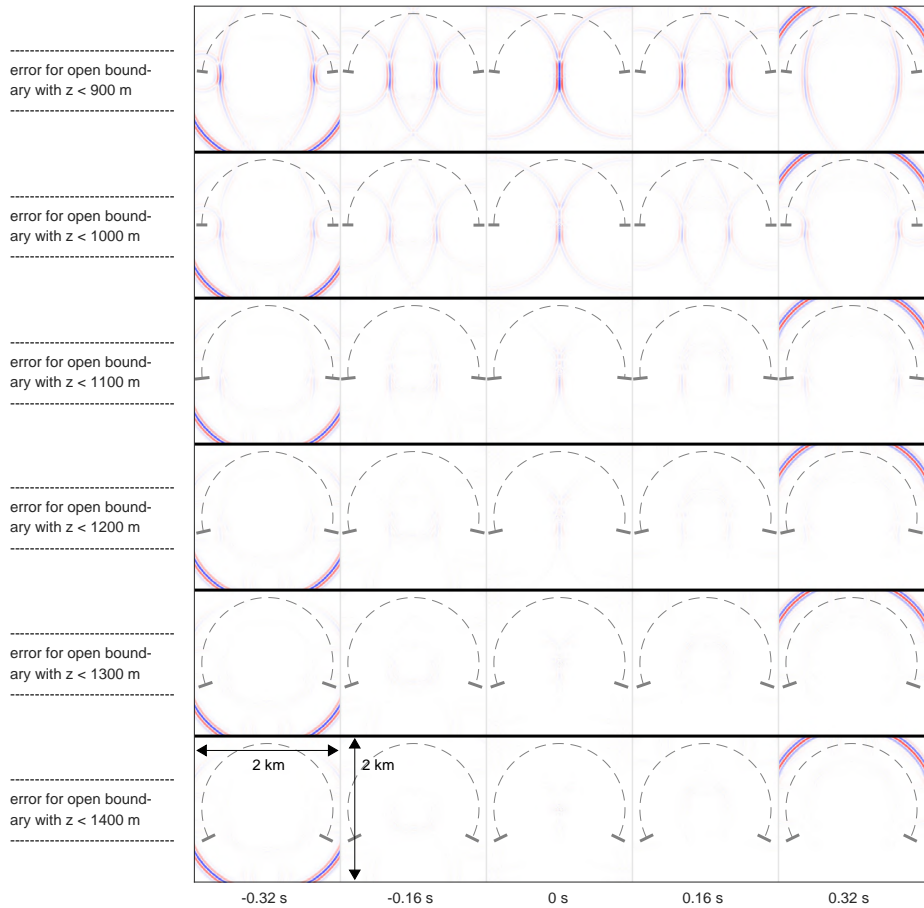


Figure 5.6: Snapshots for different wavefields and times. Left to right is increasing time, see bottom labels. All wavefields (top to bottom) show the result of adding the respective homogeneous Green's function of the second kind and its time-reversed version and then subtracting the homogeneous Green's function, similar to the bottom row in Figure 5.5. The different underlying homogeneous Green's functions of the second kind are based on different open injection boundaries. The top row for instance only uses the portion of the previous, closed boundary for which $z < 900$ m. From top to bottom the portion of the boundary that is ignored gets less, see labels on the left. The injection boundaries are indicated by the grey, dotted lines. All plots are at the same scaling as Figure 5.5.

can relate this to the wavefield in Figure 5.4 (bottom-right) in the following way: we inject the time-reversed, negative version of the wavefield in Figure 5.4 (bottom-left). This is the in-coming focusing function. As we consider a Marchenko-type focusing function, it only propagates in a particular region of the volume (the upper half-space with $z < 1000$ m). The field contracts and focuses at zero time. At positive times the wavefield keeps on propagating in the other, lower half-space with $z > 1000$ m. The interpretation of this out-going field might be counter-intuitive at first. It is actually a superposition of the (isotropic) Green's function, see Figure 5.4 (top-left), and the negative, time-reversed focusing function, see Figure 5.4 (bottom-left). As the negative, time-reversed focusing function is approximately zero in the lower half-space with $z > 1000$ m, the described superposition in Figure 5.4 (bottom-right) resembles the Green's function in that area. In the other half-space, however, we find that the negative, time-reversed focusing function and the Green's function cancel each other. This indicates that this negative, time-reversed Marchenko-type focusing function resembles a negative Green's function in this half-space.

A similar experiment that follows an easier intuition is this: decompose a Green's function into an up-going Green's function (the portion of the field that propagates towards small values of z) and a down-going Green's function (the portion that propagates towards high values of z). If we inject the time-reversed, up-going Green's function from the upper half of the volume the wavefield would propagate towards \mathbf{x}_f , contract, focus and then keep on propagating in an expanding manner, governing the (non time-reversed) down-going Green's function. This experiment delivers a very similar half-hour-glass structure, Figure 5.4 (bottom-right). We return to this thought experiment later.

The wavefields in Figure 5.4 are also shown as snapshots in Figure 5.5. The top two rows are for the Green's function and the negative, time-reversed focusing function. In addition to the previous observation that the focusing function vanishes in the lower half-space, its snapshot at zero time now reveals distinct features apart from the central focal spot. These features translate to field contributions that break the otherwise perfectly half-circular structure of the wavefronts at positive times. Note that these features belong to the solution and are not undesired artefacts. The homogeneous Green's function and the homogeneous Green's function of the second kind are displayed in the third and fourth row of Figure 5.5. We stress that the snapshot of the homogeneous Green's function of the second kind at zero time exhibits a clean focal spot, similar to that of the Green's function in the top row. Note that we inject the focusing function from the full, closed boundary here.

In order to further investigate the inverted focusing function we make use of the fact that adding the homogeneous Green's function of the second kind, Equation 5.6, and its time-reversed version delivers the conventional homogeneous Green's function. This is shown in the penultimate row of Figure 5.5. Subtracting the homogeneous Green's function from this estimated wavefield (obtained from the homogeneous Green's function of the second kind) should consequently deliver zero, see last row in Figure 5.5. In fact, the wavefield is nearly zero (white color) within the injection boundary. This is expected as the underlying partial differential equations are obeyed perfectly with our inversion approach. Any inaccuracies in this result (see faint, cross-like structure at 0 s) are due to

inaccuracies of the numerical modelling.

We stated in the beginning of this section that we want to study the accuracy of Equation 5.13. We do this now by modelling the homogeneous Green's function of the second kind with an open injection boundary, similar to Equation 5.8. In fact, we compare different open injection boundaries. As the resulting wavefields are all similar to the closed boundary homogeneous Green's function of the second kind in Figure 5.5 (fourth row), we show the error plots (similar to the last row in Figure 5.5) in Figure 5.6. Note that we used the upper part (with $z < 1000$ m) of the closed injection boundary in Figure 5.5 as ∂V_0 in the source inversion process and the lower part (with $z > 1000$ m) as ∂V_1 . When we use an open injection boundary that ignores some of ∂V_0 (top row in Figure 5.6), we get significant artefacts. Note that we do not use spatial tapering for the injected wavefield. These errors are primarily occurring in a depth of about 1000 m, where the open injection boundary ends. This is a consequence of ignoring a portion of the incoming wavefield in the time reversal modelling. Remember that the focusing function is non-zero everywhere in the upper half-space, compare Figure 5.2. When we use an open injection boundary with $z < 1000$ m, i.e. ∂V_0 from the inverse source design process, there are still artefacts, but they are much weaker – a consequence of the fact that the focusing function is nearly zero at the remaining boundary. These remaining artefacts illustrate that Equation 5.13 is not obeyed perfectly. This might be related to, e.g., the limited bandwidth of the wavelet or the generally smooth character of wave equation solutions, only allowing for a smooth transition from zero to non-zero wavefields. Enlarging the open injection boundary to also include some of ∂V_1 leads to vanishingly small artefacts, compare four lower-most rows in Figure 5.6.

We mentioned previously that injecting a time-reversed, up-going Green's function from the upper boundary delivers a similar half-hour-glass structure as that in Figure 5.4. We stress that the up-/down-decomposition in this thought experiment would not lead to a perfect, full-spectrum focus at zero time though. This is due to missing field contributions and propagation artefacts from the edges of the injected wavefield (comparable to the top rows in Figure 5.6). Hence, this experiment is inherently approximative. Our focusing function on the other hand, delivers a perfect focal spot when injected into a source-free medium from its closed (or a sufficiently large open) boundary, see Figures 5.5 and 5.6.

For the case of a homogeneous medium we illustrated that Marchenko-type focusing functions exist which are nearly zero on a particular portion of an enclosing boundary. This allows for approximating time reversal modelling by only injecting the focusing function from an open boundary. Similarly, this approximate vanishing of the Marchenko-type focusing function justifies the Marchenko integral (Chapter 3). The actual quality of this approximation depends on the medium properties and the geometry of the open boundary. In fact, some heterogeneous media might allow for significantly smaller open injection boundaries to be accurate approximations. Hence, further research is required to investigate arbitrarily heterogeneous media. In the next section we want to make a first step in that direction.

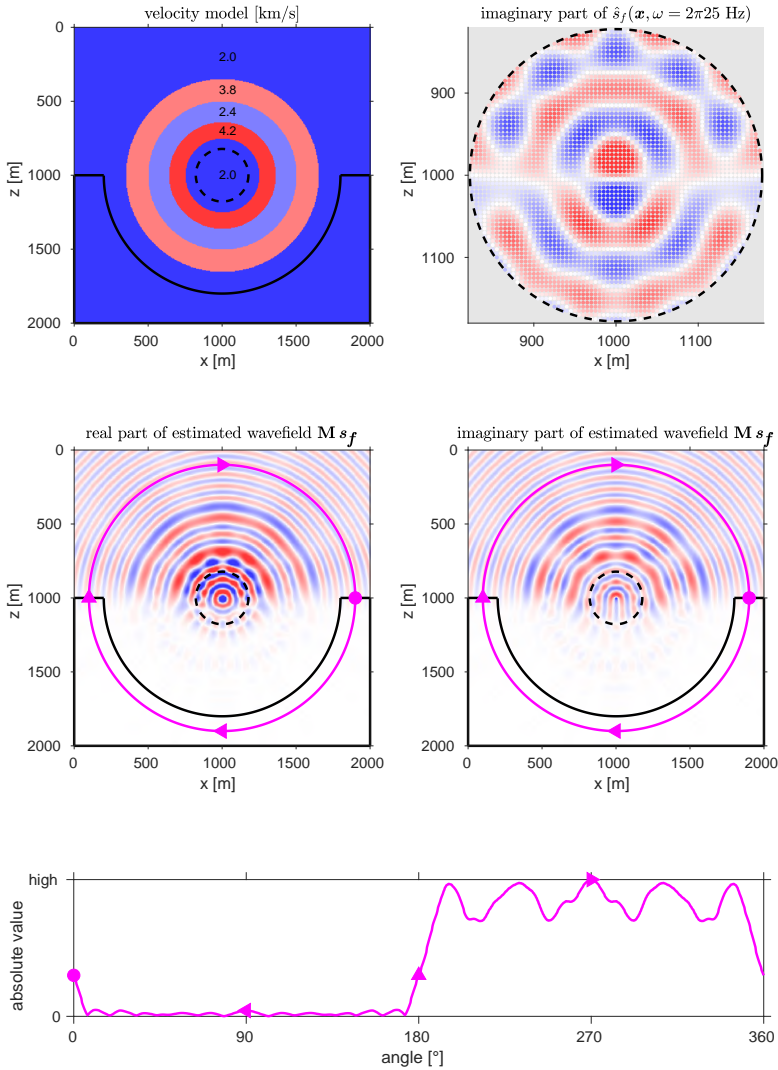


Figure 5.7: Top-left: heterogeneous velocity model. Top-right: imaginary part of inverted source term $s_f(\mathbf{x}, \omega)$ at 25 Hz. Centre: estimated wavefield, obtained by applying the modelling operator \mathbf{M} to the inverted focusing function source vector \mathbf{s}_f . Real part (centre-left) and imaginary part (centre-right) at the same scaling. The dashed black circles denote the active region, the solid black lines show the outline of the matching region. The magenta circles mark a distance of 900 m to \mathbf{x}_f , where the circular marker denotes an angle of 0° and the different triangles mark 90° , 180° and 270° . The orientation of these triangles is the same in the wavefield plots (centre) and the bottom plot such that, e.g., the left-facing triangle is at 90° . Blue colors indicate negative and red colors positive values. Bottom: absolute value (power) of estimated wavefield in a distance of 900 m as a function of angle, see magenta circles in wavefield plots.

5.7. A NOTE ON EXTENDING THE METHOD TO HETEROGENEOUS MEDIA

In general the theory presented in this manuscript is directly extendable to heterogeneous media. However, there are two main things that need to be considered. Firstly: when we have an acoustic wave equation for variable velocity $c(\mathbf{x})$ and density $\rho(\mathbf{x})$ in the form of

$$\left(\rho(\mathbf{x}) \nabla \cdot \left(\frac{1}{\rho(\mathbf{x})} \nabla \right) - \frac{1}{c^2(\mathbf{x})} \frac{\partial^2}{\partial t^2} \right) u(\mathbf{x}, t) = -\rho(\mathbf{x}) \frac{\partial s(\mathbf{x}, t)}{\partial t} \quad (5.24)$$

we can not use an analytical expression like that in Equation 5.4 to estimate the Green's functions in Equation 5.9 but we have to use a numerical solver. Note that all partial differential equations, see Equations 5.5 and 5.6, can easily be adjusted to heterogeneous media by using the respective wave operator (Chapter 3). Secondly: the active region in the inverse source design process might have to be adjusted depending on the scattering properties of the medium. In heterogeneous media there are scattered waves from impedance changes across the model. If we aim to find a Marchenko-type focusing function, Equation 5.13, the active region has to not only emit a directional wavefield but also to cancel all scattered waves that travel towards the boundary ∂V_1 . This implies a potentially large active region which makes the inverse source design more computationally expensive.

The simplest, heterogeneous example is a medium that is radially symmetric around \mathbf{x}_f like the velocity model in Figure 5.7 (top-left). In such a model all scattered waves pass through the source location \mathbf{x}_f . Hence, it is sufficient to have a small sphere around \mathbf{x}_f as the active region, just as in the previous, homogeneous medium example. This active region can then emit a directional wave and cancel all downwards propagating scattered waves such that the wavefield vanishes at ∂V_1 . The imaginary part of the inverted source is displayed in Figure 5.7 (top-right). This is clearly different to the source in Figure 5.2 (top-right), implying that this heterogeneous model does indeed require a different focusing function source to account for the scattered waves. Note that the real part of the source is (per definition) identical to that in Figure 5.2 (top-left). Regarding the estimated frequency domain wavefield, Figure 5.7 (centre), one can see the different velocity layers of the model in terms of changing wavelengths across space. The radiation condition, meaning that the focusing function vanishes at the lower boundary ∂V_1 according to Equation 5.13, appears to be fulfilled similarly well as in the previous, homogeneous medium example, see also bottom plot in Figure 5.7.

We show this as a first example and suggest further studies of this approach for modelling Marchenko-type focusing functions in heterogeneous media.

5.8. DISCUSSION

The research presented in this paper is fundamentally related to the Marchenko integral, but it also has implications for general acoustics, where directional source multipoles

and open boundary wavefield focusing are relevant topics.

While Equation 5.13 holds true and can directly be used for modelling Marchenko-type focusing functions in 1D (Chapter 4), we presented a first study of its accuracy in 2D in this paper. In contrast to other methods for modelling Marchenko-type focusing functions, see Elison et al. (2021), Wapenaar and de Ridder (2022), Hajjaj et al. (2022) and Chapters 3 and 4, our inverse source design approach allows for retrieving perfectly accurate focusing functions that obey Equations 5.5 and 5.6. Consequently, these focusing functions lead to perfect, full-spectrum wavefield focusing within the homogeneous Green's function of the second kind. The radiation property of Marchenko-type focusing functions on the other hand, see Equation 5.13, is only satisfied in a least-squares sense. As with other optimisation problems, one could envision the use of other metrics (e.g. L1 or mixed L2 and L1), as well any number of additional constraints – both of which could create distinctively different focusing-related sources in practice.

Based on our homogeneous medium analysis, one might think that Marchenko-type focusing functions are inherently approximate in 2D and 3D. However, we also found that this approximation appears to be relatively accurate, see only small artefacts in Figure 5.6. Hence, we can inject focusing functions from open boundaries and still obtain a close-to-perfect wavefield focus.

When the Marchenko integral is used to estimate Green's functions from boundary measurements, see Wapenaar et al. (2014b) and Chapter 6, the radiation condition is obeyed perfectly while the related focusing functions and Green's functions are approximated. This is comparable to enforcing that Equation 5.13 holds true, while Equations 5.5 and 5.6 are only approximated – exactly opposite to our modelling approach in this paper. This may become problematic when Equation 5.13 is a poor approximation. We propose further studies of inverse source design for heterogeneous media to gain a more general understanding of Marchenko-type focusing functions in 2D and 3D. We already presented a first study towards heterogeneous media with promising results. While this appears to be a computationally more expensive problem, it should follow the same theoretical concept. Further such studies will help to understand limitations of the Marchenko integral in higher dimensions.

More generally, inverse source design allows for estimating wavefields when given some constraints on their appearance. In the case of Marchenko-type focusing functions we have some limitations about the source term and know that the wavefields should vanish in the matching region. This is enough to compute a wave-equation-consistent solution that approximately obeys our assumptions. This might be useful for other fields of research as well, where wavefields with particular properties are desirable.

We found that in a homogeneous medium the focusing function is similar to a decomposed Green's function. Hence, we can build source multipoles like that in Figure 5.3 that appear to emit a Green's function in one direction and are zero in the other. This could be useful for acoustical engineering but also for, e.g., seismic imaging problems where ghost reflections (undesired reflections from the surface of the sea with a source in the water) bias the measurement of scattering data from below.

Furthermore, these inverted, Marchenko-type focusing functions might be useful when a wave is injected into a medium in order to focus but the medium is only accessible from an open portion of its boundary. This includes medical applications (Thomas and

Fink, 1996; Meles et al., 2019a) as well as geophysical, e.g., source localisation methods (Gajewski and Tessmer, 2005; Li et al., 2020).

5.9. CONCLUSION

We present an inverse source design approach for modelling Marchenko-type focusing functions that, when injected into a source-free volume from its open boundary, lead to a nearly perfect, full-spectrum wavefield focus. Our method allows for a reliable analysis of Marchenko-type focusing and might help to understand limitations of the Marchenko integral in 2D and 3D. Our numerical studies suggest that Marchenko-type focusing functions are inherently approximate in 2D but fairly accurate at least in homogeneous and radially symmetric media. Furthermore, the underlying concepts of directional source multipoles and open boundary wavefield focusing might have interesting applications in fields such as acoustical engineering.

ACKNOWLEDGEMENTS

Leon Diekmann was funded by the Utrecht Consortium for Subsurface Imaging (UCSI).

FOCUSING AND GREEN'S FUNCTION RETRIEVAL IN THREE-DIMENSIONAL INVERSE SCATTERING REVISITED: A SINGLE-SIDED MARCHENKO INTEGRAL FOR THE FULL WAVEFIELD

The Marchenko integral, key to inverse scattering problems across many disciplines, is a long-standing equation that relates single-sided reflection data and Green's functions for virtual source locations inside of an inaccessible, one-dimensional volume. The concept was later expanded to two and three dimensions, yielding important advances in imaging complex media, particularly in the context of geophysics. However, this expansion is based on a set of coupled Marchenko equations which requires up-/down-decomposition of the wavefields at both the level of the measurement surface and the level of the virtual source of the desired Green's function. The underlying theory implies that the recently developed Marchenko relations, while enabling novel applications, carry intrinsic limitations. For example, this scheme cannot incorporate evanescent or refracted waves, and in turn practical implementations must discard data to meet such requirements. We present a derivation that circumvents these limitations, thereby yielding a Marchenko integral akin to those in recent advances, but that is more general than previously assumed. We set up a wave-equation-based framework to describe the physical concept of focusing functions by introducing homogeneous Green's functions of the second kind. Based on this, we derive integral representations for both closed and open boundary volumes. Owing to our new perspective on the integral formalism, we present an inverse scattering approach for retrieving Green's functions from single-sided

The content of this chapter was published as Diekmann and Vasconcelos (2021a). Note that the Green's function and the focusing function are defined with different signs in this chapter compared to the published paper. They were changed to accomplish consistency of the equations in this thesis. However, we stress that in this chapter (and the published paper) the out-going focusing function is referred to as a time-reversed field – in contrast to all other chapters in this thesis. This is the conventional definition which, given that the following chapter is related to our first publication on the topic, we initially adapted.

reflection data – with the same practical applicability of recent methods, but without any limitations due to one-way decomposition. Finally, we illustrate the capability of the Marchenko method to obtain the full wavefield, including evanescent and refracted waves, within an unknown scattering medium by means of a numerical example.

6.1. INTRODUCTION

Imaging the interior of an object that is only accessible at its boundary is a key problem in many fields, such as seismology (Etgen et al., 2009; Virieux and Operto, 2009), helioseismology (Rickett and Claerbout, 1999), quantum mechanics (Snieder and Tarantola, 1989), medical imaging (Szabo, 2004; Hoskins et al., 2019; Bernard et al., 2017; Boehm et al., 2018; Guasch et al., 2020; Lambert et al., 2020) or non-destructive testing (Müller et al., 2012; Kalogeropoulos et al., 2013). Imaging methods rely on acoustic, seismic (Malcolm et al., 2004) or electromagnetic (van den Berg and Abubakar, 2001) waves to probe the interior of objects with sources and receivers located on their boundaries. The objective of inverse scattering theory (Colton and Kress, 1998) is the retrieval of the physical characteristics of the medium from measuring its remotely-observed scattering response.

The Marchenko integral is an elementary equation in one-dimensional inverse scattering theory (Burrige, 1980; Rose, 2001; Chadan and Sabatier, 2012). While the medium-parameters, e.g. the scattering potential, can be directly inferred from the Marchenko equation in one dimension (Ware and Aki, 1969), Broggin et al. (Broggin et al., 2012; Broggin and Snieder, 2012) studied the Marchenko integral's capability to produce Green's functions for virtual sources inside of an inaccessible medium. In contrast to popular interferometric methods for Green's function retrieval (e.g. Wapenaar and Fokkema, 2006; Curtis and Halliday, 2010; Wapenaar et al., 2010a), the Marchenko method allows for retrieving Green's functions from single-sided reflection measurements.

Recognising the potential of Marchenko-based Green's function retrieval and its role in inverse scattering, Wapenaar et al. (Wapenaar et al., 2013, 2014b, 2016) expanded the Marchenko theory to two and three dimensions. Their derivation builds on up-/down-decomposition of the involved wavefields, both at the acquisition surface and at the depth-level of the virtual source of the Green's function. They use convolution- and correlation-type reciprocity theorems for these decomposed wavefields and describe two different wave states in the true and the truncated medium, i.e. a version of the true medium which is reflection-free everywhere underneath the virtual source location. Ultimately, this approach delivers a set of coupled Marchenko equations. Their derivation implies several limitations regarding the retrievable Green's functions. Firstly, using up-/down-decomposition along with correlation-type reciprocity in depth leads to a neglect of evanescent waves inside the medium under investigation. Secondly, using a truncated medium leads to a neglect of refracted and diving waves, i.e. waves that would arrive before the direct arrival in the truncated medium. These issues were partially addressed lately (Wapenaar, 2020a). However, this recent study is based on the conventional coupled Marchenko equations and currently limited to laterally homogeneous media.

One of the main achievements of the three-dimensional Marchenko method (e.g. Wape-

naar et al., 2013, 2014b; van der Neut et al., 2015b), in addition to the theoretical advancement, is the fact that those representations can be reliably translated into practical approaches to retrieve the Green's functions of real unknown media from single-sided reflection data (Ravasi et al., 2016). While there are certain Marchenko-based primary estimation methods (van der Neut and Wapenaar, 2016; Zhang and Slob, 2019) that require no a priori knowledge of the medium, solving the three-dimensional Marchenko scheme for in-volume Green's functions requires knowledge of a background medium-parameter model, i.e. a wavespeed model that allows for approximating the direct arrivals of the intended Green's functions – but that does not contain information on the unknown scatterers within the medium. Furthermore, the solution is tied to certain causality arguments that generally hold for one dimension, but become less general in higher dimensions (Wapenaar et al., 2014b). Hence, complicated models with spatially varying, strong-contrast medium perturbations can pose an issue for the Marchenko method (e.g. Vasconcelos and Sripanich, 2019; Vargas and Vasconcelos, 2020). Nonetheless, the Marchenko integral proved to be a valuable extension of existing Green's function retrieval methods (Wapenaar and Thorbecke, 2017; Wapenaar et al., 2017) and is becoming widely used for geophysical applications (e.g. Ravasi et al., 2016; Brackenhoff et al., 2019b; Staring and Wapenaar, 2020; Staring et al., 2020).

In this paper, we present a more general, alternative strategy to deriving Marchenko-type integral relations for Green's function retrieval from remote, single-sided scattering data. We start by introducing homogeneous Green's functions of the second kind, which are an extension of the concept of conventional homogeneous Green's functions. Using reciprocity, we obtain integral representations of these fields for both closed and open boundary systems. The open boundary representation is similar to the previously introduced Marchenko equations (Wapenaar et al., 2014b), but it is obtained without the need for: *i*) defining an auxiliary, truncated medium wave state or *ii*) imposing wavefield decomposition within the medium at the location of the desired Green's function. Hence, the Marchenko integral we propose here can be used to obtain the full Green's function – with wave components propagating in all directions, i.e. including the medium's evanescent and refracted field response. Finally, relying on constraints used by previous approaches, we present a practical scheme to solve our single-sided Marchenko equation for an unknown scattering medium's Green's function. We illustrate our findings with a numerical example.

6.2. INTEGRAL REPRESENTATIONS FOR FOCUSING AND GREEN'S FUNCTIONS

In the following section we present a derivation for integrals that relate so-called focusing functions and Green's functions. While previous derivations (Wapenaar et al., 2014b) do not include evanescent and refracted waves, our new approach is applicable to the full wavefield. We start by introducing a partial differential equation (PDE) for focusing functions. Then we use reciprocity to obtain integral representations.

6.2.1. THE HOMOGENEOUS GREEN'S FUNCTION OF THE SECOND KIND

The acoustic wave equation in the frequency domain is given by

$$\mathcal{L}(\mathbf{x}, \omega)u(\mathbf{x}, \omega) = \rho(\mathbf{x})i\omega s(\mathbf{x}, \omega) \quad (6.1)$$

with the wave operator

$$\mathcal{L}(\mathbf{x}, \omega) = \rho(\mathbf{x})\nabla \cdot \frac{1}{\rho(\mathbf{x})}\nabla + \frac{\omega^2}{c^2(\mathbf{x})} \quad , \quad (6.2)$$

where $u(\mathbf{x}, \omega)$ is the acoustic pressure field at location $\mathbf{x} = (x_1, x_2, x_3)$ and frequency ω . The source function is of volume injection rate density and denoted by $s(\mathbf{x}, \omega)$, i.e. there are no force sources. The medium is defined by density $\rho(\mathbf{x})$ and propagation velocity $c(\mathbf{x})$. The variable i denotes the imaginary unit. Although we consider acoustics in the frame of this paper, the following derivations should be applicable for other PDEs as well (e.g. Snieder et al., 2007; Wapenaar and Douma, 2012).

A Green's function $g(\mathbf{x}, \omega; \mathbf{x}_f)$ is a wavefield that obeys

$$\mathcal{L}(\mathbf{x}, \omega)g(\mathbf{x}, \omega; \mathbf{x}_f) = \rho(\mathbf{x})i\omega\delta(\mathbf{x} - \mathbf{x}_f) \quad . \quad (6.3)$$

It is the medium's response to a filtered impulse source at \mathbf{x}_f . Adding the complex conjugate of Equation 6.3 to Equation 6.3 delivers the so-called homogeneous Green's function, i.e. a source-free superposition of Green's functions, according to

$$\mathcal{L}(\mathbf{x}, \omega)\left(g(\mathbf{x}, \omega; \mathbf{x}_f) + g^*(\mathbf{x}, \omega; \mathbf{x}_f)\right) = 0 \quad . \quad (6.4)$$

In the context of this paper, we refer to this equation as the homogeneous Green's function of the first kind. The star denotes complex conjugation in the frequency domain which is similar to time-reversal in the time domain. The Green's function $g(\mathbf{x}, \omega; \mathbf{x}_f)$ is a causal wavefield, i.e. the wave propagates after the source triggering at time $t = 0$. Furthermore, it is an out-going wavefield, i.e. with respect to a certain volume of interest that contains the source location \mathbf{x}_f . Thus, $g^*(\mathbf{x}, \omega; \mathbf{x}_f)$ in Equation 6.4 is an in-coming wavefield for times $t < 0$. This wavefield focuses at the source location and then, according to Equation 6.4, keeps on propagating as the forward Green's function, i.e. as an out-going field for times $t > 0$. At time $t = 0$, when focusing occurs, both the in-coming and out-going fields coalesce to equal impulsive sources of opposite polarity, thus satisfying Equation 6.4.

As a next step we rewrite the time-reversed Green's function, i.e. we replace it by

$$\begin{aligned} \mathcal{L}(\mathbf{x}, \omega)g^*(\mathbf{x}, \omega; \mathbf{x}_f) = \\ \mathcal{L}(\mathbf{x}, \omega)\left(f(\mathbf{x}, \omega; \mathbf{x}_f) - f^*(\mathbf{x}, \omega; \mathbf{x}_f)\right) \quad , \end{aligned} \quad (6.5)$$

where

$$\mathcal{L}(\mathbf{x}, \omega)f(\mathbf{x}, \omega; \mathbf{x}_f) = -\frac{\rho(\mathbf{x})i\omega\delta(\mathbf{x} - \mathbf{x}_f)}{2} + q(\mathbf{x}, \omega; \mathbf{x}_f) \quad . \quad (6.6)$$

These equations hold for real-valued $q(\mathbf{x}, \omega; \mathbf{x}_f)$, such that $q(\mathbf{x}, \omega; \mathbf{x}_f) - q^*(\mathbf{x}, \omega; \mathbf{x}_f) = 0$. Apart from this restriction, the source field $q(\mathbf{x}, \omega; \mathbf{x}_f)$ is arbitrary up to this point. Its argument \mathbf{x}_f does not actually represent a necessary dependence but is kept for the sake of consistency. This reformulation allows for replacing the Green's function by a superposition of so-called focusing fields $f(\mathbf{x}, \omega; \mathbf{x}_f)$. We note here that although we refer to $f(\mathbf{x}, \omega; \mathbf{x}_f)$ as focusing fields, these are more general than in previous definitions (e.g. Wapenaar et al., 2014b), since they are tied to the arbitrary source fields $q(\mathbf{x}, \omega; \mathbf{x}_f)$. The Green's and focusing functions are different wavefield realisations but obey the same source function. When modelling numerically, we conventionally propagate the source energy forwards in time from $t = 0$. This new representation is different in that the source produces a causal and an anti-causal field, suggesting the corresponding wave excitation may also be active at $t < 0$ relative to reference origin time that is associated with the Green's function. Take for instance $q(\mathbf{x}, \omega; \mathbf{x}_f) = 0$. We can then write

$$f(\mathbf{x}, \omega; \mathbf{x}_f) - f^*(\mathbf{x}, \omega; \mathbf{x}_f) = \frac{1}{2} g^*(\mathbf{x}, \omega; \mathbf{x}_f) - \frac{1}{2} g(\mathbf{x}, \omega; \mathbf{x}_f) \quad . \quad (6.7)$$

One way of visualising the physics behind this choice is to imagine an in-coming field, in this case $g^*(\mathbf{x}, \omega; \mathbf{x}_f)$ with half amplitude, that interacts with the source at zero time. The source energy is larger than the field energy, i.e. the in-coming field gets absorbed and additionally a new field, in this case $-g(\mathbf{x}, \omega; \mathbf{x}_f)$ with half amplitude, is created. Note that the focusing function $f(\mathbf{x}, \omega; \mathbf{x}_f)$ is, in contrast to the Green's function, not unique – because $q(\mathbf{x}, \omega; \mathbf{x}_f)$ can be chosen arbitrarily, so long as it satisfies Equation 6.6.

We may now write the homogeneous Green's function of the second kind according to

$$\mathcal{L}(\mathbf{x}, \omega) \left(g(\mathbf{x}, \omega; \mathbf{x}_f) + f(\mathbf{x}, \omega; \mathbf{x}_f) - f^*(\mathbf{x}, \omega; \mathbf{x}_f) \right) = 0 \quad . \quad (6.8)$$

Mathematically, this is equivalent to Equation 6.4, but it gives an additional physical insight. Let $f(\mathbf{x}, \omega; \mathbf{x}_f)$ be an in-coming field. This field focuses at \mathbf{x}_f and, afterwards, keeps on propagating as the forward Green's function. On the way to the focal point, however, it also produces a scattered field which is not related to the Green's function, namely the out-going field $f^*(\mathbf{x}, \omega; \mathbf{x}_f)$. The choice which of the two, $f(\mathbf{x}, \omega; \mathbf{x}_f)$ or $-f^*(\mathbf{x}, \omega; \mathbf{x}_f)$, is the in-coming field is, because of the fields' time symmetry, indeed arbitrary. We call the field that satisfies Equation 6.8 the homogeneous Green's function of the second kind for it is a source-free field that yields the causal Green's function. The involved fields, however, are not necessarily the same as those in Equation 6.4 – this distinction is essential to our approach.

While we did not specify the source $q(\mathbf{x}, \omega; \mathbf{x}_f)$ in more detail, this subsection introduced the general idea of the homogeneous Green's function of the second kind. In the next subsection we discuss the interferometric representation of the partial differential Equation 6.8.

6.2.2. INTEGRAL REPRESENTATIONS

In this subsection we derive an integral representation for the wavefields in Equation 6.8. The derivation is similar to derivations for multi-dimensional convolution and deconvolution (Wapenaar et al., 2008; Wapenaar and van der Neut, 2010; Wapenaar et al.,

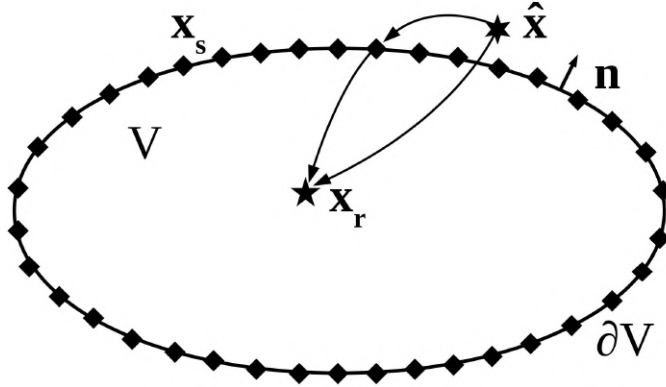


Figure 6.1: Sketch of the wave state setup for a closed boundary. The rays indicate involved Green's functions, i.e. from $\hat{\mathbf{x}}$ to \mathbf{x}_s , from \mathbf{x}_s to \mathbf{x}_r and from $\hat{\mathbf{x}}$ to \mathbf{x}_r .

2011). We start our derivation from the general form of Rayleigh's reciprocity theorem for acoustic waves (Fokkema and van den Berg, 1993; Vasconcelos et al., 2009), i.e.

$$\begin{aligned}
 & \int_{\mathbf{x}_s \in \partial V} (u^A \mathbf{v}^B - u^B \mathbf{v}^A) \cdot d\mathbf{S} = \\
 & \int_{\mathbf{x} \in V} \mathbf{f}^A \cdot \mathbf{v}^B + s^B u^A - \mathbf{f}^B \cdot \mathbf{v}^A - s^A u^B dV \\
 & + \int_{\mathbf{x} \in V} i\omega(\kappa^B - \kappa^A)u^A u^B - i\omega(\rho^B - \rho^A)\mathbf{v}^A \cdot \mathbf{v}^B dV, \quad (6.9)
 \end{aligned}$$

where the superscripts A and B mark two different wave states. In addition to the previously introduced pressure field $u = u(\mathbf{x}, \omega)$ we also require the particle velocity field $\mathbf{v} = (v_1, v_2, v_3) = \mathbf{v}(\mathbf{x}, \omega)$. The quantities $\mathbf{f} = (f_1, f_2, f_3) = \mathbf{f}(\mathbf{x}, \omega)$ and $s = s(\mathbf{x}, \omega)$ denote sources of volume force density and volume injection rate density, respectively. The compressibility is given by $\kappa = \kappa(\mathbf{x}) = 1/(\rho(\mathbf{x})c^2(\mathbf{x}))$ and density by $\rho = \rho(\mathbf{x})$. We are investigating a volume V , bounded by the smooth surface ∂V .

We consider two states with identical compressibility and density in a lossless volume V , thus the last integral in Equation 6.9 vanishes. Furthermore, we choose not to have any force sources within the volume, i.e. $\mathbf{f}^A = \mathbf{f}^B = \mathbf{0}$. This yields $\mathbf{v} = 1/(\rho i\omega)\nabla u$ (e.g. Fokkema and van den Berg, 1993). Inside the volume we use

$$s^A = \delta(\mathbf{x} - \mathbf{x}_r) \quad (6.10)$$

$$u^A = g(\mathbf{x}, \omega; \mathbf{x}_r) \quad (6.11)$$

$$s^B = 0 \quad (6.12)$$

$$u^B = p(\mathbf{x}, \omega; \hat{\mathbf{x}}) \quad (6.13)$$

Note that \mathbf{x}_r lies in V , while the sources for u^B are outside of the volume. The variable $\hat{\mathbf{x}}$ shows the dependency of u^B on the source distribution and appearance of s^B outside V .

This wave state configuration is sketched in Figure 6.1. Inserting these definitions into Equation 6.9 delivers

$$p(\mathbf{x}_r; \hat{\mathbf{x}}) = - \int_{\mathbf{x}_s \in \partial V} \frac{1}{\rho(\mathbf{x}_s) i \omega} \left(g(\mathbf{x}_s; \mathbf{x}_r) \nabla p(\mathbf{x}_s; \hat{\mathbf{x}}) - p(\mathbf{x}_s; \hat{\mathbf{x}}) \nabla g(\mathbf{x}_s; \mathbf{x}_r) \right) \cdot d\mathbf{S} \quad , \quad (6.14)$$

where we show dependencies on space but omit those on frequency for brevity. Let the medium outside V be reflection-free. Then the Green's function is purely out-going, while $p(\mathbf{x}; \hat{\mathbf{x}})$ is both in-coming and out-going with respect to V . Hence, we can write

$$p(\mathbf{x}; \hat{\mathbf{x}}) = p^{in}(\mathbf{x}; \hat{\mathbf{x}}) + p^{out}(\mathbf{x}; \hat{\mathbf{x}}) \quad , \quad (6.15)$$

where the superscripts mark in-coming and out-going fields, respectively. Here we are neglecting waves that travel along ∂V . Using a far-field approximation (e.g. Wapenaar and Fokkema, 2006; Schuster, 2009) or pseudo-differential operator theory (Fishman, 1993), the latter circumventing the need for an approximation, one finds that the terms $g \nabla p^{out}$ and $p^{out} \nabla g$ are identical, thus cancelling each other. On the other hand, the terms $g \nabla p^{in}$ and $p^{in} \nabla g$ deliver the same outcome but with opposite sign, as p^{in} is an in-coming and g an out-going field. Therefore, Equation 6.14 becomes

$$p(\mathbf{x}_r; \hat{\mathbf{x}}) = \int_{\mathbf{x}_s \in \partial V} \frac{2}{\rho(\mathbf{x}_s) i \omega} \nabla g(\mathbf{x}_s; \mathbf{x}_r) p^{in}(\mathbf{x}_s; \hat{\mathbf{x}}) \cdot d\mathbf{S} \quad . \quad (6.16)$$

If $p^{in}(\mathbf{x}; \hat{\mathbf{x}})$ happens to be a time-reversed field, i.e. $p^{in*}(\mathbf{x}; \hat{\mathbf{x}})$, this equation still holds when neglecting evanescent waves on the boundary ∂V (Wapenaar, 2020b). As a next step, we can insert the fields from the wave Equation 6.8 into Equation 6.16. This is possible because the respective overall field is source-free, i.e. just like our previously defined field $p(\mathbf{x}; \hat{\mathbf{x}})$ it has no sources in V . Furthermore, we replace the variable $\hat{\mathbf{x}}$ by \mathbf{x}_f in order to emphasise the dependence on the focusing location \mathbf{x}_f . The effective sources, however, are at $\hat{\mathbf{x}}$ and inject the in-coming field. This in-coming field is then given by $f(\mathbf{x}; \mathbf{x}_f)$, thus we get

$$g(\mathbf{x}_r; \mathbf{x}_f) + f(\mathbf{x}_r; \mathbf{x}_f) - f^*(\mathbf{x}_r; \mathbf{x}_f) = \int_{\mathbf{x}_s \in \partial V} \frac{2}{\rho(\mathbf{x}_s) i \omega} \nabla g(\mathbf{x}_s; \mathbf{x}_r) f(\mathbf{x}_s; \mathbf{x}_f) \cdot d\mathbf{S} \quad . \quad (6.17)$$

This is the integral form for a closed boundary. We note here that this is the most general representation relating focusing and Green's functions, potentially having applications of its own, which will be the subject of further research.

Ultimately, one is not limited to the case of a closed boundary. This is important because one of our main goals is to retrieve a medium's Green's function response from remote, single-sided wave data – without access to enclosing boundaries. To that end, let the volume be bounded by a horizontal interface ∂V_0 , e.g. at $x_3 = 0$, and a half-sphere ∂V_1 . Setting the radius of the half-sphere to infinity and considering only the subset of focusing functions for which $f(\mathbf{x} \in \partial V_1; \mathbf{x}_f) = 0$ the contribution of the respective surface

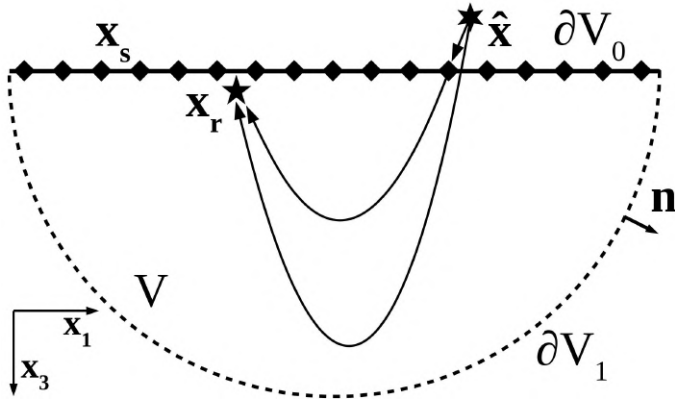


Figure 6.2: Illustration of the wave state setup for an open boundary. Rays indicate involved Green's functions.

integral vanishes. In-coming and out-going fields are now down- and up-going fields, respectively. Let \mathbf{x}_r and $\hat{\mathbf{x}}$ be immediately below and above ∂V_0 , respectively, i.e. both are very close to the surface but the receiver is still in V and the source outside V . As the medium is reflection-free outside V and the down-going field $p^{down}(\mathbf{x}; \hat{\mathbf{x}})$ is as such not propagating along the horizontal boundary ∂V_0 , it follows that the field $p(\mathbf{x}_r; \hat{\mathbf{x}})$ on the left-hand side of Equation 6.16 becomes purely up-going, i.e.

$$p^{up}(\mathbf{x}_r; \hat{\mathbf{x}}) = - \int_{\mathbf{x}_s \in \partial V_0} \frac{2}{\rho(\mathbf{x}_s) i \omega} \frac{\partial}{\partial x_3} g(\mathbf{x}_s; \mathbf{x}_r) p^{down}(\mathbf{x}_s; \hat{\mathbf{x}}) d^2 \mathbf{x}_s \quad , \quad (6.18)$$

where we assume a downwards pointing x_3 axis. This is also sketched in Figure 6.2. Inserting Equation 6.8 into Equation 6.18 again we now get

$$g(\mathbf{x}_r; \mathbf{x}_f) - f^*(\mathbf{x}_r; \mathbf{x}_f) = \int_{\mathbf{x}_s \in \partial V_0} R(\mathbf{x}_s; \mathbf{x}_r) f(\mathbf{x}_s; \mathbf{x}_f) d^2 \mathbf{x}_s \quad , \quad (6.19)$$

with

$$R(\mathbf{x}_s; \mathbf{x}_r) = - \frac{2}{\rho(\mathbf{x}_s) i \omega} \frac{\partial}{\partial x_3} g(\mathbf{x}_s; \mathbf{x}_r) \quad . \quad (6.20)$$

This relation has exactly the same form as the single-sided Green's function representation shown by, e.g., Wapenaar et al. (2014b). However, given our PDE-based derivation, the wavefields in our equation are significantly more general than previously understood. Because we rely on up-/down-decomposition only on the surface ∂V_0 , the integral fully accounts for evanescent waves inside the medium V . Furthermore, the concept of a truncated model space becomes unnecessary, so refracted and diving waves are included in the representation. Additional notes regarding a comparison with the

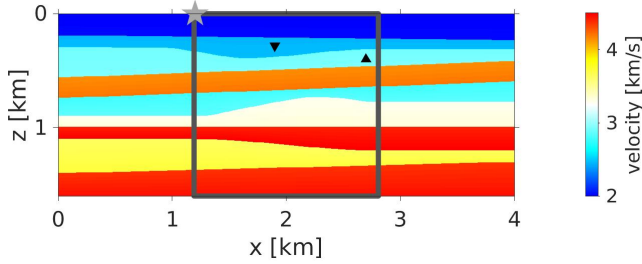


Figure 6.3: Velocity model. The star denotes the location of an exemplary source for which we investigate its wave propagation through the medium. The dark rectangle marks the volume of interest, which is considered for this propagation study. The two black triangles refer to virtual source locations that are examined in more detail in the Appendix.

traditional Marchenko scheme can be found in the Appendix.

We want to stress that integral Equation 6.17 is entirely general with respect to the focusing function $f(\mathbf{x}_s; \mathbf{x}_f)$. If we consider the special case of $q(\mathbf{x}; \mathbf{x}_f) = 0$ for instance, Equation 6.17 represents injecting the half-amplitude, time-reversed Green's function governing the half-amplitude homogeneous Green's function. In fact, it is well known that this time-reversal homogeneous Green's function retrieval works for closed boundaries, but not for open boundaries as depicted in Equation 6.19 (Wapenaar and Thorbecke, 2017). This representation generally produces non-physical artefacts. In the next section we present a way of solving a particular form of Equation 6.19, i.e. the Marchenko integral, for the Green's and focusing function based on an estimate of the first arrival of the Green's function. We also discuss the approach in the context of the aforementioned artefacts arising from the open boundary representation.

6.3. SOLVING THE MARCHENKO INTEGRAL FOR THE GREEN'S FUNCTION

In this section, we want to focus on solving the open boundary Equation 6.19 for the medium's unknown Green's function, based on having an estimate of its first arrival as a priori information. The physical arguments closely follow those of Wapenaar et al. (2014b), however, we are directly solving the more general un-coupled Marchenko integral, i.e. without up-/down-decomposition. For the sake of brevity, we neglect all arguments in the following equations and instead use the discrete matrix-operator form (van der Neut et al., 2015a) of Equation 6.19, i.e.

$$\mathbf{g} - \mathbf{f}^* = \mathbf{R}\mathbf{f} \quad , \quad (6.21)$$

where we assume any numerical integration details, such as scaling, to be included within the discrete kernel of the \mathbf{R} operator. In this paper we use the composite rectangle rule for numerical integration. We want to stress that the focusing function \mathbf{f} which we

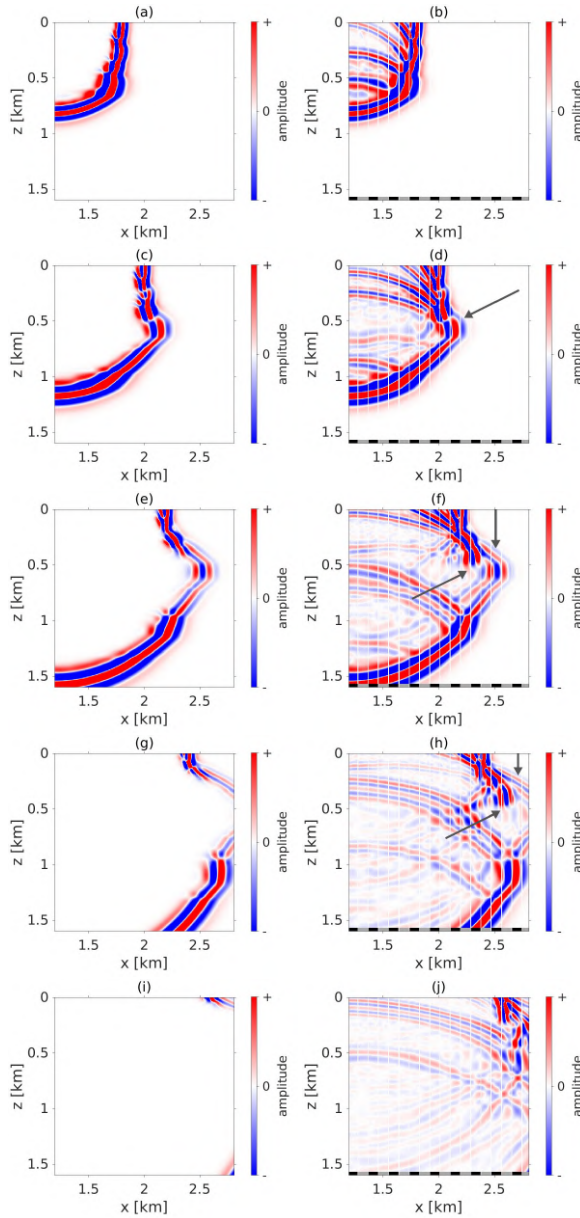


Figure 6.4: Snapshots showing the wave propagation for the source and area marked in Figure 6.3. The left column, (a) to (i), shows the first arrival. The right column, (b) to (j), shows the true wavefields and the Marchenko solutions in an interlaced manner. The bottom colours black and grey specify columns showing the true and the estimated wavefield, respectively, separated by white lines. The first row, (a) and (b), is for 0.3 s, (c) and (d) are for 0.4 s, (e) and (f) for 0.5 s, (g) and (h) for 0.6 s and (i) and (j) for 0.7 s. The colour bars are clipped at 1% of the overall absolute maximum amplitude.

investigate in the following is just one of many possible realisations of $f(\mathbf{x}; \mathbf{x}_f)$ in Equation 6.8, i.e. for a particular source $q(\mathbf{x}; \mathbf{x}_f)$. The realisation that we are interested in is defined by certain causality arguments, more specifically, that \mathbf{f} and \mathbf{g} are separable in time-space domain such that \mathbf{f} is preceding \mathbf{g} . These conditions are numerically imposed by introducing the windowing function Θ (Wapenaar et al., 2014b; van der Neut et al., 2015b). This function acts as a mask, i.e. Θ is zero for times $|t| > t_d(\mathbf{x}_r; \mathbf{x}_f) + \epsilon$ and one elsewhere. In this context $t_d(\mathbf{x}_r; \mathbf{x}_f)$ is the first arrival time for a source at \mathbf{x}_f and a receiver at \mathbf{x}_r and ϵ being greater zero accounts for the limited bandwidth of the wavelet (Zhang et al., 2018). We postulate that this is the realisation of $f(\mathbf{x}; \mathbf{x}_f)$ that is most compact in the time-space domain. This focusing function has to extend up to the time-reversed first arrival of the Green's function in order to be able to produce a focus at \mathbf{x}_f but can be assumed to be zero before it. In fact, this bound has to be symmetric in time, since we can not record anything before having injected energy, thus the up-going, time-reversed focusing function must be zero before the time-reversed first arrival of the Green's function, too. These separability assumptions hold in the reflection regime, however, they break in complex media with significant diffracted energy and laterally localised velocity perturbations that induce caustics on the first arrivals.

When presenting the open boundary integral representation above, we alluded to the fact that artefacts may arise in the retrieval of the Green's function. Such artefacts are well-known to arise from open-boundary systems when retrieving Green's functions by means of time-reversal (Wapenaar and Thorbecke, 2017). It is absolutely key that we solve for the injected field instead of simply injecting, e.g., the time-reversed Green's function as done in the context of time-reversal. This important distinction is what makes our Green's function retrieval a full wavefield inverse scattering approach, as opposed to a direct application of conventional time-reversal principles. Hence, we find a focusing field that only produces its own time-reversed copy with opposite sign as well as the desired causal-only Green's function when injected from a single-sided measurement surface, but no noise or artefacts by apparently missing boundary data. This specific focusing function is therefore not only defined by the temporal preconditioning, i.e. the window function Θ , but also by the general form of the integral representation itself, i.e. \mathbf{f} for an open boundary is different from \mathbf{f} for a closed boundary. The window function Θ is designed such that

$$\Theta \mathbf{g} = \mathbf{g}_d \quad (6.22)$$

$$\Theta \mathbf{f} = \mathbf{f} \quad (6.23)$$

where $\mathbf{g} = \mathbf{g}_d + \mathbf{g}_m$, i.e. the sum of the first arrival \mathbf{g}_d and the coda \mathbf{g}_m . Note that we use the subscript d which was originally proposed in the Marchenko context to denote the direct arrival in a truncated medium (Wapenaar et al., 2014b), but we are in fact referring to the first arrival in the actual medium, which not only propagates upwards towards the boundary, but also in all other directions. This important difference means that, here, \mathbf{g}_d and also the respective travel times $t_d(\mathbf{x}_r; \mathbf{x}_f)$ include diving and refracted waves from the medium below \mathbf{x}_f . Because the window operator is a filter in the time domain, it acts as a convolutional operator in the frequency domain (Wapenaar et al., 2014b). Applying

this windowing to Equation 6.21 gives

$$\mathbf{g}_d - \mathbf{f}^* = \Theta \mathbf{R} \mathbf{f} \quad . \quad (6.24)$$

This represents the three-dimensional Marchenko integral. It follows from Equation 6.19 when choosing the most compact focusing function in time along with consequent causality arguments. Time-reversing this relation yields

$$\mathbf{g}_d^* - \mathbf{f} = \Theta \mathbf{R}^* \mathbf{f}^* \quad , \quad (6.25)$$

noting that Θ is symmetric in time. Applying the window operator $\Lambda = \mathbf{I} - \Theta$ to Equation 6.21 we also get

$$\mathbf{g}_m = \Lambda \mathbf{R} \mathbf{f} \quad . \quad (6.26)$$

Rearranging Equation 6.24 for \mathbf{f}^* and inserting it into Equation 6.25, we obtain

$$\mathbf{f} = (\mathbf{I} - \Theta \mathbf{R}^* \Theta \mathbf{R})^{-1} (\mathbf{g}_d^* - \Theta \mathbf{R}^* \mathbf{g}_d) \quad . \quad (6.27)$$

Inserting this into Equation 6.26 and adding \mathbf{g}_d , we get

$$\mathbf{g} = \mathbf{g}_d + \Lambda \mathbf{R} (\mathbf{I} - \Theta \mathbf{R}^* \Theta \mathbf{R})^{-1} (\mathbf{g}_d^* - \Theta \mathbf{R}^* \mathbf{g}_d) \quad . \quad (6.28)$$

This expression delivers the Green's function for a virtual source inside of an inaccessible volume measured at receivers on the surface from an estimate of the first arrival of the Green's function \mathbf{g}_d , the windowing function Θ and the single-sided reflection data \mathbf{R} . While \mathbf{R} can be obtained from a measurement, one needs to have an estimate of the physical medium to approximate \mathbf{g}_d . Generally, we assume that a smooth, kinematically correct version of the actual model is sufficient. Similarly, we require such a model to build the windowing operator Θ , i.e. to find the first arrival times, e.g., via ray-tracing. Rather than solving for either \mathbf{g} or \mathbf{f} we can also solve for

$$\mathbf{b} \equiv \mathbf{R} \mathbf{f} = \mathbf{R} (\mathbf{I} - \Theta \mathbf{R}^* \Theta \mathbf{R})^{-1} (\mathbf{g}_d^* - \Theta \mathbf{R}^* \mathbf{g}_d) \quad , \quad (6.29)$$

such that both \mathbf{f} and \mathbf{g} follow from the respective filtering in the time domain, i.e.

$$\mathbf{g} = \mathbf{g}_d + \Lambda \mathbf{b} \quad (6.30)$$

and

$$\mathbf{f}^* = \mathbf{g}_d - \Theta \mathbf{b} \quad . \quad (6.31)$$

If the operator norm of $\Theta \mathbf{R}^* \Theta \mathbf{R}$ is smaller than one, we can use a Neumann series to estimate the inverse in Equations 6.27, 6.28 and 6.29, i.e.

$$(\mathbf{I} - \Theta \mathbf{R}^* \Theta \mathbf{R})^{-1} = \sum_{k=0}^{\infty} (\Theta \mathbf{R}^* \Theta \mathbf{R})^k \quad . \quad (6.32)$$

Regarding the accordingly gained infinite series for \mathbf{g} , i.e.

$$\mathbf{g} = \mathbf{g}_d + \Lambda R \mathbf{g}_d^* - \Lambda R \Theta R^* \mathbf{g}_d + \dots, \quad (6.33)$$

one can indeed derive the same result from the coupled Marchenko equations (Wapenaar et al., 2014b). However, the previous result assumes up-/down-decomposition inside the volume, which means that laterally propagating waves and those which are evanescent in the vicinity of \mathbf{x}_f are excluded. Furthermore, the previous \mathbf{g}_d is defined in a truncated medium, and thus excludes refracted or diving waves that are often present in real media. We derived the solution without the need of a truncated medium, circumventing up-/down-decomposition at the focusing level. As a result of this, our newly adjusted Marchenko method is, in principle, able to retrieve the full wavefield response of the medium. We did not prove that the focusing function always exists under the above conditions, i.e. separated from the Green's function and for an open boundary. We suspect, however, that it does as long as the model complexity is moderate. If it exists, the inverse in Equations 6.27, 6.28 and 6.29 exists and we can use the described method to estimate the Green's function. There are of course still limitations with regard to, e.g. finite apertures (e.g. Sripanich and Vasconcelos, 2019), spatial sampling of the integrands (Peng and Vasconcelos, 2019; Wapenaar and van IJsseldijk, 2020), model complexity (Vasconcelos and Sripanich, 2019), band limitation (Dukalski et al., 2019) and the accessible background model information. In the next section we show a numerical example in support of our theoretical findings and illustrate some remaining issues.

6.4. NUMERICAL EXAMPLE: FULL WAVEFIELD RETRIEVAL IN A HETEROGENEOUS MEDIUM

In this section we investigate a numerical example in the geophysical context. We want to show that the Marchenko integral can be used to retrieve the full wavefield, including evanescent and refracted waves. Here, we focus on the single-sided integral representation in Equation 6.19 and solve it as suggested in Equation 6.33. Hence, we rely on wavefield observations at the horizontal upper boundary of a heterogeneous, scattering half-space. In real-life applications, such measurements are typically limited to a finite aperture, i.e. sources and receivers only cover a certain extension of ∂V_0 . We use the two-dimensional model in Figure 6.3 with constant mass density $\rho = 2000 \text{ kg/m}^3$. We rename x_1 and x_3 for two dimensions, i.e. $\mathbf{x} = (x, z)$. We use 501 equally spaced receivers on the surface and record 501 shots for sources on the same grid. Note that the model is more complex than conventional velocity media used for numerical studies of the Marchenko integral (e.g. Wapenaar et al., 2014b, 2017), i.e. here we consider a shallow high velocity layer and relatively large velocity contrasts.

In order to visualise the estimated wave propagation through the volume, we solve the Marchenko integral for the Green's functions of all points within the dark rectangle in Figure 6.3 according to Equation 6.33 – regularly sampled from $x = 1192 \text{ m}$ to $x = 2808 \text{ m}$ and from $z = 0 \text{ m}$ to $z = 1600 \text{ m}$ at every 4 m both in x- and z-direction. Then we make use of source-receiver reciprocity and choose the same receiver location \mathbf{x}_r for all these Green's functions to get the Green's function for a source at the respective surface location \mathbf{x}_r measured at all \mathbf{x}_f in the volume under investigation.

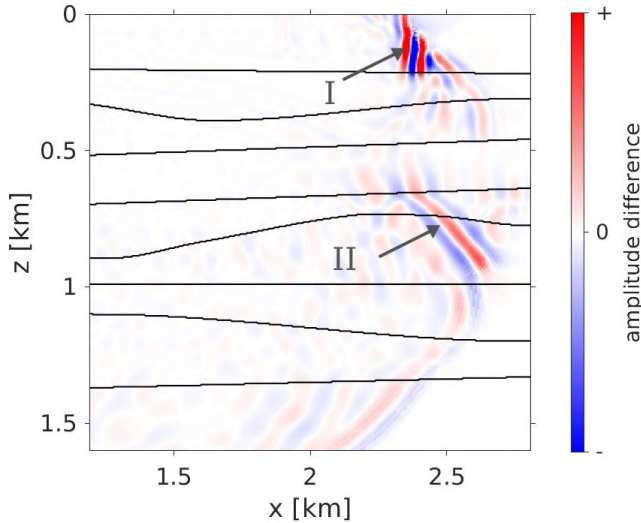


Figure 6.5: Difference of the true and the estimated snapshot for 0.6 s, compare Figure 6.4 (h). The black contours show the geometry of the velocity model. The colour bar is clipped at the same values as in Figure 6.4.

We start by using the correct first arrival wavefield \mathbf{g}_d and window operator Θ , which in this particular case we obtain from modelling in the correct velocity model. This is done solely as a proof of concept, i.e. to show that the Marchenko integral performs sufficiently well. Figure 6.4 presents five snapshots of the wave propagation for a source in the top left corner of the target volume. In the left column we show \mathbf{g}_d . As we are using the correct medium, these wavefields actually show the correct Green's function, however, they are masked by Θ as we only use the first arrivals. In the right column we show the correct and the estimated snapshots. The two wavefields are superimposed and visualised in an alternating fashion to facilitate their comparison. These snapshots show a very good match between true and estimated fields. In particular, the estimated wavefields include refracted and evanescent waves, observable, e.g., in the region of the fourth layer, see arrows in Figures 6.4 (d), 6.4 (f) and 6.4 (h). While one can only see a single event in Figure 6.4 (d), Figures 6.4 (f) and 6.4 (h) show a separate refracted (vertical arrow) and evanescent (diagonal arrow) wave. Looking more closely into the accuracy of the estimated field, Figure 6.5 depicts the absolute error of the true and the estimated wavefield at 0.6 s. Note that the colour bar is clipped at the same amplitudes as in Figure 6.4. Hence, Figure 6.5 shows that the fields match well almost everywhere within the medium, but it also reveals regions where the Marchenko field is reconstructed slightly worse. These errors mainly manifest as poorly matched amplitudes rather than unwanted wavefield artefacts. The first of these poorly matched regions, marked by I in Figure 6.5, refers to the nearly horizontally travelling wave near the surface. Given the

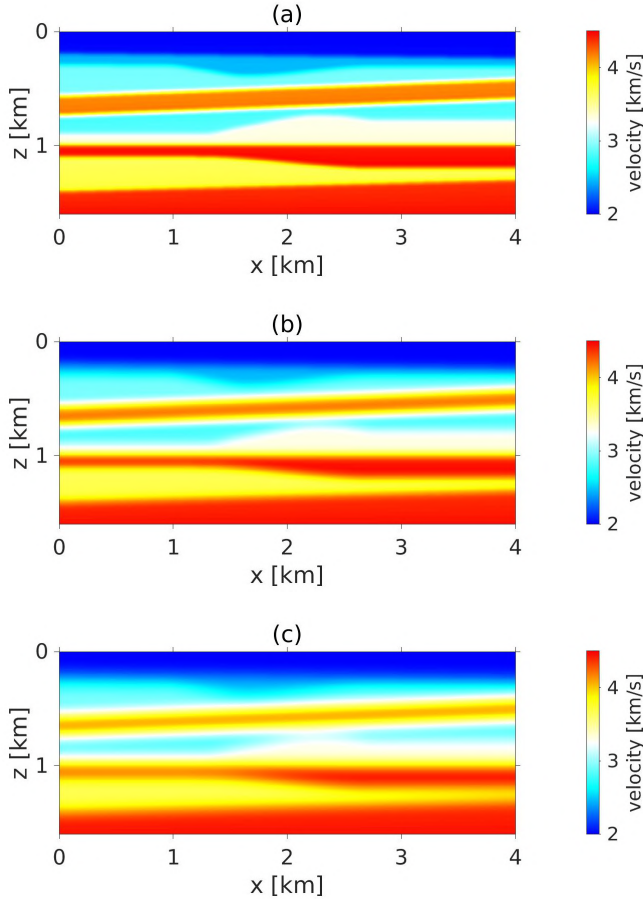


Figure 6.6: Smoothed versions of the model in Figure 6.3. The smoothing degree increases linearly from (a) to (b) to (c).

up-/down-decomposition at the surface ∂V_0 in our derivation, it might be challenging for the Marchenko integral to incorporate the energy of this particular field that arrives at the receivers under such a near-horizontal propagation angle. This would probably improve for wider bandwidth and/or larger aperture data. Furthermore, the misfit is right at the edge of the window function Θ , i.e. right after the first arrival of the Green's function. This makes it hard for the method to retrieve accurate amplitudes. The second poorly matched area, marked by II, refers to a rather steep, deeper event. As this up-going wavefront is yet to travel through the fourth, high-velocity layer, its slope, i.e. in terms of horizontal wavenumber, can be assumed to increase even further on its way up. We surmise that this amplitude mismatch is mainly caused by the limited aperture of the numerical experiment, i.e. missing sources and receivers, especially at $x > 4$ km.

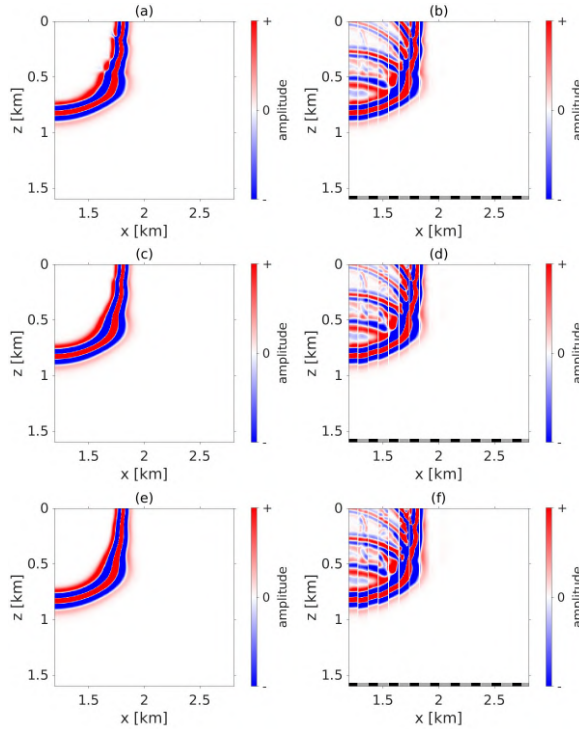


Figure 6.7: Snapshots showing the wave propagation for the source and area marked in Figure 6.3. Left and right column show, as before, the first arrival and the true/estimated wavefield, respectively. Black bottom colour marks the true, grey the estimated wavefield columns. The first row (a, b) is obtained for the lightly smoothed velocity model in Figure 6.6 (a), the second row (c, d) for the moderately smoothed model in Figure 6.6 (b) and the last row (e, f) for the considerably smoothed model in Figure 6.6 (c). The colour bars are clipped at 1% of the overall absolute maximum amplitude. All snapshots show the same propagation time, i.e. 0.3 s.

We want to stress that the Neumann expansion was truncated at a constant term for this experiment. Including additional terms may also lead to potentially further improved amplitudes for I and II. Overall, our numerical example supports the claim that our un-coupled Marchenko integral can be used to reproduce the full non-linear scattering of the Green's function, including evanescent and refracted waves within the medium. There are still limits in the accuracy of the here retrieved wavefields mainly related to the band limitation of the data, the windowing operator and the limited extension of the measurement surface.

In most practical scenarios, one does not typically have access to the correct first arrival. Therefore, we want to analyse the outcomes for three different approximations of \mathbf{g}_d based on smooth estimates of the correct wavespeed model, displayed in Figure 6.6, with increasing degrees of inaccuracy relative to the actual medium. Such models may be obtained by tomographic inversion methods for instance (e.g Rawlinson et al., 2010). While the models are potentially too smooth to produce reflections they can be used

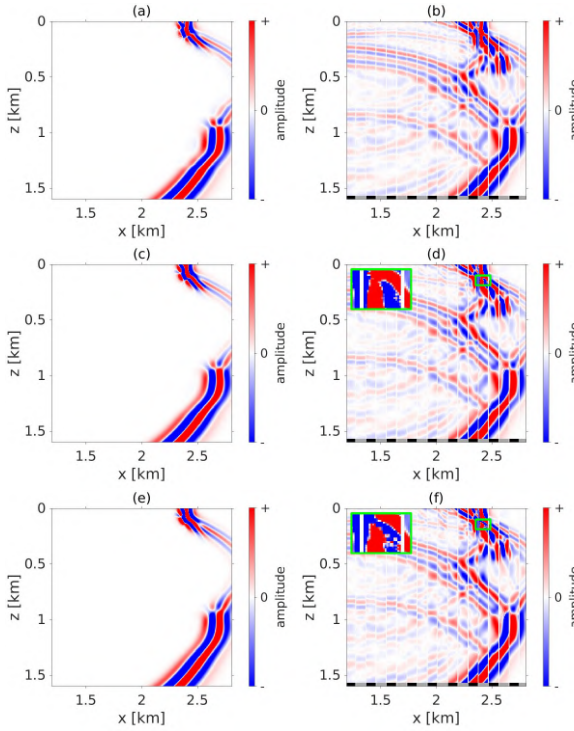


Figure 6.8: Similar to Figure 6.7, but for a propagation time of 0.6 s. The big green windows in (d) and (f) show zoomed-in regions. Their respective locations are marked by the small green windows.

to approximate the first arrival \mathbf{g}_d and the window operator Θ . Then, the Marchenko integral can be utilised to approximate all orders of scattering inside the medium. Generally speaking, the estimated Green's function combines the kinematic information of the background model comprised in the first arrival with the reflection measurement, seeking to find a consistent wavefield that matches both. Figure 6.7 shows the estimated wavefields for a propagation time of 0.3 s. At first glance, all three estimated fields show comparable results. While the reflections are not known a priori, we retrieve them through the Marchenko scheme, using the information from the smooth background models. It is, however, easily observed that the estimated wavefields also contain a significant amount of noise. There are artefacts, mostly in form of apparently steep, coherent events. While they are lower in amplitude than the desired signal, they are not negligible. Furthermore, we observe that these artefacts become more pronounced for smoother background models, i.e. the field in Figure 6.7 (b) is better than that in Figure 6.7 (f). Figure 6.8 presents the snapshots at a later propagation time of 0.6 s. Again, all estimated fields appear to be of similar, good quality. In fact, the wavefields seem to be better for higher propagation times, i.e. there are fewer visible artefacts compared to the earlier-time counterparts in Figure 6.7. Evanescent and refracted waves are

still retrieved, albeit with lower accuracy. Upon closer inspection, however, there are still evident biases. Especially for the smoothest model, Figure 6.6 (c), the interlaced snapshot, Figure 6.8 (f), reveals significant phase shifts between true and estimated arrivals. This is a result of an inaccurate \mathbf{g}_d estimate, which is observable by comparing the first arrivals in the bottom right area of Figure 6.8 (f) between true and estimated fields. This misfit affects all later reflections and produces significant phase and amplitude errors at all orders of scattering. Both local and coherent artefacts can be inspected in greater detail in the zoomed-in regions in Figures 6.8 (d) and 6.8 (f). While the wavefield is still rather good for the former, it reveals a different shape and several point-like structures in the latter. In fact these artefacts also relate to the stability of the Marchenko integral. It is not evident that the inverse in Equations 6.27, 6.28 and 6.29 should always exist, in particular when considering complex media and/or inaccurate background models, the latter reflecting upon the quality of the window operator Θ . Empirically, we find this inverse to be generally stable for moderately heterogeneous media, e.g., media where velocity increases rather monotonically with depth. In these cases, even strong smoothing of the true model delivers an appropriate Θ and a stable inverse. Furthermore, the Neumann expansion in Equation 6.33 appears to deliver a convergent series then. For more complex settings, as, e.g., the model in Figure 6.3, the inverse can become unstable, in particular as the background models used to obtain Θ become smoother. We also observed, in addition, that using a truncated model as required by the original Marchenko approach (Wapenaar et al., 2014b) leads to even greater instability (see Appendix). Finally, we point out that we use a finite Neumann series to solve the Marchenko equation in this paper, where the order of the last term can be thought of as playing a regularisation role. In fact, the leading-order solution already yields an accurate first guess, while remaining stable even for relatively inaccurate background models, i.e.

$$\begin{aligned} \mathbf{g} \approx & \mathbf{g}_d + \Lambda R \mathbf{g}_d^* - \Lambda R \Theta R^* \mathbf{g}_d + \Lambda R \Theta R^* \Theta R \mathbf{g}_d^* \\ & - \Lambda R \Theta R^* \Theta R \Theta R^* \mathbf{g}_d \quad . \end{aligned} \quad (6.34)$$

For the results shown in this paper, we use the tenth-order truncated series. This order is chosen for its accuracy seems adequate and the computational cost reasonable, while still delivering sensibly regularised results for the investigated smoothed models.

These numerical results support our hypothesis that the Marchenko integral is generally valid for the full wavefield. The quality of the reconstructed wavefields is shown to depend on the quality of the required a priori model in terms of producing an accurate first arrival estimate. While we can use smooth medium-parameter estimates, they can introduce artefacts and phase shifts in the resulting wavefields. We found these effects to be strong for highly complex media and addressing a better practical scheme for Green's function retrieval in such cases is the topic of current research. However, with the current practical scheme, the Marchenko integral can generally be used to obtain a rather reliable approximation of the entire wavefield within a volume of interest for a wide range of medium configurations.

6.5. DISCUSSION

We present a new derivation for the Marchenko integral which proves that the equation is more general than previously assumed. Introducing the concept of the homogeneous Green's function of the second kind is the key point in this derivation. While previous versions of Marchenko representations target very particular choices for the focusing function, e.g., defined by means of the transmission operator of an auxiliary, truncated medium (Wapenaar et al., 2014b), we present a generalisation of focusing functions, which encompasses previous choices but accommodates for new approaches. Using conventional reciprocity theorems one can easily obtain integral representations that relate the Green's and focusing functions to observed reflection data. These data can either be obtained on a closed or an open boundary, and for either case our respective Marchenko-like formalism is well-defined. Furthermore, we present a new, general strategy for solving the un-coupled Marchenko integral to infer the medium's response from open boundary observations, i.e. for a single-sided reflection experiment. The physical arguments that lead this solution are generally equivalent to those by Wapenaar et al. (2014b). To obtain the Green's function from Equation 6.19 we rely on the special realisation of a focusing function that is most compact in time-space. This focusing function has the benefit of being separable from the Green's function in time, thus allowing for a solution of the Marchenko integral based on an estimate of the first arrival \mathbf{g}_d . Additionally, the method circumvents artefacts that are conventionally introduced by open boundary integral representations, delivering, in principle, an unbiased Green's function estimate. Kiraz et al. (2020) recently presented a heuristic, iterative scheme to solve the closed boundary integral Equation 6.17 using the very same, time-compact, physical realisation of a focusing function. In this case, injecting $f(\mathbf{x}; \mathbf{x}_f)$ into the medium delivers a wavefield that, when adding its complex conjugate, equals the homogeneous Green's function of the first kind. Our generalised framework for focusing functions might be useful for future studies, e.g. directly involving the partial differential Equation 6.8. In particular, there might be possibilities of including focusing functions in other inverse scattering approaches without explicitly relying on the Marchenko equation, such as full waveform inversion (Virieux and Operto, 2009) or the contrast source method (van den Berg and Abubakar, 2001).

Our numerical studies show that the Marchenko integral can be used to obtain an accurate approximation of the full wavefield Green's function from only an estimate of its first arrival and single-sided reflection data. The necessary a priori estimate of the first arrival can be based on a reference model, i.e. a smooth estimate of the actual model. We show how, under this new theory, the corresponding adaptations to the existing Marchenko workflow produce reliable wavefields for relatively complex models – with the key addition of retrieving evanescent and refracted fields within an unknown scattering medium. Furthermore, we present the estimated wavefields for an entire volume allowing for a more thorough, spatially dependent analysis of propagation effects. Finally, we discuss the impact of the accuracy of the background model used to approximate \mathbf{g}_d . For complex media, a poor estimate of the first arrival from an inaccurate reference model can produce significant local artefacts and phase shifts in the recovered fields, but it still allows for a good approximation of the global, scattered field. When in

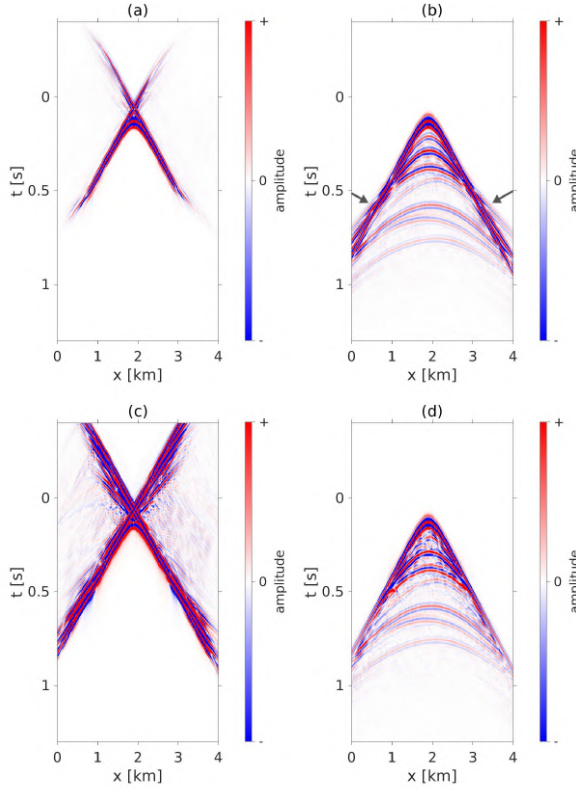


Figure 6.9: Time-reversed focusing function f^* (a) and Green's function g (b) obtained with our approach. Time-reversed focusing function f^* (c) and Green's function g (d) obtained with the conventional approach. All fields are for the virtual source location \mathbf{x}_f marked by the downwards pointing triangle in Figure 6.3 and show the respective fields for all receivers \mathbf{x}_r on the surface of the model. All colour bars are clipped at the same value, i.e. at about one percent of the absolute maximum amplitude of all four wavefields.

doubt about the quality of the reference medium in achieving sufficiently accurate first arrival estimates, we suggest to use a first-order truncated Neumann series, generally allowing for a stable yet reasonably accurate estimate of the Green's function. Alternatively, one may solve Equations 6.27, 6.28 and 6.29 directly using a numerical solver like LSQR (Paige and Saunders, 1982; Dukalski and de Vos, 2017).

As mentioned earlier, there are variations of the conventional Marchenko scheme that can be used for primary estimation, i.e. multiple reflections can be filtered out (van der Neut and Wapenaar, 2016; Zhang and Slob, 2019). Such primary estimation schemes can be applied without the need for a parameter, e.g. wavespeed, model, making them rather attractive for processing wavefield data. It is yet to be investigated, how our findings can be linked to these methods. While we only consider acoustic waves in this paper, some studies already investigated the conventional Marchenko method for elastic

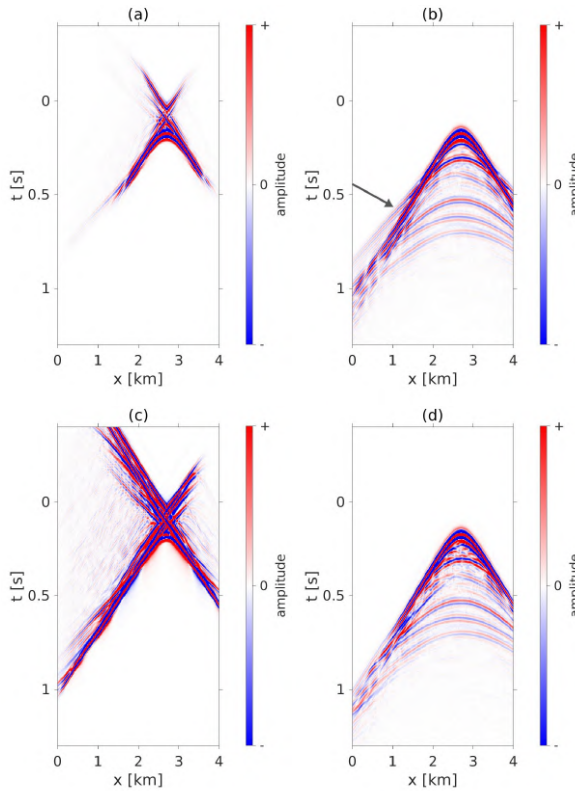


Figure 6.10: Similar to Figure 6.9, but for the virtual source location \mathbf{x}_f marked by the upwards pointing triangle in Figure 6.3.

waves (da Costa Filho et al., 2014; Wapenaar and slob, 2015; Reinicke et al., 2020). This extension is valuable for certain data applications, e.g. seismic imaging or medical elastography, and it will be a topic of future research to connect our new insights with these studies.

We note that the coupled Marchenko system (Wapenaar et al., 2014b) remains very useful. In the example of geophysical applications, there is purpose to directly estimate the decomposed up- and down-going Green's functions at a certain level in the medium. This allows for so-called redatuming and target-oriented imaging, independent of model perturbations above the redatuming level (e.g. Singh and Snieder, 2017; Cui et al., 2020). The implicit model truncation, however, that is inherent to the coupled Marchenko approach, might be an issue in complex media. In these cases it might be beneficial to solve the un-coupled Marchenko integral first, see Section 6.3, and then decompose the estimated Green's functions afterwards if desired or, alternatively, to adjust the coupled Marchenko equations to match our new scheme. There are also applications that can make use of the full Marchenko-estimated wavefield inside a volume of interest. Such a

wavefield might for instance be used to estimate the scattering potential, i.e. the perturbations of the medium that are missing in the reference model and induce the scattered wavefield (Cummings and Curtis, 2020; Diekmann and Vasconcelos, 2020). It will be a topic of future research to see what other ways there are for the Marchenko approach to add value to related inverse scattering and imaging schemes and, in this regard, for it to be applied not only in geophysical, but also in, e.g., medical applications and non-destructive testing.

6.6. CONCLUSION

We introduce the homogeneous Green's function of the second kind delivering a framework for focusing functions that is substantially more general than in previous Marchenko related applications. Based on the resulting partial differential equation, we can construct integral representations for the involved wavefields. The single-sided representation is identical in its form to the previously derived three-dimensional Marchenko relations, however, our new derivation imposes significantly fewer limitations on the retrievable wavefields, while accommodating also for closed boundary representations. As such, we find that the Marchenko equation is therefore more general than previously assumed and can indeed be used to obtain the full wavefield response from an unknown scattering medium including evanescent and refracted waves. For practical Green's function retrieval, we present a direct solution of the un-coupled Marchenko integral that follows certain causality assumptions – in a manner analogous to the current approach for the coupled Marchenko representation. It is only in this step, that we make use of a particular realisation of the focusing function that is purposefully chosen to be separated from the Green's function in time. Lastly, we show numerical examples that illustrate the Marchenko integral's capability of estimating the entire, full field Green's function from an estimate of the first arrival and single-sided reflection data. This paves the way for more complex data applications and a potentially broader usage in related imaging sciences.

ACKNOWLEDGEMENTS

The authors want to thank David Vargas, Andreas Tataris, Haorui Peng and Tristan van Leeuwen for fruitful discussions. Furthermore they are grateful to the Utrecht Consortium for Subsurface Imaging (UCSI) for funding and support.

APPENDIX: COMPARISON WITH THE CONVENTIONAL MARCHENKO SCHEME

In the following, we want to illustrate and discuss differences of our newly interpreted Marchenko-based Green's function retrieval approach and the conventional method. For the theory of the conventional method we refer the interested reader to previous works (e.g. Wapenaar et al., 2013, 2014b, 2016; van der Neut et al., 2015b).

In the conventional approach, the focusing function is defined as the inverse transmission response in a truncated medium and its direct arrival is approximated by the time-

reversed direct Green's function (Wapenaar et al., 2014b). This approximation of the direct arrival of the focusing function is conventionally regarded as the necessary a priori information when solving for a virtual Green's function. However, the approximation is known to be insufficiently accurate when complex models are considered (Vasconcelos et al., 2015). In our approach, we do not define the focusing function via an inverse transmission response. Instead, we show that there are many functions $f(\mathbf{x}; \mathbf{x}_f)$ that obey Equation 6.19. It is only for the most compact of these focusing functions in time-space domain, however, that we are able to solve the system for the Green's function. Furthermore, we use a different window operator Θ , i.e. as suggested by, e.g., Zhang et al. (Zhang et al., 2018) versus the conventional window (Wapenaar et al., 2014b). This window operator shifts the a priori information from the direct arrival of the focusing function (in the conventional approach) to the first arrival of the Green's function (in our approach). Hence, we indeed require an accurate guess of the first arrival Green's function as a priori information and not an inverse transmission response. As already pointed out several times throughout the paper, we never consider a truncated medium wave state. Therefore, the required a priori information is the first arrival of the Green's function in the actual medium, including diving and/or refracted waves – no approximations involved.

Our newly adjusted Marchenko scheme can incorporate diving and refracted as well as evanescent waves. While we show results to proof these points for our method above, we want to do a comparison with the conventional approach here to directly highlight differences. Figures 6.9 and 6.10 show time-space domain focusing functions $f(\mathbf{x}_r; \mathbf{x}_f)$ and Green's functions $g(\mathbf{x}_r; \mathbf{x}_f)$ for the two virtual source locations marked in Figure 6.3 both using our approach and the conventional approach. We use the correct first arrival and direct arrival Green's functions, respectively, where the latter is obtained by modelling in the accordingly truncated, correct medium. For both approaches we use the same, unfiltered reflection data, i.e. including also, e.g., refracted arrivals. The arrows in Figures 6.9 (b) and 6.10 (b) denote refracted waves that are reconstructed by our scheme, but not by the conventional one. The conventional method can not obtain any Green's function contributions before the direct arrival in the truncated medium, neglecting refracted waves and, in general, diving waves, as they obey the same physics. Regarding evanescent waves, we note that the traditional theory excludes them (Wapenaar et al., 2014b) while our new theory includes them.

Last but not least, Figures 6.9 and 6.10 illustrate the instability of the conventional approach. Comparing the focusing functions in Figures 6.9 (a) and 6.10 (a) with those in Figures 6.9 (c) and 6.10 (c) one clearly sees largely increased amplitudes in the latter. This indicates a divergence related energy growth of the Neumann series for the conventional approach.

A NOTE ON MARCHENKO-LINEARISED FULL WAVEFORM INVERSION FOR IMAGING

Full waveform inversion and least-squares reverse time migration are the leading technologies for imaging with seismic waves. Both of them usually rely (in one way or another) on a single-scattering approximation, i.e. the Born approximation, to compute gradients and obtain an updated model. This approximation linearises the relation between modelled data and model by ignoring multiple scattering. We propose to use the Marchenko integral, an equation originating from inverse scattering theory, to obtain an alternative linear equation. Using the Marchenko method we can retrieve Green's functions, including all orders of scattering, for virtual sources anywhere within the volume of interest – without prior knowledge of the high-wavelength model variations that induce scattering. Plugging these estimated Green's functions into the Lippmann-Schwinger integral delivers a Marchenko-linearised relation between the full waveform data and the model. We present this new linearisation strategy and illustrate its advantages and disadvantages by comparing numerical results for different inversion kernels. Our new linearisation is exact, i.e. it does not exclude any orders of scattering, however, it relies on the quality of the Marchenko-derived Green's functions. These Marchenko-based Green's functions require an estimate of the first arrivals of the Green's functions – commonly obtained by modelling in a background medium. Although these first arrival estimates strongly bias our results for inaccurate background models, we find the Marchenko-linearisation to deliver overall slightly better inverted models than the single-scattering approximation.

7.1. INTRODUCTION

Inferring the physical properties of a volume from its scattering response to incident, e.g., acoustic waves is essential for many applications, ranging from non-destructive testing (Grohmann et al., 2017) over medical imaging (Bernard et al., 2017; Guasch et al., 2020) to seismic imaging (Warner et al., 2013). Regarding high-resolution imaging with seismic waves there are two main state-of-the-art strategies in Geophysics: least-squares

The content of this chapter was published as Diekmann et al. (2023b).

reverse time migration (LSRTM) and full waveform inversion (FWI). Both of these methods rely on reducing the misfit between the measured, scattering data on the medium's boundary and the respectively estimated data, obtained from numerical modelling.

LSRTM requires a background model, containing the long-wavelength variations of the physical properties, and aims to retrieve the missing reflection model, i.e. the short-wavelength model structures that induce scattering (Dai et al., 2012). The background model can for instance be obtained via tomography (Rawlinson et al., 2010). LSRTM is based on the Born integral (Born and Wolf, 1999) which provides an approximate, linear relation between the modelled data and the desired reflection model. This Born integral is at its core a single-scattering approximation, meaning that multiply scattered waves can not be handled accurately in LSRTM (in particular if the unknown, short-wavelength model perturbations are large). There are, however, various strategies to include multiple scattering in LSRTM, dealing with both surface-related multiples (Zuberi and Alkhalifah, 2014) and internal multiples (Malcolm et al., 2009; Zhang and Schuster, 2014; Wang et al., 2020).

FWI on the other hand attempts to estimate the model from as little prior information as possible – usually starting with a rather simple initial model (Tarantola, 1984; Virieux and Operto, 2009; Virieux et al., 2017). FWI is a non-linear inversion strategy, i.e. it accurately represents the non-linear relation between modelled data and model. It can be solved in the following way: modelling in the initial model delivers wavefields that can be plugged into the Born integral. This linear system can be solved to obtain an updated model. This new model can then be used for remodelling the wavefields, using Born again and so on. Starting by matching the low-frequency content of the measured data and sequentially including higher frequencies, FWI attempts to avoid artefacts from the single-scattering approximation underlying its gradient computations. To further overcome local minima, i.e. converging to wrong models when, e.g., low frequency data are unavailable, improved formulations of FWI, such as extended FWI (Huang et al., 2018; van Leeuwen, 2019), adaptive waveform inversion (Warner and Guasch, 2016) or inversion based on optimal transport (Métivier et al., 2019; Engquist and Yang, 2022), were presented.

We note that there are also reflection FWI approaches that focus on inverting for high-frequency model perturbations (Yao et al., 2020) as well as non-linear formulations of LSRTM (Yao and Jakubowicz, 2012). In practice, LSRTM and FWI depart in three main aspects. Firstly, their goal: FWI is generally used as a high-end, long-spatial-scale velocity model building tool, whereas LSRTM aims at retrieving the sharp components – the details – of the subsurface structure, commonly referred to as an image. Secondly, because of their different goals, different parts of the data are employed for FWI (e.g., long-offset data, diving/head waves) and LSRTM (e.g., short-offset data, reflected and diffracted waves) to condition the input data for inversion toward the desired length scales. Thirdly, owing to the different desired scales in target models, FWI and LSRTM often differ on how the models are parametrised in the inverse problem, both in terms of separating background versus update components, as well as physical quantities themselves, e.g., FWI favouring velocity parametrisation and LSRTM favouring impedance or reflectivity parameters. These three key differences often result in significantly different practical strategies in data-misfit metrics, gradient preconditioning/shaping and opti-

misation.

In this paper, we discuss an alternative to the single-scattering approximation, i.e. another way to obtain a linear relation between the modelled data and the model and thus to compute a model update. Our proposed strategy is fundamentally based on using the Marchenko integral (Wapenaar et al., 2014b). The Marchenko integral was originally introduced in the context of one-dimensional inverse scattering theory (Burrige, 1980; Rose, 2001; Brogini et al., 2012). It relates Green's functions and so-called focusing functions via the reflection response of the medium measured on its boundary. Its extension to 2D and 3D about ten years ago enabled various applications regarding imaging in complex media (Wapenaar et al., 2013; Meles et al., 2015; Ravasi et al., 2016; Vargas et al., 2021). Most importantly for this paper, the Marchenko integral allows for retrieving the Green's function for a virtual source inside of an inaccessible medium – it does, however, require an estimate of the first arrival of the desired Green's function. This first arrival is usually obtained by modelling in a smooth background, i.e. a long-wavelength-accurate, medium. This means, that one can obtain the full Green's function, including all orders of scattering, for a virtual source located anywhere inside of the volume of interest without requiring an actual physical source inside the volume or having to know the medium's high-frequency, scattering-inducing physical property perturbations.

Marchenko Green's functions can be used for LSRTM and FWI in various ways. Commonly, the Marchenko method is used for redatuming the wavefields to a target level, where different inversion strategies can be used to image the medium (Cui et al., 2020; Shoja et al., 2020, 2022). Instead, we propose to use Marchenko-based Green's functions inside the kernel of the inverse problem (Diekmann and Vasconcelos, 2020; Diekmann et al., 2021): by plugging the estimated Green's functions into the Lippmann-Schwinger integral (Lippmann and Schwinger, 1950) we obtain a new, linear relation between modelled data and model. This linear relation can be used to obtain a model update, i.e. to invert for the model. The linearisation is (in theory) exact, i.e. by using the full Green's functions with all orders of scattering rather than background Green's functions (as done in the Born integral) we get an exact, linear system. There are, however, other assumptions and approximations underlying the Marchenko scheme and, consequently, this new linearisation. Hence, we do not necessarily consider this a superior method to well-established schemes, but we aim to explain, discuss and illustrate the possibilities and limitations of using Marchenko methods to linearise seismic imaging. We will refer to our approach as Marchenko-linearised full waveform inversion, although the approach is generally quite similar to LSRTM – it is, however, not based on a single-scattering approximation but supposed to accurately include multiple scattering and, therefore, the full wavefield.

We start by introducing the Lippmann-Schwinger integral which forms the basis for gradient computations in seismic inversion. Then we discuss Green's function retrieval by the Marchenko method. Next, we discuss our Marchenko-linearised full waveform inversion strategy. Finally we show numerical results for different kernel approximations to compare and evaluate the quality of our new Marchenko-linearisation.

7.2. LIPPMANN-SCHWINGER INTEGRAL

The constant-density acoustic wave equation is given by

$$\mathcal{L}(\mathbf{x}, \omega) u(\mathbf{x}, \omega) = \rho i \omega s(\mathbf{x}, \omega) \quad (7.1)$$

with the wave operator

$$\mathcal{L}(\mathbf{x}, \omega) = \nabla^2 + \frac{\omega^2}{c^2(\mathbf{x})} \quad , \quad (7.2)$$

the wavefield $u(\mathbf{x}, \omega)$ at location $\mathbf{x} = (x_1, x_2, x_3)$ and frequency ω and the volume injection rate density source term $s(\mathbf{x}, \omega)$. The constant mass density is denoted by ρ and velocity by $c(\mathbf{x})$, i marks the imaginary unit.

The Green's function is the causal wavefield that obeys

$$\mathcal{L}(\mathbf{x}, \omega) g(\mathbf{x}, \omega; \mathbf{x}_s) = \rho i \omega \delta(\mathbf{x} - \mathbf{x}_s) \quad , \quad (7.3)$$

i.e. it is the medium response to an impulse source at location \mathbf{x}_s . Similarly, we can define a background Green's function in a background medium, i.e. a medium with different physical properties, for a source at \mathbf{x}_r according to

$$\mathcal{L}_0(\mathbf{x}, \omega) g_0(\mathbf{x}, \omega; \mathbf{x}_r) = \rho i \omega \delta(\mathbf{x} - \mathbf{x}_r) \quad (7.4)$$

with

$$\mathcal{L}_0(\mathbf{x}, \omega) = \nabla^2 + \frac{\omega^2}{c_0^2(\mathbf{x})} \quad (7.5)$$

and the velocity $c_0(\mathbf{x})$. We will assume that $c_0(\mathbf{x})$ is a smooth background model, while $c(\mathbf{x})$ is the actual model. As before, this background Green's function is a causal wavefield.

Making use of reciprocity (Schuster, 2009; Fokkema and van den Berg, 1993; Snieder and Van Wijk, 2015), we can combine Equations 7.3 and 7.4 to obtain the following volume integral:

$$g_s(\mathbf{x}_r, \omega; \mathbf{x}_s) = \alpha(\omega) \int_{\mathbf{x} \in V} g_0(\mathbf{x}, \omega; \mathbf{x}_r) g(\mathbf{x}, \omega; \mathbf{x}_s) v(\mathbf{x}) dV \quad , \quad (7.6)$$

where we use the scattered Green's function

$$g_s(\mathbf{x}_r, \omega; \mathbf{x}_s) = g(\mathbf{x}_r, \omega; \mathbf{x}_s) - g_0(\mathbf{x}_r, \omega; \mathbf{x}_s) \quad , \quad (7.7)$$

the scattering potential

$$v(\mathbf{x}) = \frac{1}{c^2(\mathbf{x})} - \frac{1}{c_0^2(\mathbf{x})} \quad , \quad (7.8)$$

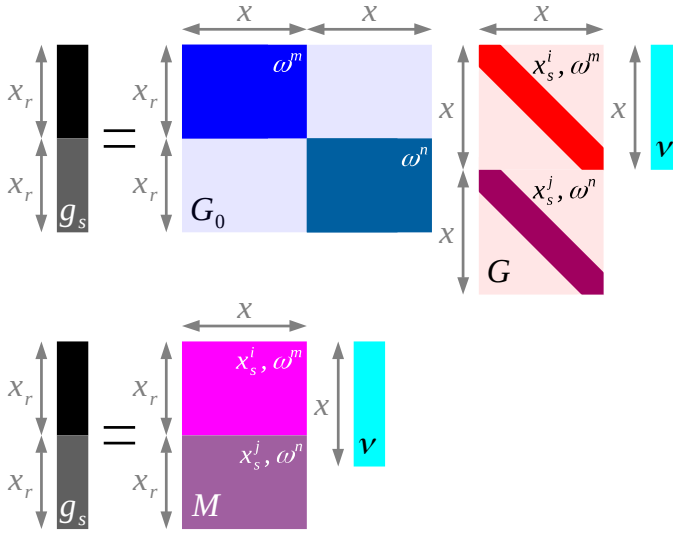


Figure 7.1: Sketch to illustrate the matrix-operator Equations 7.10 (top) and 7.11 (bottom). The matrix \mathbf{G} (red) is diagonal, whereas \mathbf{G}_0 (blue) has dense batches (number of receivers \times number of volume sample points) along its diagonal. The matrix \mathbf{M} (magenta) is dense. The arrows represent which variable, i.e. the receiver location \mathbf{x}_r or volume sample \mathbf{x} , is changing in the respective direction and range. The variables \mathbf{x}_s^i and \mathbf{x}_s^j and ω^m and ω^n denote different source locations and frequencies, respectively.

and the scaling factor

$$\alpha(\omega) = \frac{i\omega}{\rho} \quad , \quad (7.9)$$

see Appendix for details. The volume V contains \mathbf{x}_r and \mathbf{x}_s as well as all perturbations of the scattering potential, i.e. $\nu(\mathbf{x} \notin V) = 0$. Equation 7.6 is the Lippmann-Schwinger integral (Lippmann and Schwinger, 1950).

We can write the Lippmann-Schwinger integral in matrix-operator form as

$$\mathbf{g}_s = \mathbf{G}_0 \mathbf{G} \mathbf{v} \quad , \quad (7.10)$$

where the matrices \mathbf{G}_0 and \mathbf{G} contain the respective background Green's functions and Green's functions. Note that \mathbf{G}_0 also contains the scaling term, see Equation 7.9, as well as an additional scaling factor to account for the integration, e.g. Δx^2 for a square grid in two dimensions where Δx is the spacial sampling interval. The vector \mathbf{g}_s contains the scattered Green's function, Equation 7.7, and the vector \mathbf{v} the scattering potential, Equation 7.8. Equation 7.10 accurately represents a discretized Lippmann-Schwinger integral for multiple receiver locations \mathbf{x}_r , source locations \mathbf{x}_s and frequencies ω , however, it is a fairly big and sparse system, compare Figure 7.1. A more convenient way of setting up the linear system is

$$\mathbf{g}_s = \mathbf{M} \mathbf{v} \quad , \quad (7.11)$$

where $\mathbf{M} = \mathbf{G}_0 \mathbf{G}$ is a dense matrix, see Figure 7.1.

7.3. MARCHENKO-BASED GREEN'S FUNCTION RETRIEVAL

We define the focusing function as the wavefield (Chapter 6)

$$\mathcal{L}(\mathbf{x}, \omega)(-f^*(\mathbf{x}, \omega; \mathbf{x}_f)) = -\frac{\rho i \omega \delta(\mathbf{x} - \mathbf{x}_f)}{2} - q(\mathbf{x}, \omega) \quad , \quad (7.12)$$

where $-f^*(\mathbf{x}, \omega; \mathbf{x}_f)$ obeys a radiation condition of in-coming waves at infinity, i.e. it is an anti-causal wavefield, and we use the same, non-dissipative wave operator as before, Equation 7.2. The source term $q(\mathbf{x}, \omega)$ has to be real-valued, but is otherwise arbitrary. The symbol $*$ denotes complex conjugation (or time-reversal in the time domain). The negative, conjugate focusing function consequently follows from

$$\mathcal{L}(\mathbf{x}, \omega)f(\mathbf{x}, \omega; \mathbf{x}_f) = -\frac{\rho i \omega \delta(\mathbf{x} - \mathbf{x}_f)}{2} + q(\mathbf{x}, \omega) \quad . \quad (7.13)$$

Note that $f(\mathbf{x}, \omega; \mathbf{x}_f)$ is in fact a causal, out-going wavefield. Combining Equation 7.3 for a source at \mathbf{x}_f with Equations 7.12 and 7.13 we get the homogeneous Green's function of the second kind (Chapter 3) as the wavefield that obeys:

$$\mathcal{L}(\mathbf{x}, \omega)(g(\mathbf{x}, \omega; \mathbf{x}_f) + f(\mathbf{x}, \omega; \mathbf{x}_f) - f^*(\mathbf{x}, \omega; \mathbf{x}_f)) = 0 \quad . \quad (7.14)$$

This is a source-free, i.e. homogeneous, wavefield that relates focusing and Green's functions.

Using reciprocity, we can obtain the following integral equation from the homogeneous Green's function of the second kind:

$$-\int_{\tilde{\mathbf{x}} \in \partial V_0} r(\tilde{\mathbf{x}}, \omega; \mathbf{x}_s) f^*(\tilde{\mathbf{x}}, \omega; \mathbf{x}_f) d\mathbf{S} = g(\mathbf{x}_s, \omega; \mathbf{x}_f) + f(\mathbf{x}_s, \omega; \mathbf{x}_f) \quad , \quad (7.15)$$

where

$$r(\tilde{\mathbf{x}}, \omega; \mathbf{x}_s) = -\frac{2}{\rho i \omega} \frac{\partial}{\partial \tilde{x}_3} g(\tilde{\mathbf{x}}, \omega; \mathbf{x}_s) \quad , \quad (7.16)$$

see Appendix for details. ∂V_0 is a horizontal, open boundary at $x_3 = 0$ bounding the half-space below. Both the focusing location \mathbf{x}_f and the source location \mathbf{x}_s are in this half-space, but \mathbf{x}_s is close to the boundary ∂V_0 (in practice source locations are usually collocated with receivers $\tilde{\mathbf{x}}$). Note that Equation 7.15 only holds true for a very specific type of focusing functions (and thus a specific type of sources $q(\mathbf{x}, \omega)$ in Equation 7.12), i.e. these wavefields $f(\mathbf{x}, \omega; \mathbf{x}_f)$ only propagate between \mathbf{x}_f and ∂V_0 but vanish in other directions of the half-space (Chapter 3). We refer to this as a radiation assumption because we assume focusing functions with a very particular radiation pattern. Equation 7.15 generally relates focusing and Green's functions via the surface reflection data $r(\tilde{\mathbf{x}}, \omega; \mathbf{x}_s)$. In order to use this integral for Green's function retrieval, an additional step is

necessary.

Building on experiences in one-dimensional inverse scattering theory, Wapenaar et al. (2014b) suggested to rewrite Equation 7.15 to

$$-\Theta(\mathbf{x}_s, \omega; \mathbf{x}_f) \star \int_{\tilde{\mathbf{x}} \in \partial V_0} r(\tilde{\mathbf{x}}, \omega; \mathbf{x}_s) f^*(\tilde{\mathbf{x}}, \omega; \mathbf{x}_f) dS = g_{first}(\mathbf{x}_s, \omega; \mathbf{x}_f) + f(\mathbf{x}_s, \omega; \mathbf{x}_f) \quad (7.17)$$

with $\Theta(\mathbf{x}_s, \omega; \mathbf{x}_f)$ being a time-symmetric filter in the time domain, a so-called windowing operator, that mutes everything at $|t| > t_{first}(\mathbf{x}_s; \mathbf{x}_f)$, where $t_{first}(\mathbf{x}_s; \mathbf{x}_f)$ is the first arrival travel time for a source at \mathbf{x}_f and a receiver at \mathbf{x}_s . The symbol \star denotes convolution (along the frequency axis). The first arrival of the Green's function is given by $g_{first}(\mathbf{x}_s, \omega; \mathbf{x}_f) = \Theta(\mathbf{x}_s, \omega; \mathbf{x}_f) \star g(\mathbf{x}_s, \omega; \mathbf{x}_f)$, i.e. the windowing operator removes everything after the first arrival from the Green's function. Note that we assume that the focusing function $f(\mathbf{x}_s, \omega; \mathbf{x}_f)$ remains unchanged by the windowing operator, meaning that the focusing function is supposed to be zero for $|t| > t_{first}(\mathbf{x}_s; \mathbf{x}_f)$. We refer to this as a time-separability assumption because it means that the focusing function and the Green's function appear separated from each other in time (apart from a small overlap at the first arrival of the Green's function). Equation 7.17 is a Marchenko-type integral. In matrix-operator form we can write the Marchenko-type equation as

$$-\Theta \mathbf{R} \mathbf{f}^* = \mathbf{g}_{first} + \mathbf{f} \quad (7.18)$$

and Equation 7.15 as

$$-\mathbf{R} \mathbf{f}^* = \mathbf{g} + \mathbf{f} \quad (7.19)$$

where $-\mathbf{f}^*$ is the focusing function vector, \mathbf{g}_{first} is the vector that contains the first arrivals of the Green's functions and \mathbf{g} is the full Green's function vector. The matrix \mathbf{R} comprises the reflection data, Equation 7.16, as well as a scaling factor for the integration, e.g. multiplication with the spatial sampling interval Δx for a one-dimensional boundary. The matrix Θ accounts for the convolution with the windowing operator.

If both the radiation assumption and the time-separability assumption are met such that Equation 7.18 holds, we can solve Equations 7.18 and 7.19 for the full Green's function \mathbf{g} given the boundary data measurement \mathbf{R} and an estimate of \mathbf{g}_{first} (which also governs the associated first arrival travel times for the construction of the windowing operator Θ) according to

$$\mathbf{g} = \mathbf{g}_{first} + \Lambda \mathbf{R} (\mathbf{I} - \Theta \mathbf{R}^* \Theta \mathbf{R})^{-1} (\mathbf{g}_{first}^* - \Theta \mathbf{R}^* \mathbf{g}_{first}) \quad , \quad (7.20)$$

where $\Lambda = \mathbf{I} - \Theta$, i.e. it mutes all data at $|t| \leq t_{first}(\mathbf{x}_s; \mathbf{x}_f)$, and \mathbf{I} is the identity operator (Chapter 6). Usually, the estimate of the first arrival Green's function \mathbf{g}_{first} is obtained by modelling in a background medium, i.e. a smooth approximation of the actual model. We can either solve Equation 7.20 directly (van der Neut et al., 2015a; Revelo et al., 2022) or approximate it by a truncated Neumann expansion (van der Neut et al., 2015b):

$$\begin{aligned} \mathbf{g} = & \mathbf{g}_{first} + \Lambda \mathbf{R} \mathbf{g}_{first}^* - \Lambda \mathbf{R} \Theta \mathbf{R}^* \mathbf{g}_{first} \\ & + \Lambda \mathbf{R} \Theta \mathbf{R}^* \Theta \mathbf{R} \mathbf{g}_{first}^* - \Lambda \mathbf{R} \Theta \mathbf{R}^* \Theta \mathbf{R} \Theta \mathbf{R}^* \mathbf{g}_{first} + \dots \quad . \end{aligned} \quad (7.21)$$

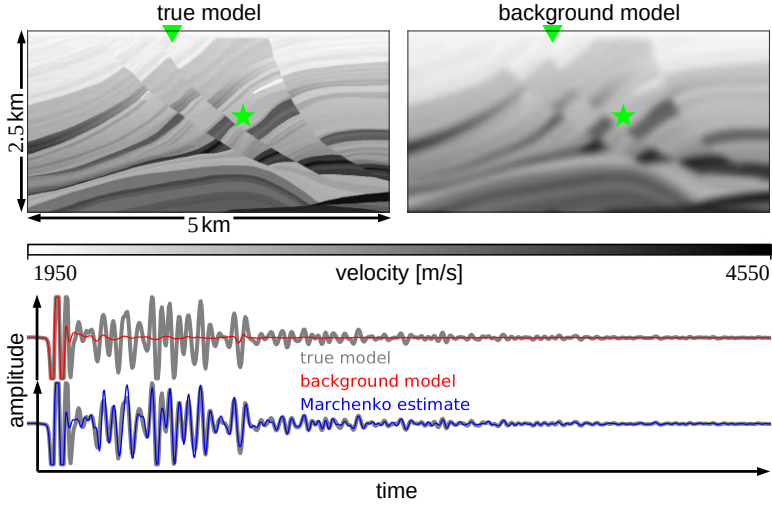


Figure 7.2: True Marmousi model (top left) and smooth background model (top right). Comparison of different Green's functions (bottom): the grey line is the Green's function modelled in the true medium (top left), the red line is the one modelled in the background medium (top right) and the blue one is obtained by using the background medium (top right) in a Marchenko-based Green's function retrieval scheme. All Green's functions are for a source inside the volume (green star) and a receiver at the surface (green triangle). Note that amplitudes at later arrival times are consistently magnified to allow for a good comparison.

For the numerical examples in this paper we use a Neumann expansion that is truncated after the last explicitly given term in Equation 7.21. This rather early truncation ensures a relatively stable Green's function estimation even if our assumptions about radiation and time-separability (and thus the theoretical justification for the Marchenko-type integral) are not perfectly satisfied. This might for instance happen, when dealing with complicated models or when only a poor estimate of the first arrival Green's function is given.

Finally, we illustrate the capability of Marchenko-based Green's function retrieval in Figure 7.2. We compare different Green's function traces for a source inside the volume and a receiver on its surface. We use a slightly modified version of the Marmousi model. Modelling in the true medium delivers various events, see multitude of wiggles, because the wavefield is reflected at the sharp interfaces between different velocity layers, inducing multiple scattering. Modelling in the smooth background medium on the other hand, delivers a very similar first arrival but hardly any multiple scattering. By muting everything after the first arrival of the background Green's function, we obtain an estimate of $\mathbf{g}_{\text{first}}$. Using this estimate along with the consequent window operator Θ and the surface data \mathbf{R} in Equation 7.21 we get the Marchenko-based Green's function. This Green's function is quite similar to the true-model Green's function. Note that we did not need an actual source or receiver inside the true model to obtain this estimate. This demonstrates how we can obtain full Green's functions, i.e. including all orders of scattering, for virtual sources inside of an inaccessible volume from a smooth background

matrix	meaning
\mathbf{G}	Green's function in true model
\mathbf{G}_0	Green's function in background model
\mathbf{G}_0^M	Marchenko-reconstructed Green's function using first arrival in background model
\mathbf{G}^F	first arrival of Green's function in true model
\mathbf{G}^M	Marchenko-reconstructed Green's function using first arrival in true model

Table 7.1: Overview of different Green's function matrices.

kernel	name
$\mathbf{G}_0\mathbf{G}$	reference
$\mathbf{G}_0\mathbf{G}_0$	single-scattering
$\mathbf{G}_0\mathbf{G}_0^M$	Marchenko
$\mathbf{G}_0\mathbf{G}^F$	single-scattering reference
$\mathbf{G}_0\mathbf{G}^M$	Marchenko reference

Table 7.2: Different inversion kernels and their names.

model and surface scattering data.

7.4. SOLVING THE MARCHENKO-LINEARISED LIPPMANN-SCHWINGER INTEGRAL FOR THE SCATTERING POTENTIAL

To this point, we introduced the Lippmann-Schwinger integral and the Marchenko-type integral. In this section, we present the concept of Marchenko-linearised full waveform inversion by sequentially making use of both integrals. We want to stress right away that although we refer to the following procedure as FWI, it is quite similar to LSRTM as well. We will discuss this ambiguity at the end of the section.

Using a Tikhonov regularisation with $\beta \in \mathbb{R}^+$ we can estimate the real-valued scattering potential \mathbf{v} from Equation 7.11 by minimising the objective function

$$s(\mathbf{v}; \beta) = \|\mathbf{M}\mathbf{v} - \mathbf{g}_s\|_2^2 + \beta \|\mathbf{v}\|_2^2 . \quad (7.22)$$

The first term is the residual norm, the second term the solution norm. Note that for our example the scattering potential is given by Equation 7.8 and indeed real-valued. While this does not necessarily imply a real-valued velocity $c(\mathbf{x})$ and therefore a physically reasonable result, it is easy to implement and significantly reduces the model space. The matrix \mathbf{M} denotes the kernel, \mathbf{g}_s the data, i.e. it comes from a measurement. Hence, the objective function depends on the unknown scattering potential \mathbf{v} as well as the regular-

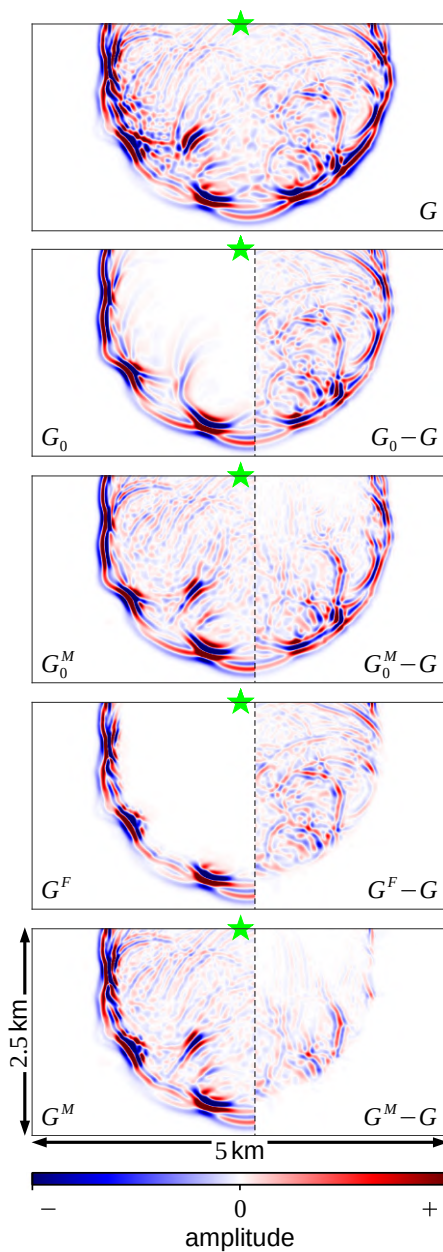


Figure 7.3: Examples of snapshots at 0.8 s for different Green's functions using the true model and the background model as shown in Figure 7.2. The names are analogous to Table 7.1. For the four approximations (second panel to last panel) of G (first panel) the left parts of the panels shows the actual fields, whereas the right parts show the differences. The green stars denote the source location. All fields (Green's functions and wavefield differences) are clipped at the same values for a direct comparison. Note that these clip values are relatively small to enhance the visibility of multiple scattering and wavefield differences.

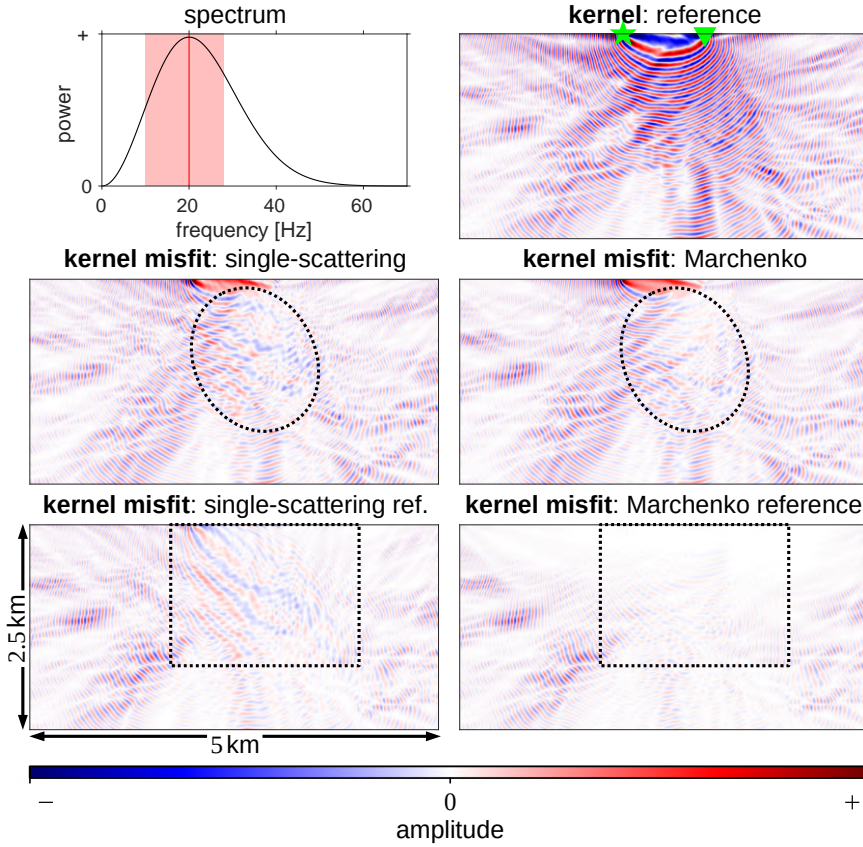


Figure 7.4: Top left: frequency spectrum of the source wavelet (20 Hz Ricker). The red area denotes the frequencies used for inversion, the red line marks 20 Hz, i.e. the frequency for which we analyse the kernels. Real part of the reference kernel (top right). Source and receiver are denoted by the green star and the green triangle, respectively. Real parts of the kernel misfits (lower four panels) for the single-scattering, Marchenko, single-scattering reference and Marchenko reference approximations. All kernels are based on the models in Figure 7.2, kernel names are analogous to Table 7.2. Kernel and kernel misfits are clipped at the same values for a direct comparison. Hence, white colour in a kernel misfit indicates a good approximation. Dashed, black ellipses and rectangles outline areas that are compared in the text.

isation value β . We minimise $s(\mathbf{v}, \beta)$ for a given β by solving the following linear system:

$$\underbrace{\begin{bmatrix} \Re(\mathbf{M}) \\ \Im(\mathbf{M}) \\ \sqrt{\beta}\mathbf{I} \end{bmatrix}}_{\mathbf{Q}} \mathbf{v} = \underbrace{\begin{bmatrix} \Re(\mathbf{g}_s) \\ \Im(\mathbf{g}_s) \\ \mathbf{0} \end{bmatrix}}_{\mathbf{d}}, \quad (7.23)$$

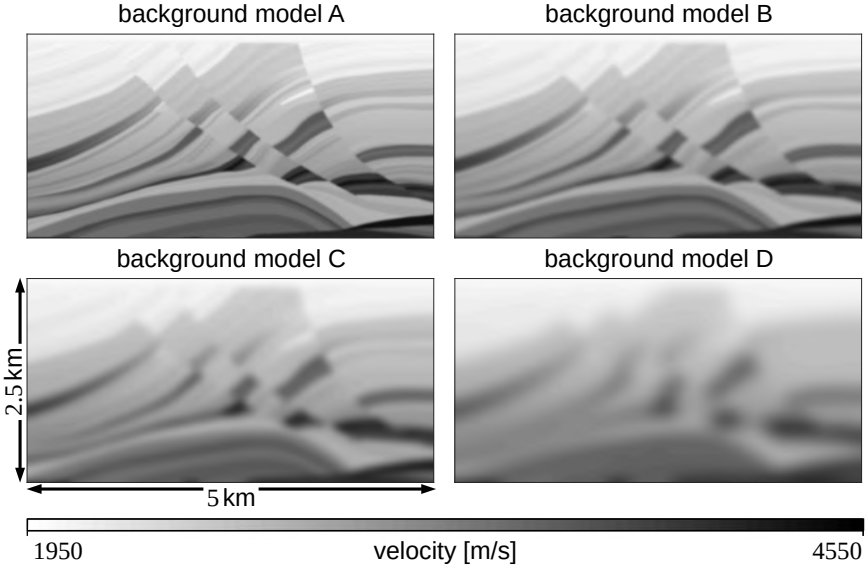


Figure 7.5: Four different background models with increasing smoothness from model A to model D. Background model C is the same as the background model in Figure 7.2.

where $\Re(\mathbf{M})$ and $\Im(\mathbf{M})$ are the real and imaginary parts of the matrix \mathbf{M} , respectively, and $\mathbf{0}$ is a vector full of zeros. The explicit solution consequently is

$$\mathbf{v} = (\mathbf{Q}^\dagger \mathbf{Q})^{-1} (\mathbf{Q}^\dagger \mathbf{d}) \quad , \quad (7.24)$$

where \dagger generally denotes the adjoint but in this case simplifies to the transpose as \mathbf{Q} is real-valued. Since \mathbf{Q} easily becomes very large when looking at multiple sources, receivers and frequencies, we do not explicitly build this matrix. Instead, we use a matrix-free approach to solve Equation 7.23 via LSQR (Paige and Saunders, 1982). We do, however, use a great number of iterations in LSQR to make sure that we converge (within some pre-defined tolerance) to the actual solution in Equation 7.24 if possible.

Apart from the size of the inverse problem, we also have to deal with its non-linearity. In fact, the kernel matrix $\mathbf{M} = \mathbf{G}_0 \mathbf{G}$ used in \mathbf{Q} is usually unknown. This is because we do not have any measurements of the Green's function \mathbf{G} within the volume but only at its surface. Note that we do know \mathbf{G}_0 , i.e. we use modelling in a background model (usually a smooth, tomographic approximation of the actual model) to obtain it.

Conventionally, \mathbf{G} is approximated by \mathbf{G}_0 under the assumption that \mathbf{v} is small, leading the kernel $\mathbf{M} \approx \mathbf{G}_0 \mathbf{G}_0$. This is called the single-scattering approximation, i.e. this kernel is generally able to reproduce primary reflections but all higher order scattering is neglected. This kernel is also at the core of the Born approximation (Born and Wolf, 1999). The Born approximation, however, involves an additional linearisation in order to, e.g., directly invert for the velocity perturbation $c(\mathbf{x}) - c_0(\mathbf{x})$ rather than the scattering potential $v(\mathbf{x})$.

We propose an alternative to the single-scattering approximation. Using the smooth background model, that we would use for the single-scattering approximation, in a Marchenko-based Green's function retrieval scheme we are able to obtain full, i.e. including all orders of scattering, Green's functions $g(\mathbf{x}_s, \omega; \mathbf{x}_f)$ – for sources \mathbf{x}_f anywhere inside the volume and receivers \mathbf{x}_s on the boundary ∂V_0 . By actually stepping through the entire discretised volume, i.e. solving for all \mathbf{x}_f within some bounds, we are able to obtain an estimate of the matrix \mathbf{G} by source-receiver reciprocity, i.e. we get $g(\mathbf{x}_f, \omega; \mathbf{x}_s)$ for all $\mathbf{x}_f \in V$. Obviously, it is an important question how to discretise the volume: with a fine grid the amount of Green's functions that need to be estimated is very high, whereas a coarse grid comes with significantly fewer Green's function estimations but also sets limits to the achievable inversion accuracy in terms of wave number. We will refer to this Marchenko-based Green's function matrix as \mathbf{G}_0^M . It allows for the kernel approximation $\mathbf{M} \approx \mathbf{G}_0 \mathbf{G}_0^M$ which we will call the Marchenko approximation. Although we call it an approximation it is important to note that \mathbf{G}_0^M contains all orders of scattering and is, as we have shown visually in Figure 7.2, very similar to \mathbf{G} even when the respective \mathbf{G}_0 , i.e. the Green's function which is modelled in the same background model that we use for Marchenko, is not. In that sense, this kernel appears to represent the physics significantly better and we are hoping to achieve improved inversion results for \mathbf{v} in terms of reduced artefacts and increased resolution (Diekmann and Vasconcelos, 2020). Note, however, that \mathbf{G}_0^M remains an approximation due to the impact of the first arrival Green's function, which is conventionally approximated by modelling in a background medium, as well as the Marchenko scheme, i.e. the potentially approximate procedure of solving the inverse in Equation 7.20. Additionally, there might be a bias from the Marchenko-type equation itself when the radiation assumption or the time-separability assumption is broken.

Because we want to have a sort of reference kernel for both the single-scattering and the Marchenko approximation we also introduce the wavefields \mathbf{G}^F and \mathbf{G}^M . The Green's functions \mathbf{G}^F are obtained from the actual Green's functions, i.e. modelled in the true medium, by muting everything that arrives after the respective first arrivals. Hence, only the very first event of each Green's function remains. From this we can construct the single-scattering reference kernel $\mathbf{M} \approx \mathbf{G}_0 \mathbf{G}^F$. Note that this is not a representation of what actually happens within the single-scattering framework when \mathbf{v} goes to zero. Instead, we want to use this reference kernel to distinguish between the effects of missing higher order scattering versus having a wrong background model. The matrix \mathbf{G}^M is the Marchenko-based estimate that uses the first arrival of the actual Green's function, i.e. \mathbf{G}^F , rather than the first arrival of the background Green's function. Thus, we can build the Marchenko reference kernel $\mathbf{M} \approx \mathbf{G}_0 \mathbf{G}^M$.

Table 7.1 gives a quick overview of the different Green's function matrices, while Table 7.2 summarises the different kernels and their names.

Figure 7.3 shows exemplary Green's function snapshots for the different scenarios discussed above. The Green's function approximations that use the background model, i.e. \mathbf{G}_0 and \mathbf{G}_0^M , exhibit a distinct error around the first arrival. This is because they are based on a different velocity model, implying different travel times and amplitudes. \mathbf{G}_0^M does, however, recover most of the multiple scattering. The approximations based on the true model on the other hand, i.e. \mathbf{G}^F and \mathbf{G}^M , match the first arrival of the true Green's func-

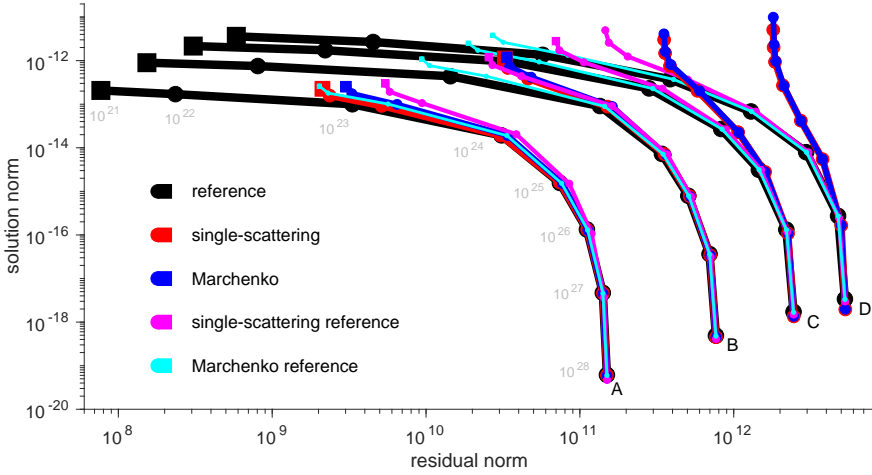


Figure 7.6: L-curves for the four different background models (A, B, C and D from sharpest to smoothest as shown in Figure 7.5) and the five different inversion kernels, see Table 7.2. While kernels can be differentiated by colour, the different background models are marked in the vicinity of the respective first, i.e. highest regularisation value β in Equation 7.22, sample point of each line in the bottom right corner. Note that all L-curves for different kernels start out in the same region for the same background model, but diverge for decreasing regularisation values β towards the top left corner. We use the same eight regularisation values β (from 10^{28} to 10^{21}) to sample all L-curves. Exemplarily, the different β sample points are written into the plot for the lowermost black curve. The residual norm is the first term and the solution norm the second term (without the factor β) in Equation 7.22. Circles denote convergent (for the tolerance and maximum number of iterations as described in the text), squares denote non-convergent inversion runs – the latter only occur for some of the experiments and only for the lowermost regularisation value β . Note that the solution norm is related to a summation over $(c^{-2}(\mathbf{x}) - c_0^{-2}(\mathbf{x}))^2$ for all \mathbf{x} such that its small values are due to the velocity unit being m/s here.

tion. The Marchenko estimate \mathbf{G}^M indeed recovers nearly the entire Green's function with only small errors.

Figure 7.4 shows the frequency spectrum of the source wavelet along with an exemplary reference kernel and the misfits of the respective kernel approximations. All fields are in the frequency domain at 20 Hz. The intricate scattering behaviour of the medium leads to complicated interference patterns within the kernel. As expected, the background-based kernel approximations, i.e. the single-scattering and the Marchenko kernel, exhibit overall larger misfits than the true-model-based approximations, i.e. the single-scattering reference and the Marchenko reference kernel. The Marchenko results, however, are superior to the respective single-scattering results in both cases: the Marchenko kernel matches the reference kernel significantly better in the top central part of the model compared to the single-scattering kernel (see black ellipses) and the Marchenko reference kernel is a close to perfect match in the central model area whereas the single-scattering reference kernel is not (see black rectangles).

We introduced two different ways to linearise the inverse problem of solving Equation 7.23 for \mathbf{v} based on a background model: the single-scattering approximation and the

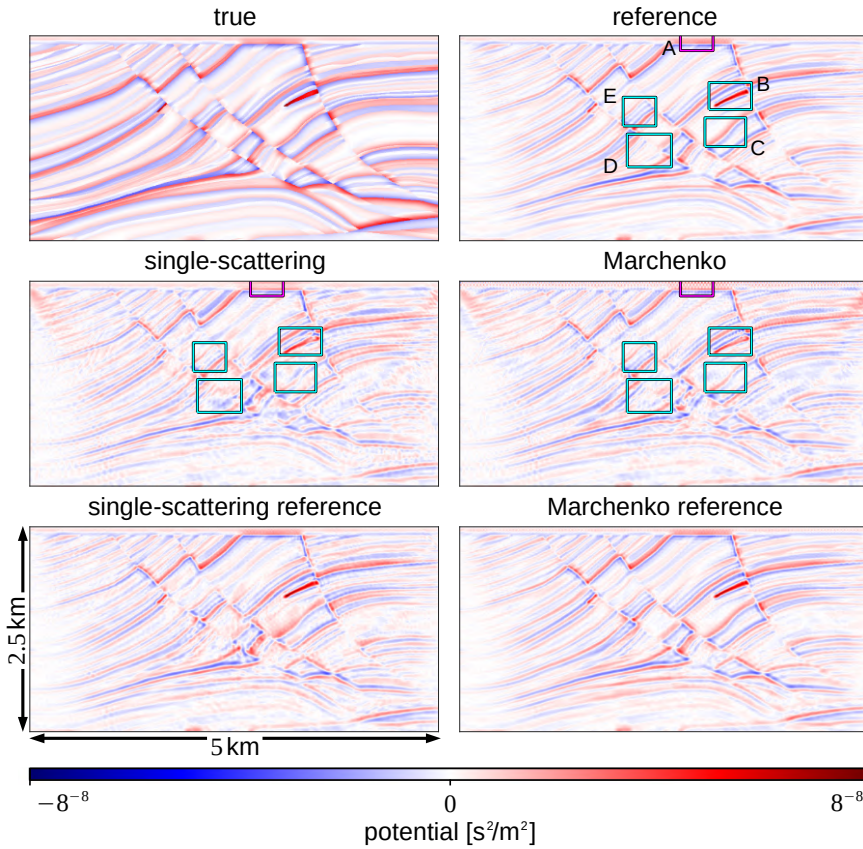


Figure 7.7: Scattering potentials for the true model in Figure 7.2 and background model C, Figure 7.5. The true potential (top left) follows from Equation 7.8. The five inverted potentials are for the different kernels in Table 7.2. All inversion results are for a regularisation parameter $\beta = 10^{22}$. The magenta box denotes artefacts in the Marchenko solution. Cyan boxes denote areas where the Marchenko result is better than the single-scattering result. See Figure 7.8 for zoomed boxes.

Marchenko approximation. The process of using the single-scattering approximation to solve Equation 7.23 is conventionally referred to as least-squares reverse time migration. This is a linear inverse problem and requires a relatively accurate background model. Full waveform inversion, on the other hand, is based on non-linear inversion. It is similar to reverse time migration in that it uses a single-scattering approximation to obtain model updates. However, FWI is an iterative process: it starts with \mathbf{G}_0 from some initial background model and computes a model update based on the single-scattering approximation. Then, the wavefield \mathbf{G}_0 is remodelled in the new, updated medium. From this new \mathbf{G}_0 one gets a new model update and so on. In that sense, FWI uses wave-equation modelling and is not solely build on Born modelling, i.e. the single-scattering approximation. In the light of these differences we call our proposed Marchenko-linear-

ised inversion a full waveform inversion strategy because it is not based on a single-scattering approximation or Born modelling. It is, however, a linear inversion strategy and its outcome is a scattering potential, i.e. a perturbation with respect to the background model, rather than a model. We note that our approach can also be used for gradient computations only, i.e. it can be incorporated in a non-linear FWI strategy.

7.5. NUMERICAL EXAMPLES

In this section we show and discuss inversion results for the different kernels in Table 7.2 and various background models, see Figure 7.5. The true model is shown in Figure 7.1. The model space is discretised with an interval step of 5 m in both directions, i.e. x_1 and x_3 . We use a 20 Hz Ricker wavelet, see Figure 7.4, for forward modelling wavefields. The Marchenko-based Green's functions are estimated with a truncated Neumann expan-

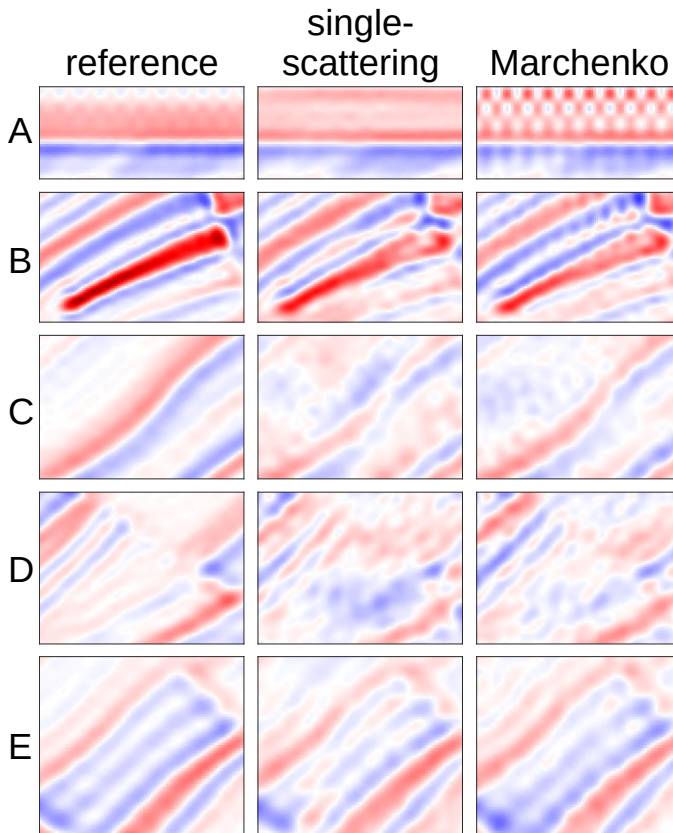


Figure 7.8: Zoomed versions of the highlighted areas in Figure 7.7. The letters A, B, C, D and E refer to the different boxes, see Figure 7.7. We show these zoomed images for the reference kernel, the single-scattering kernel and the Marchenko kernel, see Table 7.2.

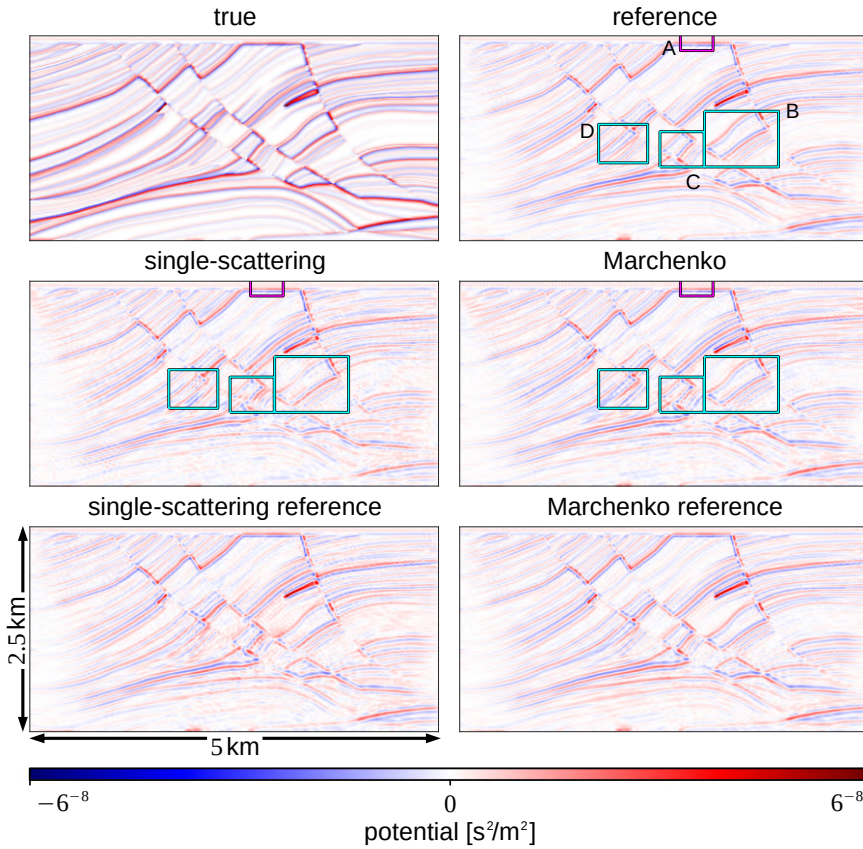


Figure 7.9: Scattering potentials for the true model in Figure 7.2 and background model B, Figure 7.5. The true potential (top left) follows from Equation 7.8. The five inverted potentials are for the different kernels in Table 7.2. All inversion results are for a regularisation parameter $\beta = 10^{22}$. The magenta box denotes artefacts in the Marchenko solution. Cyan boxes denote areas where the Marchenko result is better than the single-scattering result. See Figure 7.10 for zoomed boxes.

sion according to Equation 7.21. To save computation time we estimate these Green's functions on a coarse grid, i.e. with a 20 m increment, covering the same 2.5 km \times 5 km volume. For the inversions we use 25 frequencies from 10 Hz to 28 Hz with a sampling interval of 0.75 Hz, see again Figure 7.4. The upper limit of 28 Hz is related to the coarse spatial grid on which we estimate the Marchenko-based Green's functions. Assuming a minimum medium velocity of 2000 m/s and a maximum frequency of 28 Hz we get a minimum wavelength of about 71 m. Such a wavefield is therefore sampled more than 2.5 times (in the diagonal grid direction) per wavelength on the coarse grid, allowing for an accurate computation of the volume integral, see Equation 7.6, in the inversion. Including higher frequencies in the inversions would require estimating the Green's functions on a finer grid. For the inversions we use 126 sources and 125 receivers, all located

on the surface of the volume ($x_3 = 0$, i.e. the top boundary) and equally distributed over the 5 km model range. Hence, we have a source at 0 m, a receiver at 20 m, a source at 40 m, a receiver at 60 m and so on. We solve for the respective scattering potentials via LSQR with a tolerance of 10^{-4} and a maximum of 250 iterations for all sources, receivers and frequencies simultaneously. As indicated before, we use LSQR with a MATLAB function handle rather than explicitly defining the matrix \mathbf{M} in Equation 7.11 – for double-precision variables in our scenario this matrix \mathbf{M} would consume nearly 200 GB of memory.

In order to analyse the quality of different inversion strategies, i.e. for various kernels and background models, we propose to look at the L-curves in Figure 7.6. An L-curve is obtained by solving Equation 7.24 for different values of β (the kernel \mathbf{M} and data \mathbf{g}_s are fixed of course). Conventionally, an L-curve is used to determine the optimal regularisation value β . However, it also carries information on the general behaviour of the respective inverse problem, i.e. on how ill- or well-posed it is. Note that we use LSQR to mimic the L-curves, i.e. our L-curves will be less divergent for small regularisation values. We stress that we use noise-free data. However, all the kernels that we investigate (with the exception of the reference kernel) are approximative and we investigate their L-curves as a measure of how ill- or well-posed the respective inverse problems become. For instance, we find that at large regularisation values β the type of kernel used in our inversion does not matter very much: all kernels lead similar results for a large value of β and this is true for all background models, see Figure 7.6. Note that we do not actually look at the inverted scattering potentials here but only at the respective residual norms and solution norms. Hence, coinciding L-curves do not imply identical models, however, they imply models of similar quality (as measured by our objective function). We stress here that this quality comparison is not perfectly accurate because we are using different kernels, i.e. the residual norms are computed in different ways.

As we go to lower regularisation values, we observe different results depending on the kernel and background model. For all background models, the reference kernel performs much better than any of the four approximated kernels. Even for low regularisation values it delivers reasonable results with relatively small solution norms. This means that we require a small regularisation for the inverse problem using the reference kernel because it accurately represents the physics that governed the data, while we need a high regularisation for, e.g., the single-scattering kernel which is inconsistent with the physics underlying the data.

For a bad background model, i.e. a smooth estimate similar to model D, we observe that the single-scattering and the Marchenko kernel lead to similar results. The single-scattering reference kernel delivers a much better L-curve, but the Marchenko reference kernel is clearly the best approximation. We can interpret this as follows: using the Marchenko-based Green's functions from a smooth background model does not lead to a significantly improved kernel compared to the conventional single-scattering kernel – at least in terms of model quality. Even though the Marchenko kernel contains all orders of scattering, it is fundamentally relying on the background model: travel times and amplitudes are therefore not accurate enough to enable a beneficial linearisation of the Lippmann-Schwinger integral. This limitation is, however, primarily related to our prior knowledge (the background model), not to the Marchenko scheme itself. This can

be seen by the good Marchenko reference result. While it is not perfect (due to, e.g., the limited measurement aperture and the early truncation of the Neumann series) it apparently represents a fairly good approximation – even for such a complicated model as Marmousi. Note that the single-scattering reference kernel is not as successful, i.e. the Marchenko-based retrieval of multiply scattered events in the Green’s functions is essential.

For a good background model, i.e. an estimate that is close to the true model (like background model A), the four approximated kernels generally perform comparably well. The single-scattering reference kernel is slightly worse, missing multiple scattering that is included in the Marchenko kernels and, for a sharp background model, even in the single-scattering kernel.

Figure 7.7 shows inverted scattering potentials for background model C and $\beta = 10^{22}$, i.e. the penultimate β value. The reference result is quite close to the true potential. It is, however, significantly smoother. This is because we solve for the scattering potentials on the coarse grid (20 m sampling interval). Given the L-curve, see Figure 7.6, it seems as if going to even smaller β values (beyond our last sample point at $\beta = 10^{21}$) might further push the quality of the inverted scattering potential for the reference kernel. Both the single-scattering and the Marchenko result contain a significant amount of artefacts. The Marchenko result contains high-frequency noise near the surface that is not present in the single-scattering result, see magenta box A for strongest artefacts in Figures 7.7 and 7.8. These are potentially related to the unphysical combination of the background-model-consistent arrival times/amplitudes and the Marchenko-recovered multiple scattering – ultimately this leads a Green’s function in the Marchenko kernel that is neither consistent with the true model nor with the background model. On the other hand, it seems that the Marchenko result is slightly better in several areas of the model, see cyan boxes in Figure 7.7. For zoomed versions of the boxes see Figure 7.8. Several interfaces appear to be disrupted in the single-scattering solution while they are continuous in the Marchenko and the reference result. When comparing the single-scattering reference and the Marchenko reference result, we observe that the latter is close to perfect, i.e. it is very similar to the reference solution, while the single-scattering reference solution is still prone to artefacts.

Figure 7.9 shows scattering potentials for background model B. As before, we present the true potential and the results for the five kernels in Table 7.2 for $\beta = 10^{22}$. Owing to the sharper background model, the scattering potential is overall lower than in the previous example. The general observations, however, are the same. There are still some high-frequency artefacts in the Marchenko solution, but they are less distinct than before, see box A. The Marchenko result is slightly better than the single-scattering result, see boxes B, C and D in Figures 7.9 and 7.10. The Marchenko reference result is a nearly perfect match of the reference potential and better than the single-scattering reference.

These examples demonstrate that even though the single-scattering kernel and the Marchenko kernel deliver similar-quality results in terms of residual norms and solution norms in Figure 7.6, the actual scattering potentials are different: the Marchenko kernel is slightly superior in recovering the medium structures particularly in the central model area, but it is biased by high-frequency noise. As pointed out before, the main issue of the Marchenko kernel is the inherent dependency on the background model:

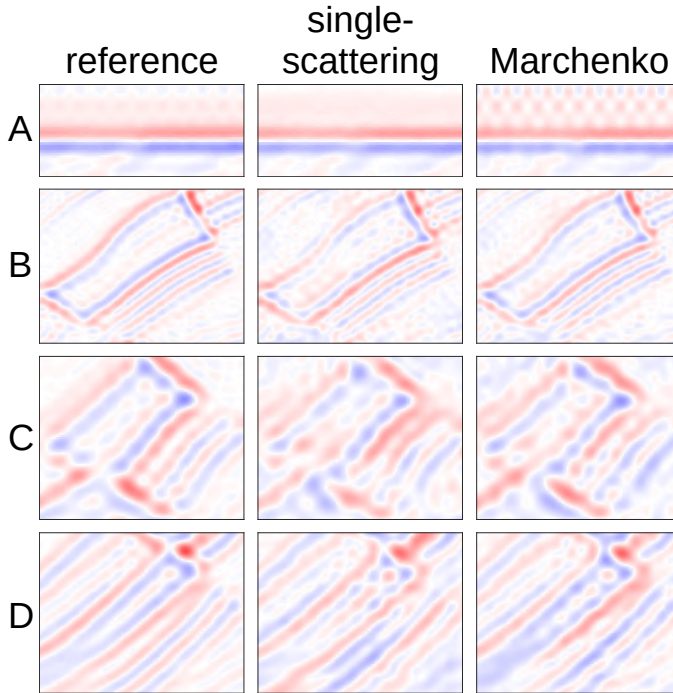


Figure 7.10: Zoomed versions of the highlighted areas in Figure 7.9. The letters A, B, C and D refer to the different boxes, see Figure 7.9. We show these zoomed images for the reference kernel, the single-scattering kernel and the Marchenko kernel, see Table 7.2.

as we do not update the first arrival Green's function in the Marchenko scheme, Equation 7.20, the final Marchenko-based Green's function becomes a sort of hybrid of the background and the true Green's function. The Marchenko reference kernel on the other hand delivers a nearly perfect result and performs significantly better than the single-scattering reference kernel – hence, including multiple scattering in the kernel generally adds considerably to the quality of the inverted potential.

7.6. DISCUSSION

We introduced an approach for Marchenko-linearised full waveform inversion. We refer to the method as full waveform inversion rather than least-squares migration because it is not based on a single-scattering approximation. Instead, the linearisation of the inverse problem is based on replacing the unknown Green's functions inside the Lippmann-Schwinger integral by Marchenko-based Green's functions. These Marchenko-based Green's functions contain all orders of scattering. They require reflection data on the surface and an estimate of the first arrival of the Green's function, e.g. from modelling in a background medium – they do, however, not rely on sharp medium contrasts in the background model to induce the scattered waves. The quality of the Marchenko-

based Green's functions appears to be quite good, see Figure 7.3, and the respective Marchenko kernel is a better approximation than the single-scattering kernel, see Figure 7.4.

The numerical examples show that the Marchenko kernel tends to deliver a slightly better scattering potential than the single-scattering approximation when comparing the inverted results, but the kernels generally deliver models of similar quality, see L-curves in Figure 7.6. The good quality of the Marchenko reference solution indicates that the errors in the Marchenko result are not due to the underlying Marchenko scheme, but due to the prior information on the first arrival of the Green's function. Using a smooth background model inevitably leads to a wrong first arrival of the Green's function in terms of arrival times and amplitudes – an error that is currently not compensated for in the Marchenko scheme. These errors lead to a Marchenko-based Green's function that includes multiple scattering (as if being related to a sharp model) but that is also consistent with the smooth background model in terms of the first arrival. Note that the Marchenko kernel $\mathbf{G}_0\mathbf{G}_0^M$ is an approximation due to the underlying background model, while the Marchenko reference kernel $\mathbf{G}_0\mathbf{G}^M$ is exact if all underlying assumptions (regarding, e.g., the radiation and time-separability of focusing functions in the Marchenko scheme) are met. Including multiples in the kernel generally leads to better results – this is also true when comparing the Marchenko reference and the single-scattering reference solutions. Brogini et al. (2014) used Marchenko-derived Green's functions for imaging via multi-dimensional deconvolution. This approach appears to have the benefit of suppressing artefacts from first arrival Green's function errors by further relying on the data domain rather than going to the model domain and using a wave equation, as done in our study. The fact that Marchenko-linearised full waveform inversion is strongly depending on the first arrival estimate of the Green's function makes it hard to exploit the full potential of Marchenko-based Green's function retrieval. For strongly scattering, high-impedance media we would expect Marchenko-based imaging to be significantly superior to Born-based approaches. These media, however, usually imply larger errors in the first arrival Green's functions due to, e.g., modelling in a background model that smooths over strong contrasts in the true medium and are consequently hard to image via Marchenko-linearised full waveform inversion.

We do not argue that our Marchenko-linearised full waveform inversion is in any way better than full waveform inversion or least-squares reverse time migration. The aim of this paper is first and foremost to study and illustrate the possibilities and limits of such a Marchenko-linearisation. We showed how the Marchenko method can be connected to conventional imaging workflows like FWI and LSRTM and hope that this might pave the way for future imaging techniques. The current Marchenko-linearised inversion workflow is computationally expensive. This is, as indicated earlier, because we wanted to compare different inversion kernels under optimal circumstances. One might of course develop more elaborate schemes. We used an early truncation of the Neumann series to approximate the Green's functions via Equation 7.21. This generally leads to relatively stable results and saves a significant amount of computation time as these Green's functions have to be estimated for all points in the volume. However, this early truncation might, especially for a good background model, not deliver the optimal Green's function estimate. Hence, further optimising our approach may not only make it computation-

ally cheaper but also more accurate. This could allow for iterating the process we described, i.e. get new Marchenko-based Green's functions using the inverted velocities as a background model and invert for a new, updated model - similar to (non-linear) full waveform inversion.

Generally, it seems that a parallel approach of combining the Marchenko scheme and full waveform inversion might indeed be desirable. Currently, we combine them in a sequential fashion: first we solve for the Marchenko-based Green's functions, then we invert for the scattering potential. This comes with the issue of the Marchenko-based Green's functions being physically inconsistent (containing features of both the background and the sharp, scattering model). As we saw in this study, the Marchenko equation itself generally performs quite well even for a complicated model like Marmousi, see good inversion results for Marchenko reference kernels in Figures 7.7 and 7.9. If we could solve both problems simultaneously we might therefore further benefit from the constraining quality of the Marchenko equation in full waveform inversion.

In this study we assumed to have unknown velocities and, for simplicity, a constant density. However, the density could in fact be arbitrarily heterogeneous in our scheme as long as it is known. Our Marchenko-linearised full waveform inversion might also be interesting in the opposite scenario, i.e. for known velocity and unknown density. Actually, this would imply better knowledge of the first arrival of the Green's function since we would only expect amplitude errors but have correct arrival times. Hence, the Marchenko kernel might perform even better when inverting for density than it did in the examples we presented in this paper, potentially leading to less artefacts and better resolution.

In general, Marchenko-based Green's function retrieval also allows for the following strategy: rather than using the retrieved Green's functions solely in the kernel, i.e. to linearise the inverse problem as discussed above, we can use them as additional data. In particular this means that we can put virtual receivers at every grid point of the volume under investigation. If we have a single source and a single frequency but we have receivers covering the entire volume, Equation 7.24 actually becomes exact – assuming that we know the Green's function perfectly, that we sample the volume at a sufficiently fine grid with respect to the investigated frequencies and that there are no scattering perturbations outside the volume (Diekmann and Vasconcelos, 2020). Or one could use the wave equation to directly invert for the medium properties, similar to seismic gradiometry (De Ridder and Curtis, 2017). An exact inverse problem implies that we can retrieve the model with perfect resolution and accuracy. If, however, we use a coarse grid or the Green's functions are slightly biased, the result will be distorted by artefacts. As we discussed earlier, the accuracy of Marchenko-based Green's functions is inherently limited by the prior knowledge of the first arrival Green's functions. Overall, this approach of using Marchenko wavefields as data in the inversion appears to be prone to artefacts and does, in our experience, not lead to beneficial results. This strategy might, however, work better for density inversion or when incorporated advantageously in a parallel Marchenko and full waveform inversion scheme.

This paper represents a first step towards using Marchenko methods for improving the kernel of full waveform inversion. These first results underline that using Marchenko-based wavefields rather than a single-scattering assumption can deliver slightly superior

inversion results.

7.7. CONCLUSION

We present a Marchenko-linearised full waveform inversion scheme. While conventional inversion strategies rely on a Born approximation to obtain a model update, our method uses Marchenko-based Green's functions to linearise the inverse problem. We demonstrate how the theory for Marchenko-based Green's function retrieval and gradient computations in full waveform inversion are connected. Marchenko-based Green's functions rely on prior knowledge of the first arrivals of the Green's functions. These first arrivals are usually obtained by modelling in a background medium. Our numerical examples demonstrate that the quality of the first arrivals of the Green's functions is crucial for the success of Marchenko-linearised full waveform inversion. While our scheme delivers slightly better inversion results than the single-scattering approximation when using the same background model, a correct first arrival Green's function allows for near-perfect inversion results. Hence, we illustrate the possibilities and limitations of Marchenko-linearisation and hope that this will help future research in developing efficient and superior imaging methods.

ACKNOWLEDGEMENTS

The authors are very grateful to Roel Snieder, Joost van der Neut, Aydin Shoja, Dominic Cummings and Andrew Curtis for fruitful discussions and feedback. Furthermore, the authors acknowledge the constructive feedback from Kees Wapenaar and Polina Zhelglova that helped to improve this manuscript. Leon Diekmann was financially supported by the Utrecht Consortium for Subsurface Imaging (UCSI).

APPENDIX

In this section we demonstrate how both the Lippmann-Schwinger integral as well as the Marchenko-type integral are related to Rayleigh's reciprocity theorem.

RAYLEIGH'S RECIPROCITY THEOREM

Rayleigh's reciprocity theorem for acoustic waves reads (Fokkema and van den Berg, 1993; Vasconcelos et al., 2009)

$$\begin{aligned}
 & \int_{\tilde{\mathbf{x}} \in \partial V} (u^A \mathbf{v}^B - u^B \mathbf{v}^A) \cdot d\mathbf{S} \\
 &= \int_{\mathbf{x} \in V} \mathbf{f}^A \cdot \mathbf{v}^B + s^B u^A - \mathbf{f}^B \cdot \mathbf{v}^A - s^A u^B dV \\
 &+ \int_{\mathbf{x} \in V} i\omega(\kappa^B - \kappa^A)u^A u^B - i\omega(\rho^B - \rho^A)\mathbf{v}^A \cdot \mathbf{v}^B dV \quad , \quad (7.25)
 \end{aligned}$$

where A and B mark two different wave states. The pressure field is given by $u = u(\mathbf{x}, \omega)$, the particle velocity field by $\mathbf{v} = (v_1, v_2, v_3) = \mathbf{v}(\mathbf{x}, \omega)$. The variable $\mathbf{f} = (f_1, f_2, f_3) = \mathbf{f}(\mathbf{x}, \omega)$ denotes the volume force density source, while $s = s(\mathbf{x}, \omega)$ is the volume injection rate density source. The compressibility is $\kappa = \kappa(\mathbf{x}) = \rho^{-1}(\mathbf{x})c^{-2}(\mathbf{x})$.

LIPPMANN-SCHWINGER INTEGRAL

In order to derive the Lippmann-Schwinger integral from Equation 7.25, we are going to use the following scenario: the density is the same in both wave states, there are no force sources, one state is for the Green's function and the other for the background Green's function, i.e.

$$\rho^A = \rho^B = \rho \quad , \quad (7.26)$$

$$\mathbf{f}^A = \mathbf{f}^B = \mathbf{0} \quad , \quad (7.27)$$

$$s^A = \delta(\mathbf{x} - \mathbf{x}_s) \quad , \quad \kappa^A = \rho^{-1} c^{-2}(\mathbf{x}) \quad , \quad u^A = g(\mathbf{x}, \omega; \mathbf{x}_s) \quad , \quad (7.28)$$

$$s^B = \delta(\mathbf{x} - \mathbf{x}_r) \quad , \quad \kappa^B = \rho^{-1} c_0^{-2}(\mathbf{x}) \quad , \quad u^B = g_0(\mathbf{x}, \omega; \mathbf{x}_r) \quad . \quad (7.29)$$

From Equation 7.27 it follows that $\mathbf{v} = (\rho i\omega)^{-1} \nabla u$. Furthermore, we assume, e.g., Sommerfeld radiation conditions on the boundary ∂V of the volume V such that the left-hand side of Equation 7.25 vanishes. Hence, \mathbf{x}_s and \mathbf{x}_r as well as all perturbations of the model $c(\mathbf{x})$ with respect to the model $c_0(\mathbf{x})$ lie within the bounded volume V . Equation 7.25 then becomes

$$\begin{aligned} 0 &= g(\mathbf{x}_r, \omega; \mathbf{x}_s) - g_0(\mathbf{x}_s, \omega; \mathbf{x}_r) \\ &+ \int_{\mathbf{x} \in V} \frac{i\omega}{\rho} \left(\frac{1}{c_0^2(\mathbf{x})} - \frac{1}{c^2(\mathbf{x})} \right) g(\mathbf{x}, \omega; \mathbf{x}_s) g_0(\mathbf{x}, \omega; \mathbf{x}_r) dV \quad . \end{aligned} \quad (7.30)$$

When using source-receiver reciprocity, that is $g_0(\mathbf{x}_s, \omega; \mathbf{x}_r) = g_0(\mathbf{x}_r, \omega; \mathbf{x}_s)$, this delivers the Lippmann-Schwinger integral, Equation 7.6.

INTEGRAL FORM OF THE HOMOGENEOUS GREEN'S FUNCTION OF THE SECOND KIND

In order to derive a Marchenko-type integral from Equation 7.25, we are going to use the following scenario: both density and velocity are identical in the two wave states, there are no force sources, one state is for the Green's function and one for the homogeneous Green's function of the second kind, i.e.

$$\rho^A = \rho^B = \rho \quad , \quad (7.31)$$

$$\kappa^A = \kappa^B = \rho^{-1} c^{-2}(\mathbf{x}) \quad , \quad (7.32)$$

$$\mathbf{f}^A = \mathbf{f}^B = \mathbf{0} \quad , \quad (7.33)$$

$$s^A = \delta(\mathbf{x} - \mathbf{x}_s) \quad , \quad u^A = g(\mathbf{x}, \omega; \mathbf{x}_s) \quad (7.34)$$

$$s^B = 0 \quad , \quad u^B = g(\mathbf{x}, \omega; \mathbf{x}_f) + f(\mathbf{x}, \omega; \mathbf{x}_f) - f^*(\mathbf{x}, \omega; \mathbf{x}_f) \quad . \quad (7.35)$$

As we consider the same medium in both wave states (same compressibility and density), the second volume integral in Equation 7.25 vanishes. From Equation 7.33 we get $\mathbf{v} = (\rho i\omega)^{-1} \nabla u$. This gives

$$\begin{aligned} \frac{1}{\rho i\omega} \int_{\tilde{\mathbf{x}} \in \partial V} (g(\tilde{\mathbf{x}}, \omega; \mathbf{x}_s) \nabla u^B - u^B \nabla g(\tilde{\mathbf{x}}, \omega; \mathbf{x}_s)) \cdot d\mathbf{S} = \\ -(g(\mathbf{x}_s, \omega; \mathbf{x}_f) + f(\mathbf{x}_s, \omega; \mathbf{x}_f) - f^*(\mathbf{x}_s, \omega; \mathbf{x}_f)) \quad . \end{aligned} \quad (7.36)$$

While $g(\tilde{\mathbf{x}}, \omega; \mathbf{x}_s)$ is a purely causal (out-going) wavefield with respect to the volume V for \mathbf{x}_s in V , u^B contains both causal, i.e. $u_{out}^B = g(\tilde{\mathbf{x}}, \omega; \mathbf{x}_f) + f(\tilde{\mathbf{x}}, \omega; \mathbf{x}_f)$, and anti-causal (in-coming), i.e. $u_{in}^B = -f^*(\tilde{\mathbf{x}}, \omega; \mathbf{x}_f)$, contributions for \mathbf{x}_f in V . Using, e.g., a far-field approximation (Schuster, 2009) we find that $g(\tilde{\mathbf{x}}, \omega; \mathbf{x}_s) \nabla u_{out}^B = u_{out}^B \nabla g(\tilde{\mathbf{x}}, \omega; \mathbf{x}_s)$ and $g(\tilde{\mathbf{x}}, \omega; \mathbf{x}_s) \nabla u_{in}^B = -u_{in}^B \nabla g(\tilde{\mathbf{x}}, \omega; \mathbf{x}_s)$ leading to

$$\begin{aligned} & \frac{2}{\rho i \omega} \int_{\tilde{\mathbf{x}} \in \partial V} f^*(\tilde{\mathbf{x}}, \omega; \mathbf{x}_f) \nabla g(\tilde{\mathbf{x}}, \omega; \mathbf{x}_s) \cdot d\mathbf{S} = \\ & -\left(g(\mathbf{x}_s, \omega; \mathbf{x}_f) + f(\mathbf{x}_s, \omega; \mathbf{x}_f) - f^*(\mathbf{x}_s, \omega; \mathbf{x}_f)\right) . \end{aligned} \quad (7.37)$$

If \mathbf{x}_s is close to the boundary ∂V , above equation will only reconstruct the out-going portion of the wavefield u^B on the right-hand side:

$$\begin{aligned} & -\frac{2}{\rho i \omega} \int_{\tilde{\mathbf{x}} \in \partial V} f^*(\tilde{\mathbf{x}}, \omega; \mathbf{x}_f) \nabla g(\tilde{\mathbf{x}}, \omega; \mathbf{x}_s) \cdot d\mathbf{S} = \\ & g(\mathbf{x}_s, \omega; \mathbf{x}_f) + f(\mathbf{x}_s, \omega; \mathbf{x}_f) . \end{aligned} \quad (7.38)$$

Finally, we split the boundary ∂V into two parts: a horizontal boundary ∂V_0 at $x_3 = 0$ and a half-sphere below, i.e. for $x_3 > 0$ and a downwards-pointing x_3 -axis. Assuming that the focusing function $-f^*(\mathbf{x}, \omega; \mathbf{x}_f)$ vanishes for all $\mathbf{x} \in \partial V_1$, we only keep the integral over ∂V_0 . Note that this requires very particular sources $q(\mathbf{x}, \omega)$ in Equation 7.12, but we will not explicitly write this dependency here in the arguments of the focusing function. Using these additional assumptions in Equation 7.38 gives Equation 7.15.

CONCLUSION AND OUTLOOK

We present and discuss several topics in this thesis, touching on wavefield focusing, inverse scattering theory, numerical modelling and imaging. Our key contributions, on which the title of this thesis is based, can be summarised as follows:

- **Generalisation of Marchenko-type focusing functions**

We present a new derivation for the Marchenko integral that is based on partial differential equations for focusing functions. Our partial-differential-equation framework generalises the concept of previously introduced Marchenko-type focusing functions. Furthermore, it allows for generalising the homogeneous Green's function. Based on this new set of equations we can use conventional seismic interferometry to obtain Marchenko-like integrals for arbitrary boundary configurations. We discuss this particularly in Chapters 3 and 6. Chapter 3 focusses on the derivation of the Marchenko integral and the justification/illustration of underlying assumptions. Chapter 6 concentrates on using this newly derived integral for Green's function retrieval. In particular, we investigate the accuracy of the retrievable Green's functions in terms of different wave types and varying a priori model information. We can retrieve the full spectrum Green's functions, including refracted and evanescent waves, but the accuracy of the fields heavily depends on our prior knowledge.

- **Modelling of Marchenko-type focusing functions**

We exploit our focusing framework to investigate the limitations of Marchenko-type integrals by modelling focusing functions. We develop different strategies for their numerical modelling. Starting with a rather cumbersome, proof-of-concept approach for 1D in Chapter 3, we then present a one-step modelling scheme for 1D in Chapter 4. Ultimately, we present a method based on inverse source design for modelling Marchenko-type focusing functions in 2D and 3D in Chapter 5. By modelling Marchenko-type focusing functions based on our partial differential equations, one ensures to obtain wavefields that are consistent with all underlying wave physics. Thus, these modelled focusing functions can be used to study and understand the limitations of the Marchenko integral in multiple dimensions, see Chapter 5. Our studies suggest that Marchenko-like integrals are inherently

approximate when regarding scattering problems in more than one dimension. Depending on the complexity of the medium, however, they can be very good approximations.

- **Imaging with Marchenko-type focusing functions**

We present a new strategy for linearising the Lippmann-Schwinger integral. This integral is used for imaging and conventionally linearised by a single-scattering approximation. We propose to use Marchenko-derived Green's functions within the Lippmann-Schwinger integral – a natural linearisation. The accuracy of this linearisation depends on the accuracy of the retrieved Green's functions. We investigate this with numerical examples and compare outcomes from different linearisation strategies in Chapter 7. Overall, our Marchenko-linearised approach performs slightly better than the single-scattering linearisation.

While we hope that this thesis answers some questions, several questions are only answered partially and new ones are posed. In these last paragraphs we want to briefly discuss some of these remaining/new questions and associated topics for future research.

- **How accurate is the Marchenko integral in arbitrarily heterogeneous 2D and 3D media?**

In both Chapters 6 and 7 we use the matrix-operator form of the integral representation that relates focusing and Green's functions via the single-sided reflection response:

$$-\mathbf{R}\mathbf{f}^* = \mathbf{g} + \mathbf{f} \quad , \quad (8.1)$$

compare Equations 6.21 and 7.19. We can rewrite this as a linear equation

$$\underbrace{\left(\begin{array}{cc} \mathbf{I} & \mathbf{0} \\ \mathbf{0} & \mathbf{I} \end{array} - \begin{array}{cc} \Re(\mathbf{R}) & \Im(\mathbf{R}) \\ \Im(\mathbf{R}) & -\Re(\mathbf{R}) \end{array} \right)}_{\mathbf{V}} \underbrace{\begin{bmatrix} \Re(\mathbf{f}) \\ \Im(\mathbf{f}) \end{bmatrix}}_{\mathbf{f}} = \underbrace{\begin{bmatrix} \Re(\mathbf{g}) \\ \Im(\mathbf{g}) \end{bmatrix}}_{\mathbf{g}} \quad , \quad (8.2)$$

where \Re and \Im denote the real and imaginary part and \mathbf{I} is the identity matrix. Given the reflection data \mathbf{R} and the Green's function \mathbf{g} , we can use $\mathbf{f} = \mathbf{V}^{-1}\mathbf{g}$ to compute what is often referred to as the *true* Marchenko-type focusing function (Vargas et al., 2021).

We discuss in, e.g., Chapter 3 that there is one key ingredient in deriving Equation 8.1 from the homogeneous Green's function of the second kind: the focusing function has to vanish on the boundary ∂V_1 . In other words, the focusing function obeys a special radiation condition which only allows energy to propagate towards the integration surface ∂V_0 . In Chapter 5 we demonstrate how to accurately model these *true* Marchenko-type focusing functions within our framework. However, these focusing functions are not identical to those that follow from $\mathbf{f} = \mathbf{V}^{-1}\mathbf{g}$. This is because the focusing functions we model in Chapter 5 obey our partial differential equation for focusing functions but they only approximate the radiation condition, i.e. the focusing functions only vanish approximately on ∂V_1 . Conversely, using $\mathbf{f} = \mathbf{V}^{-1}\mathbf{g}$ to estimate focusing functions enforces the radiation condition but

only approximates our wave equation for focusing functions. In that sense, the latter approach, via the inversion, does not actually deliver accurate wavefield focusing when injecting these focusing functions into the medium. The integral that underlies their computation (Equation 8.1) is only an approximation but solved exactly via $\underline{\mathbf{f}} = \mathbf{V}^{-1}\underline{\mathbf{g}}$.

This means that even if we were able to solve the Marchenko integral perfectly, which would lead to the same focusing function as $\underline{\mathbf{f}} = \mathbf{V}^{-1}\underline{\mathbf{g}}$, this would only be an approximation of the actual focusing function (regarding 2D and 3D scattering problems).

On top of this approximation, i.e. that solving the Marchenko integral implies a radiation condition that is only approximately true, we usually get a bias by enforcing separability of focusing and Green's functions. This separability condition is crucial if we seek to solve Equation 8.1 but we know neither $\underline{\mathbf{g}}$ nor $\underline{\mathbf{f}}$, see Chapter 6, and it is what transforms Equation 8.1 to the Marchenko integral. However, numerical studies suggest that this separability is not a realistic assumption for complicated 2D and 3D models (Vargas et al., 2021).

Furthermore, we need an estimate of the first arrival of the Green's function when using the separability constraint. Then, we can use this first arrival to estimate the focusing function. This focusing function then delivers an estimate of the Green's function. However, the first arrival of the Green's function is usually only known approximately, e.g. by modelling in a smooth estimate of the medium. Hence, it is biased by wrong velocities, leading to erroneous travel times and amplitudes in the first arrival of the Green's function.

Overall, there are many things that reduce the quality of Marchenko-based Green's functions. Nonetheless, numerical studies show that the results are often good approximations (Wapenaar et al., 2014b). If we are interested in a structural image, the quality of these Green's functions might be sufficient (Broggini et al., 2014). If we are interested in true-amplitude imaging or model building, these Green's functions appear to not be good enough, compare Chapter 7.

Hence, it would be desirable to try and increase the quality of Marchenko-based Green's functions. In that context we think that further studies of Marchenko-type focusing functions in heterogeneous media could be helpful. Using the inverse source design approach (Chapter 6) might be a helpful tool for gaining further insights. Additionally, one might be able to combine conventional Marchenko-based Green's function retrieval with wave equation constraints – involving our new partial-differential-equation framework.

- **Are there alternative strategies for combining full waveform inversion and the Marchenko integral?**

In Chapter 7 we presented an imaging approach that combines concepts of full waveform inversion and the Marchenko integral. This appears to be useful as the Marchenko integral allows for a correct allocation of primaries and multiples in the data, suppressing conventional imaging artefacts by naturally linearising the inverse problem. However, we find that this linearised Lippmann-Schwinger approach relies heavily on the quality of the Marchenko-based Green's functions.

Thus, we presume that a non-sequential or a non-linear scheme might be more appropriate. Non-sequential refers to an approach that tries to solve both the Marchenko integral and the Lippmann-Schwinger integral simultaneously rather than solving them one after another as in our current approach. A non-linear implementation could use our Marchenko-linearised Lippmann-Schwinger integral to get an update and then repeat the process rather than stopping after one iteration – similar to conventional, non-linear full waveform inversion.

Another potentially interesting research direction could be the use of Marchenko-based Green's functions in a non-linear, non-sequential version of gradiometry (De Ridder and Curtis, 2017). In gradiometry we can use the retrieved Green's functions and their derivatives directly in a wave equation to estimate the physical medium properties. This is a local problem, meaning that a local estimate of a wavefield and its derivatives is sufficient to estimate the local medium properties. This is fundamentally different to using the Lippmann-Schwinger integral, which, due to the volume integral, is global: you need to know the wavefield in the entire volume to be able to invert for medium properties. Therefore, gradiometry is computationally much cheaper. It is also a largely overdetermined problem, because the wavefield for a single frequency should in theory be enough to determine the medium's wave speed via the Helmholtz equation. However, we found that a simple linear gradiometry with Marchenko-based Green's functions is not successful – due to the deficient quality of the retrieved Green's functions. In accordance with our previous discussion, one might have to think about non-linear, non-sequential strategies. For instance one might have to solve for Marchenko-based Green's functions in some neighbourhood to get a local wavefield and its derivatives and then plug these into the wave equation. This might give an update on the model, such that the process can be repeated until convergence. Working through a medium from top to bottom, meaning starting at the surface where there might be better constraints on physical parameters and going deeper step by step, could be a beneficial strategy here.

- **Can we use the Marchenko integral directly for model building?**

When retrieving Green's functions via the Marchenko integral we rely on a background model to estimate the first arrival Green's functions as well as the mask Θ , see Chapter 6. We found that the quality of the background model strongly affects the quality of the retrieved Green's functions. We can check this in numerical tests by comparing them with the actual, forward modelled Green's functions. But is there a way to determine whether a Green's function is good or bad without having a reference? Or similarly, whether a focusing function is good or bad? In fact this boils down to the following question: is there an intrinsic quality in the Marchenko integral that can tell us whether the underlying background model is good or bad? Similar to Equation 8.2 we can write the Marchenko integral as

$$\underbrace{\left(- \begin{bmatrix} \mathbf{I} & \mathbf{0} \\ \mathbf{0} & \mathbf{I} \end{bmatrix} - \begin{bmatrix} \mathfrak{R}(\Theta\mathbf{R}) & \mathfrak{I}(\Theta\mathbf{R}) \\ \mathfrak{I}(\Theta\mathbf{R}) & -\mathfrak{R}(\Theta\mathbf{R}) \end{bmatrix} \right)}_{\mathbf{U}} \underbrace{\begin{bmatrix} \mathfrak{R}(\mathbf{f}) \\ \mathfrak{I}(\mathbf{f}) \end{bmatrix}}_{\mathbf{f}} = \underbrace{\begin{bmatrix} \mathfrak{R}(\mathbf{g}_{\text{first}}) \\ \mathfrak{I}(\mathbf{g}_{\text{first}}) \end{bmatrix}}_{\mathbf{g}_{\text{first}}}, \quad (8.3)$$

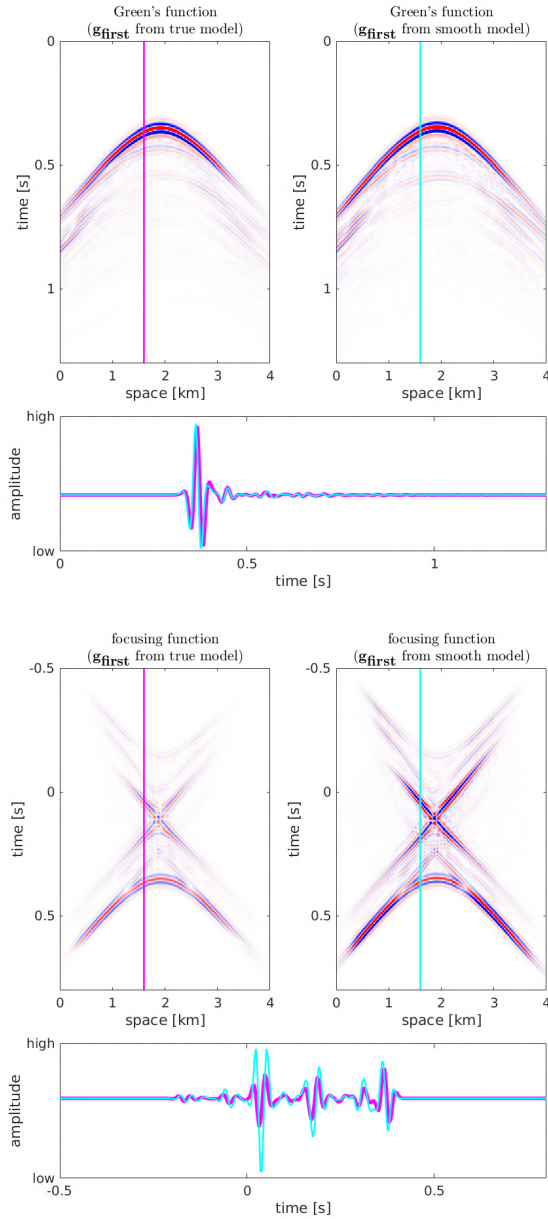


Figure 8.1: Visualising the effect of a wrong (smooth) background model on the estimated Green's function (top three plots) and focusing function (bottom three plots). Both Green's functions and both focusing functions are at the same scale. Magenta and cyan lines indicate the traces at 1.6 km that are additionally plotted for a direct comparison.

where Θ is a convolutional windowing operator, see Equations 6.24 and 7.18. Thus, the focusing function then follows from $\underline{\mathbf{f}} = \mathbf{U}^{-1}\underline{\mathbf{g}}_{\text{first}}$ while the full Green's function follows from $\underline{\mathbf{g}} = \mathbf{V}\mathbf{U}^{-1}\underline{\mathbf{g}}_{\text{first}}$. In our numerical experiments it seems as if Green's functions only change marginally for changing background models. They get shifted due to the biased $\underline{\mathbf{g}}_{\text{first}}$, but the general structure as well as the amplitudes remain relatively stable. This is why we obtain good Green's function estimates even for smooth background models. We demonstrate this effect in Figure 8.1 (top three plots). For these plots we use the model and approach from Chapter 6 (the focusing location is at $x = 1900$ m and $z = 980$ m). Focusing functions on the other hand seem to change much quicker for varying background models. In particular, their amplitudes appear to increase significantly for increasingly smooth/wrong background models, see Figure 8.1. This implies that the inverse of \mathbf{U} might become increasingly unstable if the windowing operator Θ is not consistent with the true velocity model. While this instability cancels out for the Green's function through the multiplication with \mathbf{V} ($\underline{\mathbf{g}} = \mathbf{V}\mathbf{U}^{-1}\underline{\mathbf{g}}_{\text{first}}$), it has a crucial impact on the focusing function. Consequently, we suggest to investigate this relation between the norm of $\underline{\mathbf{f}}$ and the background velocity model used to get the mask Θ . Potentially, this is linked to the ability of the background model to recreate refracted waves in the first arrival Green's function. This observation could be interesting for velocity model building as it involves the whole data, does not require any picking of arrival times and Θ can easily be computed with an Eikonal solver. However, one has to generally verify this observation and translate it to an inverse problem that can be solved efficiently with common optimisation algorithms.

In addition to these questions, there might be other interesting applications of our research. The new intuition and framework for Marchenko-type focusing functions might be stimulating progress in time reversal acoustics. Our theory could also be interesting for source characterisation problems in seismology, where focusing measured data by back-propagation is essential. Inverse source design could be a helpful tool for creating wavefields with other objectives as well. Last but not least, directional source multipoles might have interesting applications in engineering acoustics and could be investigated and validated by laboratory experiments.

BIBLIOGRAPHY

- Agranovich, Z. and Marchenko, V. A. (1963). *The inverse problem of scattering theory*. Gordon and Breach.
- Alkhalifah, T. and Guo, Q. (2019). Subsurface wavefields based on the generalized internal multiple imaging. *Geophysical Journal International*, 219(2):1212–1224.
- Bakulin, A. and Calvert, R. (2006). The virtual source method: Theory and case study. *Geophysics*, 71(4):SI139–SI150.
- Bernard, S., Monteiller, V., Komatitsch, D., and Lasaygues, P. (2017). Ultrasonic computed tomography based on full-waveform inversion for bone quantitative imaging. *Physics in Medicine & Biology*, 62(17):7011.
- Bilbao, S. and Hamilton, B. (2018). Directional sources in wave-based acoustic simulation. *IEEE/ACM Transactions on Audio, Speech, and Language Processing*, 27(2):415–428.
- Boehm, C., Martiartu, N. K., Vinard, N., Balic, I. J., and Fichtner, A. (2018). Time-domain spectral-element ultrasound waveform tomography using a stochastic quasi-Newton method. In *Medical Imaging 2018: Ultrasonic Imaging and Tomography*, volume 10580, page 105800H. International Society for Optics and Photonics.
- Born, M. and Wolf, E. (1999). *Principles of optics: Electromagnetic theory of propagation, interference and diffraction of light*. Elsevier.
- Brackenhoff, J., Thorbecke, J., and Wapenaar, K. (2019a). Monitoring of induced distributed double-couple sources using Marchenko-based virtual receivers. *Solid Earth*, 10(4):1301–1319.
- Brackenhoff, J., Thorbecke, J., and Wapenaar, K. (2019b). Virtual sources and receivers in the real Earth: Considerations for practical applications. *Journal of Geophysical Research: Solid Earth*, 124(11):11802–11821.
- Broggini, F. and Snieder, R. (2012). Connection of scattering principles: A visual and mathematical tour. *European Journal of Physics*, 33(3):593.
- Broggini, F., Snieder, R., and Wapenaar, K. (2012). Focusing the wavefield inside an unknown 1D medium: Beyond seismic interferometry. *Geophysics*, 77(5):A25–A28.
- Broggini, F., Snieder, R., and Wapenaar, K. (2014). Data-driven wavefield focusing and imaging with multidimensional deconvolution: Numerical examples for reflection data with internal multiples. *Geophysics*, 79(3):WA107–WA115.

- Burridge, R. (1980). The Gelfand-Levitan, the Marchenko, and the Gopinath-Sondhi integral equations of inverse scattering theory, regarded in the context of inverse impulse-response problems. *Wave Motion*, 2(4):305–323.
- Chadan, K. and Sabatier, P. C. (2012). *Inverse problems in quantum scattering theory*. Springer Science & Business Media.
- Colton, D. L. and Kress, R. (1998). *Inverse acoustic and electromagnetic scattering theory*, volume 93. Springer.
- Cui, T., Rickett, J., Vasconcelos, I., and Veitch, B. (2020). Target-oriented full-waveform inversion using Marchenko redatumed wavefields. *Geophysical Journal International*, 223(2):792–810.
- Cummings, D. and Curtis, A. (2020). Defining the Green's function derivative for imaging & inversion without the Born approximation. In *EGU General Assembly Conference Abstracts*, page 10804.
- Curtis, A., Gerstoft, P., Sato, H., Snieder, R., and Wapenaar, K. (2006). Seismic interferometry – turning noise into signal. *The Leading Edge*, 25(9):1082–1092.
- Curtis, A. and Halliday, D. (2010). Source-receiver wave field interferometry. *Physical Review E*, 81(4):046601.
- da Costa Filho, C. A., Ravasi, M., Curtis, A., and Meles, G. A. (2014). Elastodynamic Green's function retrieval through single-sided Marchenko inverse scattering. *Physical Review E*, 90(6):063201.
- Dai, W., Fowler, P., and Schuster, G. T. (2012). Multi-source least-squares reverse time migration. *Geophysical Prospecting*, 60(4-Simultaneous Source Methods for Seismic Data):681–695.
- de Hoop, A. T. (1995). *Handbook of radiation and scattering of waves*. Academic Press.
- De Ridder, S. and Curtis, A. (2017). Seismic gradiometry using ambient seismic noise in an anisotropic Earth. *Geophysical Journal International*, 209(2):1168–1179.
- Deift, P. and Trubowitz, E. (1979). Inverse scattering on the line. *Communications on Pure and Applied Mathematics*, 32(2):121–251.
- Diekmann, L., Snieder, R., and Vasconcelos, I. (2023a). Inverse design for directional source multipoles and wavefield focusing. *Physical Review E - under review*.
- Diekmann, L. and Vasconcelos, I. (2020). Imaging with the exact linearised Lippmann-Schwinger integral by means of redatumed in-volume wavefields. In *SEG International Exposition and Annual Meeting*. OnePetro.
- Diekmann, L. and Vasconcelos, I. (2021a). Focusing and Green's function retrieval in three-dimensional inverse scattering revisited: A single-sided Marchenko integral for the full wave field. *Physical Review Research*, 3(1):013206.

- Diekmann, L. and Vasconcelos, I. (2021b). Full-wavefield Marchenko using a generalized framework for focusing functions. In *First International Meeting for Applied Geoscience & Energy*, pages 3311–3315. Society of Exploration Geophysicists.
- Diekmann, L. and Vasconcelos, I. (2023). Direct, wave-equation-based modeling of Marchenko-type focusing functions. *JASA Express Letters*, 3(2):024001.
- Diekmann, L., Vasconcelos, I., Cummings, D., and Curtis, A. (2021). Towards exact linearized full-waveform inversion via Marchenko redatuming. In *First International Meeting for Applied Geoscience & Energy*, pages 3380–3384. Society of Exploration Geophysicists.
- Diekmann, L., Vasconcelos, I., and van Leeuwen, T. (2023b). A note on Marchenko-linearised full waveform inversion for imaging. *Geophysical Journal International*, 234(1):228–242.
- Diekmann, L., Vasconcelos, I., Wapenaar, K., Slob, E., and Snieder, R. (2023c). Wavefield focusing using a generalised, potentially asymmetric homogeneous Green's function. *Wave Motion*, 116:103071.
- Draganov, D., Heller, K., and Ghose, R. (2012). Monitoring CO₂ storage using ghost reflections retrieved from seismic interferometry. *International Journal of Greenhouse Gas Control*, 11:S35–S46.
- Dragoset, B., Verschuur, E., Moore, I., and Bisley, R. (2010). A perspective on 3D surface-related multiple elimination. *Geophysics*, 75(5):75A245–75A261.
- Dukalski, M. and de Vos, K. (2017). Marchenko inversion in a strong scattering regime including surface-related multiples. *Geophysical Journal International*, 212(2):760–776.
- Dukalski, M., Mariani, E., and de Vos, K. (2019). Handling short-period scattering using augmented Marchenko autofocusing. *Geophysical Journal International*, 216(3):2129–2133.
- Elison, P., Dukalski, M., and Van Manen, D. (2021). Quality control of under-constrained Marchenko equation solvers in complex media using reference focusing functions. In *82nd EAGE Annual Conference & Exhibition*, volume 2021, pages 1–5. European Association of Geoscientists & Engineers.
- Elison, P., Dukalski, M. S., De Vos, K., van Manen, D.-J., and Robertsson, J. O. (2020). Data-driven control over short-period internal multiples in media with a horizontally layered overburden. *Geophysical Journal International*, 221(2):769–787.
- Engquist, B. and Majda, A. (1977). Absorbing boundary conditions for numerical simulation of waves. *Proceedings of the National Academy of Sciences*, 74(5):1765–1766.
- Engquist, B. and Yang, Y. (2022). Optimal transport based seismic inversion: Beyond cycle skipping. *Communications on Pure and Applied Mathematics*, 75(10):2201–2244.

- Engquist, B. and Ying, L. (2011). Sweeping preconditioner for the Helmholtz equation: Moving perfectly matched layers. *Multiscale Modeling & Simulation*, 9(2):686–710.
- Etgen, J., Gray, S. H., and Zhang, Y. (2009). An overview of depth imaging in exploration geophysics. *Geophysics*, 74(6):WCA5–WCA17.
- Fink, M. (1992). Time reversal of ultrasonic fields. I. Basic principles. *IEEE Transactions on Ultrasonics, Ferroelectrics, and Frequency Control*, 39(5):555–566.
- Fink, M. (1997). Time reversed acoustics. *Physics Today*, 50(3):34–40.
- Fink, M. (2008). Time-reversal acoustics. In *Journal of Physics: Conference Series*, volume 118, page 012001. IOP Publishing.
- Fishman, L. (1993). One-way wave propagation methods in direct and inverse scalar wave propagation modeling. *Radio Science*, 28(5):865–876.
- Fokkema, J. T. and van den Berg, P. M. (1993). *Seismic applications of acoustic reciprocity*. Elsevier.
- Gajewski, D. and Tessmer, E. (2005). Reverse modelling for seismic event characterization. *Geophysical Journal International*, 163(1):276–284.
- Gray, S. H., Etgen, J., Dellinger, J., and Whitmore, D. (2001). Seismic migration problems and solutions. *Geophysics*, 66(5):1622–1640.
- Groenenboom, J. and Snieder, R. (1995). Attenuation, dispersion, and anisotropy by multiple scattering of transmitted waves through distributions of scatterers. *The Journal of the Acoustical Society of America*, 98(6):3482–3492.
- Grohmann, M., Müller, S., Niederleithinger, E., and Sieber, S. (2017). Reverse time migration: Introducing a new imaging technique for ultrasonic measurements in civil engineering. *Near Surface Geophysics*, 15(3):242–258.
- Guasch, L., Agudo, O. C., Tang, M.-X., Nachev, P., and Warner, M. (2020). Full-waveform inversion imaging of the human brain. *NPJ Digital Medicine*, 3(1):1–12.
- Hajjaj, R. F., de Ridder, S. A., Livermore, P. W., and Ravasi, M. (2022). Wavefield reconstruction inversion modelling of Marchenko focusing functions. *arXiv preprint arXiv:2210.14570*.
- Håkansson, A., Torrent, D., Cervera, F., and Sánchez-Dehesa, J. (2007). Directional acoustic source by scattering acoustical elements. *Applied Physics Letters*, 90(22):224107.
- Hildebrand, J., Wiggins, S., Henkart, P., and Conyers, L. (2002). Comparison of seismic reflection and ground-penetrating radar imaging at the controlled archaeological test site, champaign, illinois. *Archaeological Prospection*, 9(1):9–21.
- Hoskins, P. R., Martin, K., and Thrush, A. (2019). *Diagnostic ultrasound: physics and equipment*. CRC Press.

- Huang, G., Nammour, R., and Symes, W. W. (2018). Volume source-based extended waveform inversion. *Geophysics*, 83(5):R369–R387.
- Joannopoulos, J. D., Villeneuve, P. R., and Fan, S. (1997). Photonic crystals. *Solid State Communications*, 102(2-3):165–173.
- Jost, R. (2012). *Inverse scattering problems in optics*, volume 20. Springer Science & Business Media.
- Kalogeropoulos, A., Van Der Kruk, J., Hugenschmidt, J., Bikowski, J., and Brühwiler, E. (2013). Full-waveform GPR inversion to assess chloride gradients in concrete. *NDT & E International*, 57:74–84.
- Kiraz, M. S., Snieder, R., and Wapenaar, K. (2020). Marchenko focusing without up/down decomposition. In *SEG Technical Program Expanded Abstracts 2020*, pages 3593–3597. Society of Exploration Geophysicists.
- Kiraz, M. S., Snieder, R., and Wapenaar, K. (2021a). Marchenko without up/down decomposition on the Marmousi model and retrieval of the refracted waves: Are they caused by the Marchenko algorithm? In *First International Meeting for Applied Geoscience & Energy*, pages 3280–3284. Society of Exploration Geophysicists.
- Kiraz, M. S. R., Snieder, R., and Wapenaar, K. (2021b). Focusing waves in an unknown medium without wavefield decomposition. *JASA Express Letters*, 1(5):055602.
- Kurt, H., Colak, E., Cakmak, O., Caglayan, H., and Ozbay, E. (2008). The focusing effect of graded index photonic crystals. *Applied Physics Letters*, 93(17):171108.
- Lamb Jr, G. L. (1980). *Elements of soliton theory*. New York.
- Lambert, W., Cobus, L. A., Couade, M., Fink, M., and Aubry, A. (2020). Reflection matrix approach for quantitative imaging of scattering media. *Physical Review X*, 10(2):021048.
- Li, L., Tan, J., Schwarz, B., Staněk, F., Poiata, N., Shi, P., Diekmann, L., Eisner, L., and Gajewski, D. (2020). Recent advances and challenges of waveform-based seismic location methods at multiple scales. *Reviews of Geophysics*, 58(1):e2019RG000667.
- Lippmann, B. A. and Schwinger, J. (1950). Variational principles for scattering processes. I. *Physical Review*, 79(3):469.
- Löer, K., Meles, G. A., Curtis, A., and Vasconcelos, I. (2014). Diffracted and pseudo-physical waves from spatially limited arrays using source–receiver interferometry (SRI). *Geophysical Journal International*, 196(2):1043–1059.
- Malcolm, A. E., Scales, J. A., and van Tiggelen, B. A. (2004). Extracting the Green function from diffuse, equipartitioned waves. *Physical Review E*, 70(1):015601.
- Malcolm, A. E., Ursin, B., and De Hoop, M. V. (2009). Seismic imaging and illumination with internal multiples. *Geophysical Journal International*, 176(3):847–864.

- Marchenko, V. A. (1955). On reconstruction of the potential energy from phases of the scattered waves. In *Doklady Akademii Nauk SSSR*, volume 104, pages 695–698.
- Meles, G. A., Löer, K., Ravasi, M., Curtis, A., and da Costa Filho, C. A. (2015). Internal multiple prediction and removal using Marchenko autofocusing and seismic interferometry. *Geophysics*, 80(1):A7–A11.
- Meles, G. A., Van Der Neut, J., Van Dongen, K. W., and Wapenaar, K. (2019a). Wavefield finite time focusing with reduced spatial exposure. *The Journal of the Acoustical Society of America*, 145(6):3521–3530.
- Meles, G. A., Van Der Neut, J., Van Dongen, K. W., and Wapenaar, K. (2019b). Wavefield focusing with reduced cranial invasiveness. In *2019 IEEE International Ultrasonics Symposium (IUS)*, pages 1851–1854. IEEE.
- Métivier, L., Brossier, R., Merigot, Q., and Oudet, E. (2019). A graph space optimal transport distance as a generalization of Lp distances: Application to a seismic imaging inverse problem. *Inverse Problems*, 35(8):085001.
- Morgan, J., Warner, M., Bell, R., Ashley, J., Barnes, D., Little, R., Roele, K., and Jones, C. (2013). Next-generation seismic experiments: Wide-angle, multi-azimuth, three-dimensional, full-waveform inversion. *Geophysical Journal International*, 195(3):1657–1678.
- Müller, S., Niederleithinger, E., and Bohlen, T. (2012). Reverse time migration: A seismic imaging technique applied to synthetic ultrasonic data. *International Journal of Geophysics*, 2012.
- Newton, R. G. (1980). Inverse scattering. I. One dimension. *Journal of Mathematical Physics*, 21(3):493–505.
- Oristaglio, M. L. (1989). An inverse scattering formula that uses all the data. *Inverse Problems*, 5(6):1097.
- Paige, C. C. and Saunders, M. A. (1982). LSQR: An algorithm for sparse linear equations and sparse least squares. *ACM Transactions on Mathematical Software (TOMS)*, 8(1):43–71.
- Park, Y., Drouard, E., El Daif, O., Letartre, X., Viktorovitch, P., Fave, A., Kaminski, A., Lemiti, M., and Seassal, C. (2009). Absorption enhancement using photonic crystals for silicon thin film solar cells. *Optics Express*, 17(16):14312–14321.
- Peng, H. and Vasconcelos, I. (2019). A study of acquisition-related sub-sampling and aperture effects on Marchenko focusing and redatuming. In *SEG Technical Program Expanded Abstracts 2019*, pages 248–252. Society of Exploration Geophysicists.
- Ratcliffe, A., Win, C., Vinje, V., Conroy, G., Warner, M., Umpleby, A., Stekl, I., Nangoo, T., and Bertrand, A. (2011). Full waveform inversion: A North Sea OBC case study. In *SEG Technical Program Expanded Abstracts 2011*, pages 2384–2388. Society of Exploration Geophysicists.

- Ravasi, M. and Vasconcelos, I. (2020). PyLops - A linear-operator Python library for scalable algebra and optimization. *SoftwareX*, 11:100361.
- Ravasi, M., Vasconcelos, I., Kritski, A., Curtis, A., Filho, C. A. d. C., and Meles, G. A. (2016). Target-oriented Marchenko imaging of a North Sea field. *Geophysical Supplements to the Monthly Notices of the Royal Astronomical Society*, 205(1):99–104.
- Rawlinson, N., Pozgay, S., and Fishwick, S. (2010). Seismic tomography: A window into deep Earth. *Physics of the Earth and Planetary Interiors*, 178(3-4):101–135.
- Rayleigh, J. W. S. (1871). LVIII. On the scattering of light by small particles. *The London, Edinburgh, and Dublin Philosophical Magazine and Journal of Science*, 41(275):447–454.
- Rayleigh, J. W. S. (1894). *The theory of sound*, volume 1. Macmillan.
- Reinicke, C., Dukalski, M., and Wapenaar, K. (2020). Comparison of monotonicity challenges encountered by the inverse scattering series and the Marchenko demultiple method for elastic waves. *Geophysics*, 85(5):Q11–Q26.
- Reinicke, C. and Wapenaar, K. (2019). Elastodynamic single-sided homogeneous Green's function representation: Theory and numerical examples. *Wave Motion*, 89:245–264.
- Revelo, D., De Paula, R., Pestana, R., Santos, R., Barrera, D., and Souza, M. (2022). A least-squares formulation to solve the single-sided Marchenko integral for the full wave field. In *83rd EAGE Annual Conference & Exhibition*, volume 2022, pages 1–5. European Association of Geoscientists & Engineers.
- Ricker, N. (1953). Wavelet contraction, wavelet expansion, and the control of seismic resolution. *Geophysics*, 18(4):769–792.
- Rickett, J. and Claerbout, J. (1999). Acoustic daylight imaging via spectral factorization: Helioseismology and reservoir monitoring. *The Leading Edge*, 18(8):957–960.
- Rose, J. H. (1989). Elastic wave inverse scattering in nondestructive evaluation. In *Scattering and Attenuation of Seismic Waves, Part II*, pages 715–739. Springer.
- Rose, J. H. (2001). 'Single-sided' focusing of the time-dependent Schrödinger equation. *Physical Review A*, 65(1):012707.
- Rose, J. H. (2002a). 'Single-sided' autofocusing of sound in layered materials. *Inverse Problems*, 18(6):1923.
- Rose, J. H. (2002b). Time reversal, focusing and exact inverse scattering. In *Imaging of complex media with acoustic and seismic waves*, pages 97–106. Springer.
- Rutherford, E. (1911). LXXIX. The scattering of α and β particles by matter and the structure of the atom. *The London, Edinburgh, and Dublin Philosophical Magazine and Journal of Science*, 21(125):669–688.

- Sanchis, L., Håkansson, A., López-Zanón, D., Bravo-Abad, J., and Sánchez-Dehesa, J. (2004). Integrated optical devices design by genetic algorithm. *Applied Physics Letters*, 84(22):4460–4462.
- Schuster, G. (2009). *Seismic interferometry*. Cambridge University Press.
- Schwarz, B. (2019). An introduction to seismic diffraction. In *Advances in Geophysics*, volume 60, pages 1–64. Elsevier.
- Shea, J. D., Kosmas, P., Hagness, S. C., and Van Veen, B. D. (2010). Three-dimensional microwave imaging of realistic numerical breast phantoms via a multiple-frequency inverse scattering technique. *Medical Physics*, 37(8):4210–4226.
- Shearer, P. M. (2009). *Introduction to seismology*. Cambridge University Press.
- Shoja, A., van der Neut, J., and Wapenaar, K. (2023). Target-oriented least-squares reverse-time migration using Marchenko double-focusing: Reducing the artefacts caused by overburden multiples. *Geophysical Journal International*, 233(1):13–32.
- Shoja, S., Van der Neut, J., and Wapenaar, K. (2022). Reducing the overburden-related artifacts in target-oriented least-squares migration by Marchenko double-focusing. In *83rd EAGE Annual Conference & Exhibition*, volume 2022, pages 1–5. European Association of Geoscientists & Engineers.
- Shoja, S. A., Meles, G. A., and Wapenaar, K. (2020). A proposal for Marchenko-based target-oriented full waveform inversion. In *82nd EAGE Annual Conference & Exhibition*, volume 2020, pages 1–5. European Association of Geoscientists & Engineers.
- Singh, S. and Snieder, R. (2017). Strategies for imaging with Marchenko-retrieved Green's functions. *Geophysics*, 82(4):Q23–Q37.
- Slob, E., Wapenaar, K., Broggini, F., and Snieder, R. (2014). Seismic reflector imaging using internal multiples with Marchenko-type equations. *Geophysics*, 79(2):S63–S76.
- Slob, E., Wapenaar, K., and Treitel, S. (2020). Tutorial: Unified 1D inversion of the acoustic reflection response. *Geophysical Prospecting*, 68(5):1425–1442.
- Snieder, R. and Tarantola, A. (1989). Imaging of quantum-mechanical potentials. *Physical Review A*, 39(7):3303.
- Snieder, R. and Van Wijk, K. (2015). *A guided tour of mathematical methods for the physical sciences*. Cambridge University Press.
- Snieder, R., Wapenaar, K., and Wegler, U. (2007). Unified Green's function retrieval by cross-correlation; connection with energy principles. *Physical Review E*, 75(3):036103.
- Soupios, P., Georgakopoulos, P., Papadopoulos, N., Saltas, V., Andreadakis, A., Valianatos, F., Sarris, A., and Makris, J. (2007). Use of engineering geophysics to investigate a site for a building foundation. *Journal of Geophysics and Engineering*, 4(1):94–103.

- Sripanich, Y. and Vasconcelos, I. (2019). Effects of aperture on Marchenko focussing functions and their radiation behaviour at depth. *Geophysical Prospecting*, 67(2):443–454.
- Staring, M., Dukalski, M., Belonosov, M., Baardman, R., Yoo, J., Hegge, R., Borselen, R., and Wapenaar, K. (2020). R-EPsi and Marchenko equation-based workflow for multiple suppression in the case of a shallow water layer and a complex overburden: A 2D case study in the Arabian Gulf. *Geophysics*, 86(2):1–62.
- Staring, M. and Wapenaar, K. (2020). Three-dimensional Marchenko internal multiple attenuation on narrow azimuth streamer data of the Santos Basin, Brazil. *Geophysical Prospecting*, 68(6):1864–1877.
- Sullivan, A., Damarla, R., Geng, N., Dong, Y., and Carin, L. (2000). Ultrawide-band synthetic aperture radar for detection of unexploded ordnance: Modeling and measurements. *IEEE Transactions on Antennas and Propagation*, 48(9):1306–1315.
- Szabo, T. L. (2004). *Diagnostic ultrasound imaging: Inside out*. Academic Press.
- Tarantola, A. (1984). Inversion of seismic reflection data in the acoustic approximation. *Geophysics*, 49(8):1259–1266.
- Tataris, A. and van Leeuwen, T. (2022). A distributional Gelfand–Levitan–Marchenko equation for the Helmholtz scattering problem on the line. *Journal of Mathematical Physics*, 63(10):103507.
- Thomas, J.-L. and Fink, M. A. (1996). Ultrasonic beam focusing through tissue inhomogeneities with a time reversal mirror: Application to transskull therapy. *IEEE Transactions on Ultrasonics, Ferroelectrics, and Frequency Control*, 43(6):1122–1129.
- van den Berg, P. M. and Abubakar, A. (2001). Contrast source inversion method: State of art. *Progress in Electromagnetics Research*, 34:189–218.
- van der Neut, J., Brackenhoff, J., Meles, G., Zhang, L., Slob, E., and Wapenaar, K. (2021). On the benefits of auxiliary transmission data for Marchenko-based Green’s function retrieval. In *82nd EAGE Annual Conference & Exhibition*, volume 2021, pages 1–5. European Association of Geoscientists & Engineers.
- van der Neut, J., Brackenhoff, J., Meles, G. A., Slob, E., and Wapenaar, K. (2022). Marchenko Green’s function retrieval in layered elastic media from two-sided reflection and transmission data. *Applied Sciences*, 12(15):7824.
- van der Neut, J., Thorbecke, J., Wapenaar, K., and Slob, E. (2015a). Inversion of the multidimensional Marchenko equation. In *77th EAGE Conference and Exhibition 2015*, pages 1–5. European Association of Geoscientists & Engineers.
- van der Neut, J., Vasconcelos, I., and Wapenaar, K. (2015b). On Green’s function retrieval by iterative substitution of the coupled Marchenko equations. *Geophysical Journal International*, 203(2):792–813.

- van der Neut, J. and Wapenaar, K. (2016). Adaptive overburden elimination with the multidimensional Marchenko equation. *Geophysics*, 81(5):T265–T284.
- van IJsseldijk, J. and Wapenaar, K. (2021). Discerning small time-lapse traveltime changes by isolating the seismic response of a reservoir using the Marchenko method. In *First International Meeting for Applied Geoscience & Energy*, pages 3449–3453. Society of Exploration Geophysicists.
- van Leeuwen, T. (2019). A note on extended full waveform inversion. *arXiv preprint arXiv:1904.00363*.
- Vargas, D. and Vasconcelos, I. (2020). Rayleigh-Marchenko redatuming using scattered fields in highly complex media. In *82nd EAGE Conference and Exhibition 2020*, pages 1–5. European Association of Geoscientists & Engineers.
- Vargas, D., Vasconcelos, I., Sripanich, Y., and Ravasi, M. (2021). Scattering-based focusing for imaging in highly complex media from band-limited, multi-component data. *Geophysics*, 86(5):1–64.
- Vasconcelos, I., Snieder, R., and Douma, H. (2009). Representation theorems and Green’s function retrieval for scattering in acoustic media. *Physical Review E*, 80(3):036605.
- Vasconcelos, I. and Sripanich, Y. (2019). Scattering-based Marchenko for subsurface focusing and redatuming in highly complex media. In *81st EAGE Conference and Exhibition 2019*, volume 2019, pages 1–5. European Association of Geoscientists & Engineers.
- Vasconcelos, I., Wapenaar, K., van der Neut, J., Thomson, C., and Ravasi, M. (2015). Using inverse transmission matrices for Marchenko redatuming in highly complex media. In *SEG Technical Program Expanded Abstracts 2015*, pages 5081–5086. Society of Exploration Geophysicists.
- Verschuur, D. J., Berkhout, A., and Wapenaar, C. (1992). Adaptive surface-related multiple elimination. *Geophysics*, 57(9):1166–1177.
- Virieux, J., Asnaashari, A., Brossier, R., Métivier, L., Ribodetti, A., and Zhou, W. (2017). An introduction to full waveform inversion. In *Encyclopedia of Exploration Geophysics*, pages R1–1. Society of Exploration Geophysicists.
- Virieux, J. and Operto, S. (2009). An overview of full-waveform inversion in exploration geophysics. *Geophysics*, 74(6):WCC1–WCC26.
- Wang, G., Guo, Q., Alkhalifah, T., and Wang, S. (2020). Frequency-domain least-squares generalized internal multiple imaging with the energy norm. *Geophysics*, 85(4):S233–S240.
- Wapenaar, C. (1993). Kirchhoff-Helmholtz downward extrapolation in a layered medium with curved interfaces. *Geophysical Journal International*, 115(2):445–455.

- Wapenaar, K. (2007). General representations for wavefield modeling and inversion in geophysics. *Geophysics*, 72(5):SM5–SM17.
- Wapenaar, K. (2020a). The Marchenko method for evanescent waves. *Geophysical Journal International*, 223(2):1412–1417.
- Wapenaar, K. (2020b). Reciprocity and representation theorems for flux- and field-normalised decomposed wave fields. *Advances in Mathematical Physics*, 2020.
- Wapenaar, K. (2022). Wave-field representations with Green's functions, propagator matrices, and Marchenko-type focusing functions. *The Journal of the Acoustical Society of America*, 151(1):587–608.
- Wapenaar, K., Brogгинi, F., Slob, E., and Snieder, R. (2013). Three-dimensional single-sided Marchenko inverse scattering, data-driven focusing, Green's function retrieval, and their mutual relations. *Physical Review Letters*, 110(8):084301.
- Wapenaar, K., Brogгинi, F., and Snieder, R. (2012). Creating a virtual source inside a medium from reflection data: Heuristic derivation and stationary-phase analysis. *Geophysical Journal International*, 190(2):1020–1024.
- Wapenaar, K. and de Ridder, S. (2022). On the relation between the propagator matrix and the Marchenko focusing function. *Geophysics*, 87(2):A7–A11.
- Wapenaar, K. and Douma, H. (2012). A unified optical theorem for scalar and vectorial wave fields. *The Journal of the Acoustical Society of America*, 131(5):3611–3626.
- Wapenaar, K., Draganov, D., Snieder, R., Campman, X., and Verdel, A. (2010a). Tutorial on seismic interferometry: Part 1 – Basic principles and applications. *Geophysics*, 75(5):75A195–75A209.
- Wapenaar, K. and Fokkema, J. (2006). Green's function representations for seismic interferometry. *Geophysics*, 71(4):SI33–SI46.
- Wapenaar, K. and slob, E. (2015). Initial conditions for elastodynamic Green's function retrieval by the Marchenko method. In *SEG Technical Program Expanded Abstracts 2015*, pages 5074–5080. Society of Exploration Geophysicists.
- Wapenaar, K., Slob, E., and Snieder, R. (2008). Seismic and electromagnetic controlled-source interferometry in dissipative media. *Geophysical Prospecting*, 56(3):419–434.
- Wapenaar, K., Slob, E., Snieder, R., and Curtis, A. (2010b). Tutorial on seismic interferometry: Part 2 – Underlying theory and new advances. *Geophysics*, 75(5):75A211–75A227.
- Wapenaar, K., Snieder, R., de Ridder, S., and Slob, E. (2021). Green's function representations for Marchenko imaging without up/down decomposition. *Geophysical Journal International*, 227(1):184–203.
- Wapenaar, K. and Thorbecke, J. (2017). Virtual sources and their responses, Part I: Time-reversal acoustics and seismic interferometry. *Geophysical Prospecting*, 65(6):1411–1429.

- Wapenaar, K., Thorbecke, J., and van der Neut, J. (2016). A single-sided homogeneous Green's function representation for holographic imaging, inverse scattering, time-reversal acoustics and interferometric Green's function retrieval. *Geophysical Supplements to the Monthly Notices of the Royal Astronomical Society*, 205(1):531–535.
- Wapenaar, K., Thorbecke, J., van der Neut, J., Brogгинi, F., Slob, E., and Snieder, R. (2014a). Green's function retrieval from reflection data, in absence of a receiver at the virtual source position. *The Journal of the Acoustical Society of America*, 135(5):2847–2861.
- Wapenaar, K., Thorbecke, J., Van Der Neut, J., Brogгинi, F., Slob, E., and Snieder, R. (2014b). Marchenko imaging. *Geophysics*, 79(3):WA39–WA57.
- Wapenaar, K., Thorbecke, J., van der Neut, J., Slob, E., and Snieder, R. (2017). Virtual sources and their responses, Part II: Data-driven single-sided focusing. *Geophysical Prospecting*, 65(6):1430–1451.
- Wapenaar, K. and van der Neut, J. (2010). A representation for Green's function retrieval by multidimensional deconvolution. *The Journal of the Acoustical Society of America*, 128(6):EL366–EL371.
- Wapenaar, K., van der Neut, J., Ruigrok, E., Draganov, D., Hunziker, J., Slob, E., Thorbecke, J., and Snieder, R. (2011). Seismic interferometry by crosscorrelation and by multidimensional deconvolution: A systematic comparison. *Geophysical Journal International*, 185(3):1335–1364.
- Wapenaar, K. and van IJsseldijk, J. (2020). Discrete representations for Marchenko imaging of imperfectly sampled data. *Geophysics*, 85(2):A1–A5.
- Ware, J. A. and Aki, K. (1969). Continuous and discrete inverse-scattering problems in a stratified elastic medium. I. Plane waves at normal incidence. *The journal of the Acoustical Society of America*, 45(4):911–921.
- Warner, M. and Guasch, L. (2016). Adaptive waveform inversion: Theory. *Geophysics*, 81(6):R429–R445.
- Warner, M., Ratcliffe, A., Nangoo, T., Morgan, J., Umpleby, A., Shah, N., Vinje, V., Štekl, I., Guasch, L., Win, C., et al. (2013). Anisotropic 3D full-waveform inversion. *Geophysics*, 78(2):R59–R80.
- Weglein, A. B., Gasparotto, F. A., Carvalho, P. M., and Stolt, R. H. (1997). An inverse-scattering series method for attenuating multiples in seismic reflection data. *Geophysics*, 62(6):1975–1989.
- Wu, R.-S. and You, J. (2021). Time-boundary reflection/transmission and the dual fundamental solution in inverse scattering. In *First International Meeting for Applied Geoscience & Energy*, pages 3296–3300. Society of Exploration Geophysicists.
- Yao, G. and Jakubowicz, H. (2012). Non-linear least-squares reverse-time migration. In *2012 SEG Annual Meeting*. OnePetro.

- Yao, G., Wu, D., and Wang, S.-X. (2020). A review on reflection-waveform inversion. *Petroleum Science*, 17(2):334–351.
- Zhang, D. and Schuster, G. T. (2014). Least-squares reverse time migration of multiples. *Geophysics*, 79(1):S11–S21.
- Zhang, L. and Slob, E. (2019). Free-surface and internal multiple elimination in one step without adaptive subtraction. *Geophysics*, 84(1):A7–A11.
- Zhang, L., Slob, E., van der Neut, J., and Wapenaar, K. (2018). Artifact-free reverse time migration. *Geophysics*, 83(5):A65–A68.
- Zuberi, M. and Alkhalifah, T. (2014). Generalized internal multiple imaging (GIMI) using Feynman-like diagrams. *Geophysical Journal International*, 197(3):1582–1592.

ACKNOWLEDGEMENTS

There are a lot of people who contributed to this thesis in one way or another. Thanks go to **all of you**, even if you do not find your name explicitly below.

First of all, I want to thank **Ivan**. The last four years have been a great scientific journey and I am very happy with the direction our research has taken. Thank you for your continuous support, inspiration, guidance and motivation, for believing in me and challenging me. I hope we will stay in touch to not only talk about geophysics but also guitars and pop culture.

I initially met **Kees** when he gave a course on advanced geophysical imaging in Delft. It was a great course, and I was amazed by your clear and thorough explanations. Three years later, I am lucky enough to have had lots of conversations and discussions with you. I have learned very much from you and can not thank you enough for your insights and invaluable feedback on manuscripts.

The first time I met **Roel** in person was actually just before the end of my Ph.D. program. I went to Colorado School of Mines for a month, and it was inspiring beyond anything I had imagined – not least because of your course on science and spirituality. I deeply enjoyed our final research project and appreciate our conversations on science and everything beyond.

I also want to thank **Evert, Tristan, Andrew** and **Dom** for great scientific discussions and your help and input regarding our publications. Further thanks go to **Alison Malcolm, Andrew, Evert, Roel** and **Kees** for reading and supplying feedback on this thesis as well as to **Jeannot** for being my supervisor.

I had a great time with my UCSI colleagues: **Andreas**, thank you for multiple, delicious dinners, bike tours, walks through Utrecht and jam sessions! **David** and **Haorui**, thank you for countless discussions about science and all sorts of other things, nice lunches and funny evenings. And, of course, thank you both for paronyming me!

I also appreciate the discussions I had with **Joost, Aydin, Johno, Mert** and **Chris**. I thank **Janneke** for sharing an office and (no less important) a whiteboard. And of course big thanks to the seismology group: **Annemijn, Arie, Arwen, Ashim, Eldert** (thanks for your good coffee and checking my samenvatting!), **Elmer, Hanneke, Hen, Laura, Lisanne, Rens, Rhys, Rûna, Sahar, Simon, Su, Theo, Thomas** (special thanks for bike tours and conversations!), **Yanadet** and **Wen**. In particular I want to thank all those of you who joined for football every now and then! On that note thanks to **Alberto, Antoine, Boris** and **Dieuwertje** (I know I am missing some names here but I can find them neither on Teams nor in my memory – sorry). I also thank all colleagues from maths and medical imaging in the **IICU**.

Special thanks go to my former supervisor **Dirk**. Your generous support and motivation in my early academic life made this thesis possible in the first place. Similarly, thanks go to **Benjamin** and **Alex** for sparking the joy of science.

Further thanks go to **Fabian** for chess and football games, drinks and conversations.

Thank you, **Kostas**, for organising football! I want to thank **Tom** and **Helga** as well as **Paula**, **Jeff** and **Lisa** for their hospitality and friendship!

Further thanks go to all my friends in Bavaria, Hamburg, Berlin and elsewhere. Thanks to **Samuel** for saving the world nearly every Monday.

Special thanks go to my family: **Susanne** und **Benjamin**, ihr habt mich gefördert, mir als Vorbilder gedient und mir immer großzügig geholfen, wenn es irgendetwas zu helfen gab. Durch Corona ist sogar ein nicht unerheblicher Teil dieser Arbeit unter eurem Dach entstanden. Ich danke euch für alles! **Bella**, **Hannes** und **Juli**, ihr seid mir stets mit Rat und Tat zur Seite gestanden und immer für mich da gewesen. Um das an dieser Stelle einmal schriftlich festzuhalten: Das nächste Essen geht auf mich!

Let me start this last paragraph with a first sentence: It is a truth universally acknowledged, that I could not have done this thesis or anything else without **Laura**. You now are the very specimen of my hemispherical crex crex. Es waren wunderbare und aufregende vier Jahre zwischen London, Utrecht und Duitsland. I think the Kreuzbestäubung war äußerst successful.

CURRICULUM VITAE

PERSONAL DATA

Name Leon Daniel Diekmann
Date of birth 08.10.1993
Place of birth Erlangen, Germany

EDUCATION

2019 - 2023 Ph.D. Geophysics, Utrecht University
2016 - 2018 M.Sc. Geophysics, University of Hamburg
2012 - 2016 B.Sc. Geophysics and Oceanography, University of Hamburg

EMPLOYMENT

2023 - present R&D engineer, Carl Zeiss GOM Metrology GmbH
2018 - 2019 research associate, Institute for Geophysics, University of Hamburg
2015 - 2018 research assistant, Institute for Geophysics, University of Hamburg
2014 teaching assistant, Institute for Geophysics, University of Hamburg
2013 - 2014 research assistant, Institute for Nanostructure and Solid State Physics, University of Hamburg

JOURNAL ARTICLES

- Diekmann, L., Snieder, R. and Vasconcelos, I. (2023). Inverse design for directional source multipoles and wavefield focusing. *Physical Review E – under review*
- Diekmann, L., Vasconcelos, I. and van Leeuwen, T. (2023). A note on Marchenko-linearised full waveform inversion for imaging. *Geophysical Journal International*, 234(1): 228-242
- Diekmann, L. and Vasconcelos, I. (2023). Direct, wave-equation-based modeling of Marchenko-type focusing functions. *JASA Express Letters*, 3(2):024001
- Diekmann, L., Vasconcelos, I., Wapenaar, K., Slob, E. and Snieder, R. (2023). Wave-field focusing using a generalised, potentially asymmetric homogeneous Green's function. *Wave Motion*, 116: 103071

- Diekmann, L. and Vasconcelos, I. (2021). Focusing and Green's function retrieval in three-dimensional inverse scattering revisited: A single-sided Marchenko integral for the full wave field. *Physical Review Research*, 3(1): 013206
- Li, L., Tan, J., Schwarz, B., Stanek, F., Poiata, N., Shi, P., Diekmann, L., Eisner, L. and Gajewski, D. (2020). Recent advances and challenges of waveform-based seismic location methods at multiple scales. *Reviews of Geophysics*, 58(1): e2019RG000667
- Diekmann, L., Schwarz, B., Bauer, A. and Gajewski, D. (2019). Source localization and joint velocity model building using wavefront attributes. *Geophysical Journal International*, 219(2): 995-1007

EXPANDED ABSTRACTS

- Diekmann, L., Vasconcelos, I., Cummings, D. and Curtis, A. (2021). Towards exact linearized full-waveform inversion via Marchenko redatuming. In *SEG/AAPG/SEPM First International Meeting for Applied Geoscience & Energy*
- Diekmann, L. and Vasconcelos, I. (2021). Full-wavefield Marchenko using a generalized framework for focusing functions. In *SEG/AAPG/SEPM First International Meeting for Applied Geoscience & Energy*
- Diekmann, L. and Vasconcelos, I. (2020). Imaging with the exact linearised Lippmann-Schwinger integral by means of redatumed in-volume wavefields. In *SEG International Exposition and Annual Meeting*
- Bauer, A., Schwarz, B., Diekmann, L. and Gajewski, D. (2019). Wavefront tomography with enforced diffraction focusing. *81st EAGE Conference and Exhibition*
- Diekmann, L., Schwarz, B., Bauer, A. and Gajewski, D. (2018). Simultaneous model building and source localisation: A 3D synthetic case study. *SEG International Exposition and Annual Meeting*
- Diekmann, L., Schwarz, B., Bauer, A. and Gajewski, D. (2018). Source localisation and joint velocity model building. *80th EAGE Conference and Exhibition*

ORAL AND POSTER PRESENTATIONS

- AGU Fall Meeting, New Orleans, USA, 2021
- SEG Annual Meeting, Denver, USA, 2021
- SIAM Conference on Imaging Science, Toronto, Canada, 2020
- SEG Annual Meeting, Houston, USA, 2020
- 2nd EAGE/PESGB Workshop on Velocities, London, UK, 2019
- SEG Annual Meeting, Anaheim, USA, 2018
- EAGE Annual Meeting, Copenhagen, Denmark, 2018